INVESTIGATION OF SOLIDIFICATION DEFECT FORMATION BY THREE-DIMENSIONAL RECONSTRUCTION OF DENDRITIC STRUCTURES

by

Jonathan D. Madison

A dissertation submitted in partial fulfillment
of the requirements for the degree of
Doctor of Philosophy
(Materials Science and Engineering)
in The University of Michigan
2010

Doctoral Committee:

Professor Tresa M. Pollock, Chair
Professor Wei Shyy
Assistant Professor Katsuyo S. Thornton
Professor Peter W. Voorhees, Northwestern University

DEDICATION

To my wife and family, thank you all so much for your support.

ACKNOWLEDGEMENTS

This work would not have been possible were it not for the contributions of so many. Special appreciation is due to Tresa Pollock, for her guidance, mentorship, and having the foresight to invest in whom I could become and not simply who I was. Thank you Professor J. Wayne Jones for countless exchanges and the inspiring way you touch others with not only your work, but also your service, your life and your resources. Many thanks are due to the unparalleled technical expertise of C. Torbet. Much recognition to all the members of the Pollock and Jones research group present during my matriculation whom each taught me something valuable; A. Adharapurapu, C. Brundidge, F. Cao, D. Das, J. Dibbern, M. Echlin, A. Elliott, Q. Feng, P. Fetchko, S. Johnson, J. Kim, R. Kozar, S. Ma, J. Miao, J. Miller, L.J. Rowland (Carroll), N. Saddock, C. Szczepanski, A. Suzuki, B. Tryon, J. Ter-Bush, W. Tu, J. Van Sluytman, D. Widrevitz, A. Wu, J. Yi, X. Zhu. To those who came before, whose work was instrumental in this thesis, S. Tin and A. Elliott, additional salutations are due. Your work provided vital foundations for this thesis. Additional thanks to our associates at Sophisticated Alloys, Inc. as well as L. Graham and T. Van Vranken at PCC Airfoils, Inc. for their assistance.

Project funding from the Air Force Office Scientific Research (AFOSR) grant number FA9550-05-1-0104 and student support from the Office of Naval Research - Historically Black Engineering College Future Faculty Fellowship (ONR-HBECFF) are also both gratefully acknowledged.

TABLE OF CONTENTS

CHAPTER 6
NI-AL-W TERNARY RESULTS 104

CHAPTER 7
DISCUSSION AND CONCLUSIONS 145

CHAPTER 8
RECOMMENDATIONS FOR FUTURE WORK 174

LIST OF FIGURES

LIST OF TABLES

ABSTRACT

INVESTIGATION OF SOLIDIFICATION DEFECT FORMATION BY THREE-DIMENSIONAL RECONSTRUCTION OF DENDRITIC STRUCTURES

by

Jonathan D. Madison

Chair: Tresa M. Pollock

Convective flow within the mushy zone of directionally solidified superalloys can result in the formation of freckles and misoriented grains. These defects signal not only a disruption in the columnar or single crystal nature of the component but also a tendency toward reduction in life and performance. Approximations of the onset of convective flow in the mush have primarily used the Rayleigh criteria as a predictor for the occurrence of freckles. However, a detailed understanding of fluid flow at the scale of the dendritic structure is still lacking. This research utilizes three-dimensional dendritic structures obtained from the solid-liquid interface of directionally solidified nickel-base superalloys as direct inputs to fluid flow models. These models have been utilized to assess the permeability of the dendritic array. Implications of simulations will be discussed with reference to the Rayleigh criteria and freckle prediction.

CHAPTER 1

INTRODUCTION

1.1 METALLURGY OF SUPERALLOYS

1.1.1 Chemistry and Composition

Nickel-base superalloys are highly favored materials in the design and production of components for high temperature application. Components that experience high temperature and stress within land-based power systems, space propulsion systems and aircraft turbine engines are of particular importance. While these superalloys may be employed in various applications, there are common characteristics of chemistry and composition beyond their 50% – 75% nickel content. Generally, nickel-based superalloys have additions of aluminum in the range of 3 – 8 wt%, chromium in the range of 6 – 20 wt%, and typically smaller levels of titanium between 1 – 5 wt%. Additions of refractory elements such rhenium, tantalum and tungsten have been shown to increase strength at elevated temperatures. However, these alloying elements must be carefully controlled as they also have shown a tendency to induce defects during solidification in nickel-based superalloys [1, 2]. Additional elements such as carbon, boron and zirconium may be added in small quantities but are consistently present in controlled amounts for the control of microstructure, grain structure and mechanical properties [3]. These superalloys owe their exceptionally high strength to ordered intermetallic precipitates of

Ni_3Al, commonly referred to as γ'. The morphology and high volume fraction of γ' within the microstructure of these nickel-based alloys provide resistance to glide and climb of dislocations at both ambient and elevated temperatures. Figure 1 shows an example of this typical two-phase microstructure. As a summary, Figure 2 [3] illustrates the chemical role of major alloying elements in nickel-based superalloys while Table 1 [4-9] lists a representative set of commercial cast nickel-based superalloys and their nominal compositions by weight percent [8].

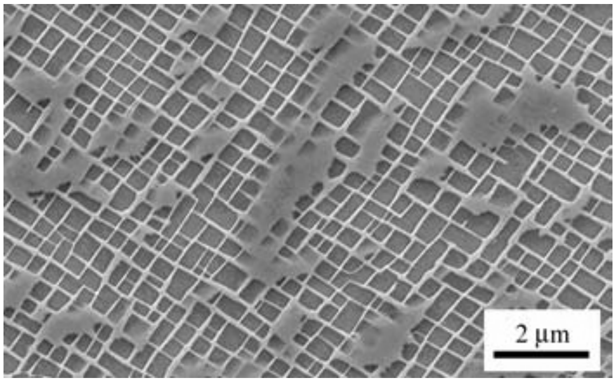

Figure 1.1 - Typical Ni-based superalloy microstructure with cuboidal γ' (Ni_3Al) precipitates dispersed throughout a γ matrix **[10]**

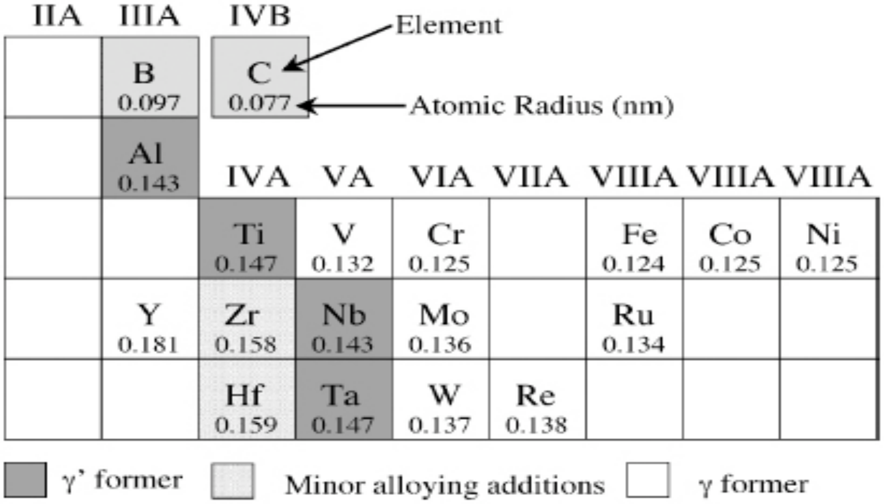

Figure 1.2 - Role of specific alloying elements in Ni-based superalloys **[11]**

Table 1.1 - Compositions of Selected Commercial Cast Nickel-Based Superalloys (*wt %*) **[8]**

Alloy	Cr	Co	Mo	W	Ta	Re	Nb	Al	Ti	Hf	C	B	Y	Zr	Ni
Conventionally Cast Superalloys															
Mar-M246	8.3	10.0	0.7	10.0	3.0	--	--	5.5	1.0	1.50	0.14	0.02	--	0.05	Bal.
IN-100	10.0	15.0	3.0	--	--	--	--	5.5	4.7	--	0.18	0.01	--	0.06	Bal.
René 80	14.0	9.5	4.0	4.0	--	--	--	3.0	5.0	--	0.17	0.02	--	0.03	Bal.
Directionally Solidified Superalloys															
IN792	12.6	9.0	1.9	4.3	4.3	--	--	3.4	4.0	1.00	0.09	0.02	--	0.06	Bal.
GTD 111	14.0	9.5	1.5	3.8	2.8	--	--	3.0	4.9	--	0.10	0.01	--	--	Bal.
First Generation Single Crystal Superalloys															
PWA 1480	10.0	5.0	--	4.0	12.0	--	--	5.0	1.5	--	--	--	--	--	Bal.
René N4	9.8	7.5	1.5	6.0	4.8	--	0.5	4.2	3.5	0.15	0.05	--	--	--	Bal.
CMSX-3	8.0	5.0	0.6	8.0	6.0	--	--	5.6	1.0	0.10	--	--	--	--	Bal.
Second Generation Single Crystal Superalloys															
PWA 1484	5.0	10.0	2.0	6.0	9.0	3.0	--	5.6	--	0.10	--	--	--	--	Bal.
René N5	7.0	7.5	1.5	5.0	6.5	3.0	--	6.2	--	0.15	0.05	--	0.01	--	Bal.
CMSX-4	6.5	9.0	0.6	6.0	6.5	3.0	--	5.6	1.0	0.10	--	--	--	--	Bal.
Third Generation Single Crystal Superalloys															
René N6	4.2	12.5	1.4	6.0	7.2	5.4	--	5.8	--	0.15	0.05	--	0.01	--	Bal.
CMSX-10	2.0	3.0	0.4	5.0	8.0	6.0	0.1	5.7	0.2	0.03	--	--	--	--	Bal.

1.1.2 Segregation and Solute Redistribution

Commercial processing of the alloys listed in Table 1 typically includes several melting and/or casting operations which occur via dendritic solidification. Neglecting situations in which high rate solidification with solute trapping exists, preferential rejection of solute into the liquid or depletion into the solid will occur during solidification. The solute redistribution is determined by the thermodynamics of the phases present and the kinetics of the diffusional redistribution process. This is chiefly quantified by the segregation or distribution coefficient, which is defined as the ratio of solute concentration in the solid phase to that in the liquid phase under equilibrium conditions [12], and is generally denoted as:

$$k = \left(\frac{C_s}{C_l}\right)_{T,P} \tag{1.1}$$

Assuming a binary system with a finite solid+liquid field, when the liquidus slope is negative and the distribution coefficient is smaller than 1, solute segregates to the liquid. When the liquidus slope is positive and the distribution coefficient is greater than 1, solute segregates into the solid [13]. The role of this segregation as a driving force for dendritic solidification and defect formation will be discussed in greater detail in Section 2.1.1. However, these changes in composition in the vicinity of the solid/liquid interface result in solidified structures possessing spatial variations in composition that differ in scale with local solidification time. Therefore interdendritic regions, which are the last to solidify, may possess a very different chemical composition when compared to the neighboring dendrite core.

1.2 DIRECTIONAL SOLIDIFICATION OF SUPERALLOYS

The intrinsically favorable properties of nickel-based superalloys have been continuously improved via advances in processing. A particular process to bring substantial improvement to the performance of this alloy class has been directional solidification. While there are a number of processing approaches that achieve directional solidification, the principal factors involved are fairly universal. Molten alloy is poured into a pre-heated ceramic mold with an open bottom. This mold rests upon a chill plate in order to allow rapid grain nucleation at the base of the mold. Resultant growth is most favored in the direction of the thermal gradient, which is maintained by lowering the mold out of the heated zone. In cases in which a single crystal is desired, the mold geometry at the base is such that only a particular orientation will grow unimpeded [14, 15]. Illustrations of these processes are included in Figure 1.3 [14].

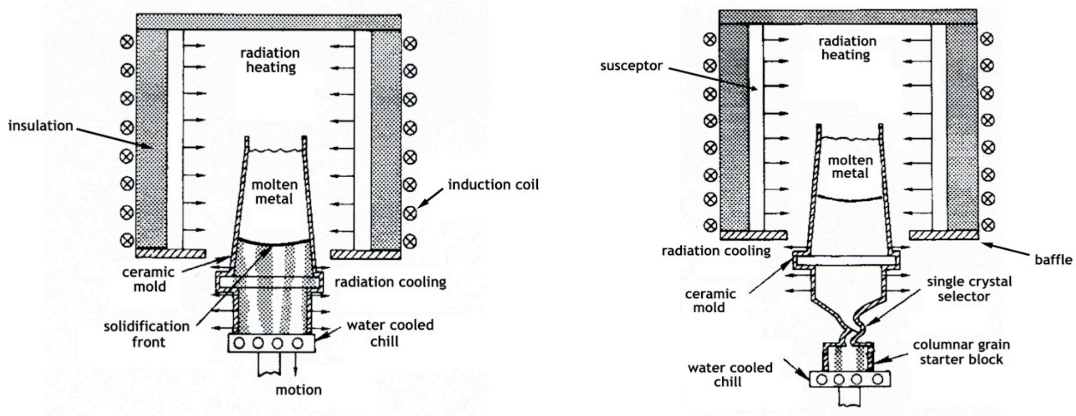

(a) **(b)**

Figure 1.3 - Schematic diagram of directional solidification for the casting of (a) columnar grains and (b) single crystals **[6]**

Damage accumulation along grain boundaries during high temperature operation is typical in turbine blade components. As a result, it has been found that orienting grain boundaries along the direction of applied stress by directional solidification improves high temperature creep properties. Furthermore, complete removal of these boundaries has provided further benefit. The improvements of creep and fatigue properties in directionally solidified materials are summarized in Figures 1.4 and 1.5, respectively [14, 16].

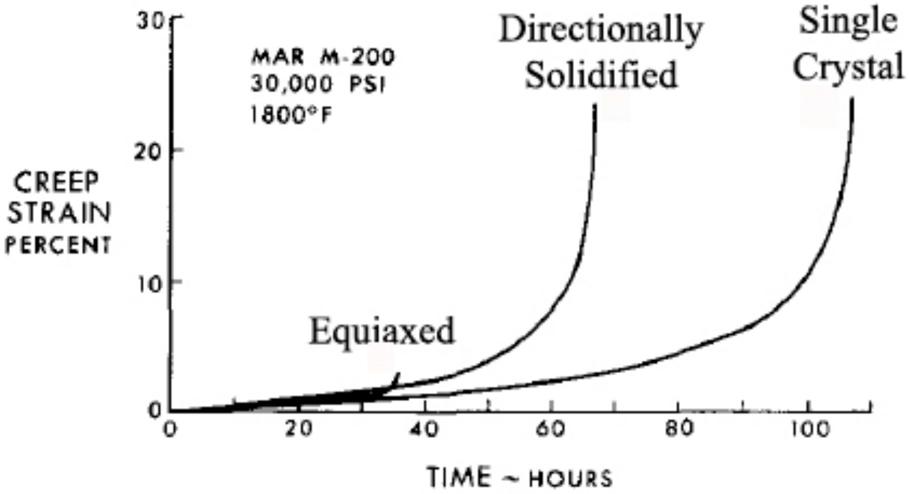

Figure 1.4 - Creep rupture curves for a Ni-based superalloy for three sample types; 1) equiaxed, 2) directionally solidified and 3) single crystal **[15]**

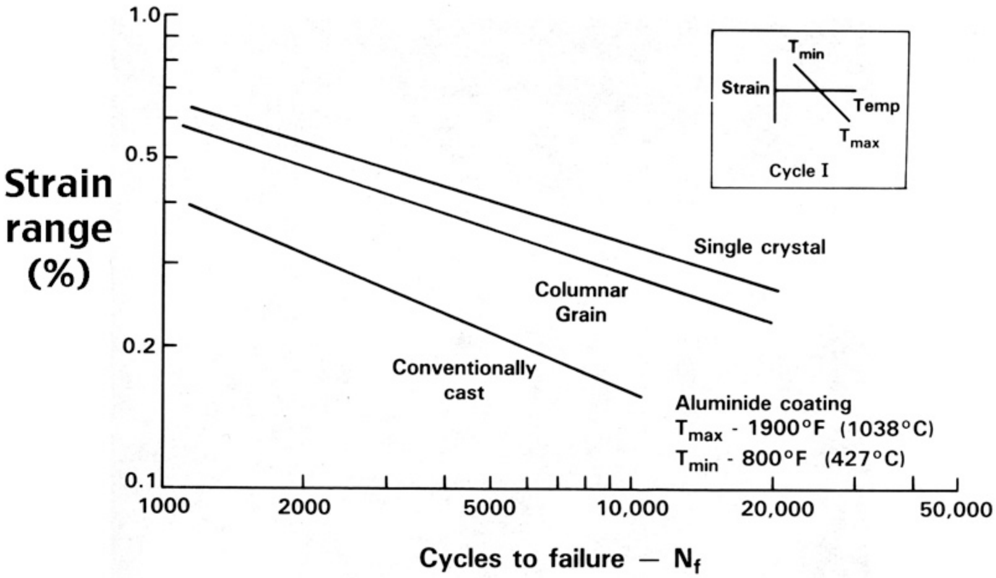

Figure 1.5 - Comparison of thermal fatigue for conventionally cast, columnar grain and single crystal castings **[14]**

These improvements in mechanical response and overall strength in extreme environments have come largely due to the development of directionally solidified and single crystal casting techniques [3, 16]. Additionally, concurrent alloy development has enabled further advances in alloy properties.

1.3 DEFECTS ASSOCIATED WITH SOLIDIFICATION OF SUPERALLOYS

The performance of directionally solidified or single crystal castings is particularly sensitive to grain defects that form during solidification, including misoriented high angle grains or freckle chains. The opportunity for the formation of such defects can be directly related to slower cooling rates, which characteristically produce coarser dendritic structures, Figure 6 [2]. These coarser structures can also yield coarser interdendritic porosity.

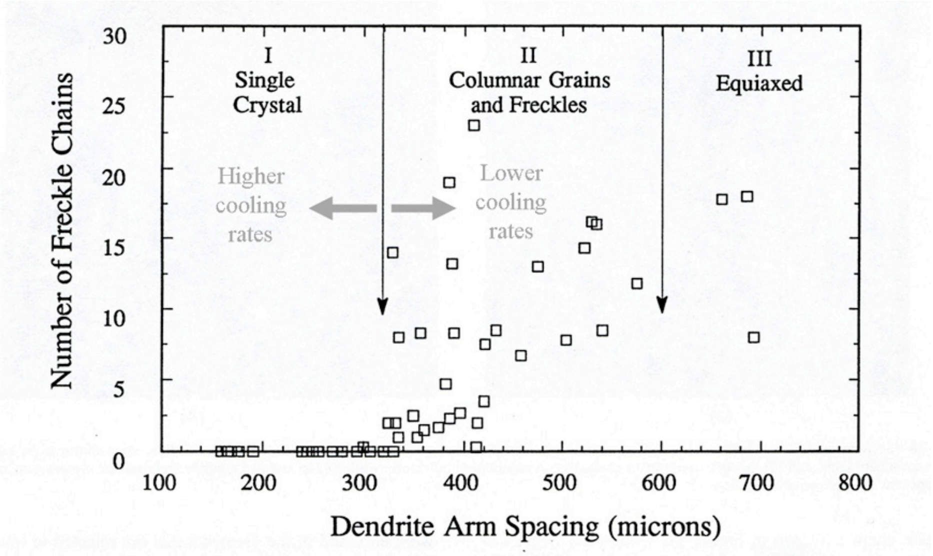

Figure 1.6 - Freckle chain quantity as a function of primary dendrite arm spacing **[2]**

Increasing levels of refractory alloying additions in nickel-base superalloys combined with increased size and complexity of cast components have made grain defects a problem of growing significance and the subject of a number of investigations [1, 8, 17, 18]. Studies have also shown that solidification conditions may reduce fatigue life due to porosity in interdendritic regions [19]. Other studies have linked coarser dendrite arm spacing with reduced corrosion resistance [20] and creep [21]. Thus, an understanding of the composition, structure and effect of defects on mechanical properties is important and has implications for optimization of composition, processing and microstructure.

Similarly, mechanisms of defect formation, including convective instabilities related to fluid flow are of equal importance. To this end, the details of the dendritic microstructure and its relation to processing environment is important and can provide insight into defect formation mechanisms as well as opportunities to mitigate and prevent their occurrence as well as improve high temperature properties. Increased understanding of the processes that occur at the scale of the dendritic structure is needed for further progress in the formulation of defect-prediction models.

1.4 THREE-DIMENSIONAL RECONSTRUCTIONS FOR MICROSTRUCTURAL STUDY

In this research, three-dimensional reconstructions will be used to examine solidification of single crystals with particular emphasis on the development of the dendritic structure at the solidification front. Characterization of these reconstructions will provide an improved understanding of dendritic structures at the solid-liquid interface under realistic directional solidification conditions. Additionally, the reconstructions themselves will serve as direct inputs for fluid flow models offering new insights on dependence of permeability on dendritic structure in this class of alloys. Ultimately, the effects of dendritic morphology and arrangement on flow within the mushy zone will be quantified and the implications for optimization of solidification processing conditions will be addressed. Chapter 2 will provide background information including an overview of solidification, details related to defect formation and prediction as well as a literature review of three-dimensional reconstructions development and advances in fluid flow modeling in dendritic networks. Chapters 3 and 4 will address the components of the experimental procedure and simulation protocols while results for both material systems used in this work will be presented in Chapters 5 and 6 respectively. Discussion and recommendations for further investigation follow in the final chapter.

CHAPTER 2

BACKGROUND

2.1 SOLIDIFICATION

During solidification, the interface between solid and liquid is highly sensitive to temperature gradients in the liquid. While ideally planar, the solid-liquid interface rarely remains so, as variations in growth rate and thermal gradient play large roles in not only the solidification morphology but also in solute distribution and local fluid flow conditions. This variation in interfacial shape is particularly complex, especially in alloys with multiple alloying elements with varying atomic weights and densities. The role of solute in multicomponent alloys is addressed in the following sections.

2.1.1 Constitutional Supercooling

As metallic alloys solidify, solute is rejected into or depleted from the liquid. Depending on solute diffusivity and solute concentration the equilibrium temperature ahead of the solidification front will vary. While overall liquid temperature may be controlled by external factors, there exists a local temperature gradient governed by the alloy composition immediately ahead of the solidification front. When the externally imposed temperature is less than the local equilibrium temperature, the conditions required for growth of protrusions on a planar interface are met, Figure 2.1 [22]. This solute induced change in local solidification temperature is known as constitutional supercooling [22-24].

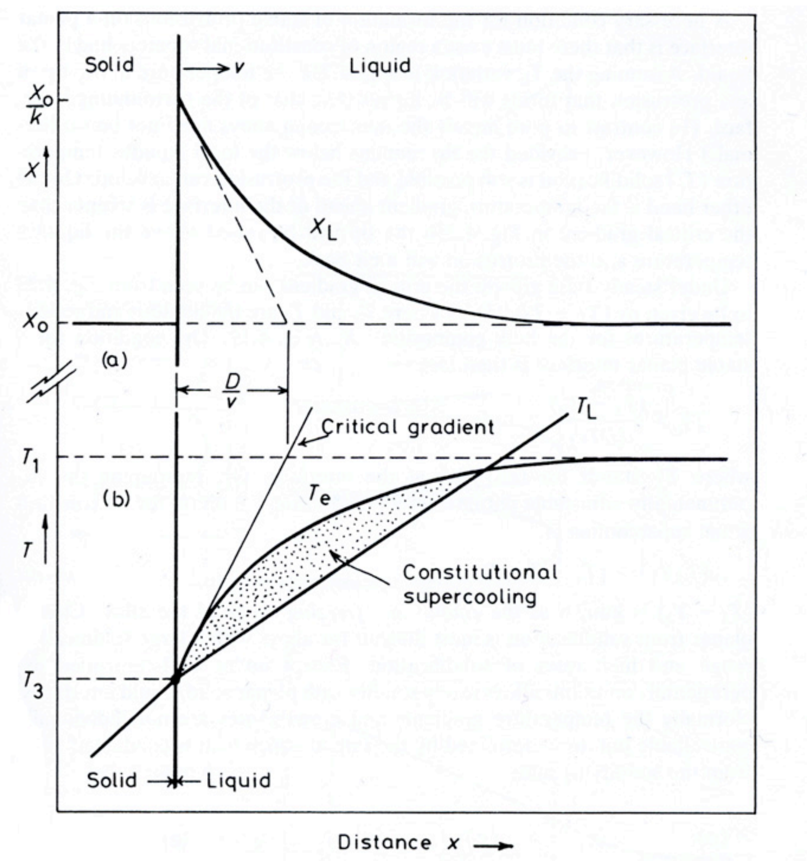

Figure 2.1 - Origin of constitutional supercooling ahead of a planar solidification front. (a) Composition profile across solid/liquid interface during steady-state solidification. (b) Equilibrium liquidus temperature shown by T_e and overall liquid temperature shown by T_L. Constitutional supercooling occurs when $T_L < T_e$ **[22]**

Beyond the initial breakdown of the planar solidification front, the thermal gradient (G) and growth rate or solidification front velocity (V) ultimately determine the morphology of the solidifying structure. In the following section, the characteristic variations of morphology will be discussed in terms of G and V. Regardless of the morphology, the region in which liquid and solid coexist is commonly referred to as the "mushy zone." It is by definition the region in which solid and liquid both exist under a range of temperatures related to concentration differences resulting from solute redistribution, Figure 2.2 [13].

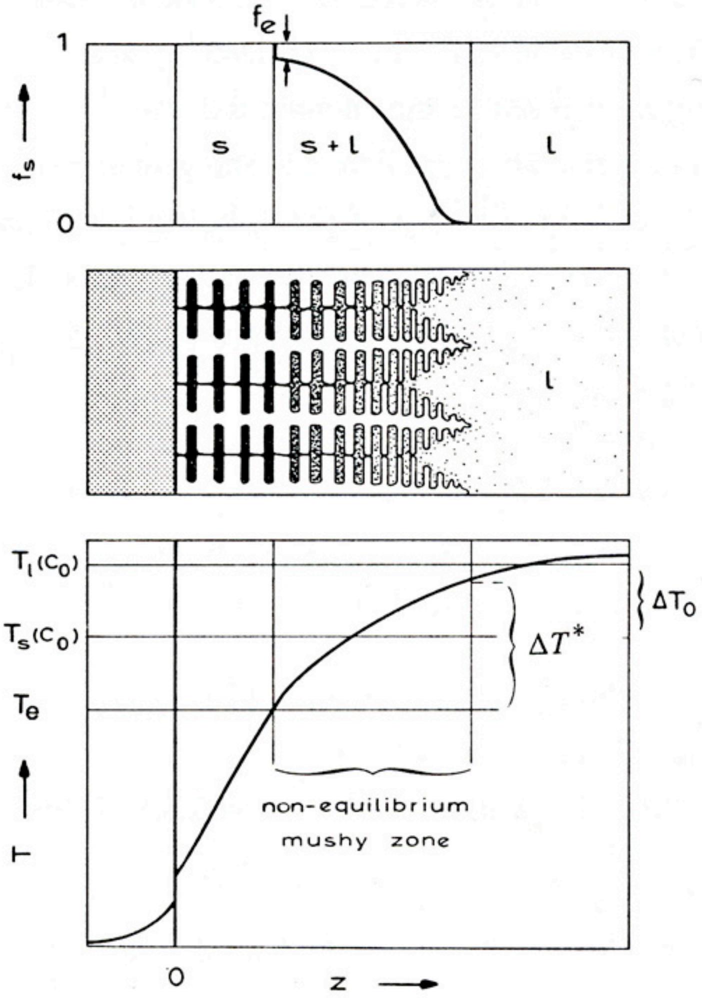

Figure 2.2 - Visualization of the equilibrium melting temperature over which the mushy zone develops. Upper images show representative dendritic structures and solid/liquid phase profile **[13]**

2.1.2 Cellular, Dendritic and Equiaxed Structures

Figure 2.3 provides useful insight into the relationship between G & V and cellular, dendritic and equiaxed cast morphologies. At high thermal gradient and low growth rate, planar front solidification occurs. When G is decreased and V is increased, cellular structures are produced.

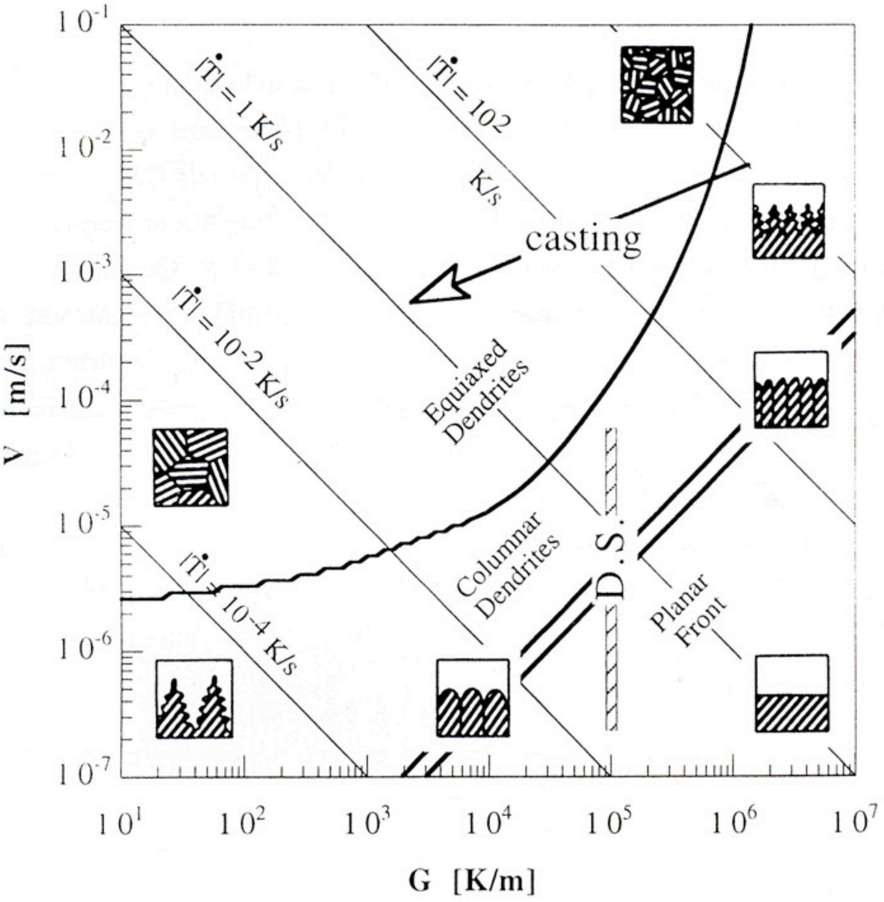

Figure 2.3 - Variation in single-phase solidification morphologies as a function of thermal gradient (G) and growth rate (V) **[25]**

This begins by the planar solid-liquid interface developing small ripples or perturbations. As the solidification process continues, these ripples can develop into semi-periodic "cells" which may begin with a rounded tip but later develop a faceted structure. A schematic diagram of the solid-liquid interface showing this transition between rounded and faceted cells is shown in Figure 2.4 [23].

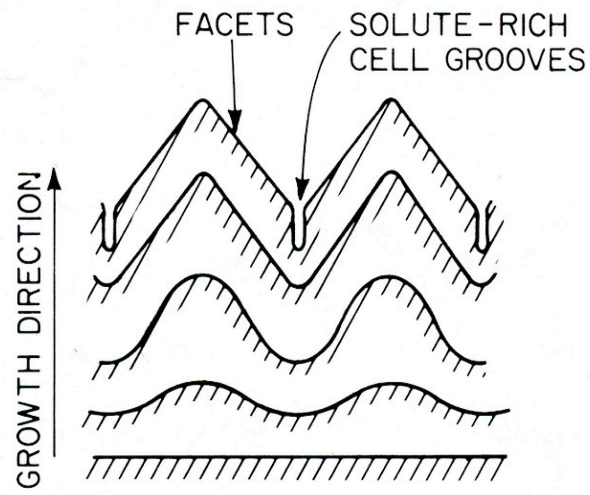

Figure 2.4 - Diagram of liquid-solid interface at increasing time illustrating the transition from planar to faceted cellular interface **[23]**

In situations in which the thermal gradient is even lower, dendritic structures can appear, if the growth rate is sufficiently low. Alternatively if the thermal gradient is high, dendritic growth can still occur with accompanying high growth rates. Again, the regimes for dendritic growth are displayed in Figure 2.3. It should be pointed out that dendrites exist over a wide range of G and V bounded by the conditions for cellular and equiaxed structures. For dendritic structures, however, the preferred crystallography of the material manifests itself in the direction(s) of growth [25]. Cubic materials, whether face-centered or body-centered share a preferred growth direction; < 1 0 0 >. Dendritic structures are chiefly recognized by their characteristic four-fold, cross structure normal to the growth direction. As growth continues, additional periodic disruptions emerge resulting in side branches parallel to the solid-liquid interface and perpendicular to the initial cell, Figure 2.5 [26]. An example of a prototypical dendritic structure is shown in an image of a transparent compound directionally grown by Huang and Glicksman in Figure 2.6, [27]. Lastly, at low values of G, and high values of V, equiaxed structures appear in which there is no overall directionality of the solidified structures.

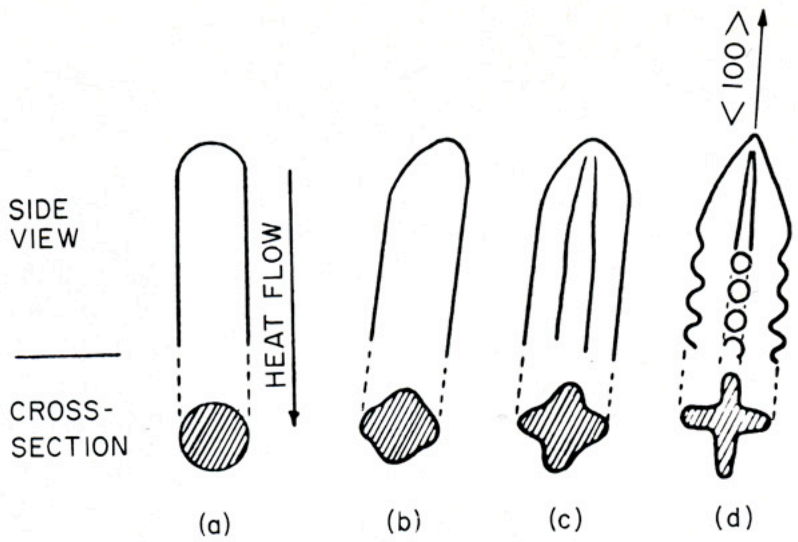

Figure 2.5 - Evolution of dendrite morphology from cell structure to flanged cross section (a) regular cell growing at low velocity; (b) regular cell growing in <100> direction; (c) flanged cell; (d) dendrite with periodic lateral branching **[26]**

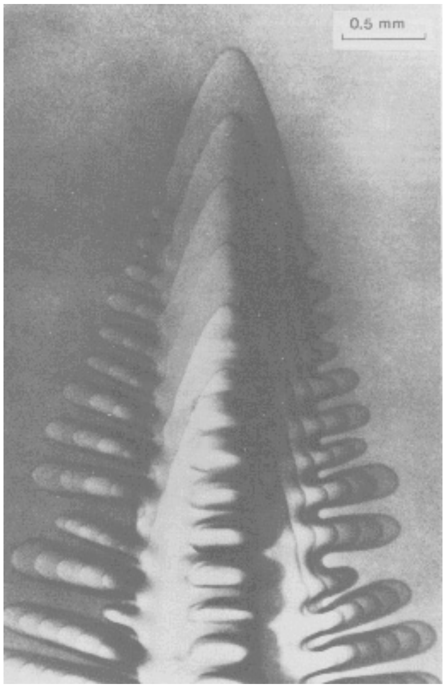

Figure 2.6 - Superimposed images of a succinonitrile dendrite growing along the <100> with orthogonal side branching in the <100> directions **[27]**

2.1.3 Dendritic Characterization

There have been fairly extensive characterization studies of experimentally produced dendritic structures [28-32]. More recently, modeling of solidification for prediction of the development of these structures has emerged as an important means of controlling and optimizing structure [33-39]. Regardless of approach, the imposed thermal gradient (G) and growth rate (V) remain primary factors in the description and correlation of most characterization models. This is due to the fact that growth rate and thermal gradient both play large roles in the resultant dendritic structure, and as a result, most characterization metrics reflect these items. The most common measures are primary dendrite arm spacing (PDAS) and secondary dendrite arm spacing (SDAS) and these are frequently used to quantify solidification phenomena across many disciplines and applications [17, 29, 31, 40-45]. As previously discussed, cells grow opposite the direction of heat flow and those that form first are chiefly referred to as “primary” dendrites. Side branches that grow from these are termed “secondary” dendrites. Under some thermal conditions, these secondary arms may form tertiary and higher-order dendrites as well. The PDAS and SDAS are useful because they allow a uniform metric for correlation of solidification phenomena with properties such as fatigue life, creep resistance, strength and grain size. Additionally, it is well documented that spacing of primary, secondary and tertiary arms vary in a predictable manner with G and V. Although variations in the general form of the models for dendrite formation exist [25, 46], the product of G and V to a given power can be scaled by a constant to derive the arm spacing, Equation 2.1.

$$\lambda_{1,2,3} = a t_f^n = b(GV)^{-n} \tag{2.1}$$

The constant, *b* is typically empirically determined by alloy composition, however, the overall basis of the relationship exists due to an ability to relate length in the thermal gradient term to length scale implicit in the solidification tip velocity. This relationship is summarized in Equation 2.1. Solidification time is given by t_f in units of seconds and λ_1 , λ_2, λ_3, are the arm spacings for primary, secondary and tertiary dendrites respectively in units of micrometers. The appropriate value of the exponent *n* depends on the order of dendrite sought after and generally ranges from $^1/_3$ to $^1/_2$ for secondary spacing and is usually on the order of $^1/_4$ and/or $^1/_2$ for primary spacing. For a collection of experiments on nickel-base single crystals within a Bridgman furnace at the University of Michigan, the PDAS and SDAS were found to vary with G and V according to the above relationship with the following values of *b* and *n.*

$$\lambda_1 = 2500(G^{-1/2} * V^{-1/4}) \tag{2.2}$$

$$\lambda_2 = 40(G * V)^{-1/3} \tag{2.3}$$

Values of G are in units of °C/m and V are in units of m/s. Primary and secondary dendrite arm spacings were measured [47], and shown to be in good agreement with the relationships denoted in Equations 2.2 and 2.3 (See Figure 2.7 and Figure 2.8).

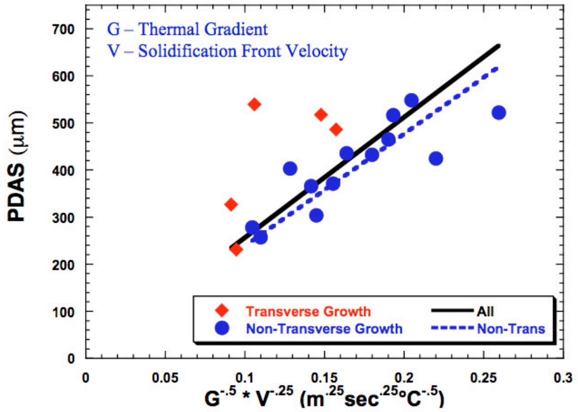

Figure 2.7 - Experimental Primary Dendrite Arm Spacing from castings in the University of Michigan's Bridgman Furnace in LMC Mode **[47]**

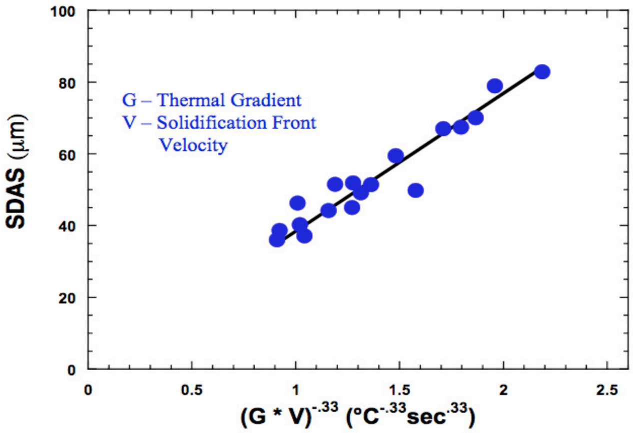

Figure 2.8 - Experimental Secondary Dendrite Arm Spacing from castings in the University of Michigan's Bridgman Furnace in LMC Mode **[47]**

2.1.4 Solidification-Induced Defects

Microstructural defects are of particular concern in the processing of single crystal and directionally solidified castings. Their presence can have deleterious effects on the mechanical properties of castings [8, 16, 48]. In this thesis, chimneys, freckles and freckle-chains are the defects of interest. Chimneys are isolated channels possessing varying chemistry and are produced by localized and comparatively accelerated upward flow through the solidification front. Freckles generally result from this phenomenon and are visually identified as small equiaxed singular or collective chains of grains aligned along the solidification direction. They consist of high angle boundary grains possessing an orientation different than the parent grain and typically are enriched in interdendritic solute. Since freckle formation is generally preceded by transport of solute via chimney formation, it should be mentioned that these local increases in fluid velocity may also fragment and transport dendritic side branches, allowing for reorientation thereby, causing multiple equiaxed grains to form. Collections of freckles are typically called, “freckle chains” [16, 49]. Illustrations of a freckle and freckle-chain are shown in Figure 2.9 [8, 48, 50]. Figure 2.10 illustrates precursory chimneys [51]. While such defects may occur at any location in the directionally solidified casting, they most frequently occur along or near the mold wall, where geometry and thermal profile experience the greatest variation.

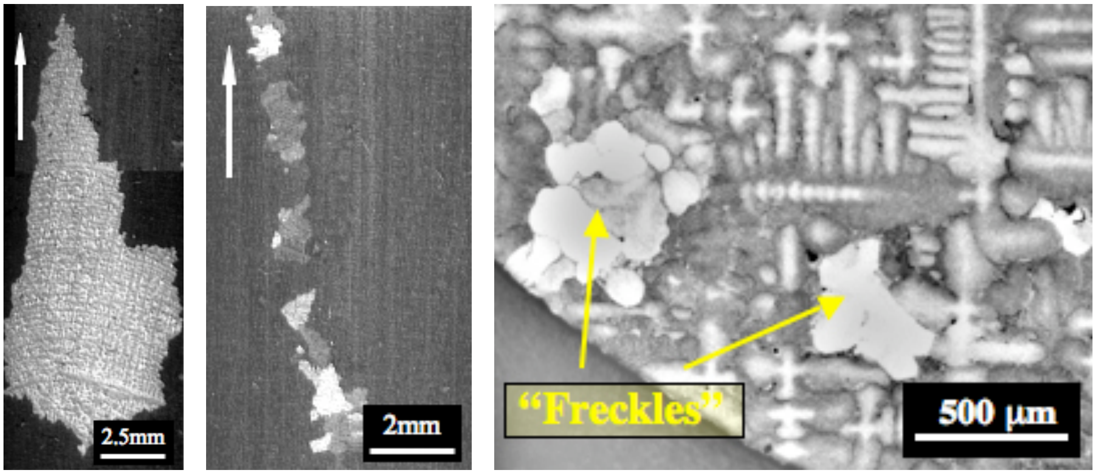

(a) (b) (c)

Figure 2.9 - Solidification Defects – arrows illustrate solidification direction where applicable; (a) Single misoriented grain; (b) Freckle chain **[8]** and (c) Transverse view of a freckle chain (Pollock, unpublished)

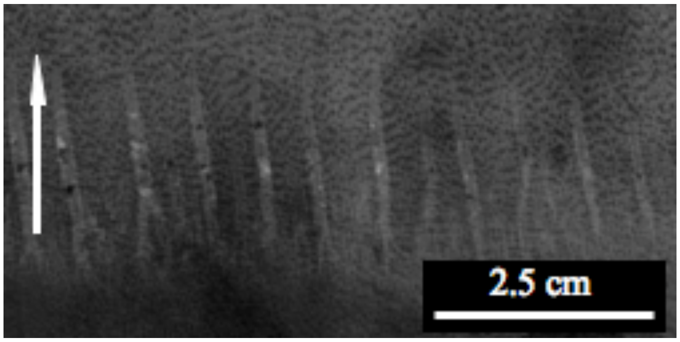

Figure 2.10 - Convection induced channels in a plate-shaped superalloy sample. Some channels possess greater degrees of porosity and/or carry greater amounts of solidified fragments to produce additional freckles or freckle chains (Pollock, unpublished)

The upward fluid flow is thermodynamically and hydrodynamically driven and results in segregation of specific alloying elements causing a density inversion allowing streams of high convection to pass upwards through the melt [16, 49, 50]. Investigations of freckles in nickel-based superalloys have shown that aluminum and titanium preferentially segregate to the interdendritic solute while tungsten and rhenium are preferentially depleted from the liquid [2, 49, 50]. These distributions of heavier elements nearer the dendrite tips above lighter elements deeper in the mushy zone create the necessary environment for the onset of convective instabilities and resulting freckles. It follows that complex solid-liquid interface shapes resulting from intricate mold geometries as well as convective instabilities encouraged by the addition of refractory elements not only enhance the opportunity for defect formation but also provide additional parameters to vary for the control of such defects [1, 11, 17].

2.1.5 Dimensionless Numbers in Fluid Flow

As mentioned briefly above, convection and local fluid flow play a fundamental role in the formation of freckles. Similarly, fluid flow on a larger scale is an important aspect of the solidification process. As discussed earlier, diffusion of solute into liquid during solidification lowers the equilibrium temperature and provides a driving force for the formation of cells or dendrites. Solute segregation also produces density variations in the liquid that incite flow. As a result, dissimilar buoyancies are unavoidable as motion within the liquid due to inertia is present as supercooling develops. Therefore, characterization of fluid flow is important for developing full control of solidification, including predictive modeling tools. Fluid flow is typically characterized in terms of dimensionless numbers; the relevant quantities for this class of solidification problems include the Grashof number (N_{GR}) the Prandtl number (N_{PR}) and the Rayleigh number (N_{RA}). The first two numbers are functions of independent measured properties while the third is a product of the previous two. The three important dimensionless quantities are defined as follows; [52].

Grashof number $$N_{GR} = \frac{g_r L^3 \beta_t \Delta T}{v^2} \tag{2.4}$$

Prandtl number $$N_{PR} = \frac{c' \mu}{K_L} \tag{2.5}$$

Rayleigh number $$N_{RA} = N_{GR} \cdot N_{PR} \tag{2.6}$$

The properties contained in the Grashof number include: g_r which is the acceleration due to gravity; L, characteristic length of the system; β_t, the coefficient of thermal expansion and v is the kinematic viscosity. For the Prandtl number, c' is specific heat while μ is viscosity and K_L is the liquid thermal conductivity [52]. While all three quantities: Grashof, Prandtl and Rayleigh numbers are dimensionless values, the Grashof number is a ratio of buoyancy to viscous forces while the Prandtl number is a ratio of the viscous diffusivity and thermal diffusivity. When these terms are multiplied the product of the two; the Rayleigh number, is a measure of the ratio between thermal buoyancy force and viscous force in the liquid [53, 54]. With these and other quantitative descriptors of the melt, these dimensionless numbers are useful for understanding regimes of fluid flow, convective instabilities, solidification, compositional segregation and a host of additional solidification phenomena [55-65]. From among these, the Rayleigh number has emerged as a useful predictor of convective instabilities that lead to freckle formation. This predictor has been employed in a number of studies in a number of forms [56, 60-62, 65, 66]. Many of these studies use an explicit definition for the Rayleigh number tailored specifically to the multicomponent solidification process in a form introduced initially by Worster [67]:

$$Ra_h = \frac{(\Delta\rho / \rho_o) g \overline{K} h}{\alpha v} \tag{2.7}$$

The Rayleigh number is an average taken over the entire height, or some fraction of, the mushy zone, denoted by h. The term ($\Delta\rho/\rho_o$) represents the density gradient in the liquid, (g) acceleration due to gravity, (α) thermal diffusivity, and (v) kinematic viscosity. The term (K) is the average permeability and is the only factor contained in the equation that is not typically derived directly from the chemistry of the system. The permeability is usually defined empirically with consideration of flow through porous media. Additionally, the suitability of alternative length scales other than mushy zone height for the characteristic height (h) in the Rayleigh number has been investigated [62, 68]. In the first instance of such an evaluation in both Pb-Sn and Ni-base alloys, it was concluded the ratio of the thermal diffusivity to withdrawal rate as the characteristic length scale for the Rayleigh criterion showed the greatest applicability to the widest set of data, with exception to the experimental results of Pollock and Murphy [2]. For these cases, the use of the mushy zone height as the characteristic height (h) performed best in identifying conditions in which defects occurred experimentally [62]. While an alloy independent Rayleigh value may be attainable in the future, for the following analysis, use of the mushy zone height will be appropriated for calculation of the local Rayleigh number (Ra_h) given the success it has achieved in single crystal Ni-base superalloys. Furthermore, suggestions based on the findings of this thesis will be directed to form of the Rayleigh criterion as shown in Equation 2.7, as nickel-base superalloys are the material system of interest herein.

2.1.6 Permeability

Permeability is defined as a measure of ease by which fluid is able to flow through a porous medium [69], and is a useful metric for not only calculation of the Rayleigh number but for quantifying flow through complex paths in general. As such, permeability in cast metallic structures has been examined in a number of research efforts to clarify and better describe the contribution of the characteristic features of dendritic structure to this property [70-80]. While there are various mathematical descriptions of the relationship between permeability and dendrite arm spacing, nearly all have a proportional scaling of permeability with the cube of the volume fraction liquid present [70, 75, 77, 80]. In any porous medium, permeability can vary strongly with volume fraction. As such, a number of empirical equations relating volume fraction to permeability have been developed. Most common are the Kozeny-Carmen (K_C) and Blake-Kozeny (K_{BK}) descriptions [78, 81-83] where;

$$K_{KC} = \frac{(1-f_s)^3}{5S_V^2} \tag{2.8}$$

$$K_{BK} = C_2 \frac{d_1^2 f_L^3}{(1-f_L)^2} \tag{2.9}$$

with f_s and f_L corresponding to volume fraction solid and liquid respectively. S_V is the solid-liquid interfacial area per unit volume, d_1 is the primary dendrite arm spacing and C_2 is a constant. Applying these relations to a directionally solidified dendritic structure poses difficulties due to the inherent anisotropy of the dendritic structure and associated permeability tensor. Poirier has modified the Blake-Kozeny relation to describe permeability in flow parallel and transverse to directional structures, Eqs. 2.10 and 2.11, respectively [78].

$$K_{BK_Y} = (4.53\times10^{-4} + 4.02\times10^{-6}(f_L + 0.1)^{-5})\frac{{d_1}^2 {f_L}^3}{(1-f_L)^2} \qquad (2.10)$$

$$K_{BK_X} = (1.73\times10^{-3}(d_1/d_2)^{1.09})\frac{d_2^2 f_L^3}{(1-f_L)^{0.749}} \qquad (2.11)$$

However, the Blake-Kozeny relation and modifications do not intrinsically consider the influence of high surface areas characteristic of dendritic structures on flow behavior. To address this, Heinrich and Poirier later suggest a three regime description for both vertical and cross flow permeabilities in directional structures by performing regression analysis on empirical data and numerical simulation for regions in which no prior experimental data existed [84], Eqs. 2.12 and 2.13.

$$K_x = K_n = \begin{cases} 1.09\times10^{-3} f_L^{3.32} d_1^2 & f_L \le 0.65 \\ 4.04\times10^{-6}\left[\dfrac{f_L}{1-f_L}\right]^{6.7336} d_1^2 & 0.65 \le f_L \le 0.75 \\ (-6.49\times10^{-2} + 5.43\times10^{-2}\left[\dfrac{f_L}{1-f_L}\right]^{0.25})d_1^2 & 0.75 \le f_L \le 1.0 \end{cases} \qquad (2.12)$$

$$K_y = \begin{cases} 3.75 \times 10^{-4} f_L^2 d_1^2 & f_L \leq 0.65 \\ 2.05 \times 10^{-7} \left[\dfrac{f_L}{1 - f_L} \right]^{10.739} d_1^2 & 0.65 \leq f_L \leq 0.75 \\ 0.074[\ln(1 - f_L)^{-1} - 1.49 + 2(1 - f_L) - 0.5(1 - f_L)^2] d_1^2 & 0.75 \leq f_L \leq 1.0 \end{cases} \tag{2.13}$$

In the formulations above, Eqs. 2.10 – 2.13, $d_{1,2}$, refer to the primary and secondary dendrite arm spacing, respectively. Irrespective of the model adopted, the predicted variation in permeability with volume fraction is three to four orders of magnitude producing a relative change in the Rayleigh value of the same order, assuming all other factors remain relatively constant in order of magnitude. This variation has a substantial influence on the Rayleigh number and thus more detailed investigation of three-dimensional dendritic structures are needed. In this study, we combine serial sectioning with numerical fluid flow analyses to examine the permeability in a three-dimensional directionally solidified structure as a function of solid fraction and dendrite morphology.

2.2 DEVELOPMENT OF THREE-DIMENSIONAL RECONSTRUCTION TECHNIQUES

Since its inception, the field of materials science has seen marked improvement in not only the scope of materials studied but also the experimental methods employed. From basic metallography to the development of x-rays, to advances in microscopy; these methods have contributed to a more quantitative understanding of material properties and performance. As such, the development of three-dimensional reconstruction techniques promises to increase the depth, scope and level of detail to which materials can be investigated and characterized.

Three-dimensional reconstructions have been assembled with a number of different sectioning techniques and are finding increasing application in materials analysis and development. For the purposes of this thesis, reference to advances in three-dimensional reconstruction will be limited to those made by serial sectioning to provide the opportunity for direct comparison of experimental techniques and results across a range of experimental materials. While early microstructural studies published utilizing serial sectioning are very few in number [85-87], metallographic image processing and computational advances have made serial sectioning a more accessible and productive analysis tool within the last decade. Collection of high-resolution images at controllable intervals, data storage and the computing power to reconstruct, visualize and analyze such structures are all basic items necessary for three-dimensional reconstruction. To this end, the primary challenges associated with serial sectioning are essentially threefold. First, uniform material removal between sections is difficult to achieve when manual material removal techniques are used. Secondly, accurate measurement of material removal during the sectioning process is at best arduous given the micron length scale for which microstructure can be reliably reconstructed. Thirdly, the digital storage and computational tools necessary to align, optimize and reconstruct the many images in a statistically representative volume of microstructure have only recently become practical for a subset of materials problems. Even in these cases, computing power and digital storage can still impose limitations. Not until the early nineties were serial sections actually reassembled to show the interconnectivity and full directionality of constituents within a microstructural volume. Select early and more recent examples of three-dimensional reconstructions will be reviewed here to illustrate the development of this

3D analysis technique and highlight its contribution to the investigation of metallurgical problems.

2.2.1 Mangan and Shiflet

In steels containing high concentrations of manganese, Mangan and Shiflet in 1994 utilized serial sectioning and reconstruction to examine the structure and orientation relationships among pearlite colonies [88]. A few years later Mangan and Shiflet further utilized their 3D techniques to examine the spatial relationships between Widmanstätten plates of cementite in austenite matrix [89]. Their method consisted of polishing with colloidal silica on Texmet polishing cloths to repeatably remove 0.2 µm thick layers of material before imaging a predetermined area of interest by scanning electron microscope (SEM). Material removal rates were verified by micro hardness indents where measurement of the indentation diagonals before and after polishing provided depth of removal information via changes in diagonal length of the indent. The indents allowed alignment of features within a single section by considering the features in the sections immediately above and below. While the authors mention the possibility of alignment based upon fiducial markers made by focused ion beam (FIB), and do so in later work [90], early reconstructions were chiefly gained using the "best fit" manual method. Additional interpolations performed to refine the volume visualized were a variation of the "watershed-based" algorithm, previously developed and published, by S. Raya and J. Udupa, as well as Herman and coworkers [91, 92]. From their work, Mangan and Shiflet showed that in a pearlite colony within Fe-0.8C-12Mn, ferrite and cementite lamellae both exist in constant contact with austenitic grains under a particular orientation relationship. Conventional 2-D observations of similar pearlite morphologies would have suggested intragranular nucleation or isolated portions of cementite were being observed. It was shown these separate intersecting plates simply possessed varying orientations and were portions of the same colony as opposed to a divided branch of cementite split during the preliminary growth process, as conventional wisdom suggested. Mangan and Shiflet's work was unique in that it was one of the first instances in which a fully rendered three-dimensional reconstruction of metallic microstructure was recorded in the materials literature and provided direct measurement of the spatial arrangement of features to reveal error in the conventionally accepted theory [89].

2.2.2 Kral and Spanos

Immediately following the work of Mangan and Shiflet, Kral and Spanos [93] reported larger volume reconstructions, further elucidating the cementite morphology and its presence as intragranular precipitates along grain boundaries as well as elongated laths within grains. In their method, the authors similarly used traditional metallographic techniques and polishing by serial sectioning with Buehler Texmet cloth and a 0.06 µm silica slurry. Uniform material removal amounts were achieved by standardizing polishing load and time while micro-hardness indents were used to verify material removal and serve as fiducial marks for alignment. Kral and Spanos also developed etching techniques to overcome inherent limitations in discerning "out of plane" precipitate features due to serial sectioning. The authors also mention that deep etching allowed for preferential removal of the austenitic matrix that made further crystallographic and interfacial studies of not only grains but also precipitate morphology and interconnectivity via SEM possible in later studies [93, 94]. This is of note due to the fact that their later reconstruction studies focus heavily upon, not only grain boundary and precipitates but also crystallography, shape and orientation of these microconstituents [95-99]. While optical microscopy with a digital acquisition system was used to obtain images for reconstruction, the authors combined SEM and TEM techniques to determine the internal structure and misorientations of precipitates as well as verification of optical methods. Beyond this, the work of Kral and Spanos further developed computer-aided three-dimensional reconstruction as a tool for not merely visualizing the reconstruction but also as a tool for isolating, managing and cropping select portions of the microstructure for direct investigation. As such, the actual size, shape and distributions of precipitate morphologies were directly measured. It was found that two fundamental types of cementite precipitates form; grain boundary and Widmanstätten. The work of Kral and Spanos further illustrated the following two points: 1) images from random planes within a microstructure can conceal the true three-dimensional nature, connectivity, and morphology of the microstructure and 2) smaller scale secondary and tertiary features such as sub-groups belonging to Widmanstätten laths as well as dendrite arms can be completely overlooked when random planes from a microstructure are the only representation of the microstructure available [93, 94].

2.2.3 Voorhees and Co-Workers

In work published by Alkemper and Voorhees in 2001, the authors present a fully developed, fully automated approach to serial sectioning which directly addressed a variety of constraints in sectioning time and handling-induced errors. Building upon a sample preparation method first published by Wolfsdorf and Voorhees [100], optical imaging capability was added to eliminate the removal and replacing of a sample during sectioning. The technique utilizes a micro-miller, micron-sensitive motorized stage, and attached microscope with digital camera. Alignment and depth measurement during sectioning are obtained by use of a linear variable differential transformer (LVDT). Instead of traditional metallographic polishing for the preparation of surfaces, milling with a diamond blade is used to prepare surfaces free of scratch, stain or any other metallographically induced defect. Previous metallographic methods for serial sectioning typically operated under rates on the order of 10 cross-sections per day, while the technique published by Voorhees and co-workers allowed for the collection of approximately 20 sections per hour with selectable slice thicknesses in the range of 1-20 μm separating imaged planes [101]. Although the technique is unsuitable for materials of high strength such as superalloys and steels, Voorhees and co-workers have focused extensively on comparatively softer materials such as Al-Cu and Pb-Sn systems [102-104]. This work represents the first instance of a self-contained, fully automated metallographic preparation and imaging instrument expressly for the purpose of three-dimensional reconstruction.

2.2.4 Spowart and Mullens

In an effort to further reduce the time and human repetition required while improving the efficiency and overall quantity of data gathered during the acquisition of three-dimensional datasets, Spowart and Mullens developed another fully automated approach to the serial sectioning [105]. By placing a 6-axis robotic arm amidst an automatic polisher, controlled pools of etchant and an inverted microscope with motorized stage, an automated operation with the ability to serial section; steels, Ni-base superalloys, Ti alloys and metallic composites was produced. This approach is trademarked as RoboMET.3D™ [106, 107]. The technique utilizes standard metallographic polishing with consumables such as diamond lapping film and polishing cloths with 0.05 μm blue colloidal silica suspension from Allied High Tech Products, Inc. Achievable material removal rates with RoboMET.3D™ range from 0.1 μm to 10 μm and depending upon the sample size and slice thickness desired, section rates of up to 20 slices/hour have been achieved. The Carl Zeiss™ Axiovert 200 MAT inverted microscope employed in the RoboMET.3D system utilizes an auto-focus and motorized stage with submicron resolution for repeated imaging of the region of interest. Polishing depth and material removal with the automated polisher is controlled through regulation of polishing load, time, sample height and revolutions per minute calculated automatically within the computerized system control and verified at user-specified intervals [105, 107]. Further discussion of the details of the RoboMET.3D system will be presented later as it has been utilized as a portion of the experimental procedure in this work. The Spowart and Mullens contribution to three-dimensional reconstructions is significant, as they have developed a nearly fully automated approach to serial sectioning suitable for high strength, high toughness materials for high temperature applications.

2.3 MILESTONES IN FLOW MODELING THROUGH DENDRITIC NETWORKS

Fluid flow near the solid-liquid interface in directionally solidified superalloys has previously been understood in many ways, primarily, by indirect investigation of the solidification process. As computational tools have advanced, the level of detail resolvable in fluid flow analysis of directionally solidified processes has increased as well. While a number of efforts have aided the understanding of flow by combining experimental and computational methods, most approaches have experienced specific limitations. Whether these limitations are inclusions of only two-dimensional geometries as experimental domains [71, 108] or the modeling of simple three to four component systems [109], the ability to encompass the full physical complexity of the fluid flow environment has remained somewhat elusive. As a review of previous efforts linking experimental processes with computational tools, select approaches will be discussed to highlight current progress to date.

2.3.1 Ganesan and Co-Workers

There have been several attempts to explicitly consider the influence of dendritic structures on fluid flow within the mushy zone. Among these, a computational approach to permeability calculation with flow parallel to the primary growth direction was performed by Ganesan *et al.* [72] due to the lack of coherency in dendritic networks at high fraction liquid. This work was also motivated by unrealistic values predicted by the Darcy equation at or near locations of high fraction liquid *i.e.* $f_L > 0.7$. Individual micrographs transverse to primary growth in Pb-Sn were taken at various heights and dendrites were identified. These structures were discretized and flow through the structures was simulated using a boundary element method. Permeabilities were calculated based upon a derivation of Darcy's Law. This approach worked well for high liquid fraction f_L regions but overestimated permeabilities experimentally observed below $f_L < 0.61$. While one of the first evaluations of permeability to explicitly consider dendritic structure, this study assumed the structures apparent in a transverse view remain entirely uniform along the flow direction. Departures from this assumption introduce a great deal of uncertainty in the theoretical formulation and approach. However, Ganesan and co-workers were among the first to suggest a transition in permeability volume fraction dependence at or near $f_L = 0.65$ [72].

2.3.2 Bhat and Co-Workers

In an effort to calculate permeability at high liquid fraction in directionally solidified alloys normal to primary growth, Bhat and co-workers performed 2-D numerical simulations on both artificial and experimentally derived dendritic cross-sections. Pb-Sn alloys were directionally cast and quenched in water abruptly interrupting the solidification process. Transverse and longitudinal micrographs were taken in order to differentiate dendritic structure from remaining interdendritic and bulk liquid. Samples with liquid volume fractions ranging from $0.5 < f_L < 0.9$ were investigated and micrographs were segmented and meshed for structures by overlaying a grid and deforming it to segmented boundaries. This work offered some of the first calculations of permeability above $0.6f_L$ in experimentally obtained structures and showed reasonable convergence with previous lower liquid fraction experimental data. Additionally, an empirical relationship between non-dimensional permeability and volume fraction that suggested changes in flow orientation laterally across dendritic arrays have little impact on permeability normal to primary growth [71].

2.3.3 Nielsen, Bernard, Fuloria and Co-Workers

Nielsen, Bernard and co-workers made significant contributions by coupling experimental measurements directly with three-dimensional flow simulations in equiaxed structures [83]. To accomplish this, experimental equipment was refined [70, 76-78, 80] for direct measurement of permeability in quenched Al-Cu alloys. Later, numerically calculated permeability in the same quenched Al-Cu samples using Darcy's Law calculations in three-dimensional renderings of dendritic/interdendritic regions obtained by x-ray microtomography [110]. This technique yielded an upper limit in volume reconstruction on the order of 1mm x 1 mm x 0.6 mm and an average resolution for all features near 1 μm [110], with likely smaller volume limits for higher density materials. Continuing this work [111] the full permeability tensor was investigated in multiple three-dimensional tomograms of quenched, directionally solidified, Al-Cu. Using x-ray microtomography, various volumes were attained and flow modeling in each of the primary orthogonal directions was performed. From these simulations, permeabilities normal and parallel to the primary growth direction were calculated using the Bernard model [110]. Results were compared to solutions obtained with the Stokes equation, the Kozeny-Carmen relation, previous measurement [83], as well as a host of other experimental data [112-115]. While agreement was found with experimental data in the literature, deviations from prior direct measurement were attributed to tomogram volumes too small for the characteristic lengths of the microstructure. It was suggested that volumes encapsulating two times the secondary dendrite arm spacing as optimum domains. Major findings confirm the anisotropy of parallel and cross flow permeabilities through columnar dendritic networks and demonstrate a general trend toward lower permeabilities for cross flow when compared to vertical flow at a given volume fraction.

Currently, opportunity exists for further investigation of fluid flow at the solidification front in nickel-base superalloys. While difficult to obtain, detailed information of the three-dimensional morphology of dendritic structures in such alloys would provide immense opportunity to better understand solidification and the formation of solidification defects in this vastly used alloy class.

CHAPTER 3

EXPERIMENTAL METHODS

In this chapter, a brief description of experimental approach will be presented providing the overall framework for this study. Details of the solidification process used to produce single crystal castings with exposed dendritic structures as well as the sectioning and reconstruction technique are discussed. Characterization of reconstructed structures will also be addressed in terms of the methods of measurement and analysis.

3.1 SOLIDIFICATION OF SINGLE CRYSTAL SUPERALLOYS

An ALD Vacuum Technologies, Inc. furnace equipped with Liquid Metal Cooling (LMC) and conventional Bridgman casting at the University of Michigan was used for all casting experiments. The furnace was used to cast single crystals of both the commercial nickel base superalloy René N4, and the model Ni-Al-W ternary alloy. René N4 possesses the elemental composition; Ni-4.2Al-0.05C-7.5Co-9.8Cr-0.15Hf-1.5Mo-0.5Nb-4.8Ta-3.5Ti-6.0W (wt%) with liquidus and solidus temperatures of 1345^0C and 1300^0C, respectively [47]. The model ternary contains a nominal composition of Ni-6.5Al-9.5W (wt%) with liquidus and solidus temperatures of 1456^0C and 1433^0C respectively, as determined by differential thermal analysis. The ternary composition was selected based on its predicted propensity to freckle. Images of freckles produced in casting this alloy are shown in Figure 3.1.

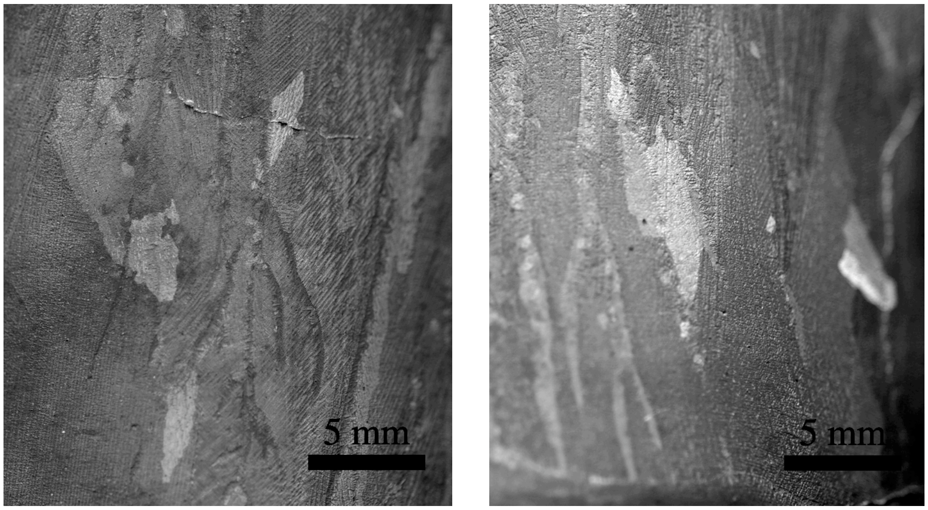

Figure 3.1 - Freckles in Ni-Al-W casting

The conventional Bridgman process was used with solidification abruptly terminated by decanting during withdrawal to isolate mid-process dendritic structures. A micrograph illustrating a portion of an exposed dendritic network obtained by decanting is shown, Figure 3.2. Diagrams of conventional Bridgman and LMC processes are shown in Figure 3.3a and b. Due to complexities associated with decanting during withdrawal, all castings in this study were performed exclusively in Bridgman mode.

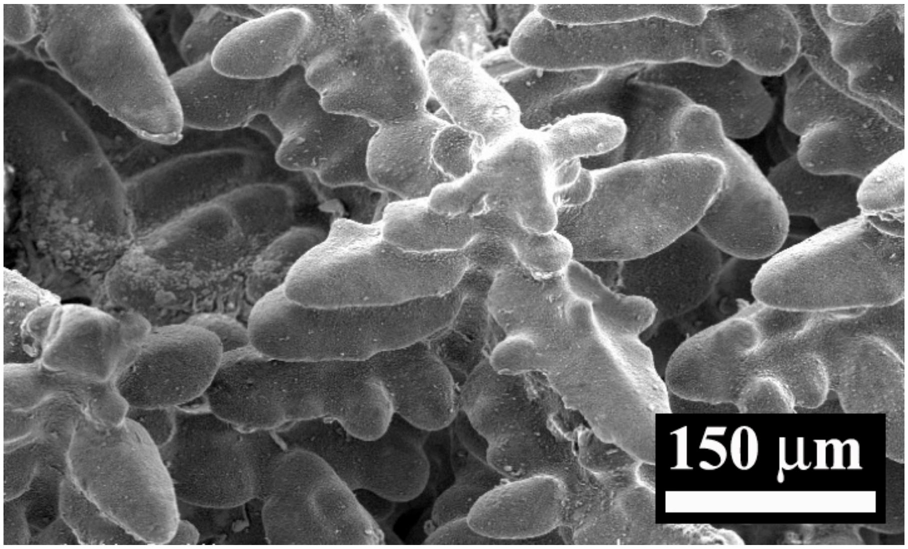

Figure 3.2 - Exposed Dendritic Network Obtained via Decanting During Directional Solidification

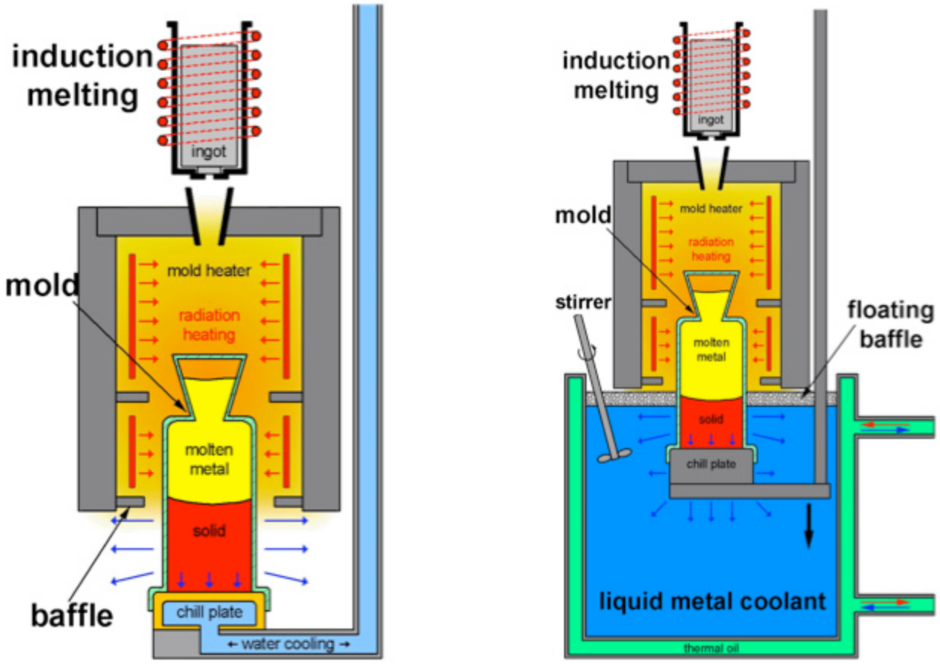

(a) (b)

Figure 3.3 - Illustration of small-scale conventional (a) Bridgman Furnace components and (b) Liquid Metal Cooling set-up at the University of Michigan

Within the furnace, two zones of resistance heating elements are present to maintain and control the heated zone while a graphite baffle is affixed to the base of the heater to partially isolate the heated zone and encourage localization of the solid-liquid interface within the high gradient region. The mold itself rests on a water-cooled copper chill plate connected directly to a uni-directional withdrawal arm that removes the mold from the heated zone at a predetermined withdrawal rate over a maximum travel distance of 0.3m, which imposes a vertical limit on viable mold size. The Bridgman mode relies entirely upon cooling by radiation, therefore successful withdrawal rates are generally slower than alternative processes such as LMC, where investment molds are lowered into a bath of molten tin and heat is removed by conduction and convection [47]. A photograph of the furnace interior is shown in Figure 3.4. For the purposes of this work, withdrawal rates of

2.5 mm/min and 3.3 mm/min were utilized, as they are consistent with previous work within the University of Michigan facilities and are within the bounds of typical commercial processes.

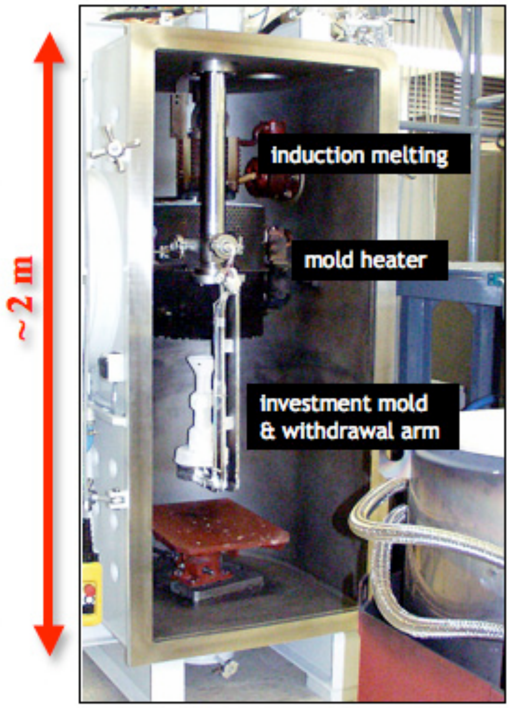

Figure 3.4 - Photo of Bridgman Furnace Interior @ University of Michigan

Prior to melting, a vacuum of 10^{-4} mbar was obtained and a mold preheat cycle with a dwell at 1500 ^{0}C and 1550 ^{0}C were used for the René N4 and the ternary alloy, respectively. Ingots weighing approximately 3 – 4.5 kg were melted by induction heating above the mold heater. Once the entire volume is molten, the alloy flows from the base of the crucible into the mold within the heated zone. Once accomplished the lower resistance element was raised to the desired temperature and withdrawal at the aforementioned withdrawal rates began. This technique for small scale Bridgman casting has been documented thoroughly and evaluated in comparison to small scale LMC casting in great detail by Elliott *et. al* [17, 47, 116, 117]. However, within the current investigation there are two distinct differences with conventional small-scale Bridgman casting. In the current experiments, intentional "decanting" was performed by removing a portion of the ceramic mold during withdrawal allowing the molten liquid to drain rapidly while preserving the solidified dendrites with minimal disturbance. Secondly, the ceramic molds used for the ternary alloy were designed specifically for decanting and to encourage a non-planar solidification front while facilitating gate removal in the mold wall during withdrawal.

3.2 DECANTED CASTING

In order to produce isolated dendritic structures accessible for investigation, a controlled fracture of the mold was used. While this event can occur accidentally, as was the case of the René N4 investigated herein, the event is rarely predictable, somewhat complicated, and not easily reproducible. To accomplish the decanting in a controlled fashion, 3" diameter, 5" tall ceramic specialty molds were fabricated at PCC Airfoils with a 3/8" vertical slot in which a cylindrical rod was affixed, Figure 3.5.

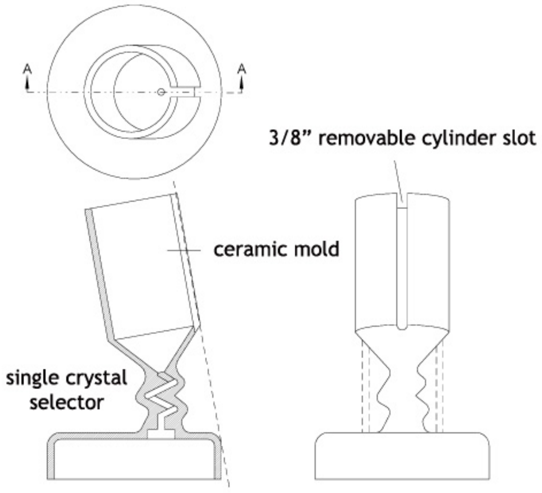

Figure 3.5 - Schematic of decanting mold designed by PCC Airfoils

These molds were then oriented in the furnace such that the cylindrical rod was held stationary during mold withdrawal to initiate an opening in the mold wall after sufficient movement of the mold allowing for evacuation of molten metal. In most cases, a diamond tip rod inserted via vacuum tight portal was used to further encourage mold opening and ensure an intentional "run-out" occurred. This method has allowed for the controlled obtaining of experimentally exposed mid-withdrawal dendrites available for further investigation in the Ni-Al-W ternary alloy.

3.3 THREE-DIMENSIONAL RECONSTRUCTION OF DENDRITIC STRUCTURES

In order to investigate the true morphology of the mushy zone, three-dimensional reconstructions of dendrites in the decanted castings were performed. This has provided greater insight into dendritic structures in single crystals but also permitted studies on: 1) the effect of solidification front curvature on dendrite morphology, 2) fluid flow through physically realistic structures and 3) permeability of the dendritic structure.

The experimental reconstruction technique required has consisted of the following three steps; serial sectioning, segmentation and reconstruction. The protocols for each are described in detail in the following sections.

3.3.1 Serial-sectioning via RoboMET.3D

Using the prototype RoboMET.3D metallography preparation and imaging instrument at Wright-Patterson Air Force Base, serial sectioning data sets were obtained. A photograph of the RoboMET.3D system is shown in Figure 3.6.

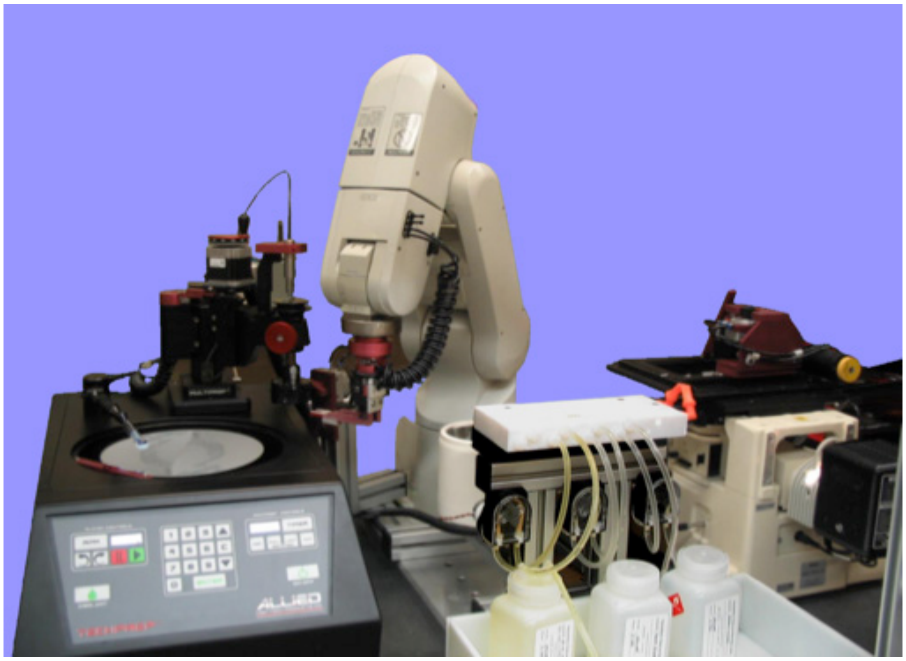

Figure 3.6 - Prototype RoboMET.3D™ system at Wright-Patterson Air Force Base, Dayton OH

The automated approach to serial sectioning provided by RoboMET.3D™ is a useful addition to the collection of emerging techniques for three-dimensional reconstruction. It should be mentioned however, that although RoboMET.3D™ is automated, it does not function fully autonomously. A user is required to monitor fluid levels, input parameters for polishing and imaging as well as physically measure material removal. In addition, while fiducial markings by hardness indents have been a widespread practice for alignment and depth measurement, the RoboMET.3D™ produces a good consistency of material removed between slices. Thus this study did not utilize fiducial markings for alignment or as a measure of material removal. Results presented later show removal rates on the order of 2 – 3 μm with standard deviations less than 0.7 μm. The uniformity of the sectioning depth with RoboMET.3D is derived from the repeatability of the polishing which is programmatically maintained with regard to time, pressure, polishing pad contact, cleaning and imaging. Data for the serial sectioning experiments of both

René N4 and the Ni-Al-W ternary are presented in detail in Chapters 5 and 6, respectively.

The volumes for reconstruction were selected to contain at least 7 – 10 primary dendrite arms to allow for representative sampling. Given the solidification rates used and expected thermal gradients, initial estimates suggested areas of approximately 2 mm x 2 mm in cross-section to be sufficient to resolve multiple dendritic structures and their local arrangement with respect to one another. Additionally, preliminary work demonstrated that ALLIED diamond lapping film containing 1μm or 3 μm particulates permitted slice thicknesses on the order of 2 – 3 micrometers and provided excellent resolution of the microstructural features present throughout the height of the mushy zone as well as the primary, secondary and emerging tertiary dendritic structures. Optimization of the polishing methods resulted in sectioning rates of 2.2 μm/slice for the commercial alloy René N4 and 3.25 μm/slice for the model ternary.

Using a user-input interface known as AxioCamMRc5™, settings for the polisher, including polishing time, specimen height, slice quantity, starting pad track location and polishing revolutions per minute were selected. Following this, another user-input program named AxioVision™ was utilized to input optical microscope settings such as light path, reflection type, magnification and focus. After optimum settings were determined, serial sectioning was performed for a set of approximately 5 to 12 slices. After each polishing set, the entire sample thickness was measured for assessment of material removal such that the nominal slice rate could be monitored throughout the duration of the sectioning experiment.

3.3.2 Image Segmentation via Photoshop and IDL

Following serial sectioning, post-processing of each image in preparation for "stacking" is one of the most critical steps in the reconstruction. This step has been chiefly referred to as "segmentation". Various methods for segmentation have been treated extensively in the medical imaging field for decades and have received attention in the materials community only recently [118-121]. In this thesis, segmentation was achieved by a seven step image refinement protocol using Adobe Photoshop™ as well as ITT's Interactive Data Language (IDL)™. Unless Photoshop is specifically mentioned as the tool for the segmentation step, it may be assumed that IDL is the tool used. Raw images are initially shifted for basic alignment of all images throughout the dataset. Next, a coarse cropping followed by a fine cropping of each image is performed to remove extraneous areas from each image. Next, using Adobe Photoshop, the images are manually "cleaned" where spurrious markings such as scratches or water spots are eliminated from each image as they may impose errors later in representation unless resolved. Following this step, all images are then converted to binary in Photoshop to reduce the file size of each image and make the entire dataset reconstruction-ready. This is also a critical step with regard to determining which voxels will later be assigned to the solid or liquid phase in the reconstruction. For this reason, clean, consistent and definitive edges accurately demarcating the individual phases are the goal of this process. Following this, a uniform size for all images is set to ensure proper stacking. Lastly, one final size reduction is imposed to further reduce the overall amount of memory required to stack, visualize and ultimately interact with the data.

3.3.3 Reconstruction via IDL

After a data set has been obtained and all images have been properly segmented, reconstruction can be performed. This is accomplished with two additional IDL™ scripts; “STACK.pro” and “REGIONVIEWER2.pro”. These IDL procedural scripts were written by D. Rowenhorst of the Naval Research Laboratory [122-124] and have been used with permission. The “STACK” procedure takes an image from the dataset, obtains a measure of in-plane dimensions and stacks each image sequentially to combine the entire dataset into a 3-D array. Subsequently, “REGIONVIEWER2” can be called to operate on this new array. Being an object-oriented graphical program, the newly created stack is inserted into a pre-developed viewing area in which the volume can be rotated in any direction, along any plane and at an assortment of magnification ranges up to 100X. Magnification and scale factors can be inserted by the user, at key points, to ensure the scaling and aspect ratio for all dimensions are correct. In this regard a companion algorithm was written by the author which calls REGIONVIEWER2 as an argument while supplying items such as dataset to be called, scaling factor, array size as well as resolution and supplies such items directly to REGIONVIEWER2 thereby streamlining the visualization process for a variety of datasets and a variety of users. From this point, additional scripts were written to traverse, characterize and examine the reconstructed volume. As such, a number of measures from the physical system and directly from the reconstruction itself are used in this study, as will be discussed in subsequent sections.

3.4 MICROSTRUCTURAL CHARACTERIZATION

3.4.1 Metallographic Preparation

To fully characterize the microstructure in the vicinity of the solid liquid interface, samples roughly 1cm^3 in size were cut from within the mushy zone using a large scale wet abrasive saw followed by an Isomet™ low-speed saw with a diamond blade. These samples were then mounted in a Buehler™ thermosetting phenolic mounting compound using a Leco PR-10 Mounting Press. The samples were mounted such that the plane of observation was oriented normal to the primary growth direction and then prepared according to standard metallographic preparation techniques down to a 0.25 μm diamond finish. All metallographic polishing was performed using a combination of the Buehler™ ECOMET 6 manual polisher and a STRUERS™ Abramin Automated Polisher. Samples were then etched by swabbing with a solution of 33% CH_3COOH : 33% HNO_3 : 33% H_20 : 1% HF and neutralized in water to discontinue the chemical reaction.

3.4.2 2-D Measurement of Dendrite Arm Spacing

Micrographs of sample surfaces were then obtained using a Nikon™ Optiphot microscope equipped with digital image capture. These micrographs were then analyzed for Primary Dendrite Arm Spacings (PDAS) according to the following relation, where *n/A* refers to the number of cores counted per cross-sectional area.

$$\lambda_1 = (n/A)^{-\frac{1}{2}} \tag{3.1}$$

After measurements were obtained, the samples were removed from their mounts then cut again through dendritic cores along the growth direction of secondary dendrite arms. The samples were then remounted, prepared, etched and re-imaged as detailed above, leaving the newly sectioned surface visible to reveal the arrangement of secondary arms growing from their primary cores as detailed by Figures 3.7a and b. Micrographs were then analyzed for Secondary Dendrite Arm Spacings (SDAS) according to Eq. 3.2 where L is the length of a line drawn next to the primary core and n represents the number of secondary arms counted along the line drawn. The PDAS and SDAS measured in the physical system provide a basis for comparison to the three-dimensional reconstructions and a means for verification of the consistency of the dendrite spacing within cast structures with the expectations for the associated withdrawal rate and solidification front velocity.

$$\lambda_2 = \frac{L}{(n-1)} \tag{3.2}$$

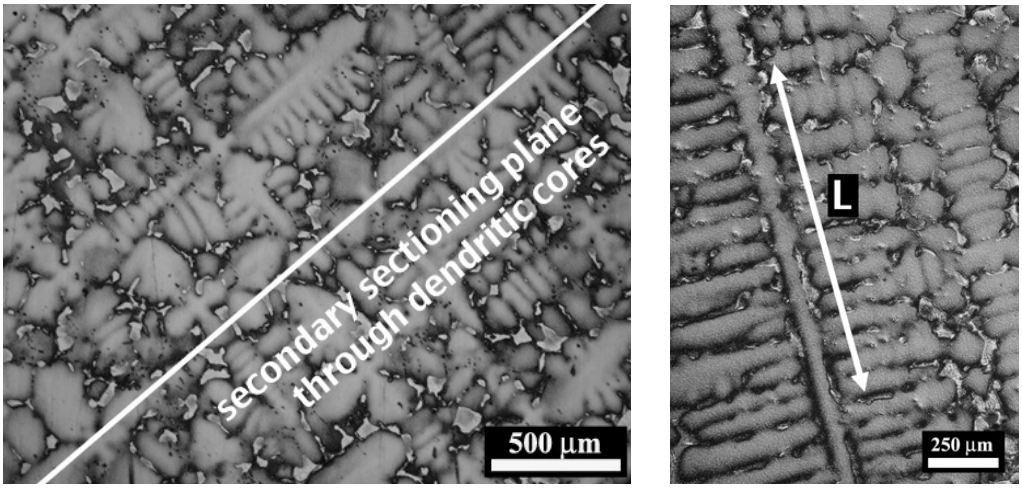

(a) (b)

Figure 3.7 - Typical micrographs for dendrite arm spacing measurement. (a) micrograph normal to the primary growth direction for assessment of PDAS with line indicating secondary sectioning plane (b) micrograph normal to secondary growth revealed by sectioning through primary dendritic cores

3.4.3 Volume Fraction of Liquid and Solid

In addition to measuring the dendrite arm spacings, protocols for measuring the volume fraction of liquid and solid directly from the reconstruction were developed within the framework of IDL. Quantitative image analyses have shown in a single binary image, volume fraction of a given phase is equivalent to the area fraction in which all pixels corresponding to that phase are divided by the total number of pixels in the image [125]. Given any arrangement of binary pixels, the relation takes the following form;

$$V_v = A_a = \left(\frac{N_p}{N_o}\right)_a \tag{3.3}$$

where A_a is the area fraction, N_p corresponds to the quantity of pixels belonging to the phase of interest and N_o corresponds to the total number of pixels in the image. Volume fraction, V_v, is attained by extrapolation of this relationship over a series of sections. In this manner, the volume fraction can be readily returned as a function of the area fractions in any of the primary orthogonal directions in which physical length corresponds directly to voxel dimension. Similarly, determinations of a physical area and/or physical volume are also possible provided the above fractions are combined with the in-plane pixel to physical dimension ratio and the physical distance(s) between planes.

3.4.4 Interdendritic Void Distributions

With a defined voxel to volumetric ratio, the entire reconstruction as well as sub-regions within the volume can also be effectively measured for volume by summing all voxels composing each region. Within IDL, a subroutine named LABEL_REGION provides a method to index each independent body. In this protocol, each independent body is defined when no adjacent voxel, using three-dimensional neighbor searching, possesses an equivalent value. Since the reconstructions in this work are binary, each voxel has the option of being only one of two phases; solid or liquid. Additional procedures were developed to capitalize on this categorization and return specific measures, particularly the volume of each body and its physical connectivity to others. This was primarily used to ascertain the connectivity, the size distribution of all liquid regions in the reconstruction, and the percentage contribution of each liquid body to the overall interdendritic voided regions.

3.4.5 Interfacial Surface Area

A method to measure the interfacial surface area (ISA) between the solid and liquid phases directly from a reconstructed dataset has also been developed. All individual element areas in the dataset surface mesh were indexed according to their location. By binning all surface elements within a pre-determined height value, measures of interfacial surface area as a function of height were obtained. By changing the bin size, measures as coarse or as fine as desired were produced. Ultimately, bins the size of the vertical resolution in the dataset were selected to maintain an equitable spatial correlation between height, volume fraction and interfacial surface area. Normalized forms of the ISA common in most discussions of flow in porous media divide ISA by the associated volume to obtain the surface area to volume ratio. In this thesis, this normalized value will be defined as (S_V). This measure of the dendritic structure will be discussed in detail in later chapters.

3.4.6 Curvature and Shape Distributions

Lastly, previously developed protocols for measurement of morphological curvature and shape variation developed by Voorhees and co-workers [102-104, 126-128] were utilized in this study to additionally characterize the reconstructed datasets for the Mean curvature (H_M), the Gaussian curvature (H_G) and Interfacial Shape Distributions (ISDs). Curvatures are an important characterization measure as they may affect flow behavior particularly over some ranges of solid fraction and can serve as an indicator of coarsening in secondary dendrite arms. H_M and H_G are significant curvature measures as they are two invariants of the curvature tensor κ_{ij} and are defined as follows where κ_1 and κ_2 are the principal curvatures;

$$H_M = \tfrac{1}{2}(\kappa_1 + \kappa_2) \tag{3.4}$$

$$H_G = (\kappa_1 \cdot \kappa_2) \tag{3.5}$$

The mean and gaussian curvatures are typically denoted by *H* and *K,* respectively. To avoid confusion with the notation for permeability, *K*, the above notations, H_M and H_G , (Eqs. 3.4 and 3.5) have been adopted and will be used throughout this thesis. Using these curvatures, methods to measure and visualize the probability of selecting a region of interfacial area corresponding to a particular pairing of principal curvatures has also been previously developed and is referred to as the interfacial shape distribution (ISD) [102-104, 128]. This probability function is illustrated via contour plot and is produced using probability plots directly obtained from the three-dimensionally reconstructed dataset. A legend for the ISD curvature plot is included below to provide explanation of principal curvature pairings as well as their depictions in relation to the liquid and solid phases. By convention, the larger of the two principal curvatures are designated as κ_2. As a result, no contours are depicted to the right of the $\kappa_1 = \kappa_2$ line in any ISD plot, as all contours must exist to the left of $\kappa_1 = \kappa_2$.

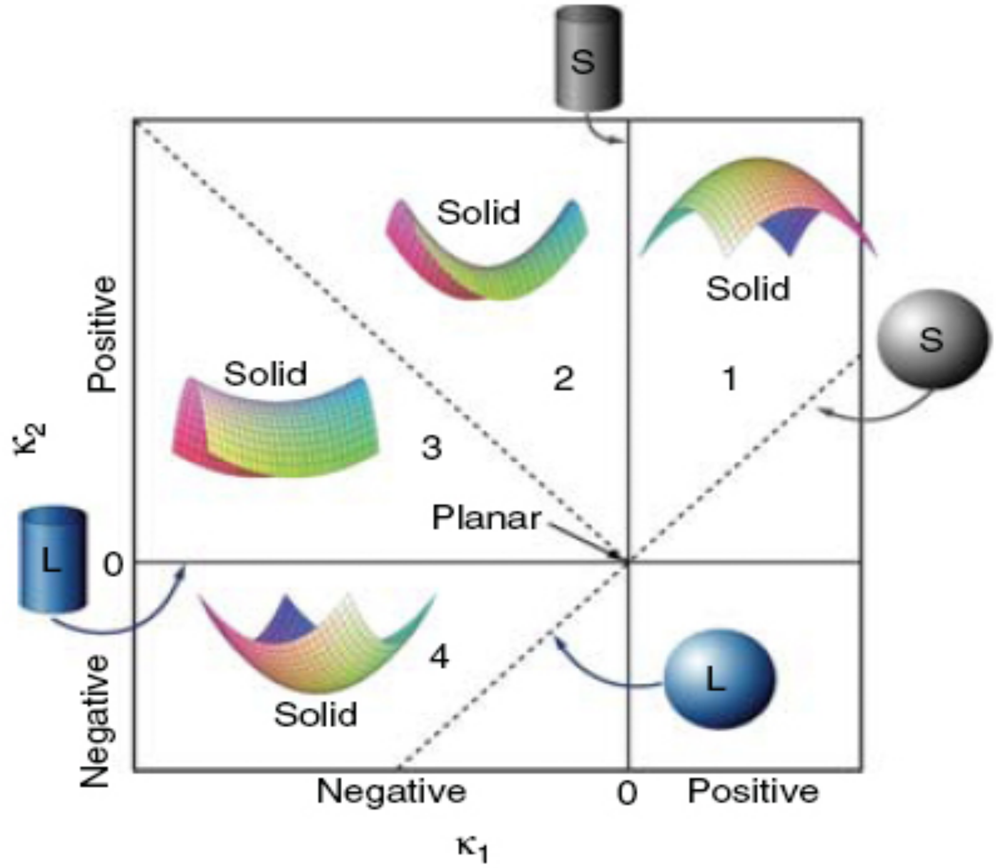

Figure 3.8 - Legend for Interfacial Shape Distribution (ISD) Plots **[102, 103, 128]**

The application of each of the above described measurement methods for characterization of the 3-D datasets for the commercial alloy René N4 and the ternary Ni-Al-W alloy is described in Chapter 5 and 6, respectively.

CHAPTER 4

SIMULATION TECHNIQUE

Numerical simulation of flow at the solid liquid interface and assumptions regarding the 3-D fluid flow analysis are considered in this chapter. Analysis software, mesh resolution, relevant model size and the basis of the numerical framework are discussed. used is central to the data that can be reliably extrapolated.

4.1 COMPUTATIONAL FLUID DYNAMICS

4.1.1 Mesh Generation

The initial step in finite element (FE) and computational fluid dynamics (CFD) simulations is the generation of the mesh for evaluation of governing equations. These meshing elements are traditionally simple or straightforward geometries such as triangles or quadrilaterals for two-dimensional surfaces and tetrahedra or hexahedra for three-dimensional volumes. Meshing considerations include retention of original body geometry, uniform element size, adequate element size as well as minimized element count as higher quantities result in slower computational times.

Due to the geometric irregularity of the dendritic network, robust and flexible meshing protocols are needed to produce numerically stable meshes. Surface meshing facilitates the transition from reconstructed serial-sectioned data to volume domains. Volume meshes are then directly input as geometries for CFD modeling. Since modeling fluid flow through the dendritic network is a primary focus of this thesis, it should be reiterated that the following meshed structures presented are the inverse of the reconstructed dendritic network as they represent the spatial arrangement of liquid at the instant in time when decanting during solidification was initiated. The first assumption associated with this visualization arises with respect to the resultant inability to differentiate liquid domains from porosity and interdendritic voids. Fortunately, the domains meshed for flow simulations address this concern by way of their selection. Flow studies in this thesis are focused upon passage of fluid through the dendritic network. As will be shown, simulation cells were limited to the bodies that present opportunity for flow through the network from 0.X f_L to the 100% f_L region. Unconnected and isolated bodies do not possess such connectivity and therefore are not considered in the flow behaviors analyzed in this study. Therefore bias in connectivity due to inclusion of unconnected voids within flow cells is highly unlikely. The second assumption related to identification of liquid domains concerns their correlation with specific volume fraction. As will be shown in Chapters 5 and 6, each flow cell is denoted by its global volume fraction for cases of cross-flow and its inlet volume fraction for cases of vertical flow. In all vertical flow cases, the designated fraction liquid for each flow cell corresponds to the minimum in each range and indicates the controlling microstructure at which the greatest resistance to flow occurs. Additionally, liquid fraction defines locations at which the maximum pressure is occurring and where the morphology is most influential in controlling the overall pressure gradient in the given flow cell.

Surface meshes were generated directly from serial sections by the commercially available software, MIMICS™ and refined manually using the companion software package, 3MATIC™. MIMICS and 3MATIC are essentially two separate user interfaces possessing a nearly identical suite of tools offering varying degrees of stability for specific portions of visualization and meshing. MIMICS possesses a number of embedded tools focused specifically on image correction, segmentation and phase identification while 3MATIC contains a number of meshing algorithms possessing greater stability and tailored for refinement of large size, high element count meshes. Surface mesh refinement requires a balance between total element quantity and the distribution of element quality, chiefly skewness. Inspection panes in 3MATIC™ produce histograms detailing the distribution of a particular measure chosen by the user (*e.g.* skewness, edge to length ratio, area, smallest edge length, etc.) for the selected domain. Figure 4.1 illustrates two such inspection panes.

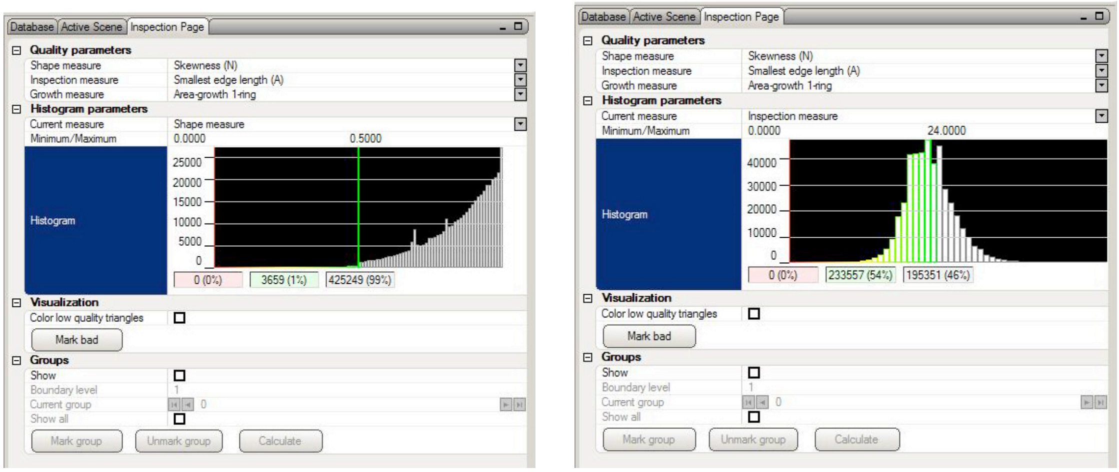

Quality parameters
Shape measure: Skewness (N)
Inspection measure: Smallest edge length (A)
Growth measure: Area-growth 1-ring
Histogram parameters
Current measure: Shape measure
Minimum/Maximum: 0.0000 0.5000
0 (0%) 3659 (1%) 425249 (99%)
Visualization
Color low quality triangles ☐
Groups
Show ☐
Boundary level 1
Current group 0
Show all ☐

Quality parameters
Shape measure: Skewness (N)
Inspection measure: Smallest edge length (A)
Growth measure: Area-growth 1-ring
Histogram parameters
Current measure: Inspection measure
Minimum/Maximum: 0.0000 24.0000
0 (0%) 233557 (54%) 195351 (46%)
Visualization
Color low quality triangles ☐
Groups
Show ☐
Boundary level 1
Current group 0
Show all ☐

(a) (b)

Figure 4.1 - Inspection Panes in 3MATIC illustrating (a) sknewness and (b) smallest element edge length histograms

It was critical to control skewness and minimum edge length and this was managed primarily using 3MATIC's "AutoRemesh" by skewness threshold and "Filter Small Edges" tools. Surfaces meshes refined to have a gaussian minimum element edge length (with a maximum of 2 times the mean) and skewness profiles no more than 1% of total elements exhibiting skewness less than 0.5 (on a 1.0 maximum scale) were acceptable. Such meshes were then converted to volume meshes using the CFD pre-processor known as GAMBIT™.

In GAMBIT™, the bodies to be volume meshed are selected, the tetrahedral/hybrid element type is specified. When GAMBIT is unable to generate a volume mesh it is generally due to one of three problems; 1) an unacceptable quantity of highly skewed elements, 2) an inability to resolve curvature due to excessively sized elements in the vicinity of small gaps or 3) overlapping elements creating infinite loops. When these occur, GAMBIT provides general user feedback for the cause of the inability to mesh and the surface mesh must be refined to eliminate the cause for error and volume meshing is attempted again via GAMBIT. This is an iterative process that converges when the mesh is sufficiently refined.

Refined volume meshes are then directly imported into FLUENT™ for computational fluid dynamics (CFD) simulation. Non-converging solutions or anomalies encountered during the volume meshing process were resolved by further refinement of the surface mesh at the location of the incongruity and the formation of a corrected surface mesh, a new volume mesh, and an additional simulation were performed until convergence was successful.

4.1.2 Navier-Stokes Relationships in Flow

When the assumption is made that a fluid possesses a constant viscosity as well as a constant density, the transport behavior of that fluid can be approximated by the Navier-Stokes equation. This equation is a special case of the differential momentum-balance equation widely applicable to various modeling situations due to its ability to relate fluid velocity, viscosity and pressure. It is given by the following equation, where ρ and μ are constant and correspond to density and viscosity, respectively [129]:

$$\rho \frac{\partial v}{\partial t} + \rho v \cdot \nabla v = -\nabla p + \mu \nabla^2 v + \rho g \tag{4.1}$$

The term v, is the fluid velocity, p is pressure and g is acceleration due to gravity. The first two terms in Eq. (4.1) are scaled by the density (ρ) with the first being the acceleration of fluid, $\frac{\partial v}{\partial t}$, and the second being the product of the velocity and velocity gradient $(v \cdot \nabla v)$. These equate to the sum of the pressure gradient, (∇p), the viscosity times the square of the velocity gradient $(\mu \nabla^2 v)$ and the product of the density times gravity (ρg). For relatively slow, steady state flow, such as solidifying metals, the fluid acceleration, the tensor derivative of velocity and the effect of gravity can be considered negligible and set equal to zero. As such, Eq. 4.1 can be rewritten as:

$$\nabla p = \mu \nabla^2 v \tag{4.2}$$

Equation 4.2 clearly illustrates the most basic principle derived from this relationship. There exists a direct proportionality of the velocity field with pressure for all Newtonian fluids in flow. Since the relationship equates differential products and sums, relationships are established across rates of change as opposed to specific variables. For this reason our simulations will capitalize on these correlations among rates of change as specific measuring and extraction of local velocity or pressure is subject to great variation throughout the irregular and rather complicated dendritic network. Equation 4.2 can be simplified further to explicitly relate flow rate and dimensions of flow domain such as length of travel inherent in the pressure gradient (∇p). In this thesis, we will utilize this simplified version of the Navier-Stokes relationship to quantify fluid flow through a tortuous dendritic medium. This simplified relationship is described by Darcy's Law and is shown in equation 4.2.

$$Q = \frac{KA\Delta P}{\mu L} \tag{4.2}$$

Q is the volumetric flow rate; A, the inlet cross-sectional area; L, the length associated with the pressure drop ΔP; and μ, the fluid viscosity. Local pressures are assessed through planar averages over the entire cross-section of the simulation normal to the principle flow direction. In vertical flow cells, average pressure drops significantly in the vicinity of the inlet and decreases to a plateau at increasing heights. In cross flow, the pressure drop occurs less rapidly across the domain. As a result, in vertical flow simulations, tangents of the maximum pressure differential were assessed from the pressure profile for identification of the pressure change. L is the length over which the maximum and minimum pressures of the tangent line are observed. In cross flow, planes offset from the inlet and outlet, free of potential boundary effects are used and ΔP is identified and assessed as the difference between their average planar pressures. L is the length of separation between the two identified planes. Since permeability is anisotropic, K_y for parallel flow and K_x for cross flow were independently calculated and will be discussed in detail in Chapters 5 and 6. Figure 4.2a and b demonstrates how ΔP and L were defined within representative pressure profiles in vertical and cross flow cases, respectively.

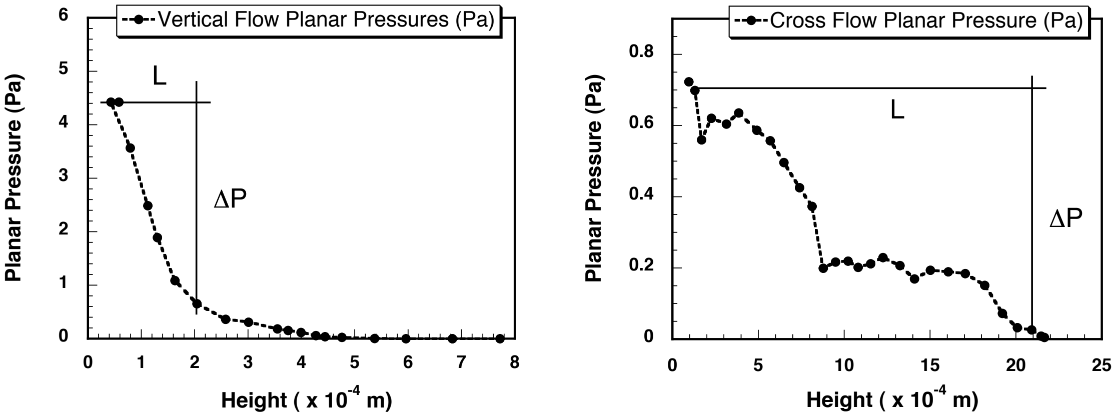

Figure 4.2 - Vertical and Cross Flow Planar Pressure Profiles with Identification of ΔP and L for Permeability Calculation

FLUENT™ 6.3.26 was used for all flow simulations and is a CFD suite produced by ANSYS® Inc. Following importation of the volume mesh, the entire volume is scaled to the proper dimension. Initial meshing protocols are performed on the mm-scale due to software difficulties produced in refining meshes on the order of microns. Material properties are input as constants based upon values reported in the literature for both density (ρ) [130] and viscosity (μ) [131] of molten nickel and nickel-base superalloys. Simulations are run to convergence such that no significant fluctuations exist in the residuals of any orthogonal flow direction or flow continuity to a value of no greater than 1×10^{-3}. This generally occurs over less than a few hundred iterations for each case. Simulations were typically run to a minimum of 300 - 500 iterations in each case for consistency.

Since simulations were performed under isothermal conditions with constants assumed for viscosity and density, it is useful to briefly consider the effects of thermal and solutal variation and the benefits of this assumption in this study. The goal of this study is to investigate flow behavior within dendritic structures independent of thermal and solutal effects. While mentioned previously, it should be reiterated that the effects of elemental segregation, resultant density gradient and temperature variation at the solidification front strongly influence chimney and freckle formation. In fact, the variability found in these factors are likely to pose more substantial impacts to variability in pressure than flow behavior alone. This can be seen by the variation in buoyant pressures over the length scales for which permeability was calculated among the alloys contained in this study, Table 4.1. These values are presented to serve as an example of the variation and orders of magnitude to be anticipated over these relatively small length scales due to buoyancy effect. Buoyancy approximations are calculated according to the following relation;

$$P_{buoyancy} = \rho g \times depth \tag{4.1}$$

where ρ is the density of the liquid and g is the acceleration due to gravity.

Table 4.1 - Variation in Buoyancy force for two mediums of uniform density

	Liquid Density $\rho = 6980$ kg/m^3	Liquid Density $\rho = 7570$ kg/m^3	Depth ($\times 10^{-4}$ m)
Buoyancy Pressures (Pa)	3.42	3.71	0.5
	6.84	7.42	1.0
	10.3	11.1	1.5
	13.7	14.8	2.0
	17.1	18.5	2.5
	20.5	22.3	3.0
	23.9	26.0	3.5
	27.4	29.7	4.0

Buoyancy pressures above were calculated using the noted approximations of 6980 kg/m^3 and 7570 kg/m^3 for densities corresponding to a commercial nickel-base alloy [130, 132] and the Ni-Al-W alloys [133] depicted in this study. Additionally, as previously noted, all simulations in the N4 and Ni-Al-W cases of Chapters 5 and 6, respectively, were performed with these values. Additional variation in density caused by solutal segregation would only increase the buoyancy further. The goal in this study however, is to isolate, investigate and quantify flow characteristics such as connectivity, the presence of high velocity channels and regions of pressure fluctuation and their relation to the local dendritic arrangement independent of temperature and composition effects. This approach was selected such that the findings of this study would not be material specific but applicable to a wide variety of directional solidification instances. This does not imply the findings of this study cannot accompany compositional variation effects. As will be discussed in Chapter 7, implementation of thermally induced density variations are best applied at the level of the Rayleigh criteria.

4.2.3 Boundary Conditions

Boundary conditions are assigned at the boundary plates of the volume located at opposite ends of the body with the primary flow direction oriented normal to these boundary plates. For both vertical, and cross flow, y and x directions respectively, boundary conditions of zero pressure at the outlet as well as no-slip on all internal boundaries and side-walls were imposed. However, for the cases of cross-flow, a zero-shear condition was set on the top and bottom surfaces to alleviate any drag or boundary layer effects caused in the simulation by the artificially imposed walls. For vertical flow cases, the nominal fluid flow velocity was prescribed to be in the range of the withdrawal rate. This was accomplished by scaling the desired inlet velocity by the area fraction available for flow in the vicinity of the inlet and optimizing from this value to arrive at a minimum velocity equal to 0.05 mm/s. This allowed for flow cells of varying volume fraction to experience flow fields comparable to the withdrawal event. For cross flow, inlet velocities were selected to yield nominal flow velocities equivalent to 0.1 those of the vertical flow cases. The boundary conditions were chosen such that nominal flow in vertical flow cases reflect withdrawal rate and cross-flow cases exhibit a ratio to the withdrawal rate on the order of those previously suggested for vertical to cross-flow relations in the vicinity of the solid-liquid interface [109, 134, 135]. Further details of the inlet boundary condition values are summarized in tabular form in Chapters 5 and 6 and listed by corresponding volume fraction specific to case.

CHAPTER 5

RENÉ N4 RESULTS

5.1 ACQUISITION OF THREE-DIMENSIONAL DATASET

As mentioned in Chapter 3, Section 3.1, RoboMET.3D™ was used for all serial sectioning experiments in this thesis. The recession rate for serial sectioning performed for René N4 is shown, Figure 5.1. Specimen thickness was measured by the use of a Mitutoyo® ABSOLUTE table-top micrometer with pneumatic actuator and digital display. Measurements demonstrated repeatability in the range of ± 2 μm for a given measure with an average recession rate of 2.2 μm/slice obtained by 1 μm lapping film. Data acquisition required a period of three weeks and three days, Figure 5.2. Over this duration, at minimum, 11 sections in a given day were successfully sectioned and documented while at most, 78 sections in a given day were obtained.

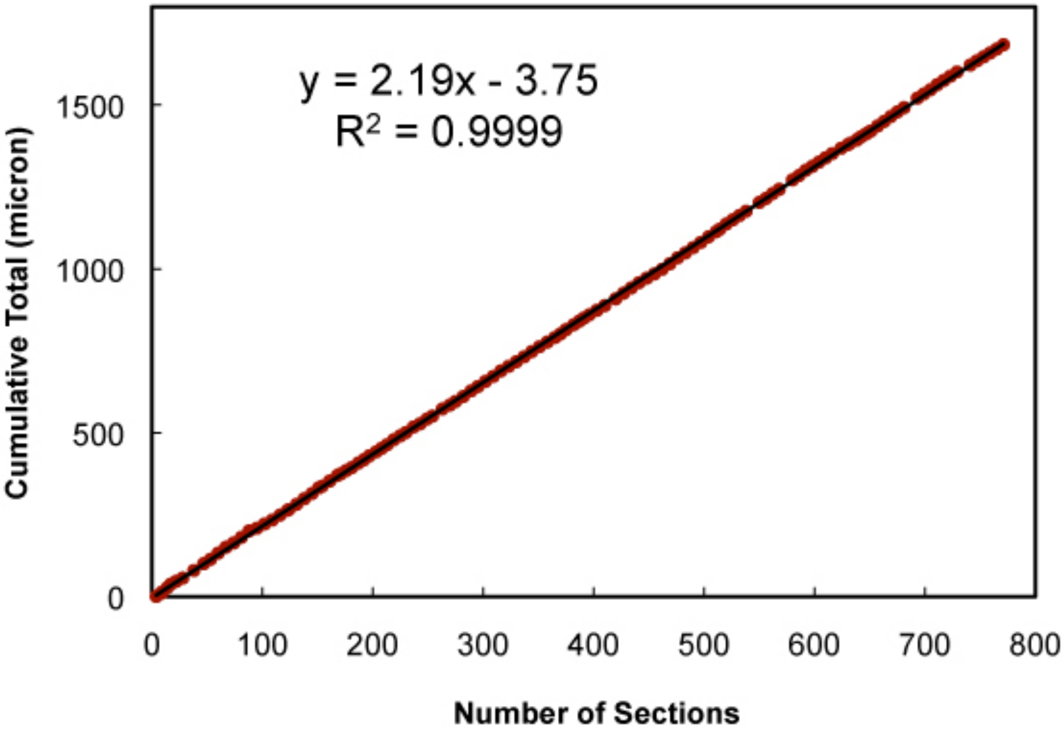

Figure 5.1 - Recession rate for RoboMET.3D serial sectioning of Rene N4 commercial alloy

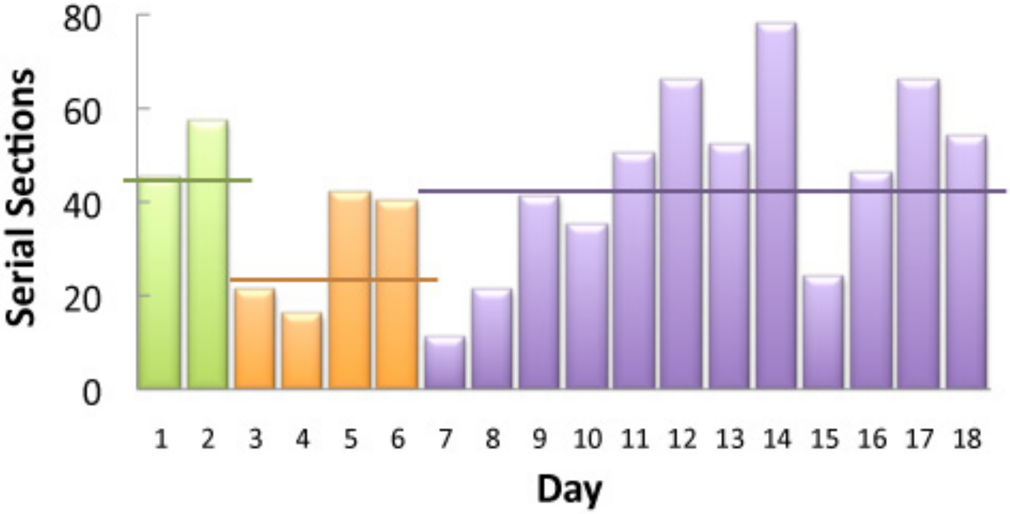

Figure 5.2 - Serial Sections Obtained per day with RoboMET.3D^{TM} system

5.2 RECONSTRUCTED VOLUMES

5.2.1 Memory Requirements

A large portion of three-dimensional datasets are gained by way of serial sectioning, as such, the memory required to maintain such information warrants consideration prior to data collection. Since high resolution and magnification are desirable, the concomitant effect of increased resolution and magnification on memory requirements generally bears an inverse relationship. For René N4, fifteen montage images taken at 10X magnification with resolutions of 0.52 μm/pixel, and stored in ".TIFF" format produce file sizes on the order of 15 - 20 MB. Each montage of this type serves as a single serial-section. When multiplied by the number of serial-sections typical of a dataset, required memory quickly accumulates. The René N4 study contains 727 such slices for a total of 12.62 GB of raw data. Table 5.1 illustrates a variety of possible configurations for RoboMET.3D's imaging system and the approximate memory allotment required for each. The first value in the configuration corresponds to the primary magnification while the second corresponds to one of two secondary objective lens used in the ZEISS inverted microscope to increase magnification options. The 10X_1.0X configuration was chosen to provide optimum trade-off between imaging time, resolution and memory allocation requirement. A montage image corresponding to a single slice from the aforementioned René N4 dataset is shown in Figure 5.3.

Table 5.1 - Imaging Configurations with RoboMET.3D for René N4 Sectioning

Magnification	Montage Images Required	Resolution (μm/pixel)	Approximate Memory Allocation (MB)
5X_1.0X	3	1.04	3
5X_1.6X	8	0.67	10
10X_1.0X	15	0.52	17
10X_1.6X	24	0.34	30
20X_1.0X	40	0.26	35
20X_1.6X	50	0.17	40
50X_1.0X	264	0.10	200*
50X_1.6X	646	0.07	500*

** estimates based on lower magnification to memory ratios*

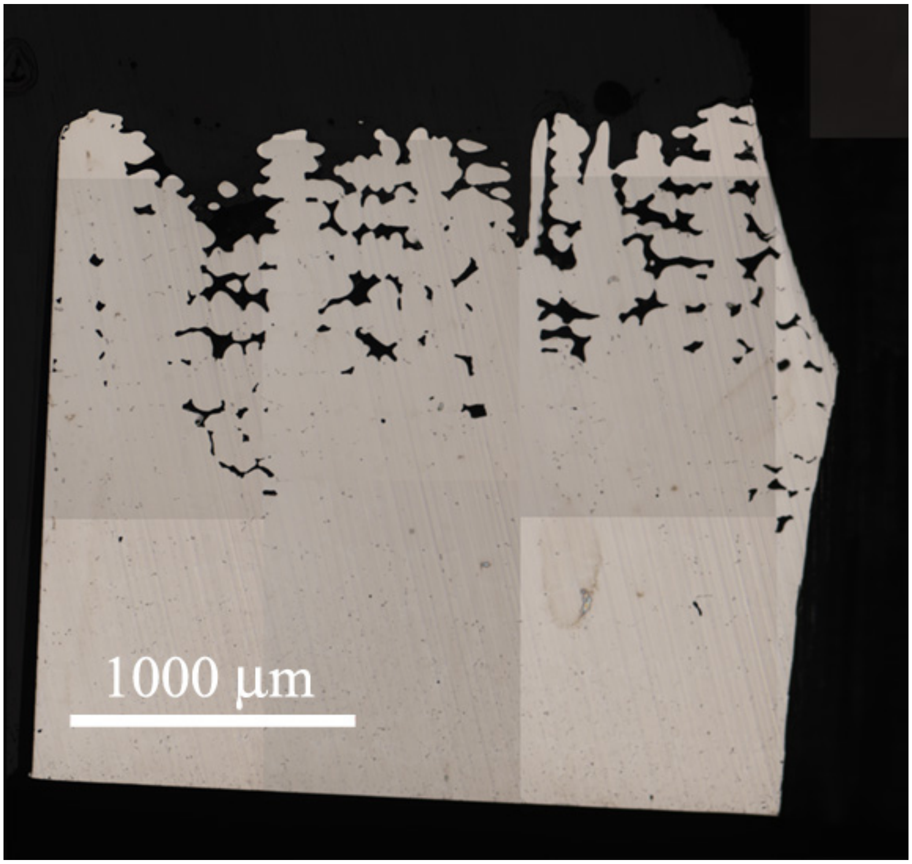

Figure 5.3 - Single data slice obtained via RoboMET.3D

5.2.2 Volume Visualized

As mentioned in Chapter 3, samples were cast while initiating a controlled fracture in the mold during withdrawal. This provided opportunity for rapid evacuation of molten liquid, thereby isolating solidified dendrites which were subsequently serial-sectioned. The reconstruction in the commercial alloy René N4 contains a volume of 2500 x 2500 x 1500 μm, Figures 5.4 and 5.5. Observation from the top of the reconstruction, oriented normal to the primary solidification direction, Figure 5.4, illustrates the four-fold symmetry and cross shape characteristic of dendritic structures. It is apparent that a collection of dendritic cores are present possessing little to no misorientation with respect to one another, indicating the presence of a single crystal. Close examination of three-dimensional morphologies present in the reconstruction also show resolution of not only secondary dendrite arms but also emerging tertiary structures as well. Alternatively, the full reconstruction is shown in Figure 5.5 in which each frame is rotated about a central vertical axis providing views from various angles surrounding the reconstruction. The arrows in each frame indicate the primary solidification direction. Fully solidified René N4 exists at the base along the x-axis where y is equal to zero. Dendrite tips are located at heights corresponding to upper portions of the y-axis.

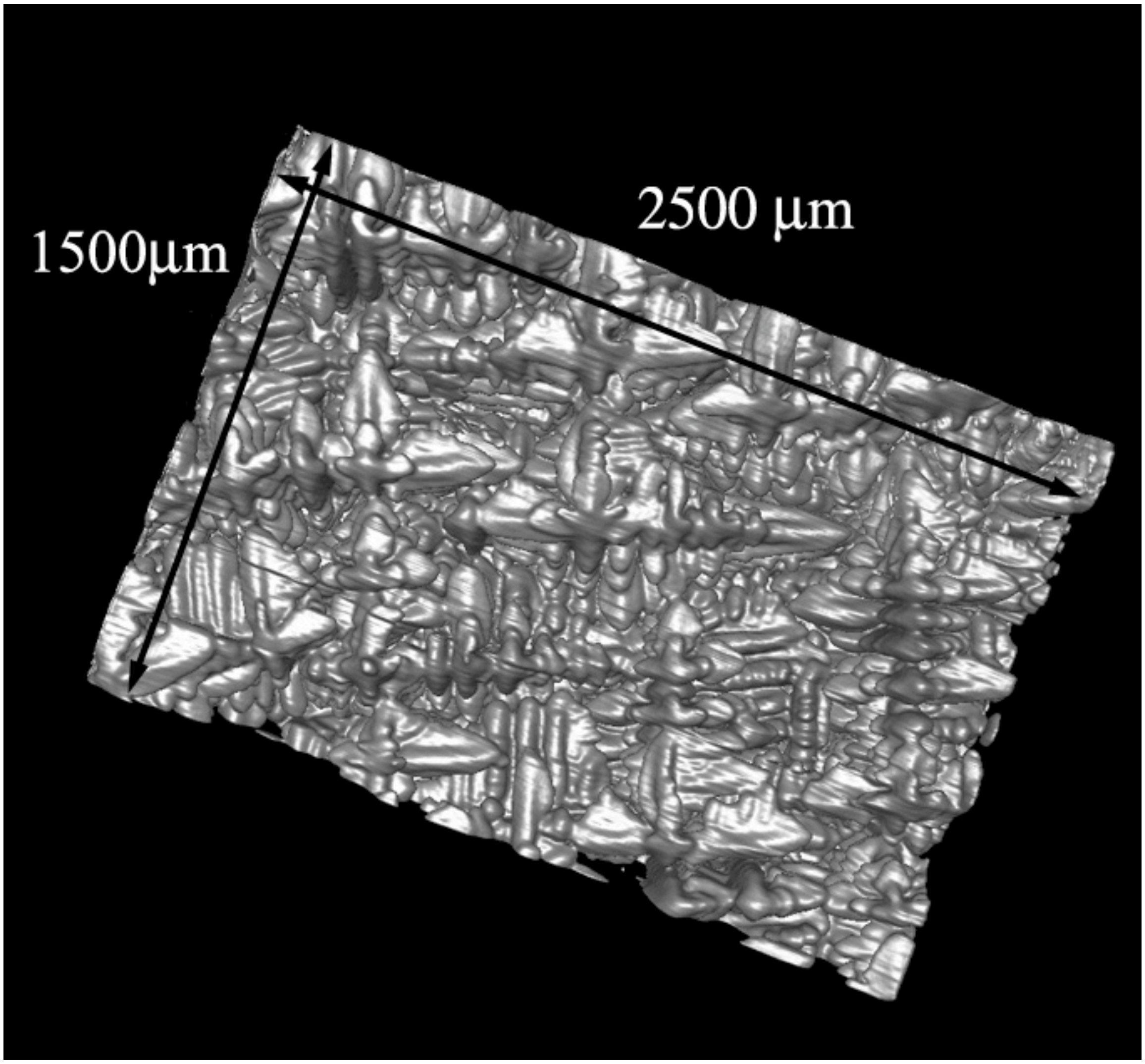

Figure 5.4 - Top View of Reconstucted René N4 illustrating a collection of dendritic structures detailing the characteristic four-fold symmetry within a single crystal

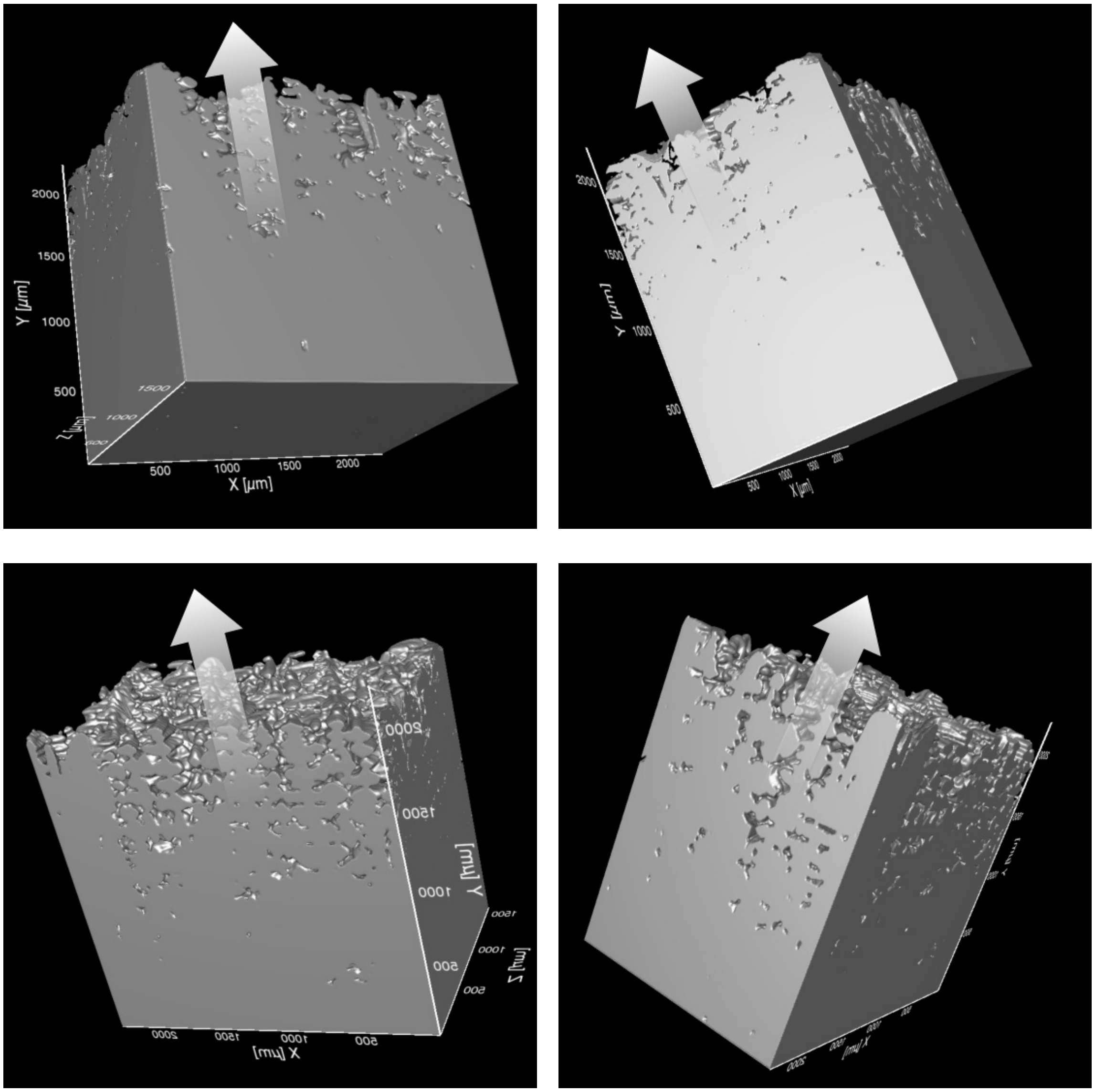

Figure 5.5 - Reconstructed volume of the mushy zone in René N4 rotated around a central vertical axis. The arrows indicate the withdrawal direction as well as primary dendritic growth direction. The xy axis corresponds to the serial-sectioning plane of the reconstruction.

5.3 CHARACTERIZATION OF DENDRITIC STRUCTURES

Measurements of relevant dendrite morphological characteristics have been taken directly from the reconstructed volume. Measures of; dendrite arm spacing ($\lambda_{1,2}$), volume fraction, void interconnectivity, interfacial surface area (ISA) as well as Gaussian and Mean curvatures, (H_G) and (H_M) respectively, have been acquired. Volume fraction will be presented primarily as a function of height in the reconstruction providing some indication of the local solidification behavior throughout the mushy zone. Dendrite arm spacing yields some indication of the adherence of the dendritic network to the expected solidification behavior given the experimental casting parameters. Void connectivity supplies an assessment of not only the quantity of interdendritic regions but also their frequencies with respect to one another as well as their size distribution within the reconstruction. Interfacial surface area quantifies the local solid-liquid ratio at a given point or domain while also providing for the calculation of a normalized value, (S_V) or ISA/unit volume, which allows for direct comparison across domains of varying size. Later, the quantitative relationship between S_V and permeability, K, will also be reported. Interfacial shape distributions (ISDs) quantify the presence of various curvature types with curvature contour maps detailing the physical location of a given curvature in the reconstructed domain.

5.3.1 Dendrite Arm Spacing

To assess the primary and secondary dendrite arm spacing (PDAS & SDAS) in the René N4 casting and reconstruction, three methods were employed. Initially, an estimate based upon the solidification rate and inferred thermal gradient as detailed in Section 2.1.3, provided a range of expected PDAS and SDAS values given the experimental conditions. As validation and examination of these predictions, conventional measurements were obtained using two-dimensional metallography on material taken directly from the casting in the vicinity of the reconstruction. Thirdly, planar measures were taken by examination of sections in the three-dimensional dataset itself.

The thermal gradient, (G) for the material under examination was 40°C/cm [17] and the solidification front velocity, (V) was 2.5 mm/min. The product of G∗V based upon the relationships dictated by Equations 2.2 and 2.3 yield $G^{-1/2} * V^{-1/4} = 0.197$ and $(G * V)^{-1/3} = 1.82$, respectively. These products suggest the expected dendrite arm spacing in the range shown in Figures 5.5 and 5.6, corresponding to a PDAS in the range of 450 - 600 μm and SDAS in the vicinity of 60 - 80 μm for this casting experiment.

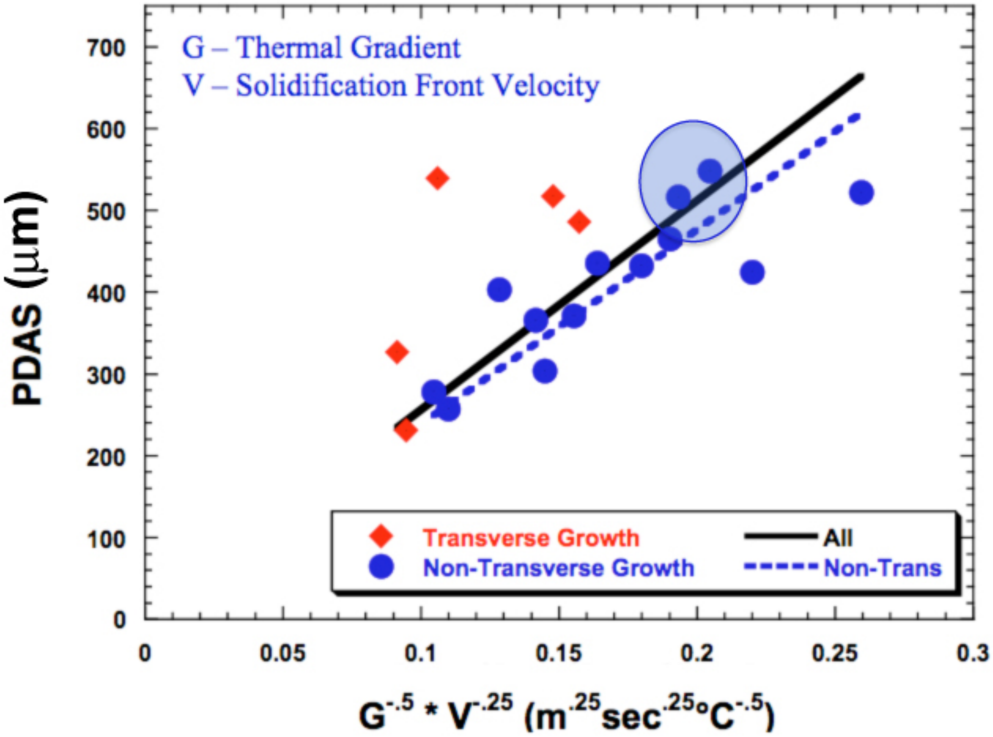

Figure 5.6 – Anticipated Primary Dendrite Arm Spacings based upon Thermal Gradient (G) and Solidification Rate Velocity (V) product ($G^{-.5} \times V^{-.25}$) with Expected Range Highlighted

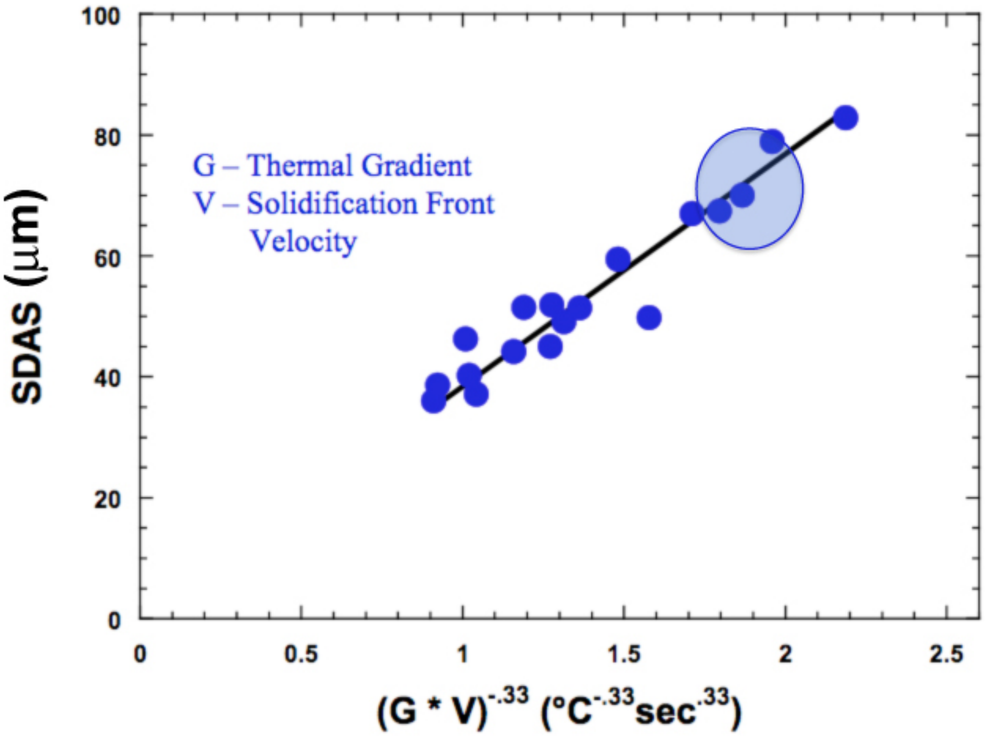

Figure 5.7 - Anticipated Secondary Dendrite Arm Spacings based upon Thermal Gradient (G) and Solidification Rate Velocity (V) product $(G^*V)^{-.33}$ for SDAS with Expected Range Highlighted

Secondly, two-dimensional metallography was performed on over 85 independent micrographs for determination of average PDAS as described in detail in Chapter 3 Section 3.4. These samples were extracted from the fully solidified region below the area from which the serial-sectioned reconstruction was obtained. With respect to SDAS, over 30 independent micrographs and measurements were collected as analyzed. The data is summarized in Table 5.2 with typical micrographs by which this data was generated, displayed in Figure 5.9.

Table 5.2 - Summary of Two-Dimensional Dendrite Arm Spacing Measurements

	Measures	Total Cores Counted	Secondary Arms Sampled	Average	Standard Deviation
PDAS	87	1460	--	560	28
SDAS	31	--	372	82	6.9

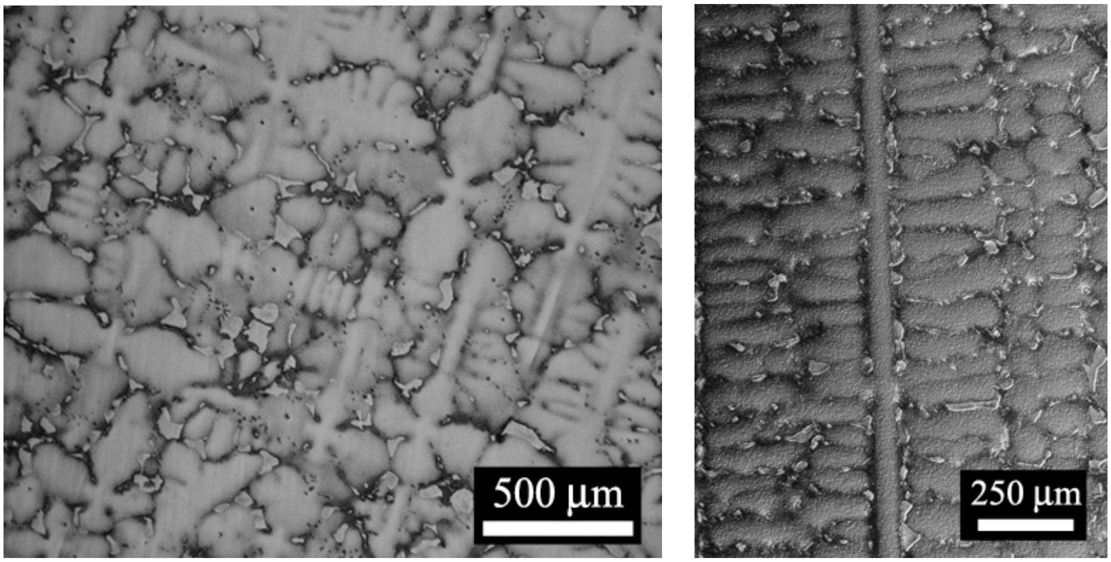

(a) (b)

Figure 5.8 – Typical Micrographs for Dendrite Arm Spacing Measurements (a) normal to the primary growth direction, (b) through a primary dendritic core revealing secondary growth direction

Similarly, using the reconstructed volume, planar measures of primary and secondary dendrite arm spacing were obtained by selecting multiple planes transverse and parallel to the primary growth direction. Although a smaller set of measures were obtained in this manner due to the volume available for sampling, good agreement is seen between measures. Notably, the size of the volume is a central limiting factor in obtaining independent planes including dendritic cores and sets of identifiable secondary arms without redundancy. A summary of PDAS and SDAS measures from within the three-dimensional reconstruction is shown in Table 5.3. Additionally, representative planes for DAS approximation from within the reconstruction are shown in Figure 5.10.

Table 5.3 - Summary of Dendrite Arm Spacing Measurements obtained from 3-D Reconstructed dataset

	Measures	Total Cores Counted	Secondary Arms Sampled	Average	Standard Deviation
PDAS	16	255	--	490	29
SDAS	6	--	41	86	6.8

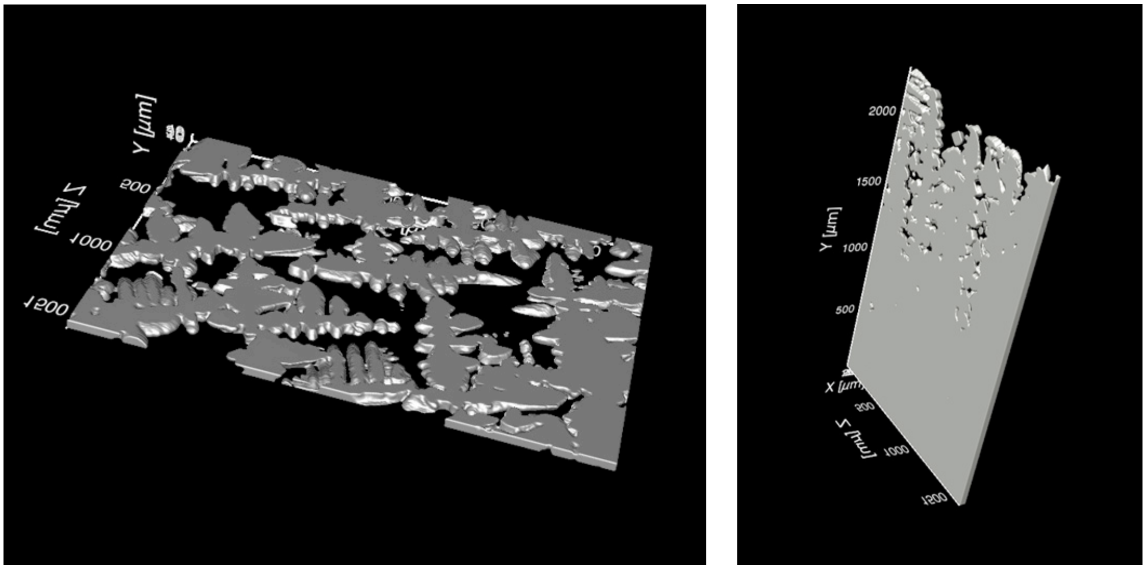

(a) (b)

Figure 5.9 - Representative Planes used for Dendrite Arm Spacing Approximation from within the 3-D Reconstruction (a) plane normal to the primary growth direction, (b) plane parallel to the primary growth direction

A comparison of the 2D and 3D measures are given in Figure 5.11.

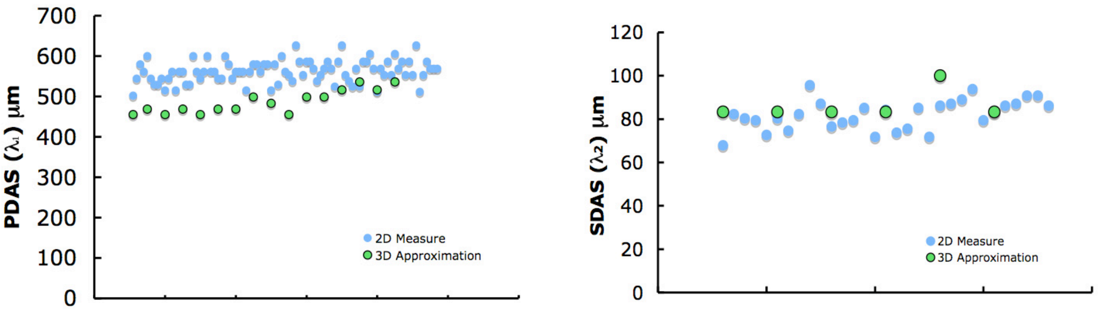

Figure 5.10 - Comparison of 2D Measures and 3D Approximations of PDAS and SDAS in René N4

The average measures of PDAS obtained from within the 3D reconstruction are lower than traditional 2D measures by a factor of 13% and show better agreement for SDAS measurements between both methods. The lower PDAS measures yielded by the reconstructed domain are likely resultant from the smaller sampling domain available in the reconstruction. While the lower values may also be indicative of the local variation of PDAS in an experimental casting, comparison of SDAS measures suggest consistency between the dendritic structures of the reconstructed volume and the fully solidified material from which 2D measures were garnered. Both 2D and 3D approximations fall well within the experimental range of values suggested by the G and V dendrite growth models in Equation 2.3 and 2.4.

5.3.2 Volume Fraction

Each cross-sectional plane along the volume height was directly measured for area fraction of solid and liquid. By visualizing each cross-sectional plane as a binary image, each pixel location represents either solid material or a void region formerly occupied by liquid or isolated porosity. Combining all individual measures and ordering them by height according to Equation 3.3, produces a measure of volume fraction. These ratios of pixel quantities represent the relative amounts of liquid and solid within successive planes along its height. This progression of ratios represent volume fraction solid (fs) and are plotted as a function of height in the reconstruction in Figure 5.11. Inspection reveals an initially moderate decrease in solid fraction followed by a rather precipitous drop wherein approximately eighty percent of the volume fraction solid decreases to zero in the upper 500 μm of the mushy zone. This indicates a curved liquidus surface where the fraction of solid as a function of temperature varies non-linearly. As will be discussed in Chapter 7, lateral flow at fraction liquid ≤ 0.4 is highly restricted suggesting that decanting may have been inhibited below volume fraction liquid of 0.4. Additionally, the smaller volume fluctuations between fractions solid of $0.5 < fs < 0.9$ exhibit periodic fluctuations. These are due to locally fluctuating solid fraction caused by the presence of secondary dendrite arms. These fluctuations range from 80 – 200 μm indicating the undulations in the volume fraction measure are indeed impacted by individual and concurrent pairs of secondary dendrite arms in the locally sampled volume.

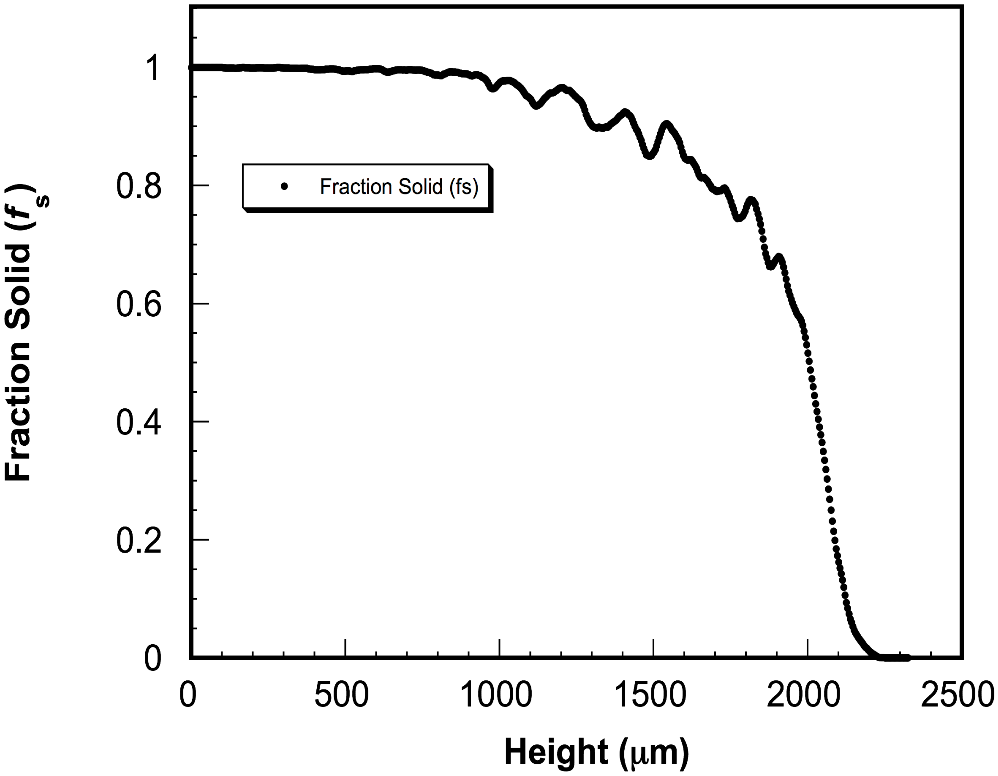

Figure 5.11 - Volume fraction solid as a function of height in the reconstructed René N4 dataset

5.3.3 Void Interconnectivity

Beyond physical measures of the reconstructed dendrites, characterization of the degree of linkage between interdendritic regions is important to fluid flow. As such, understanding the depths to which these pathways penetrate the mushy zone and are connected to less restricted regions of solute above and between dendrites is very useful. For convective instabilities to develop, fluid flow through the dendritic structure must occur, making the connectivity of interdendritic gaps therefore important. By inverting the visualization of solidified nickel-base superalloy in the reconstruction, a representation of interdendritic liquid at the point of decanting is produced, Figure 5.12.

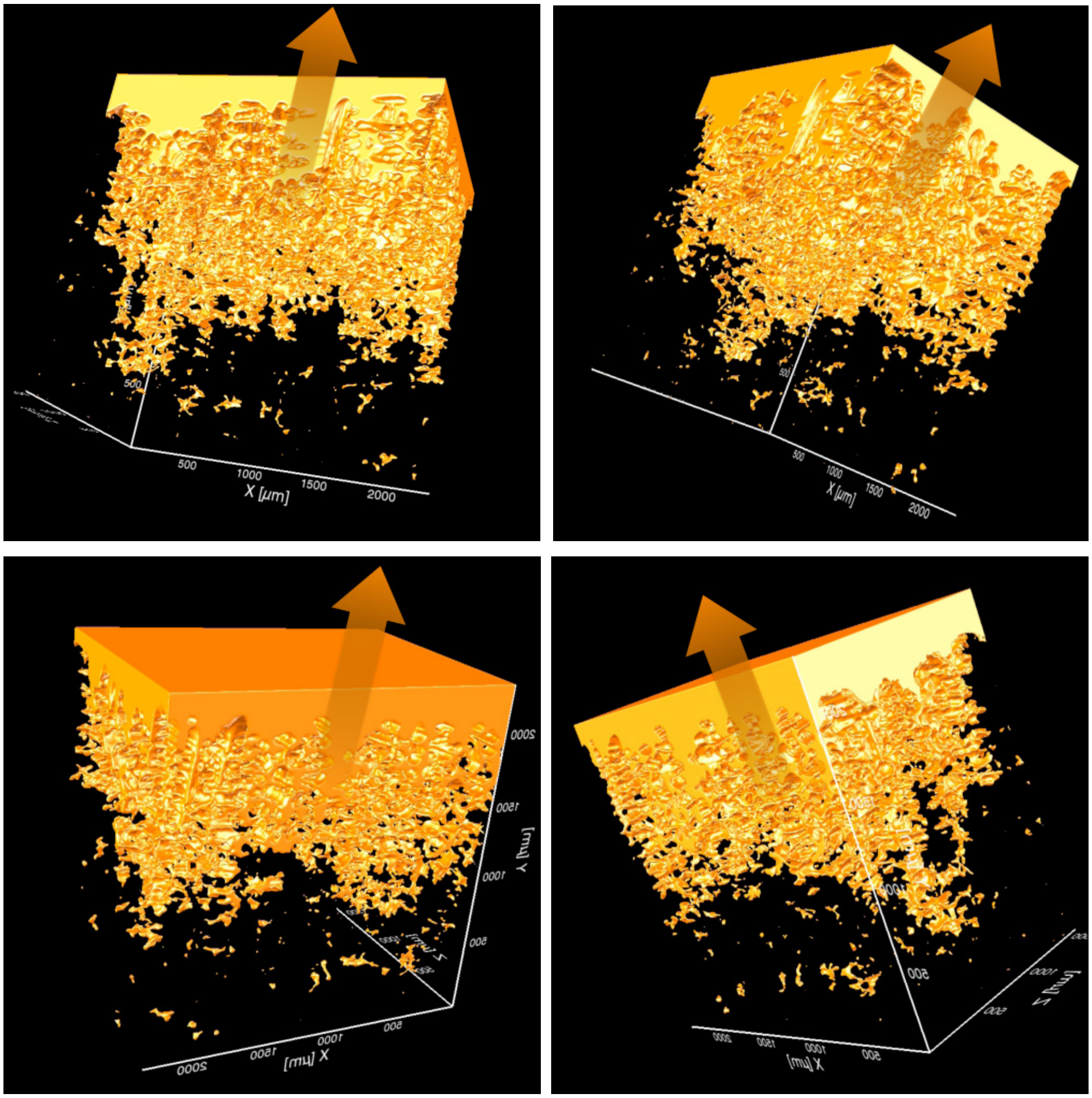

Figure 5.12 - Reconstruction of interdendritic liquid generated by visualizing the collection of all interdendritic voids. Arrows indicate the primary solidification direction.

The channels produced by the collection of interdendritic voids throughout the mushy zone possess a high degree of connectivity, yet these channels do not unify all voids. By distinguishing each independent body of interdendritic void in the reconstruction, over 800 individual regions were identified. Importantly, 97.9% of the total voided regions are composed of a single interconnected region. Additionally, this largest non-solid region is two orders of magnitude larger than that it's nearest neighbor and extends from the region above the dendritic structure well into approximately 1000 μm of the mush. Table 5.4 summarizes the number of voids and the sum of their physical sizes for a given voxel ("volume-pixel") range. It is interesting to note that the cumulative void percentage obtained by excluding the largest eighteen independent bodies is 0.13%. The largest eighty-six bodies detail the location in which molten liquid is the single or overwhelming dominant phase. The collections of remaining bodies indicate encased voiding is consistent with the range of isolated porosity, 0.02 - 0.3% [136-139], typically encountered in fully solidified single crystal materials.

Table 5.4 - Quantification of Independent Bodies Related to Interdendritic Voids

Volume Threshold (μm^3)	Voxel Threshold	No. of Independent Bodies	Cumulative Volume	Percentage Void Fraction	Contribution to Total Non-Solid Regions
380 700 000	10 000 000	1	1605996489	97.9%	97.91%
38 070 000	1 000 000	0	--	--	97.91%
3 807 000	100 000	1	4960443	0.30%	98.21%
380 700	10 000	16	18838565	1.15%	99.36%
38 070	1 000	68	8238469	0.50%	99.86%
3 807	100	139	1809311	0.11%	99.97%
380.7	10	273	338958	0.02%	99.99%
38.07	1	337	50027	0.00%	99.99%

These observations suggest interdendritic voids bear connectivity sufficient to participate in flow through the dendritic network as well as in the unrestricted region of complete liquid above dendrite tips further indicating the reconstruction is a valid domain for investigation of dendritic structure effect on flow through the mushy zone.

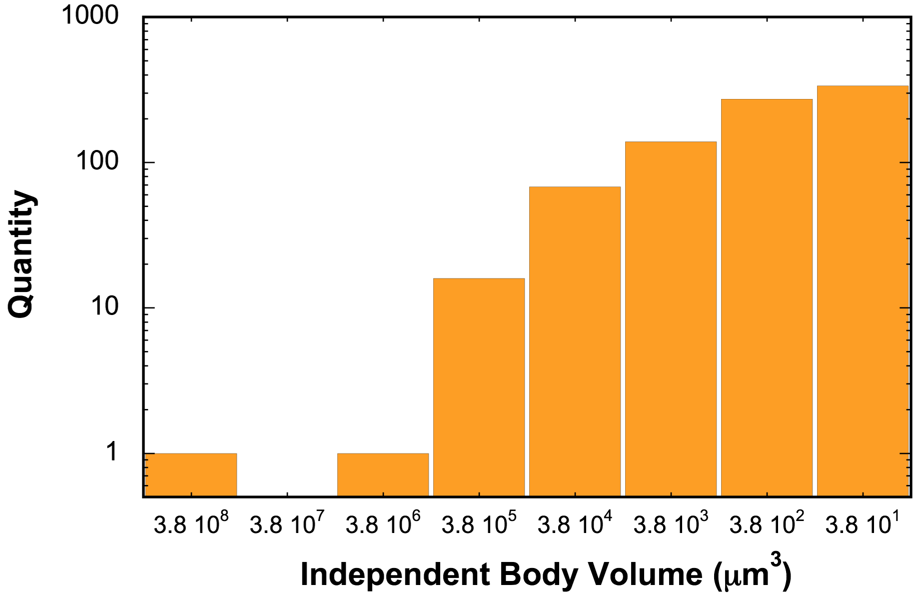

Figure 5.13 – Quantity of Non-Solid Independent Body Volumes ordered by Volume magnitude

5.3.4 Interfacial Surface Area

Interfacial surface area (ISA) as a function of height in the reconstruction was analyzed. All individual elements in the surface mesh of the dataset were compiled and indexed according to their height. By binning all surface elements within a pre-determined height value, measures of interfacial surface area as a function of height were obtained. By changing the bin size, measures as coarse or as fine as desired were obtained. Ultimately, bins the size of the vertical resolution in the dataset (4.16 μm/pixel), were selected to maintain equal spatial correlation between height, volume fraction and interfacial surface area. An ISA normalized by the associated volume was also calculated to obtain the surface area to volume ratio (S_V). The relative change in S_V with volume fraction is shown in Figure 5.15. Interestingly, S_V reaches a maximum at $f_s = 0.65$. Undulations in the ISA measure correspond directly with local fluctuations in the volume fraction solid caused by collections of secondary dendrite arms. The undulating peak widths range from

80 – 200 μm and indicate that undulations are impacted by individual and concurrent pairs of secondary dendrite arms. In the S_V curve, however, undulations are definitively more pronounced and offer greater resolution of the fluctuations indicating that local ISA can be largely influenced by the presence of secondary dendrite arms over relatively small distances.

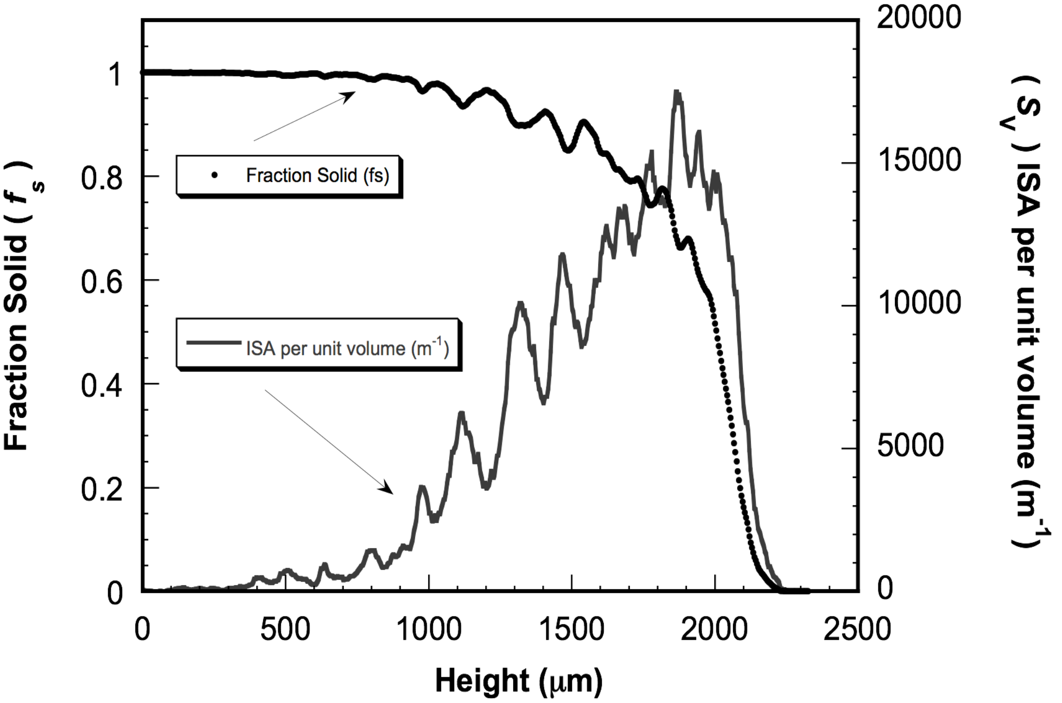

Figure 5.14 - Variation of Measured Interfacial Surface Area per unit Volume (S_v) with Volume Fraction Solid

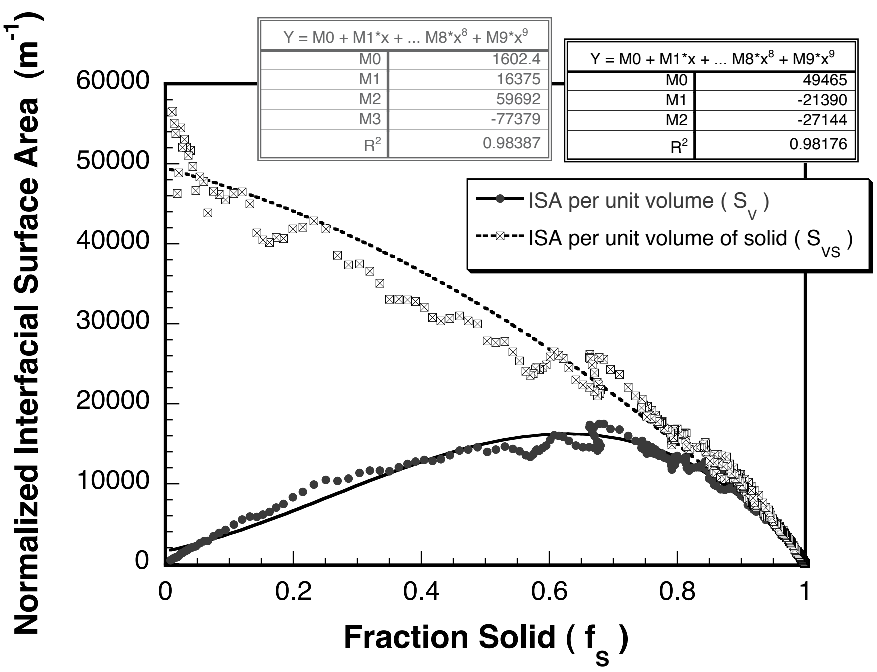

Figure 5.15 - Measured Interfacial Surface Area per unit Volume (S_V) and Interfacial Surface Area per unit Volume Solid (S_{VS}) in René N4 Reconstruction

5.3.5 Curvature

Mean curvature data of the reconstructed solid indicate that the highest curvatures occur between secondary dendrite arms and at dendrites tips. The interfacial shape distribution (ISD) plot for the René N4 dataset is shown in Figure 5.16 where the κ_1 and κ_2 axes are normalized by the interfacial surface area per unit volume (S_V). Recall, by definition, the principal curvatures, κ_1 and κ_2, are inverses of the principal radii of curvature for any given point on the reconstruction surface with κ_2 being the larger of the two. As shown in the ISD, the greatest amount of curvature lies on the $\kappa_1 = 0$ axis where κ_2 is just positive. Curvatures existing on the $\kappa_1 = 0$ axis describe the cylindrical solid which is evidence of the trunk-like shapes indicative of primary dendrite cores growing into liquid. The high probability density in this region is well within expectation given the directionally solidified sample. It is interesting to note however, the presence of an elongated tail in the

ISD where κ_1 is negative and κ_2 is slightly greater than zero. In this location of the ISD map, the positive association of κ_2 corresponds with saddle-shaped curvature encapsulating liquid. These regions are indicative of the valleys found between secondary dendrite arms and at the joint in which secondary dendrite arms emerge from their primary core. The ISD illustrates the existence of a large range of curvature pairs exhibiting this characteristic. Mean (H_M) and Gaussian (H_G) curvature color-contour depictions are displayed on the dendritic microstructure in Figures 5.16 and 5.17 respectively. As discussed in Chapter 3, Section 4.6, Mean and Gaussian curvatures are defined as follows:

$$H_M = \tfrac{1}{2}(\kappa_1 + \kappa_2) \tag{5.1}$$

$$H_G = (\kappa_1 \cdot \kappa_2) \tag{5.2}$$

The color ranges illustrated correspond to positive and negative values of H_M and H_G respectively, as defined by their associated scale bar. Initial inspection of the H_M color-contour depiction illustrates H_M is very effective at highlighting dendrite tips whereas H_G readily demonstrates the variation between concave and convex saddle shapes between the solid and liquid phases. Concave shapes are found on collections of closely neighbored dendrite tips whereas convex saddles correspond to valleys located between secondary dendrite arms and the locations where secondary arms grow out from primary cores as described in the ISD plot. Additionally, visual comparison of shared positive and negative curvature associations in Figures 5.16 and 5.17 reveal primary, secondary and tertiary dendrite tips all show positive Mean and Gaussian curvatures while valleys between secondary arms clearly exhibit negative Mean and Gaussian curvatures.

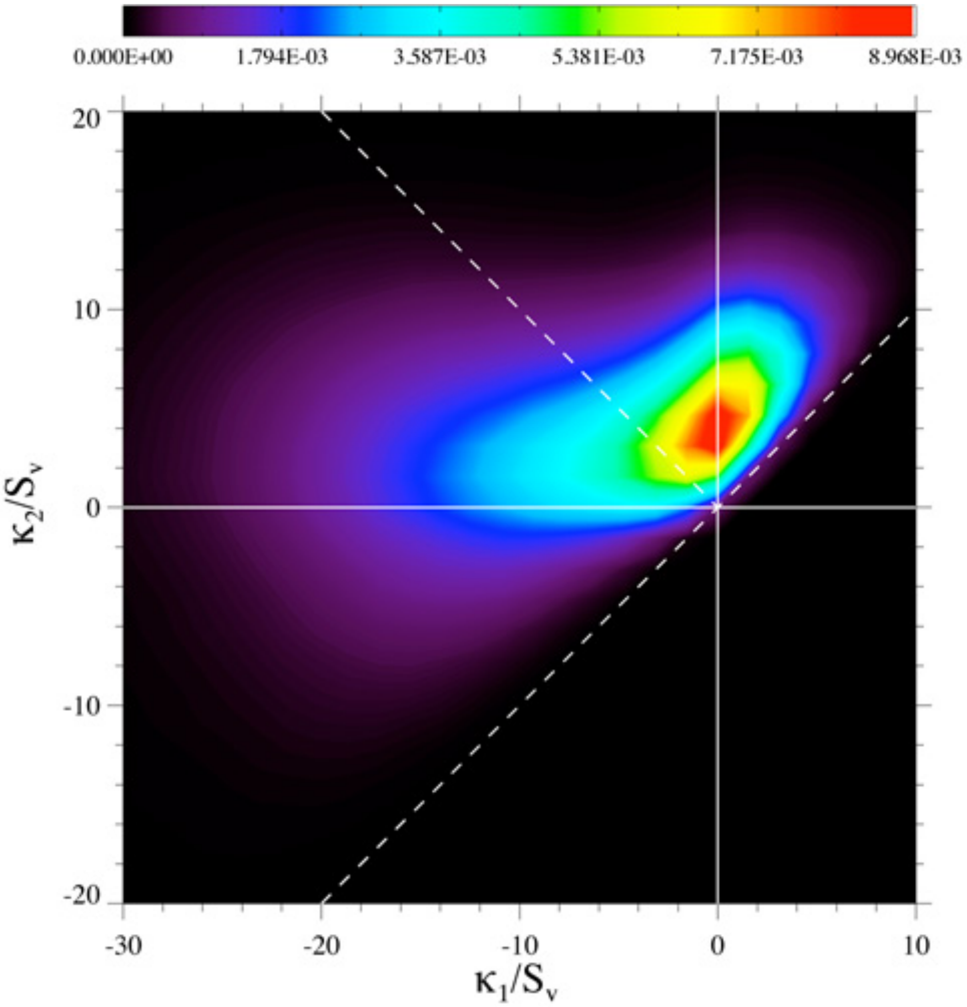

Figure 5.16 - Interfacial Shape Distribution Plot for René N4 reconstruction. κ_1 and κ_2 axes are normalized by the interfacial surface area per unit volume (S_V)

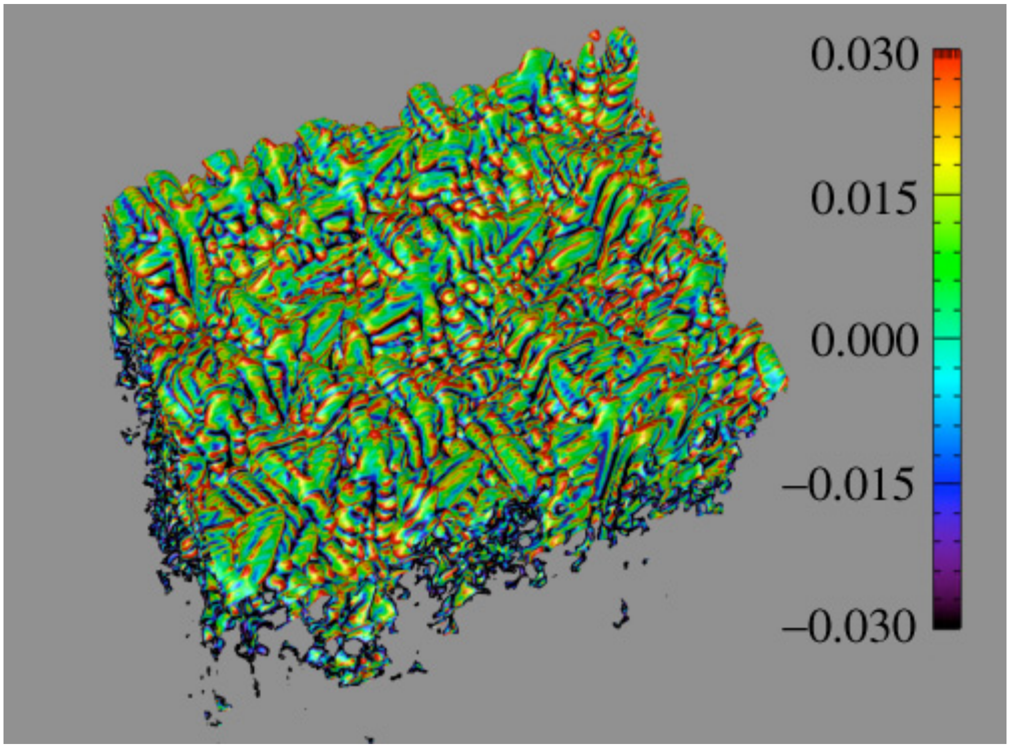

Figure 5.17 – Color-coded Mean Curvature (H_M) Contour Plot in René N4 reconstruction

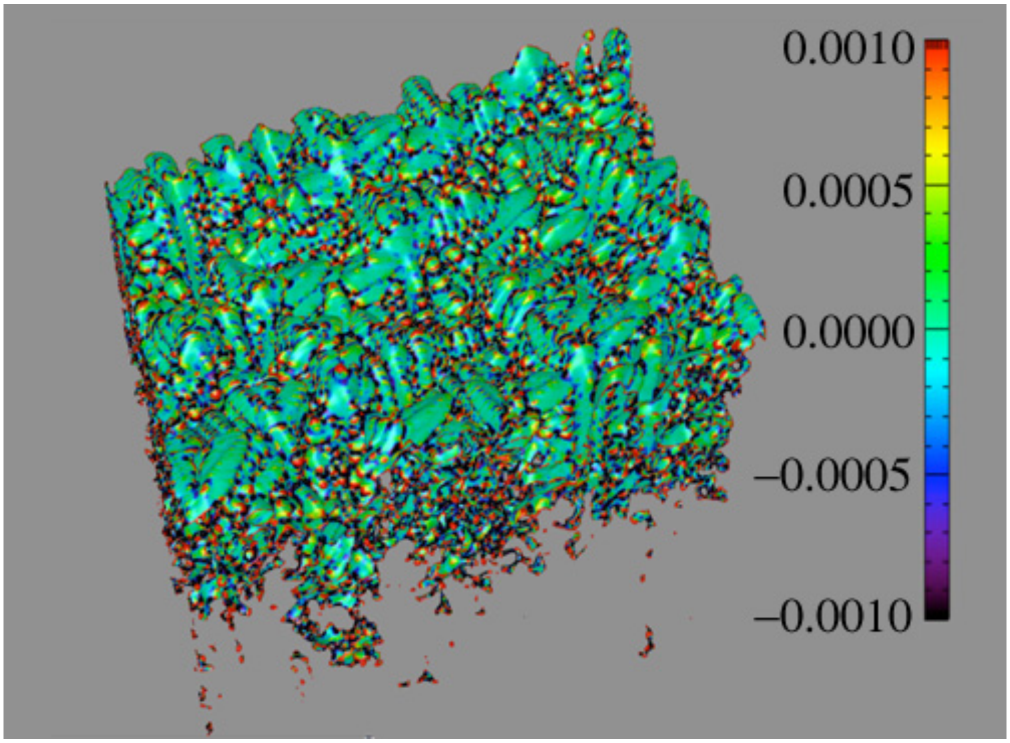

Figure 5.18 – Color-coded Guassian Curvature (H_G) Contour Plot in René N4 reconstruction

5.4 MESHED STRUCTURES

While the software packages selected for mesh generation have been presented in Chapter 4, details of the mesh results for René N4 will be presented here. The two mesh types generated are surface meshes and their resultant volume meshes. The element size and physical dimension of each simulated flow case in René N4 will be presented with representative, refined meshes shown for each class of simulated flow type.

5.4.1 Surface Meshes

The global meshed structure for the René N4 dataset is shown, Figure 5.18. The meshed domain is 2160 x 1619 x 1044 μm in dimension and is composed of a total of 290,286 elements. It should be mentioned that the mesh presented, Figure 5.18, provided only the preliminary basis from which additional meshes were generated. Each additional flow domain was obtained by selecting and isolating subsets of the structure shown, Figure 5.18. The aforementioned mesh refinements described in Chapter 4, Section 2.1 where then performed on each subset. For René N4, a total of 10 separate meshes were generated and refined with each mesh corresponding to a specific solid-liquid ratio. Six meshes, focusing specifically on modeling flow in the vertical direction were created with their flow inlet boundaries corresponding to a specific volume fraction. Four additional meshes with very thin cross-sections focusing entirely on horizontal flow were generated whose entire body corresponds to a given volume fraction. One vertical flow surface mesh (N4-Y2) and one cross-flow mesh (N4-X2) are shown as examples in Figure 5.19 and 5.20, respectively. A summary of the details related to each surface mesh case generated in the investigation of René N4 are presented below, Table 5.5

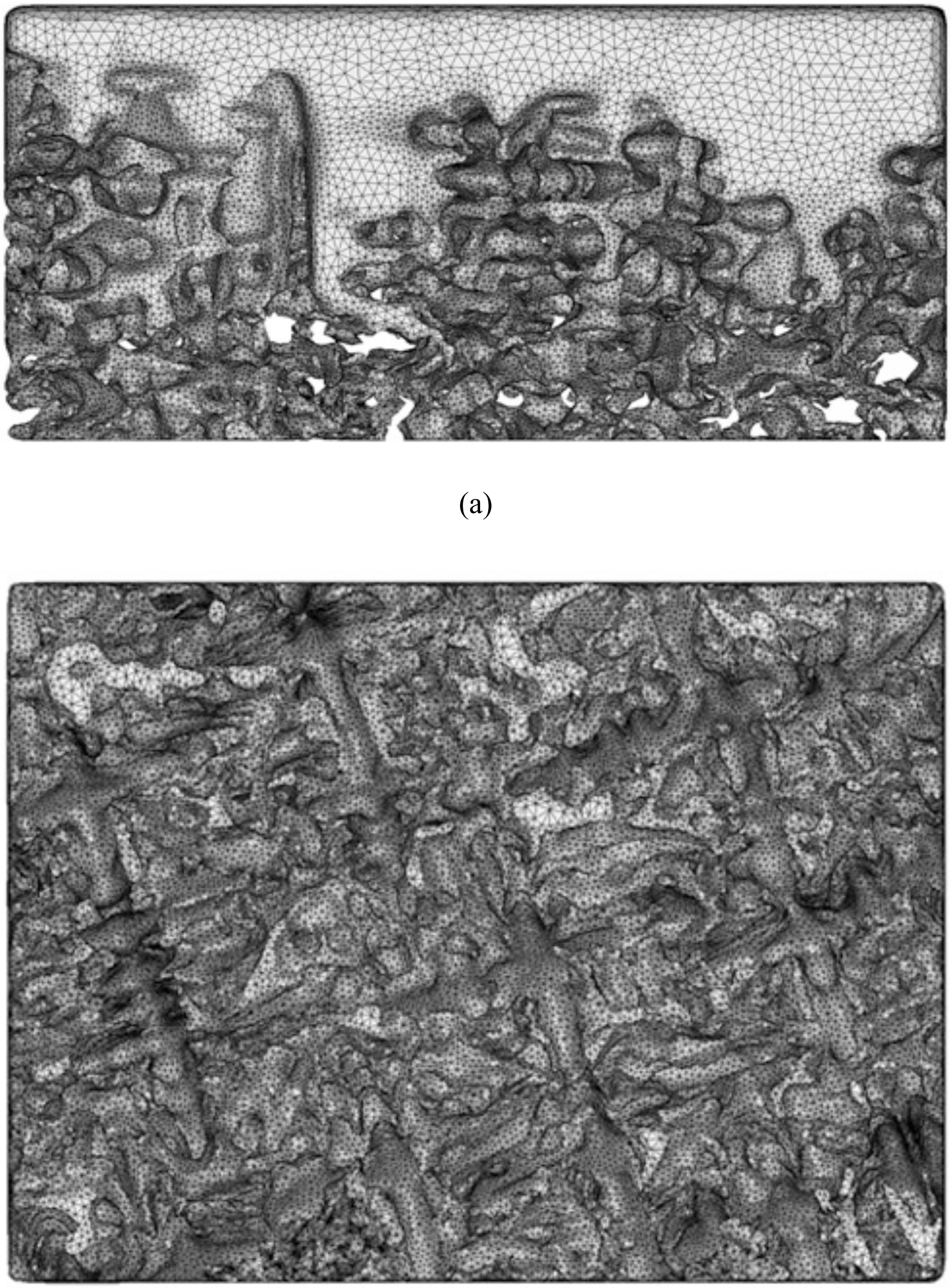

(a)

(b)

Figure 5.19 - Surface Mesh of Liquid Entrenched between and Surrounding René N4 Dendritic Network (a) View Normal to Primary Dendrite Growth (b) Upward View Along Primary Growth Direction

Table 5.5 - Summary of Surface Meshes Generated in MIMICS and Refined in 3Matic

	Case	Inlet Volume Fraction Liquid	Cell Volume (μm^3)	No. of Elements
Vertical Flow	N4-Y1	0.08	2180 × 1640 × 980	287780
	N4-Y2	0.10	2180 × 1650 × 840	279038
	N4-Y3	0.22	2180 × 1640 × 570	175734
	N4-Y4	0.32	2180 × 1650 × 480	171344
	N4-Y5	0.43	2180 × 1650 × 400	119340
	N4-Y6	0.60	2180 × 1650 × 350	111570
	Case	Volume Fraction Liquid	Cell Volume (μm^3)	No. of Elements
Cross Flow	N4-X1	0.42	2160 × 1620 × 20	46670
	N4-X2	0.56	2160 × 1620 × 20	61308
	N4-X3	0.73	2160 × 1620 × 20	42646
	N4-X4	0.89	2160 × 1620 × 20	32246

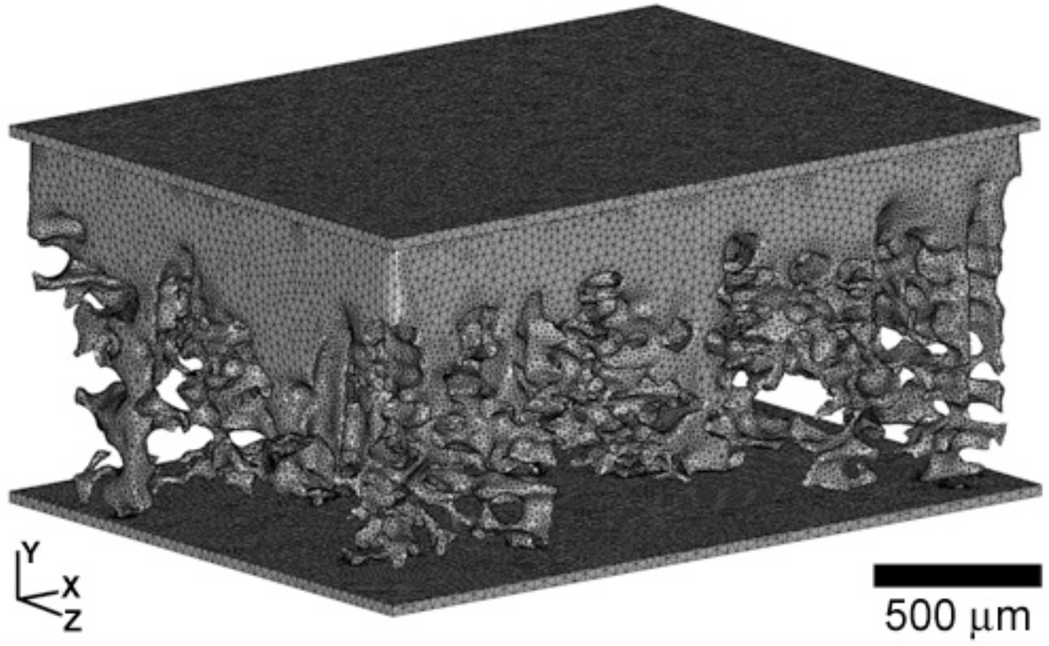

Figure 5.20 – Example of Vertical Flow Surface Mesh Refined in 3Matic from Liquid Within Rene N4 Mushy Zone

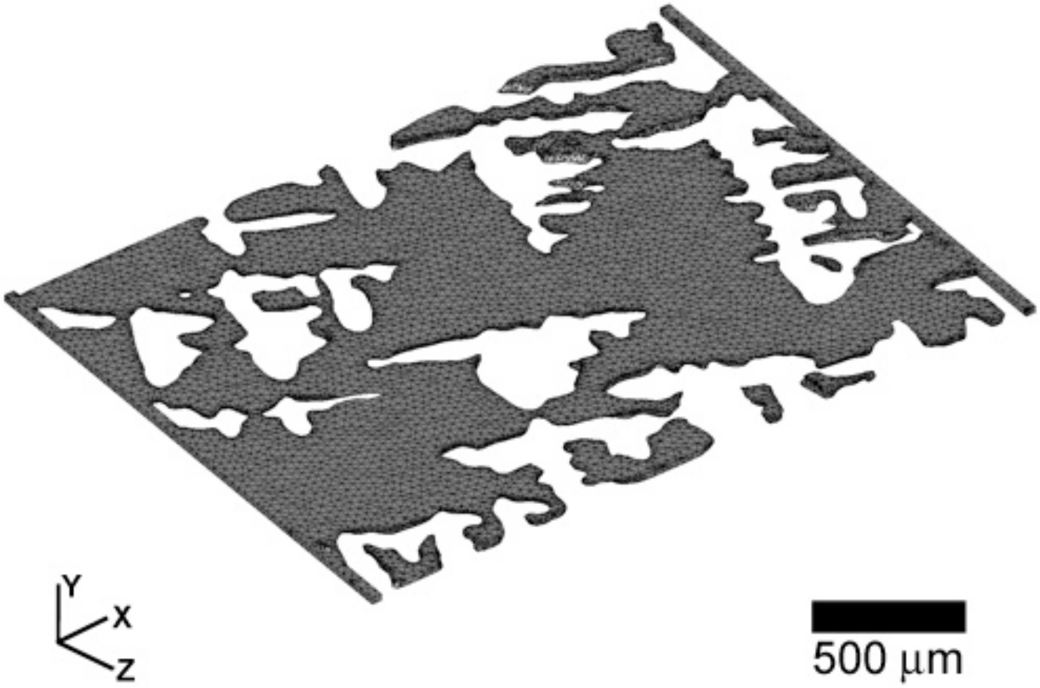

Figure 5.21 – Example of Cross Flow Mesh Refined in 3Matic from Liquid Within Rene N4 Mushy Zone

5.4.2 Volume Meshes

Volume meshes are composed of tetrahedral/hybrid elements based on the parent surface mesh used in its creation. Volume mesh element quantity generally scales by a factor of 3 to 7 for vertical flow cases and by a factor of 2 for all cross flow cases as compared to their predecessor surface meshes. Artificial plates at the inlet and outlet of each flow cell are apparent, Figures 5.21 through 5.23, and are added during the refinement of the surface mesh. These are included to facilitate the defining of uniform boundary conditions in the volume mesh flow simulation. All boundary conditions, properties and solver schemes are specified on the volume mesh elements in FLUENT following import into the CFD environment. Representative volume mesh examples for René N4 are shown, Figure 5.21 and 5.22, and correspond to those surface meshes displayed in Figures 5.19 and 5.20 and both correspond to cases Y2 and X2, respectively. Additionally, a summary of volume mesh cell details is summarized in Table 5.6.

Table 5.6 - Summary of Volume Meshes Generated in GAMBIT

	Case	Inlet Volume Fraction Liquid	Cell Volume (μm^3)	No. of Elements
Vertical Flow	N4-Y1	0.08	2180 × 1640 × 980	958650
	N4-Y2	0.10	2180 × 1650 × 840	1207040
	N4-Y3	0.22	2180 × 1640 × 570	783273
	N4-Y4	0.32	2180 × 1650 × 480	1020881
	N4-Y5	0.43	2180 × 1650 × 400	707400
	N4-Y6	0.60	2180 × 1650 × 350	828717
	Case	Volume Fraction Liquid	Cell Volume (μm^3)	No. of Elements
Cross Flow	N4-X1	0.42	2160 × 1620 × 20	88261
	N4-X2	0.56	2160 × 1620 × 20	120166
	N4-X3	0.73	2160 × 1620 × 20	79749
	N4-X4	0.89	2160 × 1620 × 20	54002

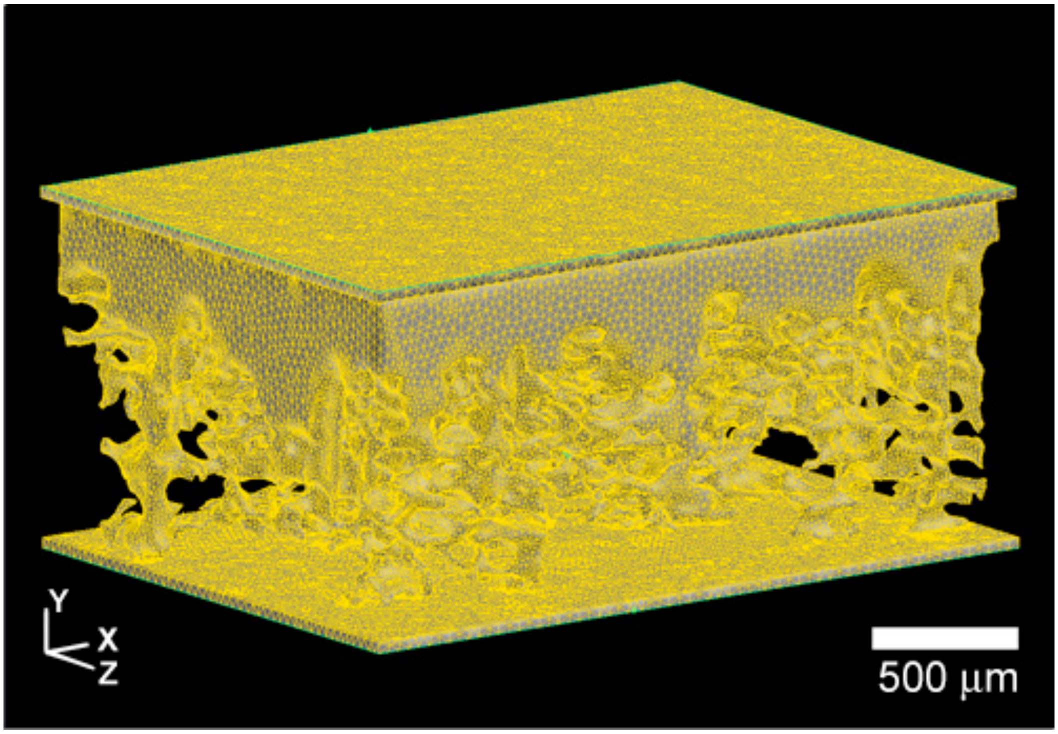

Figure 5.22 - Example of Vertical Flow Volume Mesh generated in GAMBIT

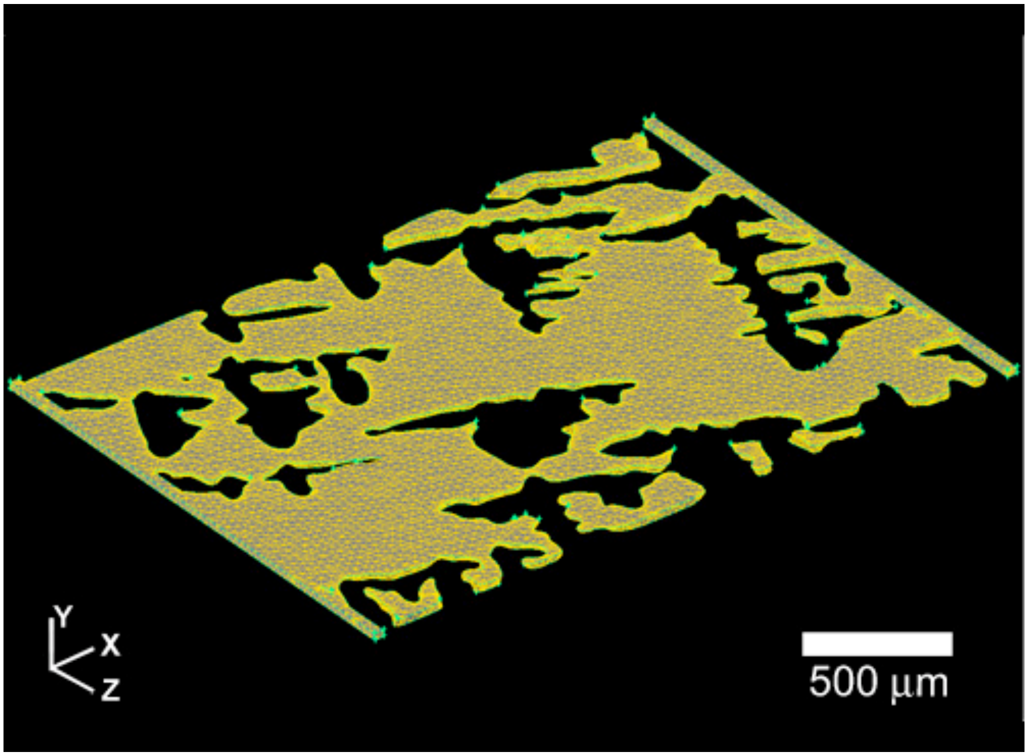

Figure 5.23 – Example of Cross Flow Volume Mesh Constructed in GAMBIT from Refined Surface mesh

5.5 QUANTIFICATION OF FLUID FLOW

Fluid flow during solidification is a widely recognized cause of irregular solute accumulation at certain areas within a casting, making full description of the mushy zone complicated. This phenomenon, though well documented [140], is difficult to model completely. Here, by capturing and reconstructing a dendritic network at the solid-liquid interface in a directionally solidified nickel-base superalloy, examination of fluid flow through these structures is possible. Flow is simulated in two major orthogonal directions; vertical and horizontal through the dendritic network. Here flow simulation results include: characteristic flow behavior, permeability, high velocity flow channels and flow tortuosity. Additionally, calculated permeability values will be compared with empirical models and values available in the literature.

5.5.1 Flow Behavior

From a qualitative standpoint, the flow behavior can be summarized in relation to the dendritic network. While a flow rate close to the minimum velocity is observed in most locations, increases in velocity occur in the regions of flow constriction. For vertical flow cases, Figure 5.24, these tend to occur at various locations throughout the mushy zone where the channel diameters are rapidly reduced and appear to correlate loosely with the secondary dendrite arm spacing. For the cases of cross-flow, Figure 5.25, these constrictions appear to coincide with the secondary dendrite arm tips where the flow path can becomes a very small fraction of the total flow area.

As mentioned previously, flow simulations were focused on the two primary orthogonal directions. Flow was studied in a total of 10 cells, with 6 vertical flow and 4 cross flow cases. A summary of the specific boundary conditions, resultant velocity ranges and pressure differences experienced across the cells is given in Table 5.7. The inlet velocities for each case are listed and were adjusted by scaling by the area fraction available in the vicinity of the inlet and optimizing from this value to arrive at a minimum velocity equal to 0.05 mm/s. This allowed for unrestricted and heavily restricted channels to experience flow fields with velocities comparable to the withdrawal velocity. This is documented by comparable velocity ranges across all vertical flow cases, (Y), and similarly among all cross-flow, (X) cells as listed in Table 5.7.

Table 5.7 - Summary of Flow Simulations by Case

	Case	Inlet Volume Fraction Liquid	Cell Volume (μm^3)	Inlet Velocity (mm/s)	$\text{Velocity}_{\text{min - max}}$ (mm/s)	Pressure Difference (Pa)
Vertical Flow	N4-Y1	0.08	2180 × 1635 × 980	0.006	0.0532 – 1.06	7.73
	N4-Y2	0.10	2180 × 1650 × 840	0.005	0.0527 – 1.05	5.40
	N4-Y3	0.22	2180 × 1640 × 570	0.0045	0.0537 – 1.07	5.15
	N4-Y4	0.32	2180 × 1650 × 480	0.004	0.0536 – 1.07	3.79
	N4-Y5	0.43	2180 × 1650 × 400	0.065	0.0538 – 1.08	5.45
	N4-Y6	0.60	2180 × 1650 × 350	0.11	0.0535 – 1.07	3.77
	Case	Volume Fraction Liquid	Cell Volume (μm^3)	Inlet Velocity (mm/s)	$\text{Velocity}_{\text{min - max}}$ (mm/s)	Pressure Difference (Pa)
Cross Flow	N4-X1	0.42	2160 × 1620 × 20	0.00195	0.00509 – 0.102	1.62
	N4-X2	0.56	2160 × 1620 × 20	0.0055	0.00520 – 0.104	0.633
	N4-X3	0.73	2160 × 1620 × 20	0.0078	0.00512 – 0.102	0.214
	N4-X4	0.89	2160 × 1620 × 20	0.0186	0.00502 – 0.100	0.079

Images of color-coded velocity vectors through the dendritic network are shown in Figure 5.24 and Figure 5.25 for cases Y2 and X2, respectively.

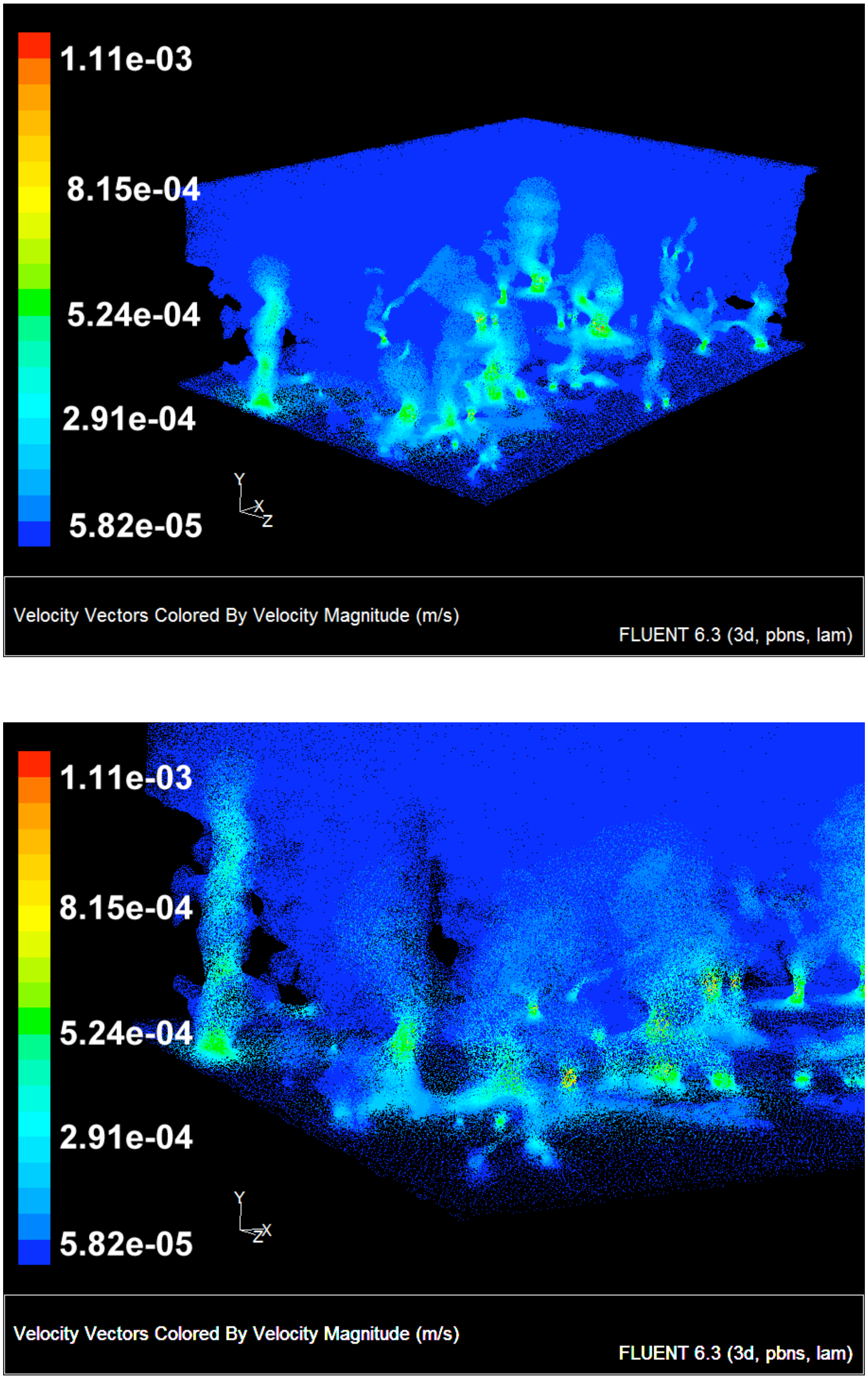

Figure 5.24 – Velocity Vectors Illustrating Flow Rate Increases in Constricted Channels for a Vertical Flow Case (a) Global View (b) Exploded View of Lower Left Quadrant

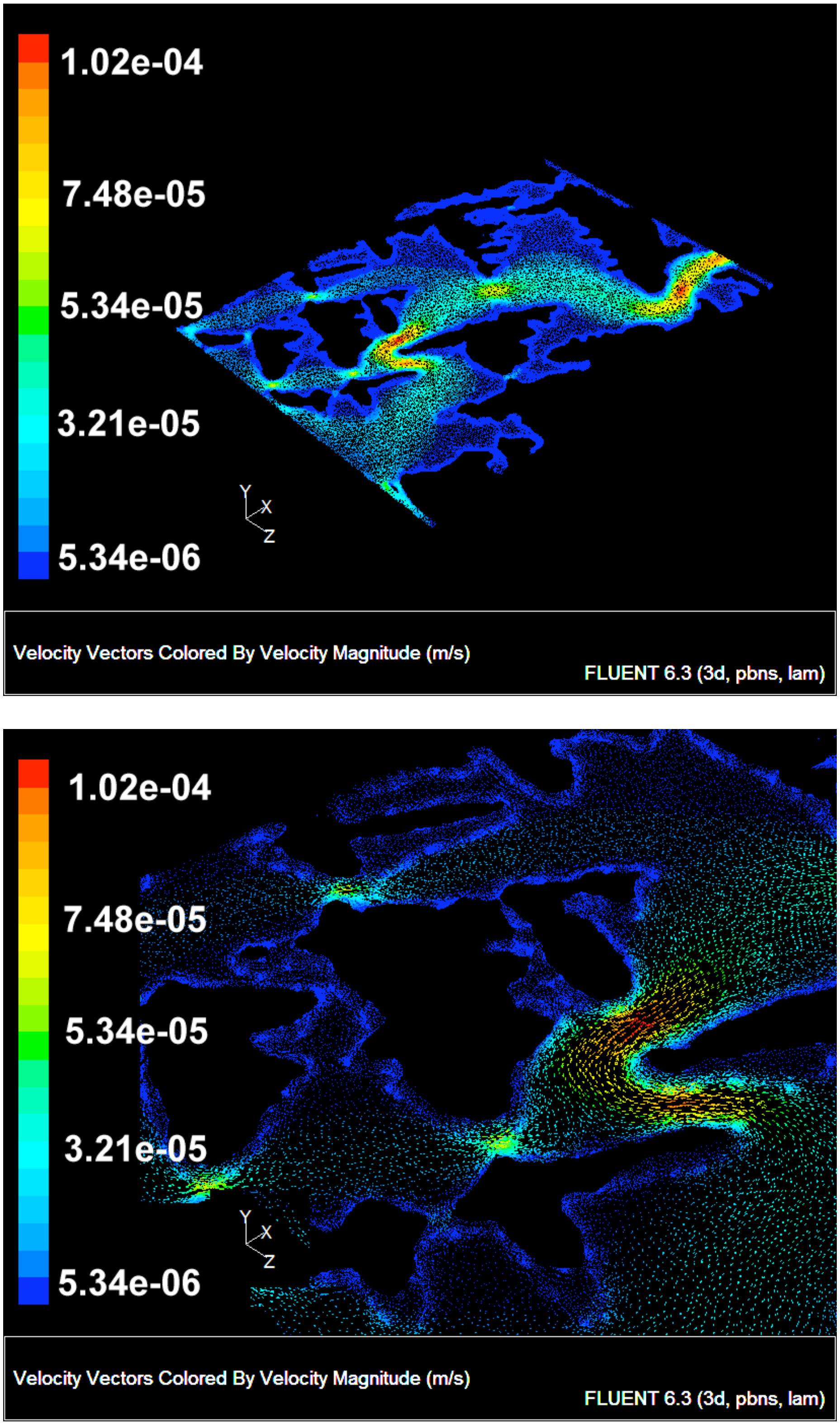

Figure 5.25 – Velocity Vectors Illustrating Flow Rate Increases in Constricted Channels for a Cross Flow Case (a) Global View (b) Exploded View of Center Field of View

5.5.2 Calculation of Permeability

As discussed in Chapter 4, by measuring the pressure gradient across a given flow direction in these simulations, Darcy's law, Eq. 4.2, as re-written in Eq. 5.1, can be utilized to calculate a global permeability for the simulation cell, where Q represents the volumetric flow rate; A, the inlet cross-sectional area; L, the length associated with the pressure drop ΔP; and μ, the fluid viscosity.

$$Q = KA\frac{\Delta P}{\mu L} \tag{5.1}$$

Since permeability is anisotropic, K_y for parallel flow and K_x for cross flow were independently calculated, and are listed as a function of volume fraction inlet for vertical flow cases and total volume fraction for cross flow cases as listed in Table 5.8 and shown graphically in Figure 5.29. The error bars indicate the total variation in volume fraction across the pressure drop used in the calculation of permeability for each case.

Table 5.8 - Calculated Permeabilities from Flow Simulations

	Case	Inlet Volume Fraction Liquid	Pressure Differential (Pa)	Length over Pressure Drop ($\times 10^{-4}$ m)	Volumetric Flow Rate ($\times 10^{-12}$ m^3/s)	Permeability ($\times 10^{-11}$ m^2)
Vertical Flow	N4-Y1	0.08	7.7	2.4	19	0.11
	N4-Y2	0.10	5.4	1.5	19	0.09
	N4-Y3	0.22	5.2	1.5	170	1.3
	N4-Y4	0.32	3.8	0.74	160	1.4
	N4-Y5	0.43	5.5	0.55	240	1.8
	N4-Y6	0.60	3.8	0.51	390	3.7
	Case	Volume Fraction Liquid	Pressure Differential (Pa)	Length over Pressure Drop ($\times 10^{-4}$m)	Volumetric Flow Rate ($\times 10^{-12}$ m^3/s)	Permeability ($\times 10^{-11}$ m^2)
Cross Flow	N4-X1	0.42	1.6	20	0.07	4.5
	N4-X2	0.56	0.63	20	0.18	21
	N4-X3	0.73	0.21	20	0.26	183
	N4-X4	0.89	0.079	20	0.59	659

5.5.3 Anisotropy of Permeability

Although there is little overlap in volume fractions for calculated K_y and K_x in this study, there is a discernable difference in the dependencies of K_y and K_x on volume fraction solid. To visualize the difference in slope between the two with the quantity $(1-f_s)^3$, dimensionless permeability (KS_{VS}^2) for K_y and K_x have been calculated by combining the simulation results with measured interfacial surface areas per unit volume solid (S_{VS}) in the three-dimensional dataset at the corresponding volume fractions. Vertical flow permeabilities, K_y, show a near 16% increase in dimensionless permeability (KS_{VS}^2) per unit increase in $(1-f_s)^3$ while cross flow simulations exhibit a much higher sensitivity to the fraction solid. These differences are likely to result from variation in flow path tortuosity. For this reason differences in flow pathlengths for vertical and horizontal flow cases have also been investigated.

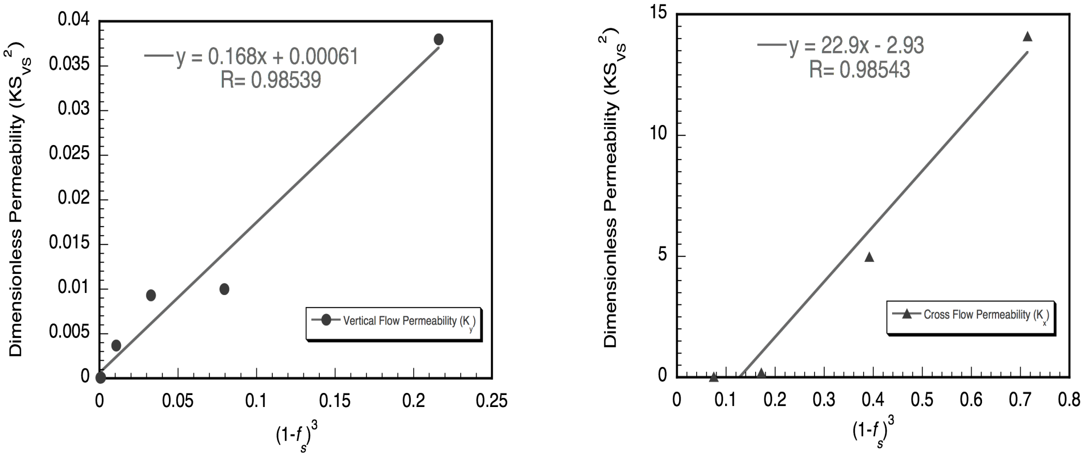

(a) (b)

Figure 5.26 - Current Study K_y and K_x detailing difference in volume fraction dependence

5.5.4 High Velocity Flow Channels

As discussed previously, convective flow can erode, fragment and transport portions of solidified material resulting in the formation of freckle chains containing high angle boundaries. While this process is driven by density gradients in the liquid, dendritic channels that permit markedly faster flow may locally increase the opportunity to fragment and transport solid material. Therefore, channels with continuous flow velocities on the order of ten times the withdrawal rate and higher were examined for physical location and relative spacing. By thresholding each simulation cell to identify regions with velocities no less than ten times the withdrawal rate and noting their occurrences throughout the vertical flow cells, a measure of the spacing of high velocity channels was obtained, Figure 5.26. The spacing of high velocity channels increases from roughly 400 – 700 μm near the inlets at f_L = 8, 10, 22, 32, 43 and 60%, to nearly 1900 μm after flow permeates through the dendritic network. The PDAS for the experimental material studied here was measured to be in the range of 450 – 600 μm, and is consistent with the thermal gradient-withdrawal rate expectation [141]. While the spacings of the flow cells at low liquid fractions is indicative of the PDAS, high velocity spacings expand to three to four times the PDAS after flow through the entire mushy zone. The larger spacing at higher locations within the mushy zone is a result of irregular flow through channels caused by dendrite morphology.

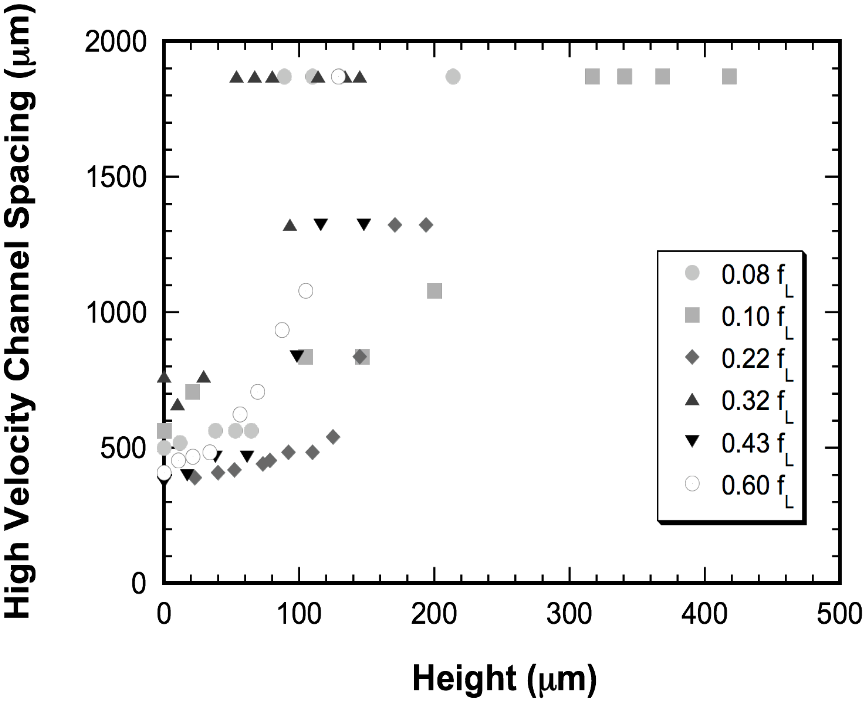

Figure 5.27 - High Velocity Spacings for Vertical Flow Cases plotted as Functions of Height

Additionally, these upward, high velocity flow paths through the dendritic array can be examined by tracing velocity profile peaks associated with them. In this way identification of high velocity channels and their relation to localized features of dendrite morphology is possible. Figures 5.27c – 5.27f illustrate velocity profiles for select paths taken from within the global flow domain of a vertical flow cell as shown in Figure 5.27a and depicted as functions of pathlength traveled. Representative flow paths corresponding to these profiles are highlighted in Figure 5.27b for reference. While not all interdendritic channels exhibit these long paths of higher velocity, those that do tend to exhibit velocity peaks on the order of 0.5 to 1 mm/s and high velocity flow regions develop and subside over very short length intervals. This indicates large velocity fluctuations can occur over relatively small paths of travel. The predominant flow direction in all vertical flow cells is upward. As such, increases in pathlength correspond to increased height and consequently, higher volume fraction liquid (f_L) levels in the meshed domain. Differences in location, profile and magnitude of peak velocities with respect to pathlength in Figures 5.27c – 5.29f, indicate an influence of dendrite morphology and not merely volume fraction solid. Local variations in dendrite arm spacing may impact these variations and give rise to rapid flow in localized regions. Within the reconstructed dataset, an average PDAS variability of ± 62 μm was determined by investigating subsets of the reconstruction. The spatial heterogeneity of high velocities and overall flow behavior suggest local dendrite morphology affects both flow speed and path.

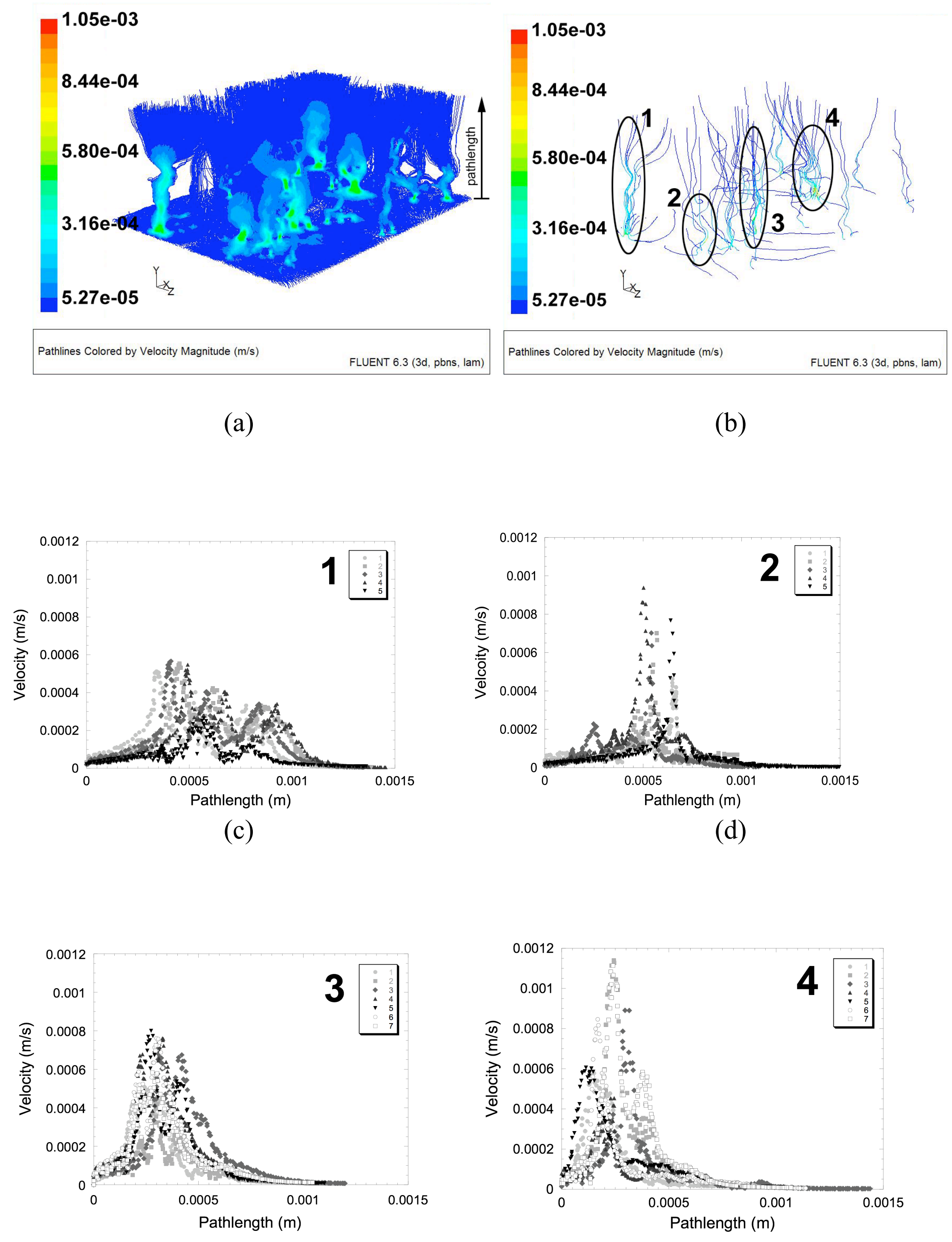

(a)

(b)

(c)

(d)

(e)

(f)

Figure 5.28 - Velocity Profiles for Selected Pathlines as a Function of Pathlength

5.5.5 Flow Path Ratios and Tortuosity

The lengths of paths traveled, Figure 5.28a and b, also provide an indication of the tortuosity associated with flow through each cell. We define tortuosity as the ratio between pathlengths of flow through the dendritic network and the length associated with the pressure drop used for permeability calculation. Average tortuosity (T_{avg}), as well as the local interfacial surface area per unit volume (S_V) for all cases are detailed, Table 5.9. Additionally, T_{avg} is performed over paths distributed uniformly over each inlet surface.

Table 5.9 - Flow Path Ratios, ISA per unit volume & Permeability by Case

	Case	Inlet Volume Fraction Liquid	T_{avg} {± Var.}	Local S_v ($\times 10^4$ m^{-1})	Permeability ($\times 10^{-11}$ m^2)
Vertical Flow	N4-Y1	0.08	2.29 ± .83	218	0.11
	N4-Y2	0.10	2.56 ± 1.4	225	0.09
	N4-Y3	0.22	1.61 ± .33	128	1.3
	N4-Y4	0.32	1.57 ± .63	86.1	1.4
	N4-Y5	0.43	1.67 ± .63	42.8	1.8
	N4-Y6	0.60	1.51 ± .32	24.6	3.7
	Case	Volume Fraction Liquid	T_{avg} {± Var.}	Local S_v ($\times 10^4$ m^{-1})	Permeability ($\times 10^{-11}$ m^2)
Cross Flow	N4-X1	0.42	1.26 ± .22	8.75	4.5
	N4-X2	0.56	1.39 ± .01	8.51	21
	N4-X3	0.73	1.21 ± .04	1.06	183
	N4-X4	0.89	1.13 ± .003	3.50	659

In cross flow cases, T_{avg} are only somewhat greater than 1. However, for vertical flow cases, average tortuosity ranges from 1.5 to 2.6. Increased tortuosity in flow would be expected with increased ISA and result in a decrease in permeability [142]. Figure 5.29a and b show the dependence of tortuosity and permeability on S_V with error bars in Figure 5.29a illustrating the variance in T_{avg}. For permeability, vertical and cross flow scale inversely with S_V by power law with an exponent ranging from 1.5 to 1.7, Fig. 5.29b. The accuracy of the curve fit is stronger for vertical flow as indicated by the R values. The low R value associated with the cross flow cases are likely due to the few data points available. While T_{avg} is only mildly affected by S_V across a large range of volume fraction for cross flow, average tortuosity in vertical flow is more strongly affected by S_V. Apparently, cross flow is largely impacted by the presence of primary arms while vertical flow is more strongly influenced by the arrangement of the secondary arms. This is understandable as primary arms are oriented parallel to vertical flow and do not hinder flow as much as secondary arms which are oriented perpendicular given the vertical flow direction. Alternatively, primary arms influence cross flow more as these are the primary microstructural feature impeding lateral flow across the dendritic network.

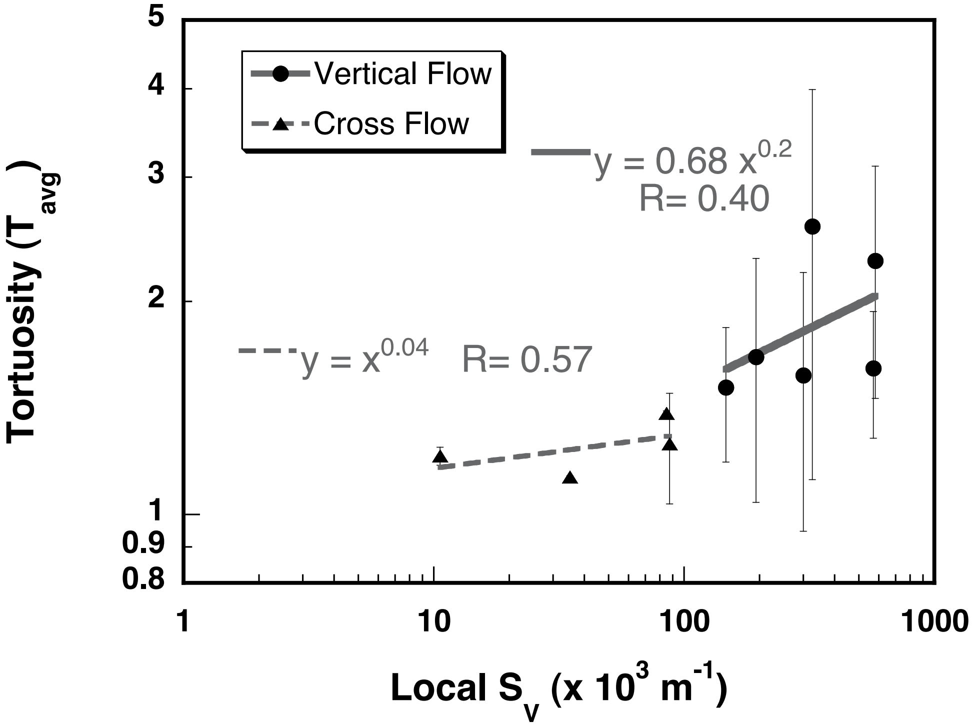

(a)

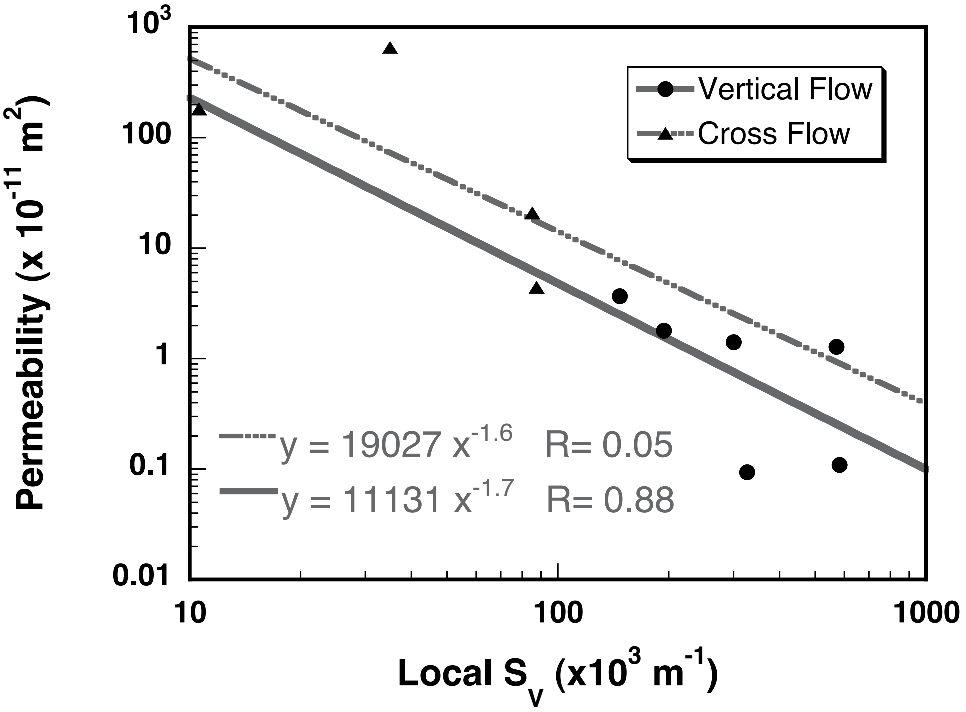

(b)

Figure 5.29 - (a) Tortuosity & (b) Permeability as Functions of Measured ISA per Unit Volume (S_V)

5.5.6 Comparisons with Kozeny Relations

Comparison of the results of this study to common empirical relations for permeability can give insight to the structural origins of changes in permeability. Figure 5.30 compares the calculated permeabilities with both the Kozeny-Carmen approximation (Eq. 2.8) [81, 83] and the Heinrich-Poirier modified Blake-Kozeny relationships for flow parallel (Eq. 2.12) and normal to (Eq. 2.13) the primary dendritic growth direction [78, 82]. Current study error bars indicate the total variation in fraction solid over the pressure gradient used in the determination of local permeability for each simulation case. K_y error bars are one-sided as the critical and maximum solid fraction in vertical flow is the solid fraction located at the inlet.

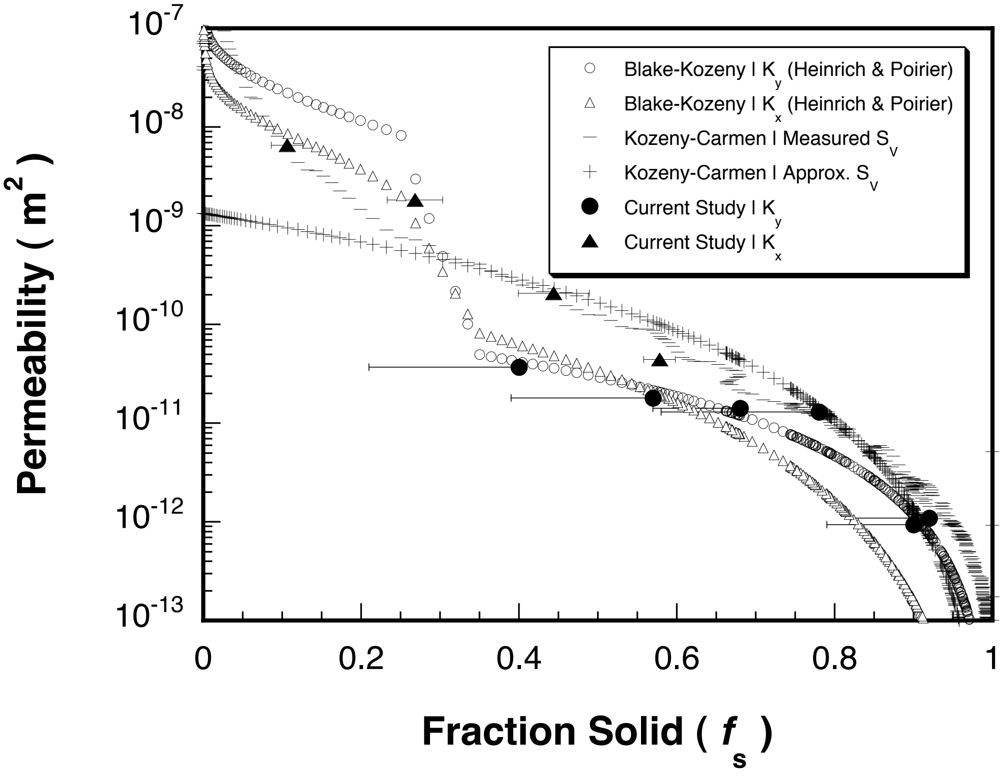

Figure 5.30 - Calculated Permeabilities Plotted as a Function of Volume Fraction Solid with modified Blake-Kozeny and Kozeny-Carmen Relations

Vertical flow permeabilities (K_y) coincide well with the predictions of the Heinrich-Poirier modified Blake-Kozeny description over all simulations. Conversely, cross flow permeabilities (K_x) are higher by a factor of 3 to 5 in the range $0.4 < f_s < 0.6$ with better agreement in the low fraction solid regime $f_s < 0.35$. With regard to the Kozeny-Carmen approximation, permeabilities in this study are in good agreement with K_y at high fraction solid, $f_s > 0.7$. For $f_s < 0.6$, when S_V is measured as opposed to approximated by the inverse of the secondary dendrite arm spacing as previously suggested [143], the Kozeny-Carmen approximation, Eq. 2, predicts K_x reasonably well. Interestingly, the maximum divergence between measured and approximated Kozeny-Carmen predictions arise at $f_s < 0.3$, which occurs near the dendrite tips where the ISA decays rapidly. It is worth noting that while the Kozeny-Carmen relation is not formulated to describe anisotropic flow, it is very effective at capturing the influence of interfacial surface area on permeability, provided ISA can be well quantified.

For volume fractions in the range $0.4 < f_L < 0.6$, the current study shows a greater resistance to vertical flow as compared to cross flow. This trend is not consistent with earlier Blake-Kozeny models (Eqs. 2.9, 2.10 and 2.11), as higher K_y across all volume fractions are predicted. However, Heinrich and Poirier's Blake-Kozeny formulation (Eqs. 2.12 and 2.13), does predict higher cross flow permeabilities within the range $0.3 < f_s < 0.55$. The simulations of the current study confirm this assertion, albeit with greater separation of K_y and K_x magnitudes.

This permeability calculation is useful for three reasons; First, this provides direct calculation of permeability from experimental structures as opposed to many previous methods that have relied on periphery measures of liquid or the accumulation of some medium after passing through a coarsening dendritic structure [70, 76, 77, 80]. Secondly, this demonstrates an approach for the extension of permeability studies to coarser, more irregularly spaced columnar structures more representative of industrial casting situations in terms of not only composition but also scale. Thirdly, these calculations approach the lower limits of volume fraction solid in permeability measurements previously attempted while providing reasonable convergence with values presented by other researchers as will be shown in Figures 7.1 and 7.2.

CHAPTER 6

NI-AL-W TERNARY RESULTS

6.1 ACQUISITION OF THREE-DIMENSIONAL DATASET

Serial-sectioning experiments for data collection of the Ni-Al-W ternary alloy were performed over the course of ten days. The experimental procedure as outlined in Chapter 3, Section 3.1 was employed and material removal rates was assessed following the methods described in Chapter 5, Section 5.1 in reference to the René N4 alloy. Recession rate as a function of slice quantity, Figure 6.1, illustrate a sectioning rate of 3.25μm/slice through a total thickness of just over 1.5 mm. At maximum, 85 sections in a given day were obtained and at minimum, 23 sections were generated in a single day.

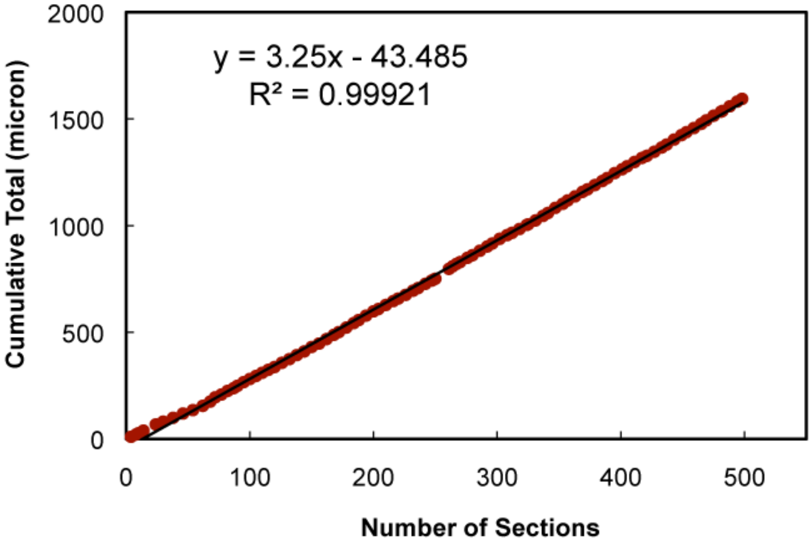

Figure 6.1 - Recession rate of RoboMet.3D serial sectioning of Ni-Al-W ternary alloy

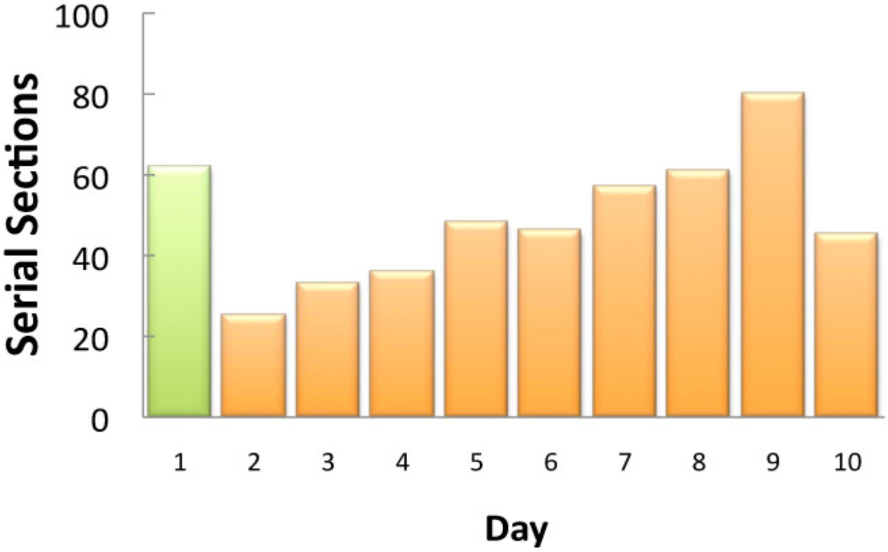

Figure 6.2 - Serial Sections Obtained per day in Ni-Al-W sectioning

6.2 RECONSTRUCTED VOLUMES

6.2.1 Memory Requirements

In serial-sectioning, cross-sectional dimension and subsequent removal rate varied from previous experimental samples of René N4. As such, the parameters of serial sectioning were adjusted to optimize time, resources and material. Primary changes of note to the serial-sectioning protocol previously described, Chapter 5, were the use of 3μm lapping film and slightly larger montage arrangements to offset the increase in cross-sectional area. Table 6.1 illustrates the tradeoffs in memory allocation and montage requirements for associated imaging configurations for the selected sample of Ni-Al-W material. Each data slice is composed of a 3 x 2 montage image taken under the 5X_1.0X configuration in which the secondary value, "_1.0X", corresponds to an exchangeable secondary internal magnification lens. 5X_1.0X corresponds to 5X magnification. Micrographs taken yield an in-plane resolution of 1.04 μm/pixel with each slice ranging from approximately 5-7 MB in digital memory. This reconstruction contains just under 500 slices for a total of 3GB of raw data. A representative cross-sectional area and apparent dendritic structures from a single serial-section are illustrated in Figure 6.3. A slight in-plane deviation in angle with the primary growth direction was present. As such, secondary arms extending from the same primary trunk are shown as disconnected solid in a given sectioning plane and successively converge into or diverge from a single body. When secondary arms are seen as one body, the sectioning plane samples the primary dendritic core from where the secondary arms have emerged. A schematic diagram illustrating this progression is depicted in Figure 6.4.

Table 6.1 - Imaging Configurations with RoboMET.3D for Ni-Al-W Sectioning

Magnification	Montage Images Required	Resolution (µm/pixel)	Approximate Memory Allocation (MB)
5X_1.0X	6	1.04	6
5X_1.6X	10	0.67	12
10X_1.0X	18	0.52	21
10X_1.6X	30	0.34	36*
20X_1.0X	50	0.26	60*
20X_1.6X	70	0.17	85*
50X_1.0X	290	0.10	356*
50X_1.6X	670	0.07	825*

** estimates based on lower magnification to memory ratios*

Figure 6.3 - Single Section Image of Ni-Al-W from Serial-Sectioning Dataset

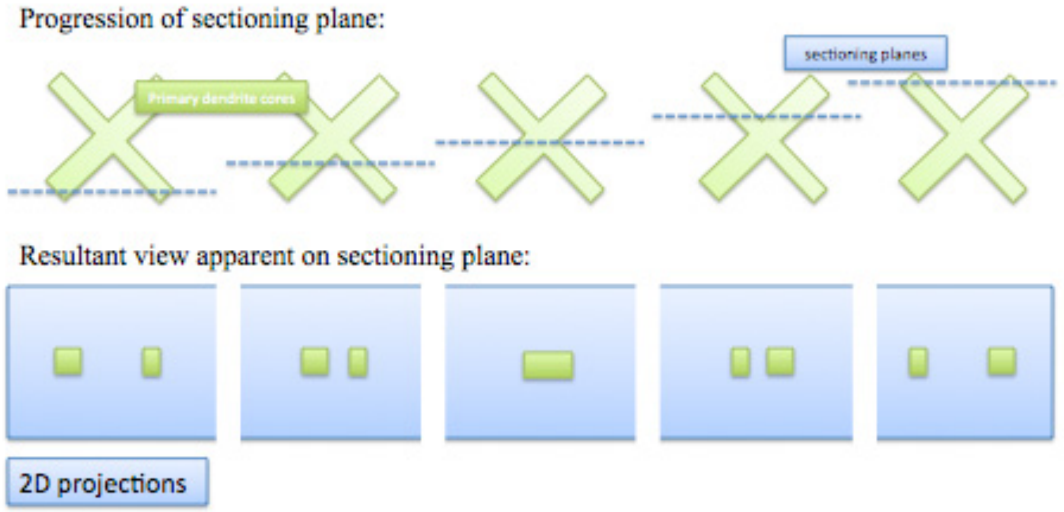

Figure 6.4 - Schematic showing progression in 2-D sectioning view for successive sectioning plane

6.2.2 Volume Visualized

The reconstructed solid for the Ni-Al-W system is given in Figure 6.5. The dimensions of the reconstruction are 2570 x 5000 x 1600 μm. Initial inspection of the volume shows a strong tendency toward elongated channels in the primary solidification direction. Additionally, it is apparent the orientation of the dendritic growth is slightly inclined to the sectioning direction. However, visual inspection of the reconstruction normal to the solidification direction, Figure 6.6, reveals the four-fold symmetry of the dendritic network. From this vantage point it is apparent that a slightly finer distribution of dendrites are contained within the ternary cross-section compared to the reconstructed René N4 dataset shown in Chapter 5, Section 2.2.

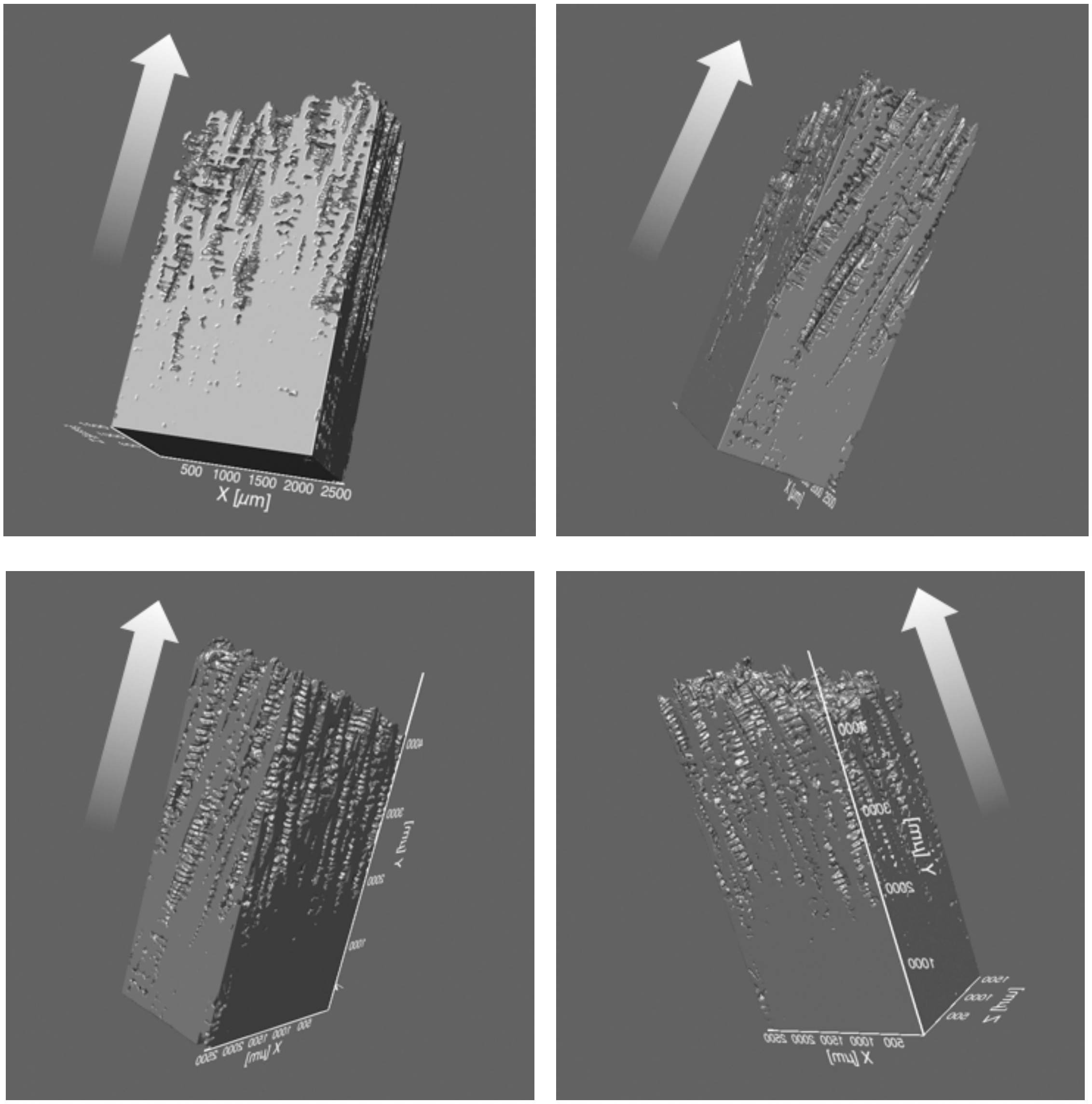

Figure 6.5 - Reconstruction from Various Angles rotated about a central vertical axis. Arrow mark the primary solidification direction.

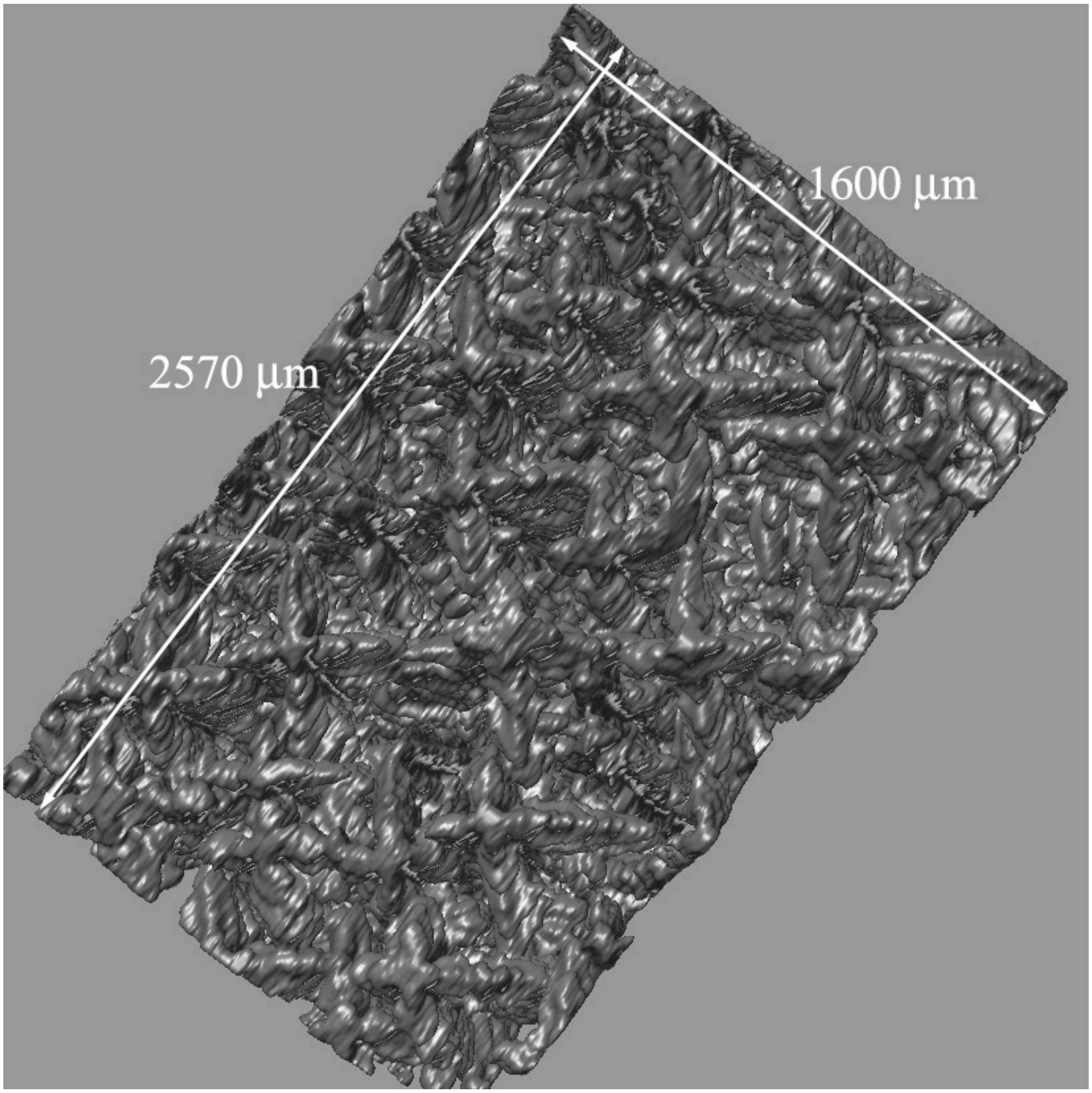

Figure 6.6 – Ni-Al-W Reconstruction viewed normal to the solidification direction

6.3 CHARACTERIZATION OF DENDRITIC STRUCTURES

6.3.1 Dendrite Arm Spacing

Primary and secondary dendrite arms spacing (PDAS and SDAS) in the model ternary were measured in accordance with the characterization methods described in Sections 2.1.3, 3.4.1 and further detailed in 5.3.1. While thermocouples were not utilized in this series of casting experiments associated with the Ni-Al-W material system due to peculiarities associated with intentional decanting, prior experimental work under Bridgman conditions at similar withdrawal rates [47, 116] demonstrated thermal gradients of 23°C/mm, 37°C/mm, and 42°C/mm for cross-sections of 51mm, 38mm and 10mm respectively. Extrapolation of these rates suggest thermal gradients for the full diameter of the casting equivalent to ~16°C/mm. However, given the irregular orientation of the casting geometry Figure 3.3, the resultant cross-section in withdrawal varied with greatest departures occurring at the beginning and end of withdrawal. The ensuing dendrite arm spacing observed and the information yielded by prior thermal gradient experiments [17, 47] suggest this variation in cross-section produced an effective cross-section on the order of one-half the full diameter of the casting at the point of decanting. The solidification front velocity, (V) is equal to the withdrawal rate and was held constant at 3.3 mm/min. With a cross-section of 39mm, a thermal gradient of 40°C/cm would be expected. Under these conditions, Equations 2.2 and 2.3 yield $G^{-1/2} * V^{-1/4} = 0.18\ m^{1/4} sec^{1/4o} C^{-1/2}$ and $(G * V)^{-1/3} = 1.7\ oC^{-1/3} sec^{1/3}$, respectively. As shown in Figures 6.7 and 6.8, these values suggest PDAS in the range of 350 – 500 μm and SDAS in the range of 55 – 75 μm.

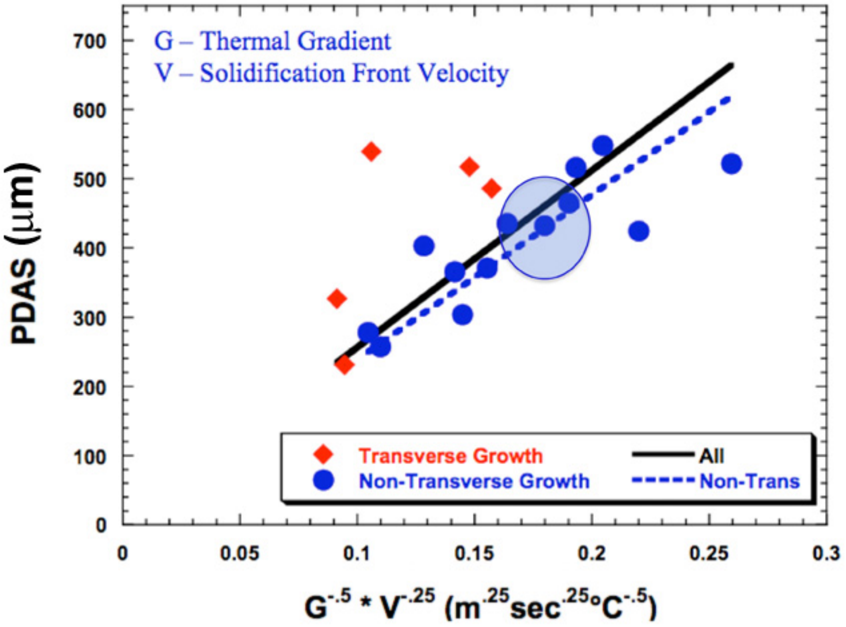

Figure 6.7 - PDAS expectation range based upon the product of the thermal gradient and solidification front velocity ($G^{-.5} \times V^{-.25}$)

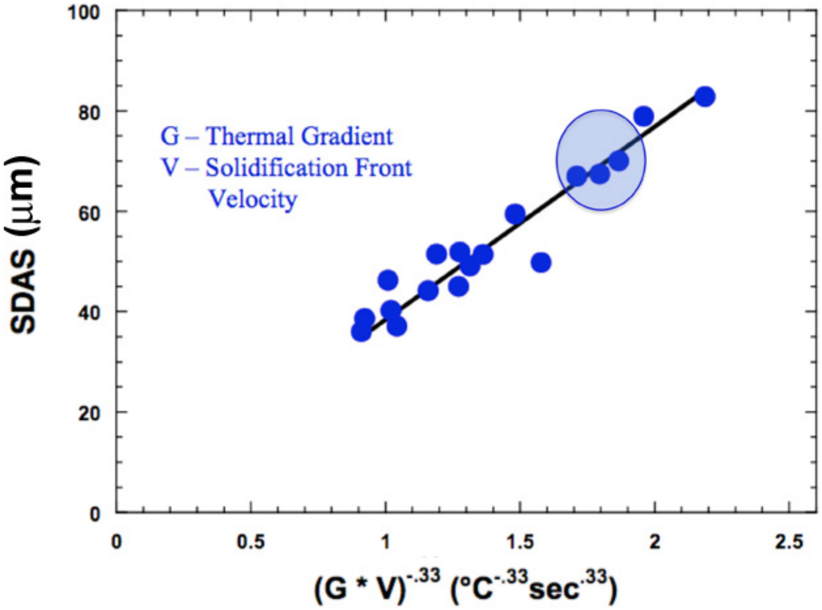

Figure 6.8 - SDAS expectation ranged based upon the product of the thermal gradient (G) and solidification front velocity $(G*V)^{-.33}$

Traditional two-dimensional metallography on over 35 independent micrographs in determination of average PDAS and over 25 independent micrographs in determination of SDAS were performed. These examinations were performed on material extracted from the fully solidified portions of the casting below the decanted solid-liquid interface. Findings are summarized in Table 6.2 with Figures 6.9a and 6.9b illustrating typical micrographs from which PDAS and SDAS were calculated using Equations 3.1 and 3.2.

Table 6.2 - Summary of Two-Dimensional Dendrite Arm Spacing Measurements for Ni-Al-W

	Measures	Total Cores Counted	Secondary Arms Sampled	Average	Standard Deviation
PDAS	32	923	--	410	23
SDAS	27	--	409	80	8.5

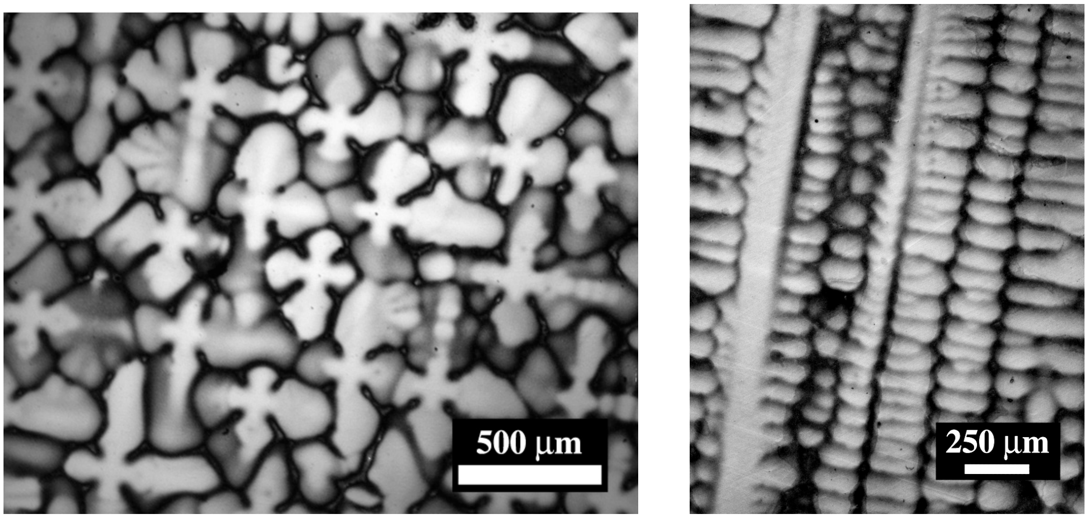

(a) (b)

Figure 6.9 – Representative Micrographs for Dendrite Arm Spacing (a) normal to the primary growth direction, (b) transverse to the primary growth direction through a primary core

Utilizing the reconstructed volume as a array of dendrites in which spacing can be measured in a manner similar to two-dimensional approaches, investigation of planar sections have allowed PDAS and SDAS measures to be taken in the reconstructed volume as well. As discussed previously with the René N4 dataset, due to the size of the reconstruction, fewer independent planes and a smaller global cross-section are generally available. However, Table 6.4 summarizes the characterization results while Figures 6.10a and 6.10b exhibit typical sections used to obtain the PDAS and SDAS directly from the reconstruction.

Table 6.3 - Summary of Dendrite Arms Spacing Measurements obtained from 3-D Reconstructed dataset

	Measures	Total Cores Counted	Secondary Arms Sampled	Average	Standard Deviation
PDAS	12	663	--	360	8.2
SDAS	21	--	120	87	10.8

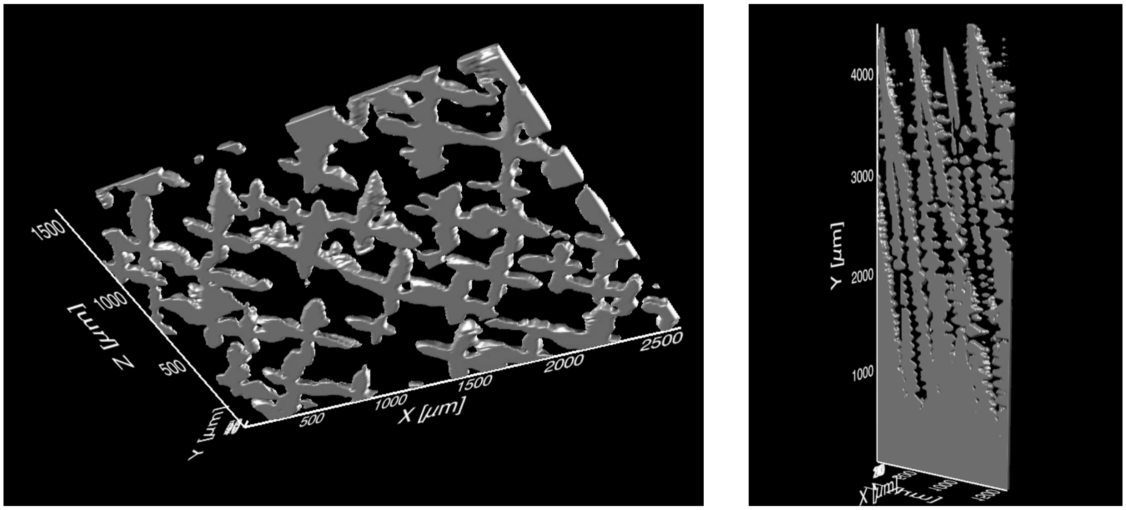

(a) (b)

Figure 6.10 - Representative Micrographs for Dendrite Arm Spacing Approximation in the 3D Reconstruction (a) normal to the primary growth direction, (b) transverse to the primary growth direction

All 2D and 3D measures for the Ni-Al-W system are compared in Figure 6.11 where the independent axis corresponds to individual measures obtained from either micrograph in the fully solidified region or a given plane in the reconstruction. Data points are color-coded as “2D Measure” or “3D Approximation” to signify the measurement approach. The average measures of PDAS and SDAS between the 3D reconstruction and the 2D dataset yield reasonable agreement. With respect to PDAS, the average measure from the

3D volume is lower by approximately 12% as compared to the average value obtained with traditional metallographic techniques. For SDAS, measures from within the 3D volume exhibit slightly higher consistency across all measures as shown in the associated standard deviation for PDAS, Table 6.3, as compared to that obtained with 2D measures, Table 6.2. Variations in this regard are likely results of arm spacing variability and experimental scatter, which is probable when sampling the entire cross-section of the casting. In the reconstruction, limitation of this variability is observed as sampling occurs over equivalent cross-sections at varying heights.

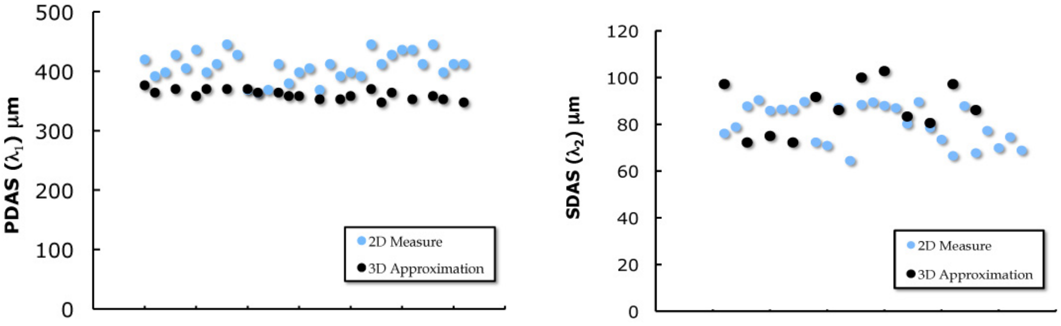

Figure 6.11 - Comparison of DAS Measurements from Micrographs and Reconstructed Domain

6.3.2 Volume Fraction

The variation in solid-liquid ratios were measured throughout successive planes according to Equation 3.3 and depicted as a function of height in the reconstruction, Figure 6.12. Volume fraction variation with height exhibits a moderate decrease in fraction solid (f_s) for heights ranging from 1 to 4 mm with a rate of -0.02% f_s /µm and a rather substantial decrease in f_s over the remaining 1mm of the reconstruction with a rate of -0.07% f_s /µm. The larger decrease in f_s corresponds to the decrease in solid material near the dendrite tips. By considering the measured volume fraction across the solidus and liquidus temperatures of the alloy (1433 °C and 1456 °C, respectively, as determined by differential thermal analysis, DTA), a thermal gradient based on the solid-liquid profile can be extracted as well. Due to the two distinct variations in f_s decrease, two curves are fit over the domains of consistent rate with resultant slopes corresponding to change in temperature derived from the secondary y-axis, Figure 6.12. These profiles suggest thermal gradients approximately 40^{o}C/cm and 170^{o}C/cm. The latter value appears rather unlikely due to the large cross-sectional geometry of the casting. It is more probable the high temperature gradient profile is an artifact of decanting. The precipitous drop in volume fraction occurs at heights corresponding to volume fraction values $\leq 0.4f_L$ in which flow becomes rather difficult posing significant challenge to achieving clear decanting. As previously mentioned, experiments by A. Elliott determined thermal gradient to cross-section ratios in Bridgman and Liquid Metal Cooling (LMC) mode for plate geometries. Based on Elliott's thermal gradient calculations for experiments in Bridgman mode [17, 47], the microstructures and solid-liquid profile over the critical temperature range are consistent. Furthermore, given the temperature interval of 23^{o}C existing between observed liquidus (1456^{o}C) and solidus (1433^{o}C) temperatures of this alloy, it would be expected for a thermal gradient of 40^{o}C/cm to produce a total mushy zone approximately 5750 μm in height. The reconstruction measures 5000 μm in height. As has been demonstrated, a ~40^{o}C/cm thermal gradient is consistent with the 2D and 3D measured PDAS and SDAS averages.

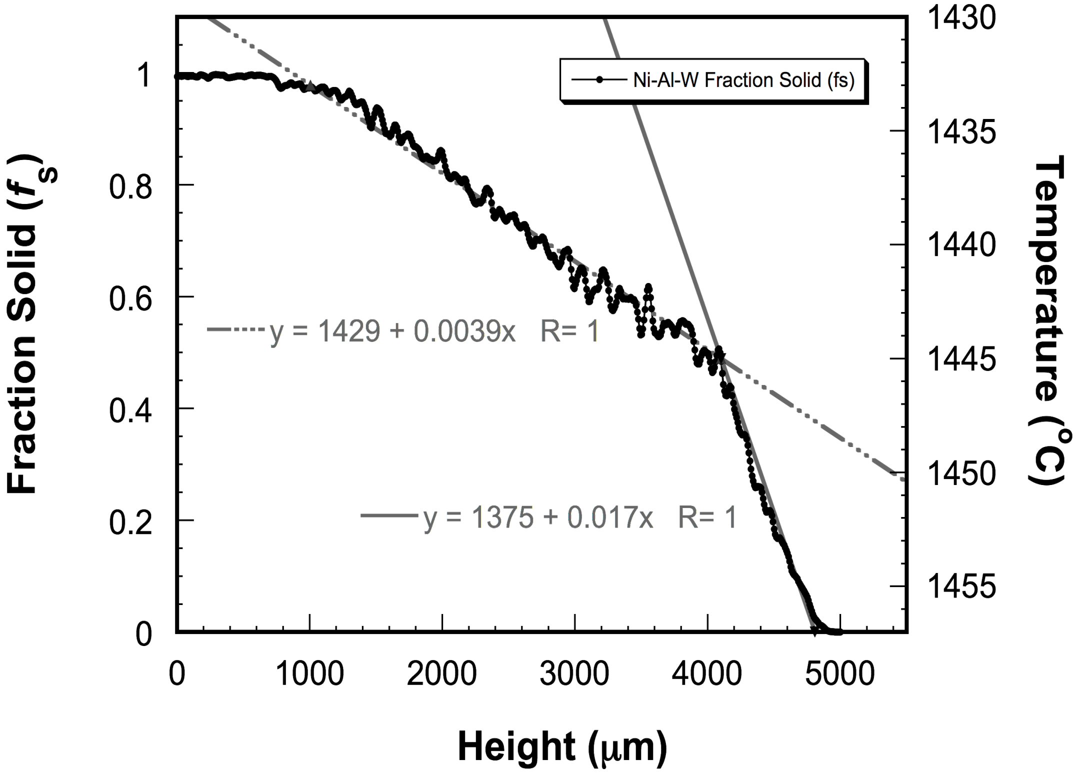

Figure 6.12 - Ni-Al-W Volume Fraction Solid as a function of height in the reconstructed volume with $T_{liquidus}$ and $T_{solidus}$ plotted on secondary vertical axis for thermal gradient determination

6.3.2 Void Interconnectivity

In order to understand the degree of percolation possible through the network of dendrites present, the connectivity of all interdendritic voids was assessed. In order to accomplish this, all individual non-solid regions contained within the Ni-Al-W reconstruction, Figure 6.13, were measured and categorized according to their voxel quantity.

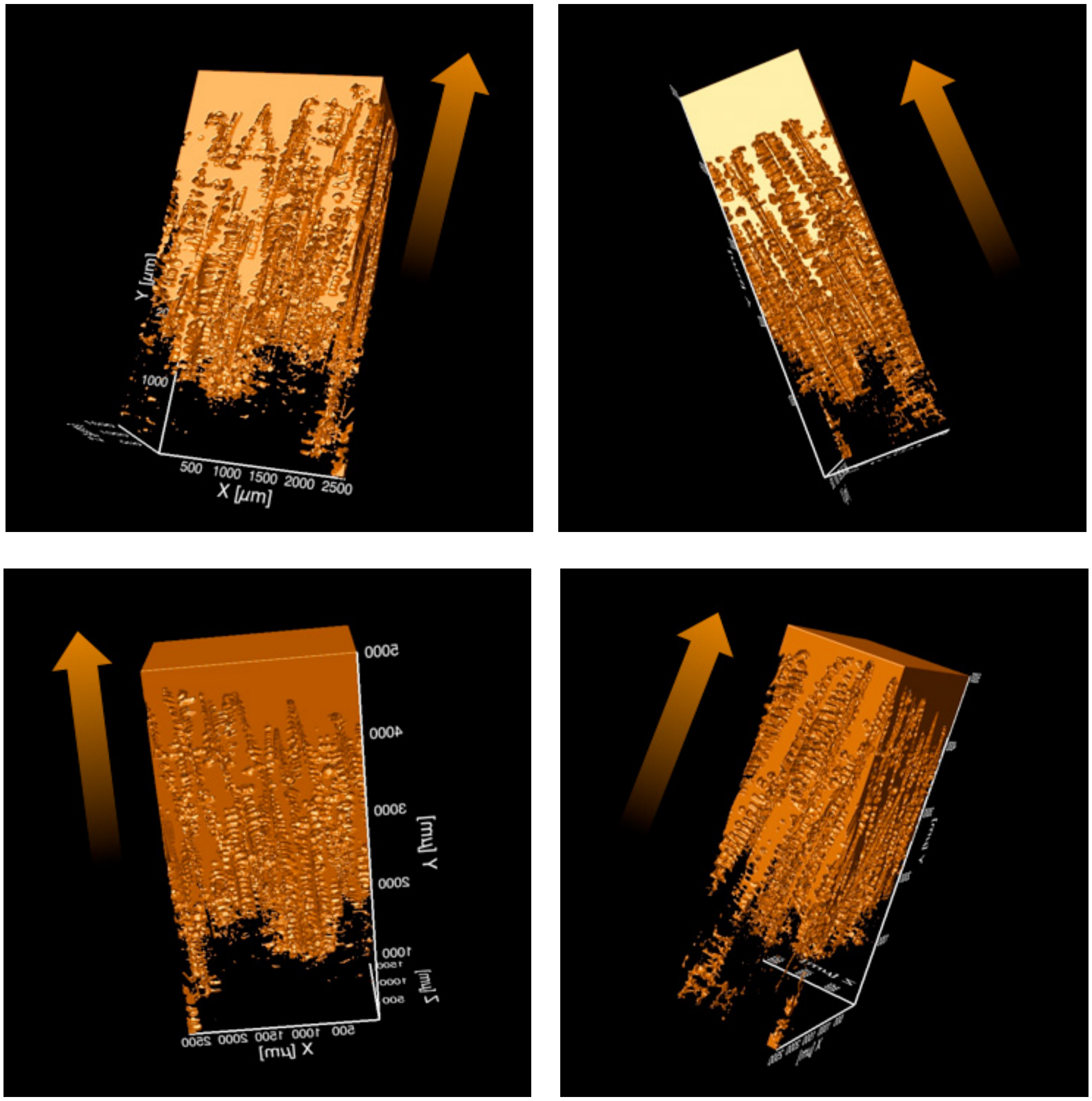

Figure 6.13 - Reconstruction of all non-solid material in Ni-Al-W reconstruction. Arrows indicate primary solidification direction

A total of over 1300 individual non-solid entities were identified and the volumes of each were measured by summing the quantity of voxels composing each body. Table 6.4 summarizes the number of bodies in a given voxel regime and couples each with the corresponding physical size of each threshold as well as the cumulative contribution of each regime to the overall voids present in the dendritic network. In the case of the ternary, high connectivity exists as illustrated by the presence of a singular volume composing over 99% of the total void or non-solid fraction. Substantially higher quantities of smaller volume voids exist but are, in the nearest case, two orders of magnitude smaller in size than the largest body, Figure 6.14. Additionally, the lowest three volume regimes, Table 6.4, correspond to isolated locations within primarily solid material. Interestingly, the total contribution of these regimes to the overall void fraction is 0.23% and is within the range of porosity reported in typical single crystal nickel-base alloys [137-139].

Table 6.4 - Size Distribution of Independent Bodies Related to Interdendritc Voids in Ni-Al-W casting

Volume Threshold (μm^3)	Voxel Threshold	No. of Independent Bodies	Cumulative Volume	Percentage Void Fraction	Contribution to Total Non-Solid Regions
2 250 000 000	10 000 000	1	6409618830	99.26%	99.26%
225 000 000	1 000 000	0	--	--	99.26%
22 500 000	100 000	0	--	--	99.26%
2 250 000	10 000	4	18569480	0.29%	99.55%
225 000	1 000	23	14074748	0.22%	99.77%
22 500	100	182	10122201	0.15%	99.92%
2 250	10	581	4401368	0.07%	99.99%
225	1	597	513613	0.01%	100.0%

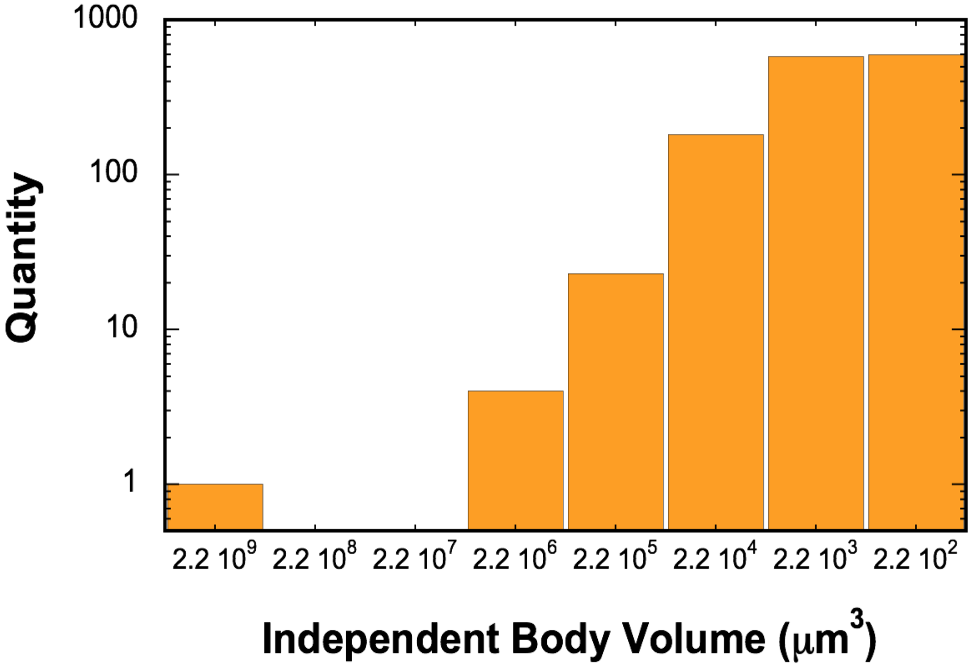

Figure 6.14 - Non-Solid Independent Body Volumes Ordered by Magnitude

6.3.2 Interfacial Surface Area

Interfacial surface area (ISA) was investigated throughout the reconstructed dataset. All elements of the domain corresponding to contours of solid-liquid interface were categorized by position and correlated to height in intervals equivalent to the vertical resolution in the reconstruction (8.32 μm/pixel). This approach allowed for direct correlation with previously measured volume fraction in the reconstructed domain. To allow for comparison across varying domain sizes, ISA is normalized by the associated unit volume, allowing for calculation of the surface area to volume ratio (S_V). In Figure 6.15, S_V and volume fraction solid are plotted over the height of the reconstruction illustrating their associated variation. Minor ripples in f_S and S_V correspond to local variations induced by secondary dendrite arms. This fraction solid profile shown here varies slightly with respect to the René N4 solid fraction profile shown in Chapter 5. The mushy zone height is taller and a more linear decrease in solid fraction is observed from 1 to 0.4 f_S. These variations are likely indicative of a more effective decanting as total mushy zone height more closely approaches the length expectation for an undisturbed solid-liquid transition in this alloy system. Interestingly, the sharp decline in fraction solid from 0.4 to 0 f_S may suggest even largely successful decanting may experience markedly higher evacuation rates of liquid at high liquid fraction levels. This may be the underlying cause in the shortening of the solid-liquid transition. Despite variation in the solid profile, S_V reaches a maximum value at 0.6 f_S and decreases rapidly over the upper 1000 μm of the height commensurate with the decrease in volume fraction solid. Figure 6.16 illustrates the direct variation in ISA with fraction solid. The variation is best described by a third order polynomial with a maximum between 0.5 – 0.6 f_S.

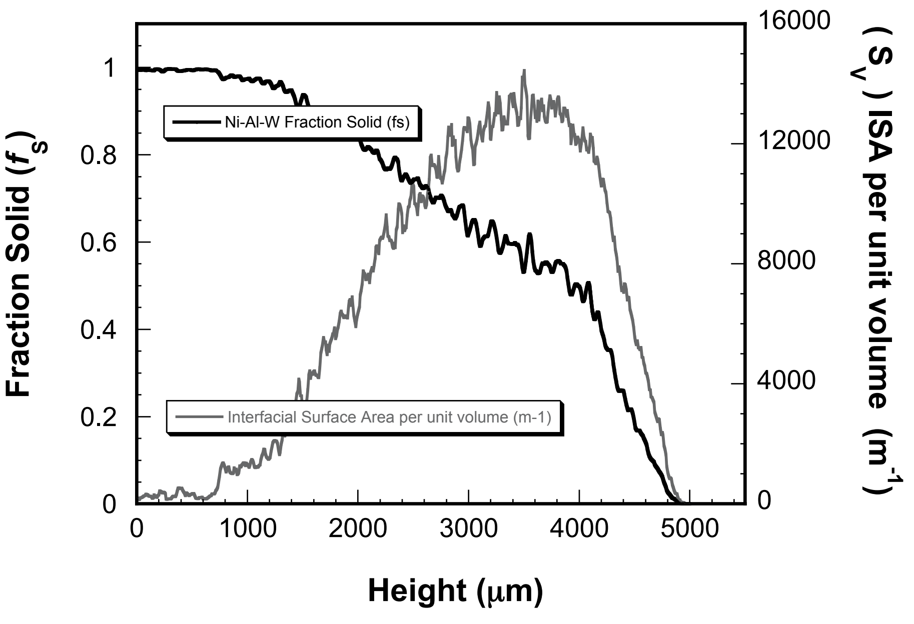

Figure 6.15 - Measured S_V plotted with Volume Fraction Solid as Functions of Height

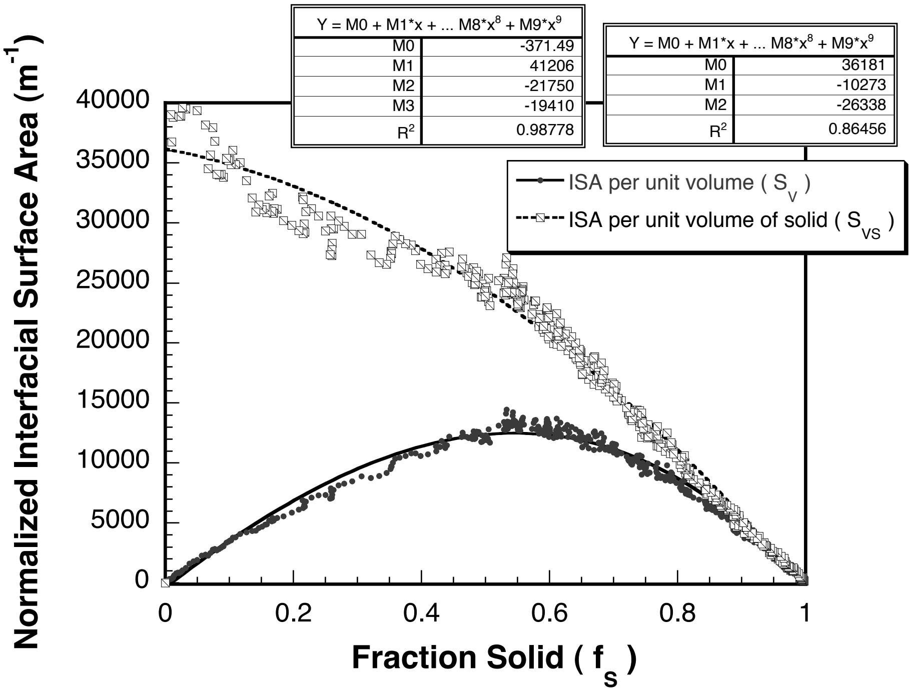

Figure 6.16 - Measured Interfacial Surface Area per unit Volume (S_V) and Interfacial Surface Area per unit Volume Solid (S_{VS}) for Ni-Al-W Reconstruction

6.3.2 Curvature

The interfacial shape distribution (ISD) plot for the reconstructed Ni-Al-W dataset is shown in Figure 6.17. The ISD indicates the most frequent, principle curvature pairings correspond to thin, deep-saddle contours (quadrant 2, Figure 3.6), while the greatest distribution of curvatures exist on and around the $\kappa_2 = 0$ axis. The concentration of curvature pairs found along the $\kappa_2 = 0$ axis corresponds to cylindrical liquid domains while the high concentration in quadrant 2 correspond to dendritic solid with crescent-like profiles amidst interdendritic liquid. Visualization of the color-coded Mean (H_M) and Gaussian (H_G) curvature contours are shown on the reconstructed microstructure in Figures 6.18 and 6.19. Figure 6.18 illustrates maximum and minimum mean curvatures existing at very minimal breadths at primary and secondary dendrite tips and between neighboring secondary arms, respectively. Figure 6.19 indicates maximum Gaussian curvatures occurring at the tips of primary and secondary dendrite arms with a greater degree of connectivity between fields of maximal curvature. Minimum Gaussian values exhibit comparatively much larger and continuous equivalent curvatures fields which are located along the length of primary dendrite cores between the principal growth directions of secondary arms. These locations support the ISD observance of a wide distribution of curvatures with, and near to, liquid cylinder-like domains and indicate the presence of rather continuous vertical flow paths through the Ni-Al-W reconstruction.

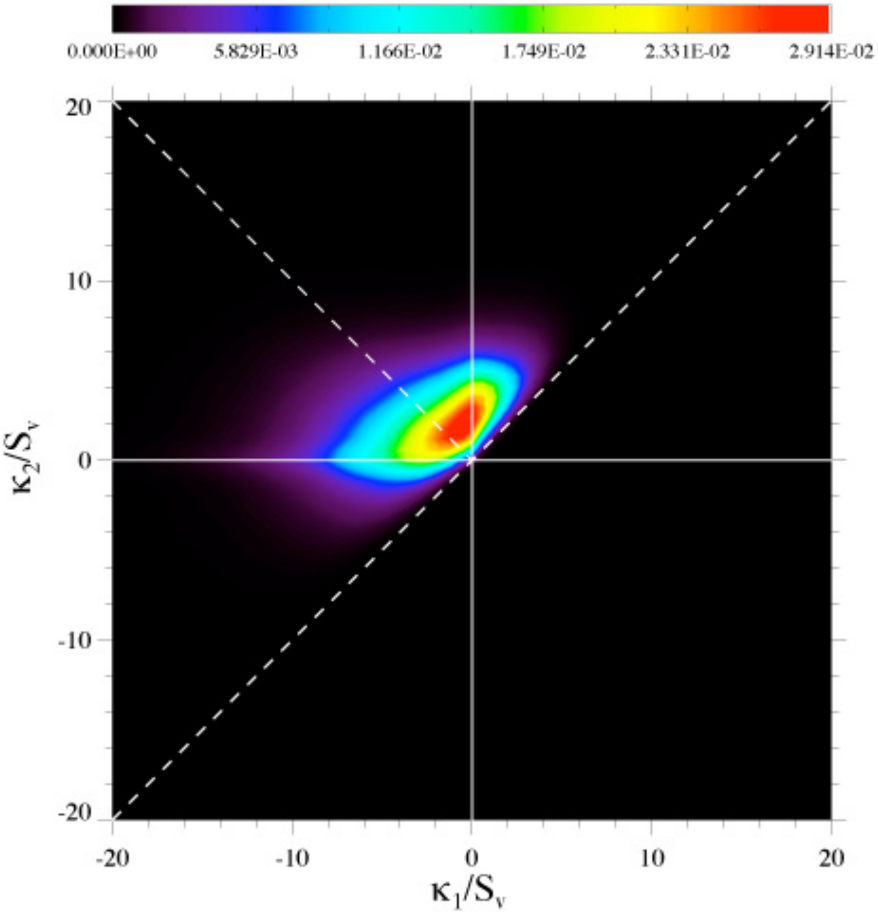

Figure 6.17 - Interfacial Shape Distribution Plot for Ni-Al-W dataset: $\kappa_{1,2}$ are normalized by S_V to allow for direct comparison of curvatures throughout the entire domain

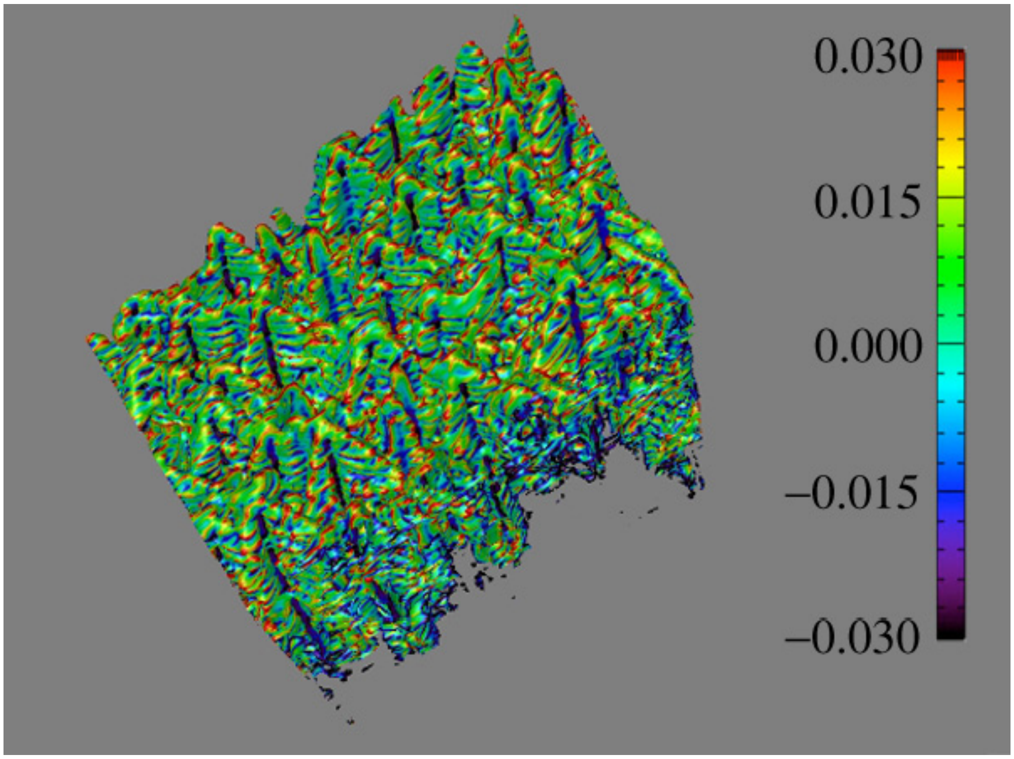

Figure 6.18 - Color-Contour Depiction of Mean Curvature (H_M) on Ni-Al-W Reconstructed Microstructure

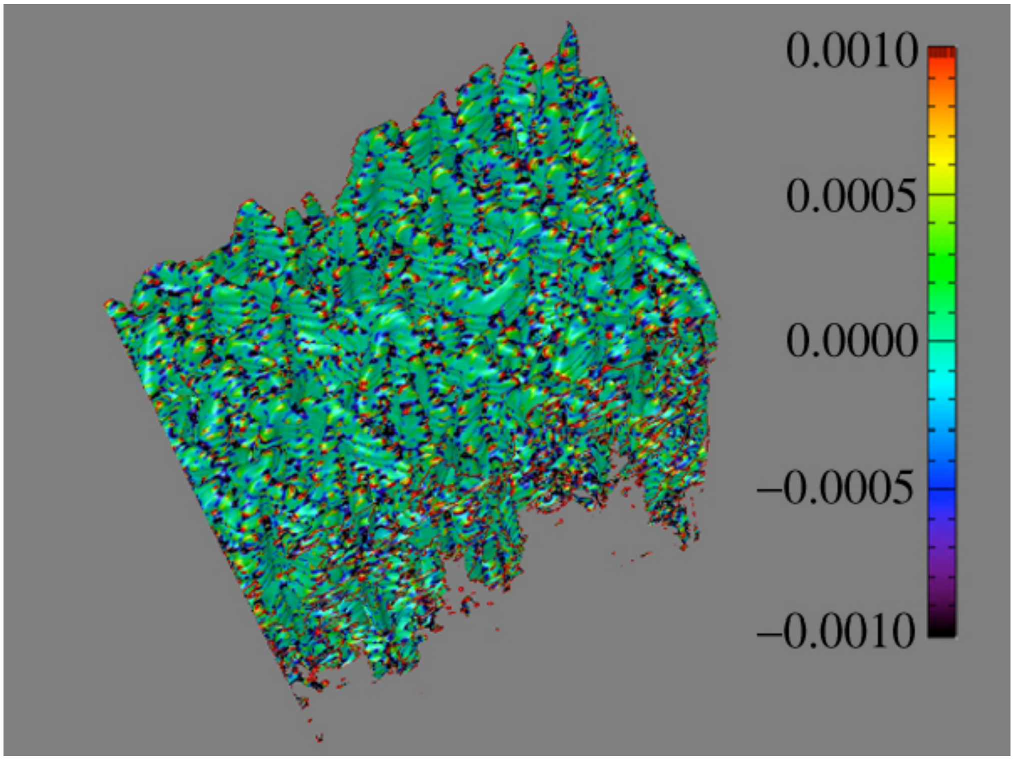

Figure 6.19 – Color-Contour Depiction of Gaussian Curvature (H_G) on Ni-Al-W Reconstructed Microstructure

6.4 MESHED STRUCTURES

As noted in Chapter 4, simulation protocols adopted in this investigation require the creation and refinement of both surface and volume meshes from the reconstructed dataset. Herein, the element count, cell volume size and representative meshes for both vertical and cross flow domains will be presented and discussed.

6.3.1 Surface Meshes

The reconstructed domains of solid and liquid in the decanted mushy zone of the Ni-Al-W system have been shown in Figures 6.5 and 6.13 respectively. From this domain one global surface mesh was generated measuring 2570 × 1600 × 4500, Figures 6.20a and 6.20b. All subsequent flow domains for both vertical and cross flow simulations were obtained through isolation and refinement of select portions of this structure. It should be mentioned, thorough and methodical refinement in accordance with the procedures detailed in Chapter 4, Section 2.1, were required on all identified flow domains to produce operational simulation cells.

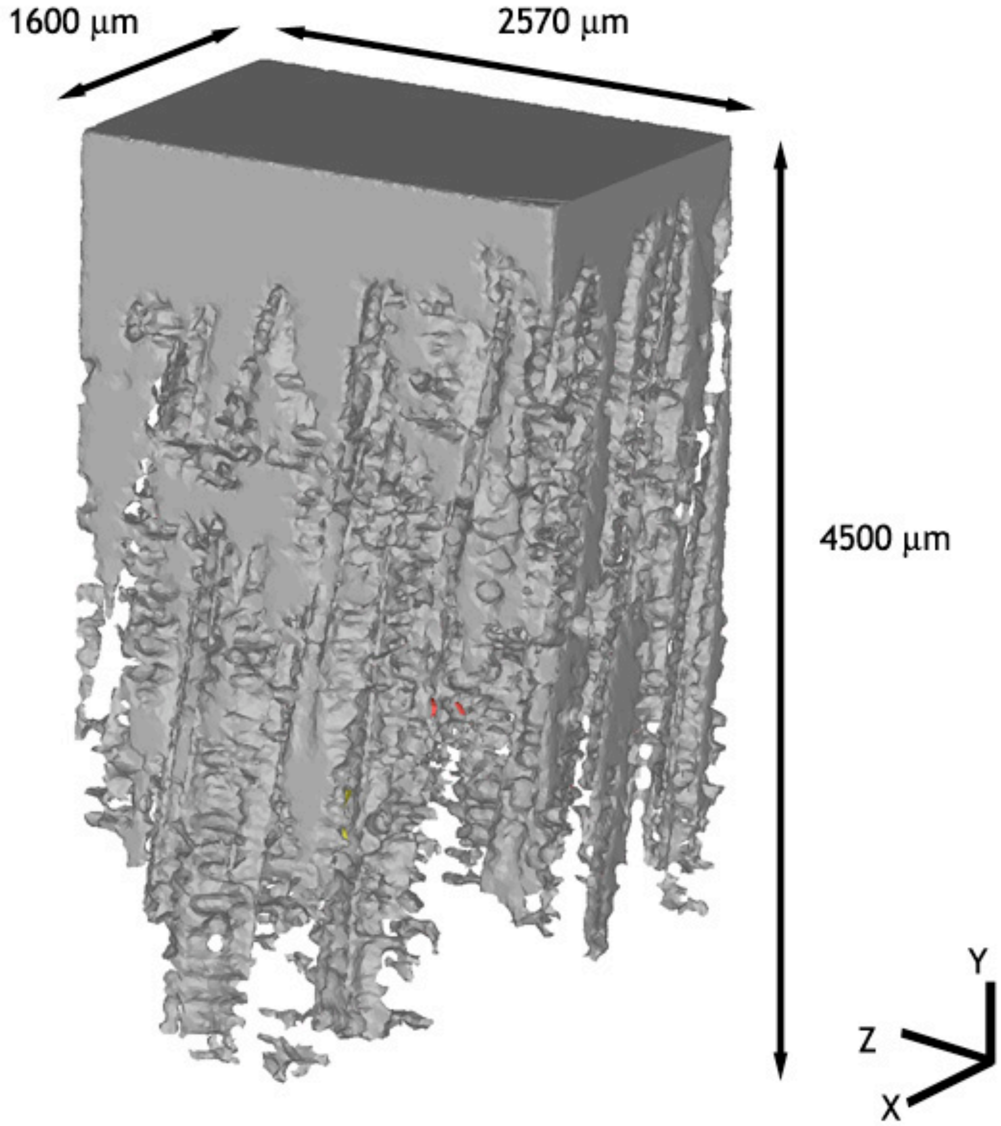

Figure 6.20 - Global Surface Mesh for Ni-Al-W Reconstructed Mushy Zone with Morphologies indicated by shaded cells

A total of 14 individual surface meshes were created and refined including 7 vertical flow cells and 7 cross-flow cells. In an effort to consider size effects of the simulation domain, cases Y6b and X1, X6 and X7 consist of approximately one half the cross-sectional area of all other flow cells. Consistent with prior convention, Chapter 5, Section 4.1, vertical flow cells were designated according to the liquid fraction at the domain inlet while cross flow cells were designated by their global liquid volume fraction. A representative vertical flow surface mesh (NAW-Y3) and cross flow surface mesh (NAW-X3) are depicted in Figures 6.21 and 6.22 respectively. Pertinent data including the fraction liquid, cell volume and total number of elements for each flow cell surface mesh are included in Table 6.5

Table 6.5 - Summary of Surface Mesh Details for Ni-Al-W Dataset

	Case	Inlet Volume Fraction Liquid	Cell Volume (μm^3)	No. of Elements
Vertical Flow	NAW-Y1	0.10	2590 × 1630 × 3600	454188
	NAW-Y2	0.20	2590 × 1640 × 2970	450828
	NAW-Y3	0.30	2590 × 1640 × 2500	414252
	NAW-Y4	0.40	2590 × 1640 × 1900	330156
	NAW-Y5	0.50	2590 × 1640 × 1200	192260
	NAW-Y6a	0.60	2590 × 1640 × 960	145518
	NAW-Y6b	0.60	1290 × 1640 × 740	74510
	Case	Volume Fraction Liquid	Cell Volume (μm^3)	No. of Elements
Cross Flow	NAW-X1	20 – 30	1340 × 1630 × 540	82430
	NAW-X2	30 – 40	2600 × 1630 × 640	238372
	NAW-X3	40 – 50	2600 × 1610 × 690	251630
	NAW-X4	50 – 60	2600 × 1630 × 250	144830
	NAW-X5	60 – 70	2600 × 1630 × 125	120858
	NAW-X6	70 – 80	1300 × 1630 × 250	54268
	NAW-X7	80 – 90	1300 × 1620 × 100	39990

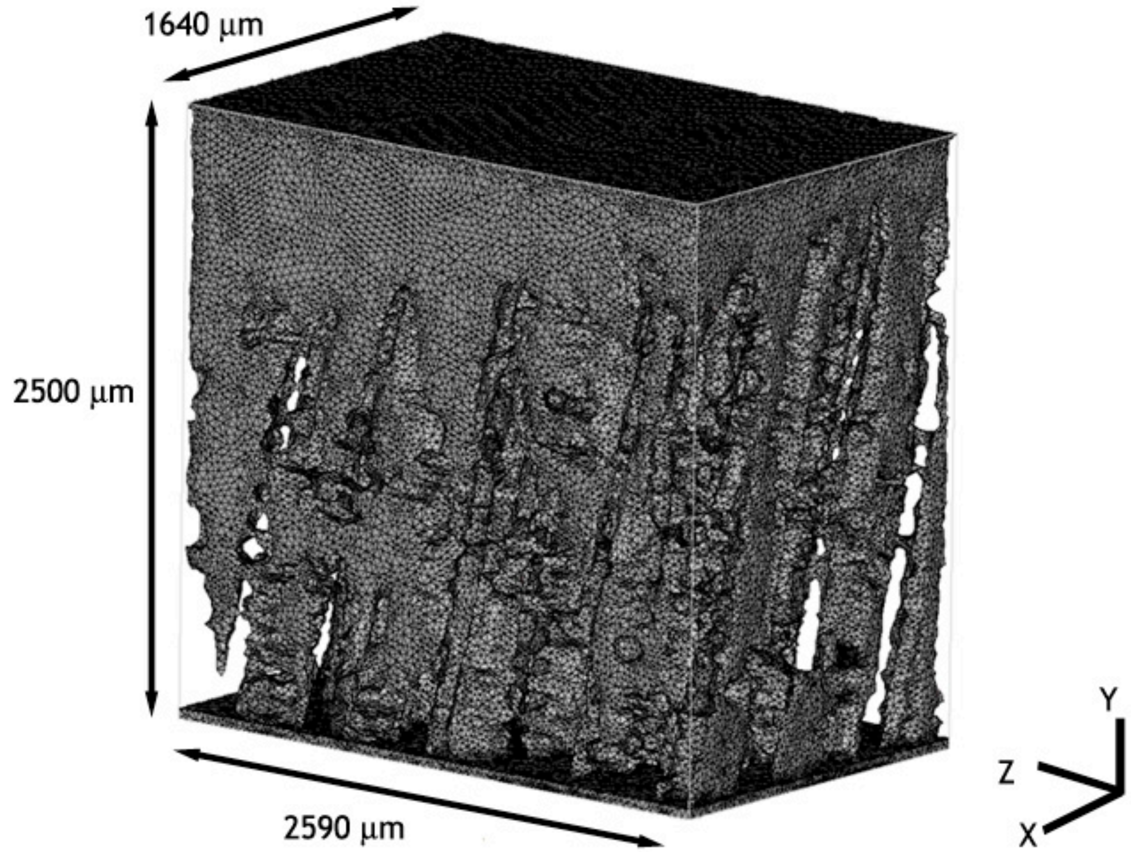

Figure 6.21 - Representative Vertical Flow Surface Mesh for Ni-Al-W Dataset

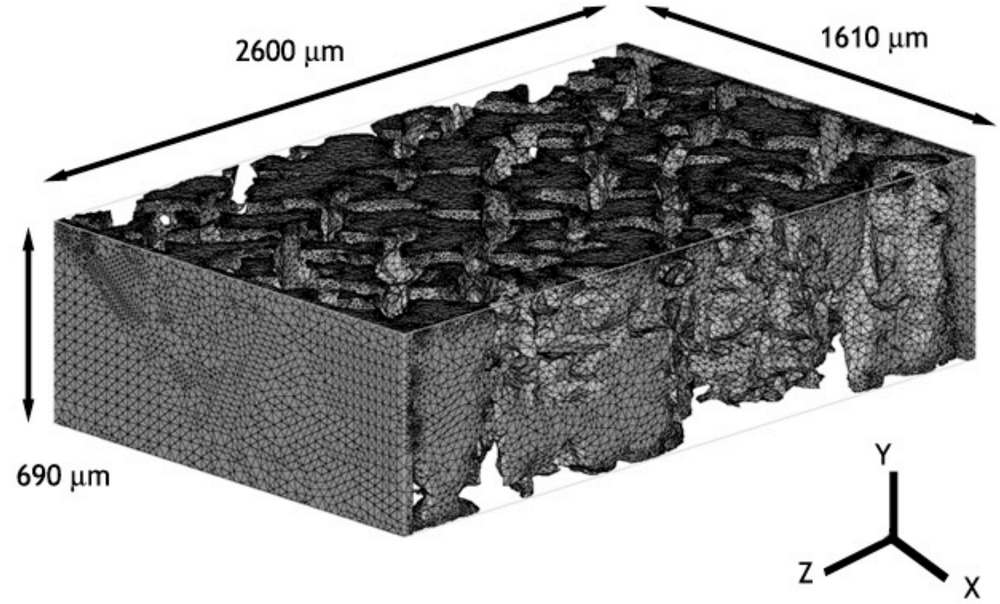

Figure 6.22 - Representative Cross Flow Surface Mesh for Ni-Al-W Dataset

6.3.2 Volume Meshes

Volume meshes were generated by creation of hybrid tetrahedral elements in GAMBIT™ from associated surface mesh refined in 3-MATIC™. Relative to the surface meshes of the Ni-Al-W reconstruction, the quantity of volume mesh elements increased by a factor of 3 - 5 for vertical flow cells and 3 to 3.5 for cross flow cells. Volume meshes for vertical flow case, NAW-Y3 and cross flow case NAW-X3 are shown in Figures 6.23 and 6.24, respectively. Details for each volume mesh simulation domain are included in Table 6.6

Table 6.6 – Summary of Volume Mesh Details for Ni-Al-W Dataset

	Case	Inlet Volume Fraction Liquid	Cell Volume (μm^3)	No. of Elements
Vertical Flow	NAW-Y1	0.10	2590 × 1630 × 3600	1376776
	NAW-Y2	0.20	2590 × 1640 × 2970	1533425
	NAW-Y3	0.30	2590 × 1640 × 2500	1526806
	NAW-Y4	0.40	2590 × 1640 × 1900	1370421
	NAW-Y5	0.50	2590 × 1640 × 1200	923308
	NAW-Y6a	0.60	2590 × 1640 × 960	780439
	NAW-Y6b	0.60	1290 × 1640 × 740	364287
	Case	Volume Fraction Liquid	Cell Volume (μm^3)	No. of Elements
Cross Flow	NAW-X1	20 – 30	1340 × 1630 × 540	240210
	NAW-X2	30 – 40	2600 × 1630 × 640	738899
	NAW-X3	40 – 50	2600 × 1610 × 690	782546
	NAW-X4	50 – 60	2600 × 1630 × 250	478178
	NAW-X5	60 – 70	2600 × 1630 × 125	412613
	NAW-X6	70 – 80	1300 × 1630 × 250	185032
	NAW-X7	80 – 90	1300 × 1620 × 100	138681

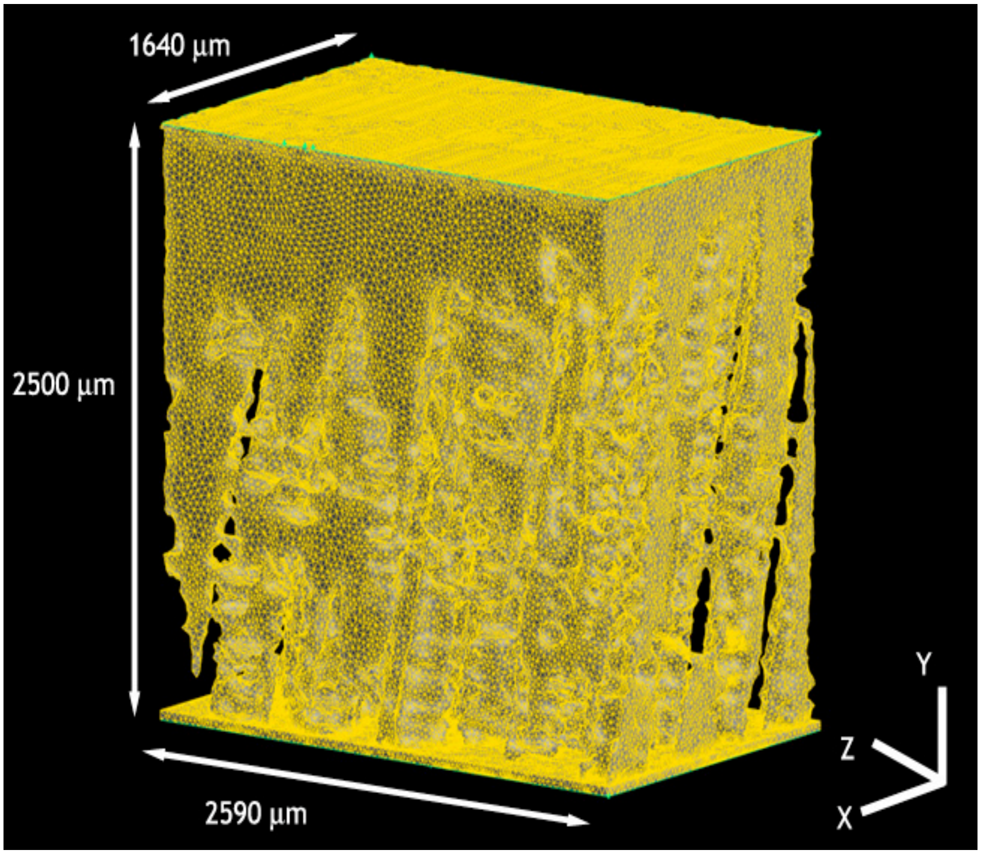

Figure 6.23 - Representative Vertical Flow Volume Mesh for Ni-Al-W Dataset

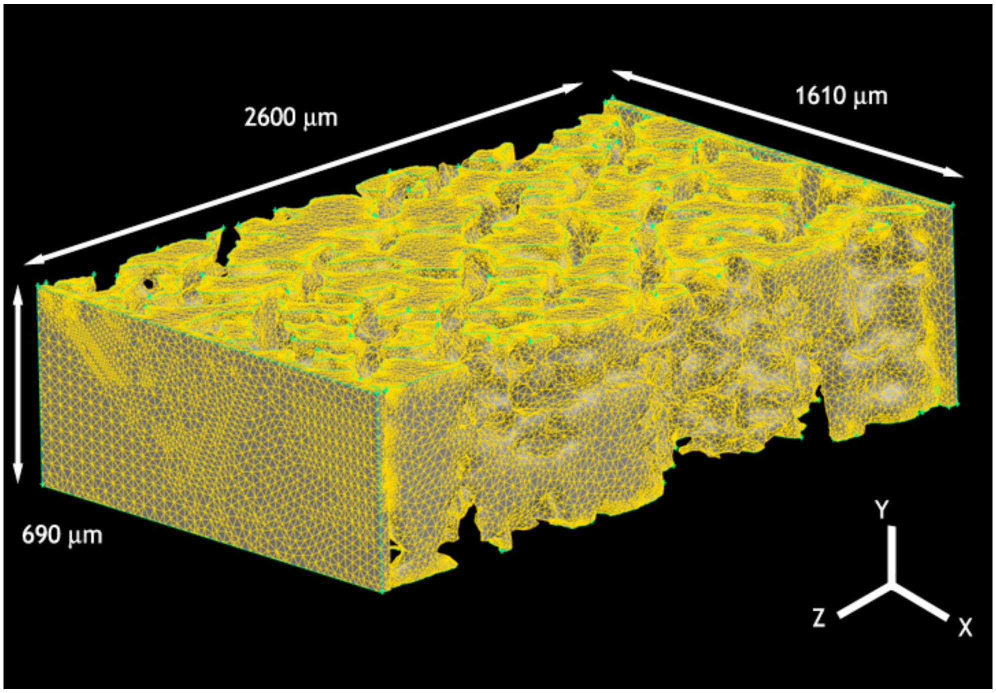

Figure 6.24 - Representative Cross Flow Volume Mesh for Ni-Al-W Dataset

6.5 QUANTIFICATION OF FLUID FLOW

Fluid flow in the Ni-Al-W reconstruction is investigated in two orthogonal directions: parallel to, and normal to, the primary growth direction. As shown in Tables 6.5 and 6.6, 7 vertical flow cases and 7 cross flow cases were developed to provide further indication of the effect of dendrite morphology on the flow of molten material at the solid-liquid interface. Ensuing results are derived from a longer resolved mushy zone with a finer primary dendrite arm spacing as compared with previously presented René N4 data, Chapter 5, and are consistent with trends and microstructural relations previously observed. Examples of flow behavior within the Ni-Al-W reconstruction will be presented along with calculations of permeability, its anisotropy, relative spacing of high velocity flow channels as well as interfacial surface area and its relation to tortuosity and permeability. Again, the findings of this study will be compared to empirical models providing a basis for further discussions in Chapter 7 regarding departures from such models and the microstructural implications of such deviations in both datasets.

6.5.1 Flow Behavior

Image maps containing flow simulation results with velocity vectors and pressure gradients for representative vertical (NAW-Y3) and cross flow (NAW-X3) cases are shown in Figures 6.25 and 6.26, as well as Figures 6.27 and 6.28, respectively. For vertical flow cases, linear vertical flow channels dominate the behavior with locally increasing velocities in constricted channels and cross-sections. The observed pressure change typically occurs over considerably longer lengths than observed in corresponding René N4 simulation cells. Alternatively, cross flow cases demonstrate low velocities over the majority of the flow domain with relatively large gradients in velocity and pressure in highly constricted zones where connectivity is possible but highly localized. Boundary conditions, resultant velocity fields and maximum pressures observed for all Ni-Al-W simulation flow cells are summarized in Table 6.7

Table 6.7 - Summary of Flow Simulations by Case in Ni-Al-W Dataset

	Case	Inlet Volume Fraction Liquid	Cell Volume (μm^3)	Inlet Velocity (mm/s)	Velocity$_{\text{min - max}}$ (mm/s)	Maximum Pressure (Pa)
Vertical Flow	NAW-Y1	0.10	2590 × 1630 × 3600	0.013	0.051 - 1.03	13.8
	NAW-Y2	0.20	2590 × 1640 × 2970	0.017	0.050 - 1.00	6.59
	NAW-Y3	0.30	2590 × 1640 × 2500	0.049	0.051 - 1.01	8.72
	NAW-Y4	0.40	2590 × 1640 × 1900	0.062	0.052 - 1.03	5.59
	NAW-Y5	0.50	2590 × 1640 × 1200	0.11	0.051 -1.02	3.61
	NAW-Y6a	0.60	2590 × 1640 × 960	0.17	0.051 - 1.02	4.00
	NAW-Y6b	0.60	1290 × 1640 × 740	0.16	0.051 - 1.02	3.27
	Case	Volume Fraction Liquid	Cell Volume (μm^3)	Inlet Velocity (mm/s)	Velocity Range (min - max) m/s	Maximum Pressure (Pa)
Cross Flow	NAW-X1	20 – 30	1340 × 1630 × 540	0.000013	0.0052 - 0.103	.989
	NAW-X2	30 – 40	2600 × 1630 × 640	0.000011	0.0054 - 0.107	2.14
	NAW-X3	40 – 50	2600 × 1610 × 690	0.00055	0.0051 - 0.101	.486
	NAW-X4	50 – 60	2600 × 1630 × 250	0.00033	0.0054 - 0.108	1.02
	NAW-X5	60 – 70	2600 × 1630 × 125	0.0013	0.0050 - 0.100	.438
	NAW-X6	70 – 80	1300 × 1630 × 250	0.011	0.0052 - 0.104	.264
	NAW-X7	80 – 90	1300 × 1620 × 100	0.015	0.0053 - 0.107	.164

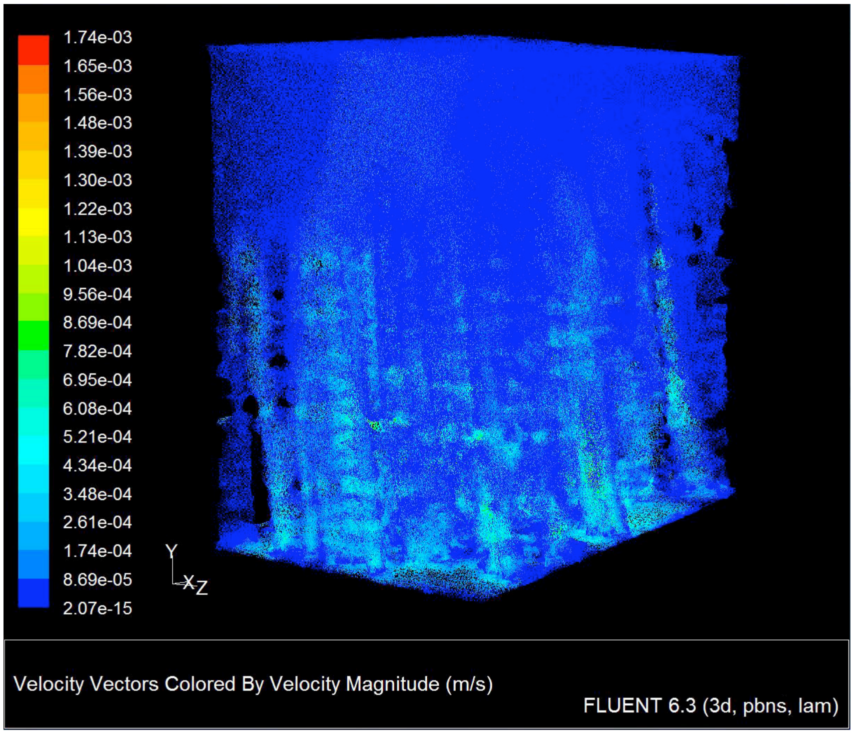

Figure 6.25 - Velocity Vector Plot in Vertical Flow Case NAW-Y3 in Ni-Al-W dataset

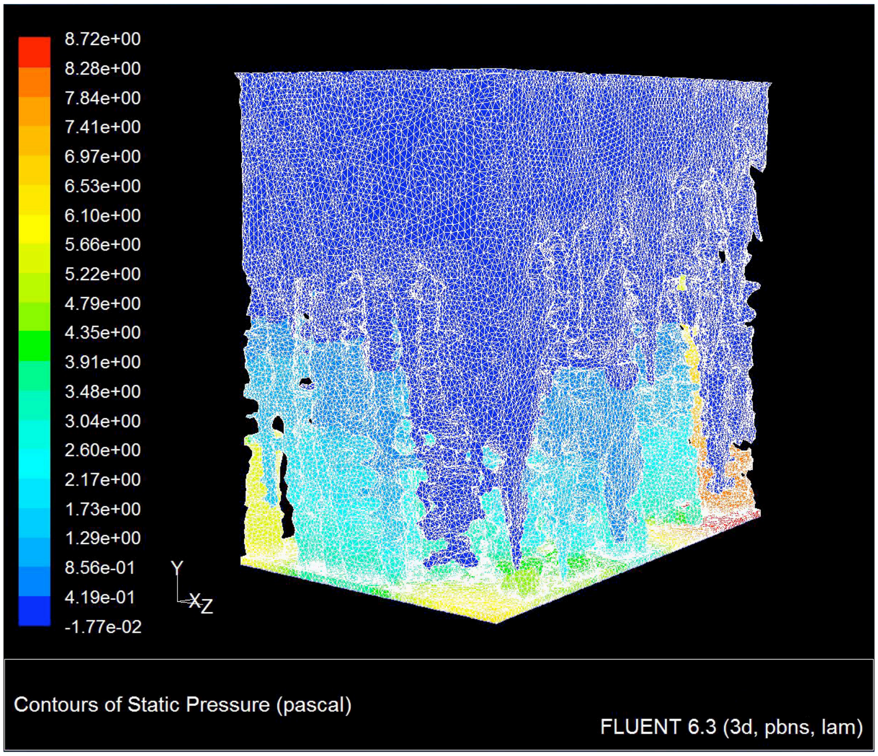

Figure 6.26 - Pressure Contour Plot in Vertical Flow Case (NAW-Y3)

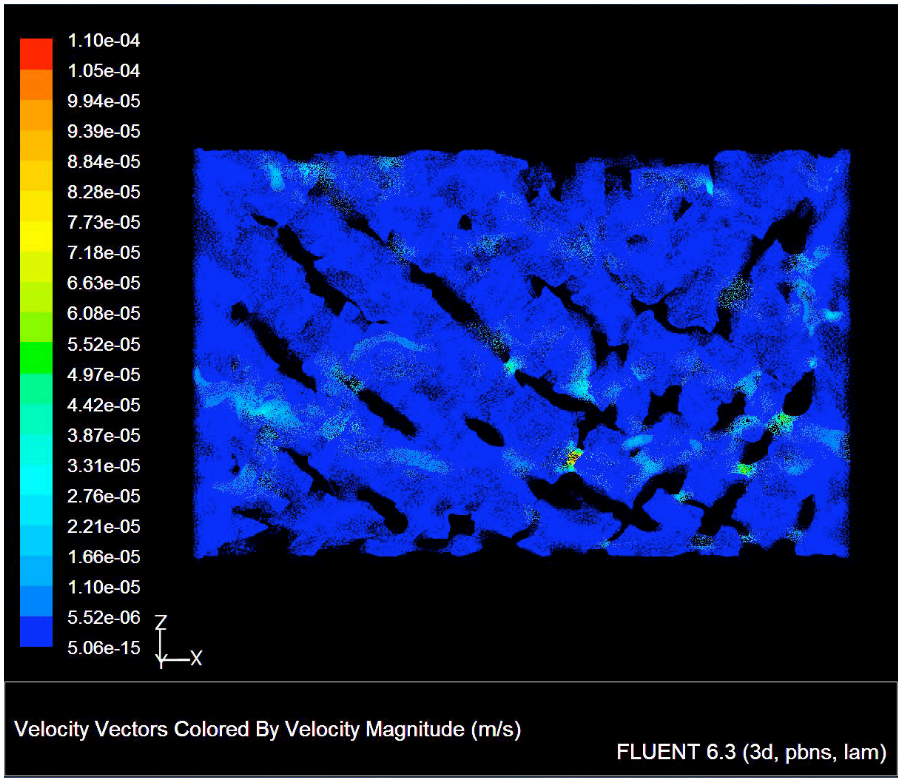

Figure 6.27 - Velocity Vector Plot for Cross Flow Case (NAW-X3) in Ni-Al-W dataset

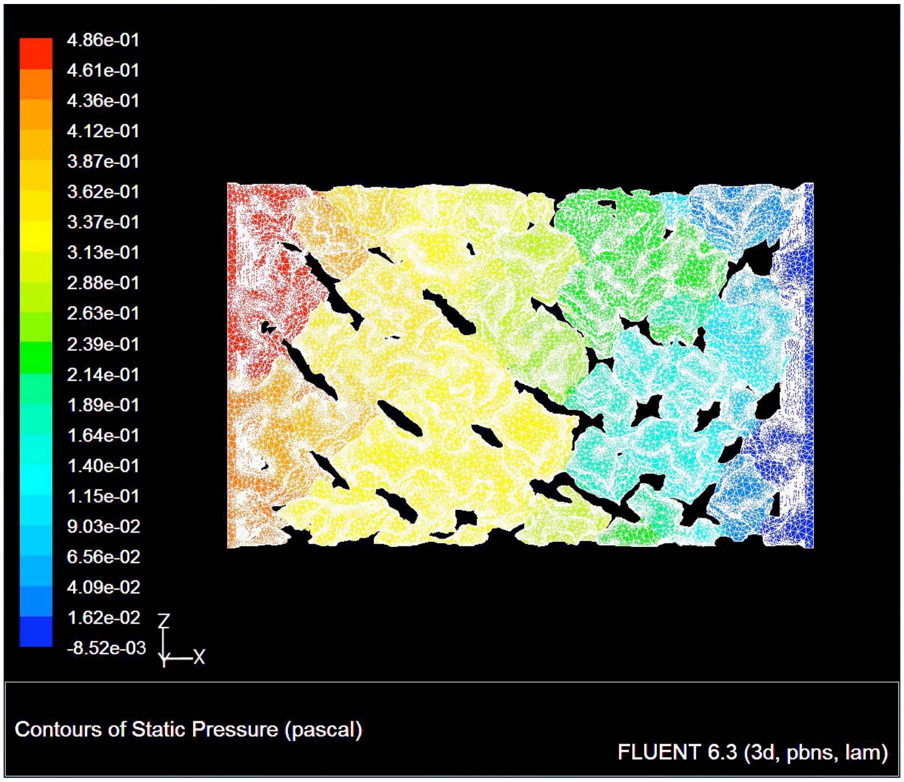

Figure 6.28 - Pressure Contour Plot for Cross Flow Case (NAW-X3) in Ni-Al-W dataset

6.5.2 Calculation of Permeability

Returning to Darcy's Law, Equation 5.1, permeabilities in each flow cell were calculated discretely. As noted in Chapter 5, each calculated vertical and cross flow permeability is then associated with its solid-liquid ratio for arrival at a volume fraction dependence for permeability in the dataset. As mentioned previously, for vertical flow cases, this solid-liquid ratio is the area fraction at the inlet while for the cross-flow cases, the local volume fraction over the entire cell is referenced. The calculated permeabilities and fundamental quantities for this calculation are represented in Table 6.8 while the volume fraction dependencies of vertical (K_y) and cross (K_x) flow permeabilities are illustrated later in Figure 6.34.

Table 6.8 - Calculated Permeabilities in Ni-Al-W Dataset and Accompanying Values

	Case	Inlet Volume Fraction Liquid	Pressure Differential (Pa)	Length over Pressure Drop ($\times10^{-4}$ m)	Volumetric Flow Rate ($\times10^{-12}$ m^3/s)	Permeability ($\times10^{-11}$ m^2)
Vertical Flow	NAW-Y1	0.10	3.01	3.00	53.2	5.20
	NAW-Y2	0.20	1.55	4.30	69.9	9.33
	NAW-Y3	0.30	1.82	4.00	200.5	13.7
	NAW-Y4	0.40	1.07	3.00	254.4	19.4
	NAW-Y5	0.50	3.57	1.40	436.3	36.5
	NAW-Y6a	0.60	1.12	0.49	691.3	52.9
	NAW-Y6b	0.60	1.47	0.50	334.8	41.7
	Case	Volume Fraction Liquid	Pressure Differential (Pa)	Length over Pressure Drop ($\times 10^{-4}$m)	Volumetric Flow Rate ($\times10^{-12}$ m^3/s)	Permeability ($\times10^{-11}$ m^2)
Cross Flow	NAW-X1	20 – 30	.922	10.7	0.106	0.43
	NAW-X2	30 – 40	2.11	22.6	0.105	0.12
	NAW-X3	40 – 50	.438	22.3	0.598	3.46
	NAW-X4	50 – 60	.206	19.9	0.132	2.99
	NAW-X5	60 – 70	.425	20.0	0.264	4.21
	NAW-X6	70 – 80	.203	11.4	1.42	27.0
	NAW-X7	80 – 90	.107	11.7	2.42	74.0

6.5.3 Anisotropy of Permeability

The data reveals variation in the volume fraction dependence of vertical flow permeabilities (K_y) compared to cross flow permeabilities (K_x). By comparing the cube of the fraction liquid (f_L) or ($1-f_S$), with variation in permeability, the contrast is shown, Figure 6.29. The term (f_L^3) or alternatively, $(1-f_S)^3$ is selected to illustrate this anisotropy as it is the fundamental term describing volume fraction dependence in both fundamental forms of both the Kozeny-Carmen and Blake-Kozeny equations, Equations 2.8 and 2.9. To further normalize the relation, dimensionless permeability, (KS_V^2) is derived and compared for vertical flow and cross flow permeabilities independently, Figure 6.29a and Figure 6.29b. In vertical flow cases for simulations in Ni-Al-W, dimensionless permeability ($K_yS_V^2$) not only demonstrates greater variation but also higher maximum values by an order of magnitude greater than cross flow dimensionless permeability ($K_xS_V^2$) with the quantity $(1-f_S)^3$. This indicates greater volume fraction dependence for *Ky* for this morphological configuration of dendritic structures. An outlier was observed in the $K_yS_V^2$ dependence (Case NAW-Y6b) due to a size effect. Case Y6b contains a cross-sectional area roughly ½ that of all other vertical flow cases as documented in Table 6.5, 6.6 and 6.7.

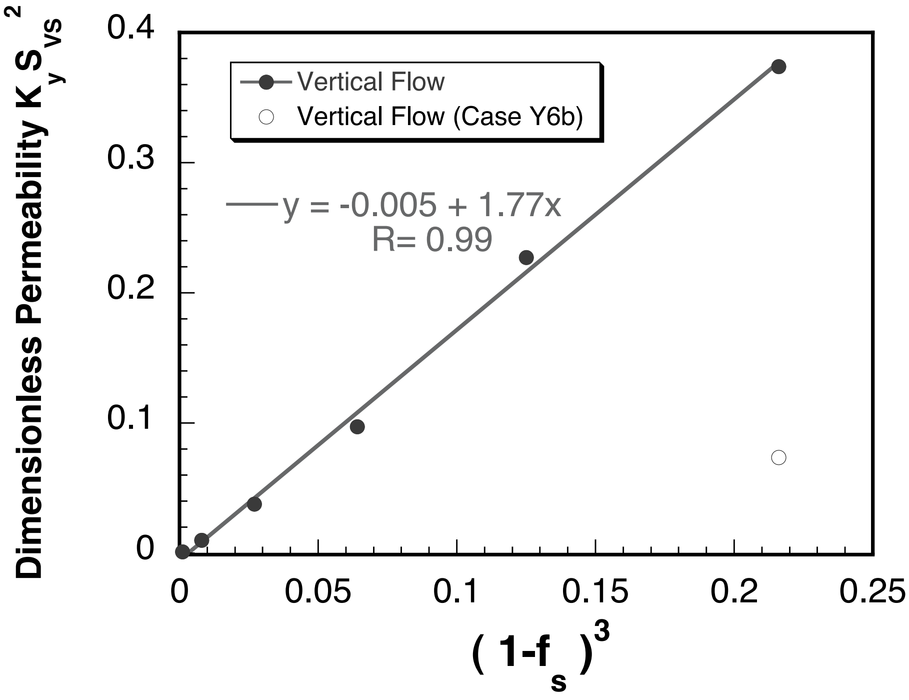

(a)

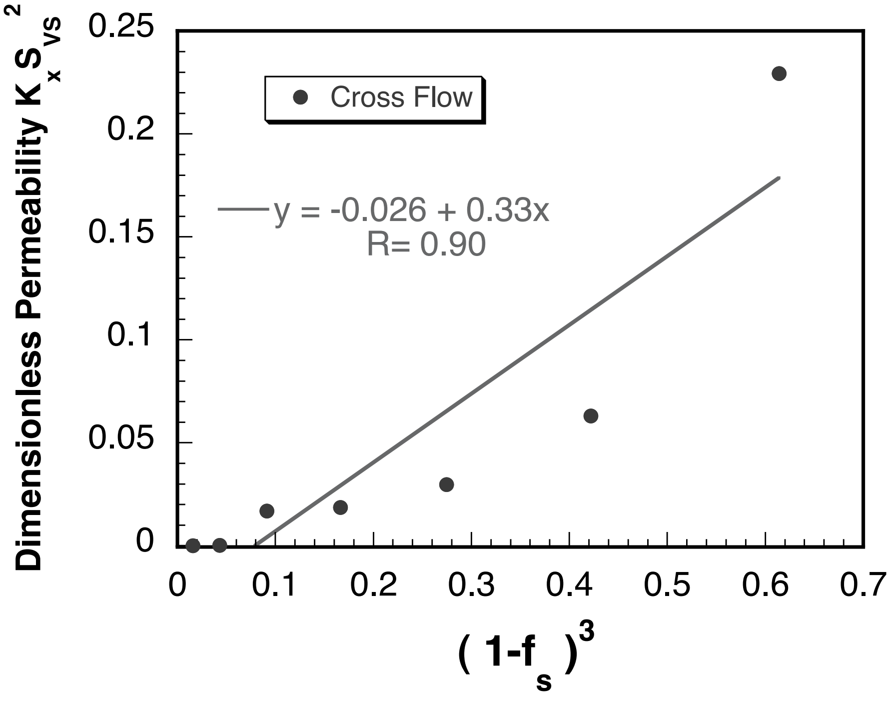

(b)

Figure 6.29 - Anisotropy of K_y & K_x as illustrated by variation in volume fraction dependence

6.5.4 High Velocity Flow Channels

Location and relative spacing among channels exhibiting comparatively higher velocities are important as they may provide opportunity for formation of chimneys and ultimately freckles and/or freckle-chains. It is interesting to note the spacing of high velocity channels and the evolution of their presence throughout the reconstructed height. Consistent with the analysis of René N4 vertical flow simulation cells, high velocity flow is defined as 10X the minimum velocity present. Planar velocity profiles normal to the solidification direction for each vertical flow cell in the Ni-Al-W study were discretized and values greater than and equal to 10X the minimum velocity were isolated and measured for relative spacing in each cross-section. High velocity flow channels were typically spaced by 350 – 500 μm. Only two cases having inlet volume fractions of .10 and .20 f_L demonstrated larger initial spacing. Over simulation domain lengths of 1 to 1.5 mm, all high velocity channel spacings converge to the upper limits of 1500 and 2000 μm, Figure 6.30. These spacings denote the presence of one or two solitary high velocity channels over the entire cross-section. The finding of note here is that high velocity channels exhibit spacings on the order of the measured dendrite arms spacing near the inlets for f_L = 0.30, 0.40, 0.50 and 0.60 but diminish such that that their spacing becomes 3X – 4X the PDAS 1 to 2 mm above the base of the mushy zone. This is the case for all simulation domains with exception to very low volume fraction simulation cells where f_L = 0.10 and 0.20 and flow is dominated by very few channels at the outset resulting in higher spacing at their initiation.

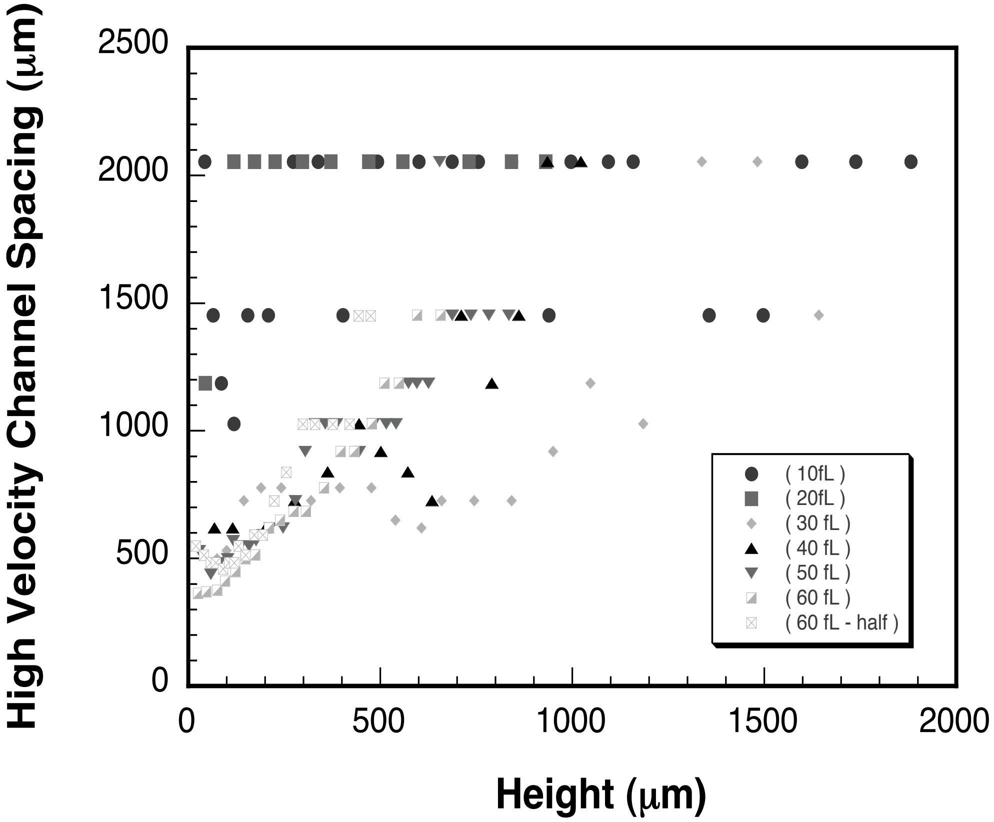

Figure 6.30 - High Velocity Channel Spacing for Vertical Flow Cases in Ni-Al-W plotted as Functions of Height

6.5.5 Flow Path Ratios and Tortuosity

The flow simulations show that vertical flow in the Ni-Al-W dataset is dominated by the presence of linear, nearly-vertical flow channels, Figure 6.31, while cross-flow cases demonstrate relatively large liquid domains connected by very small and highly restrictive linkages, Figure 6.32. To assess the complexity of flow path in relation to the dendritic network, flow path ratios and S_V have been measured directly in each simulation domain across the lengths assessed for permeability, Table 6.9.

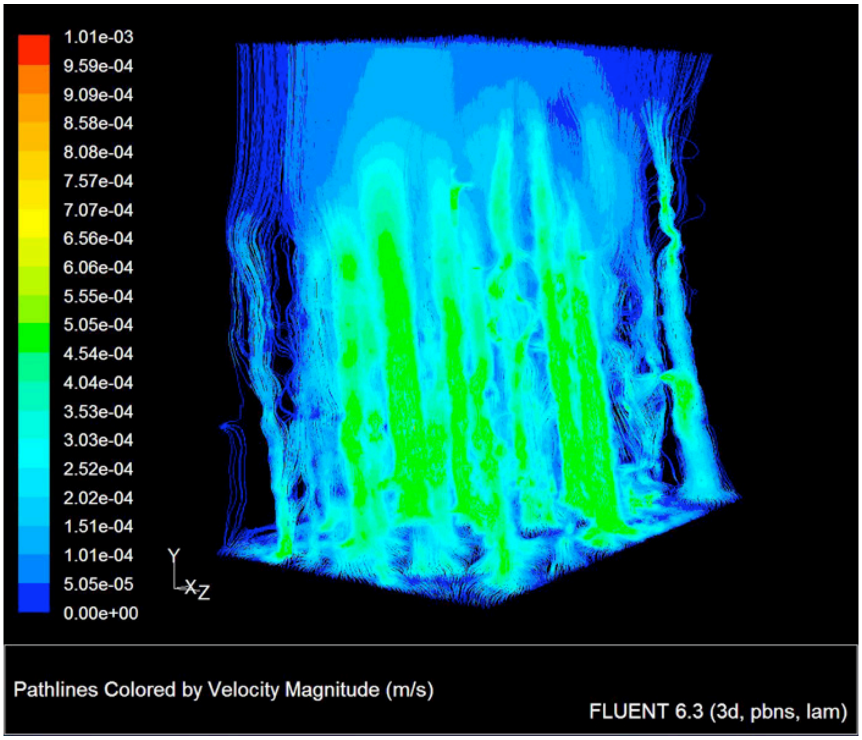

Figure 6.31 - Pathlines for Representative Ni-Al-W Vertical Flow Case (NAW-Y3) illustrating highly linear flow channels upward through the reconstruction

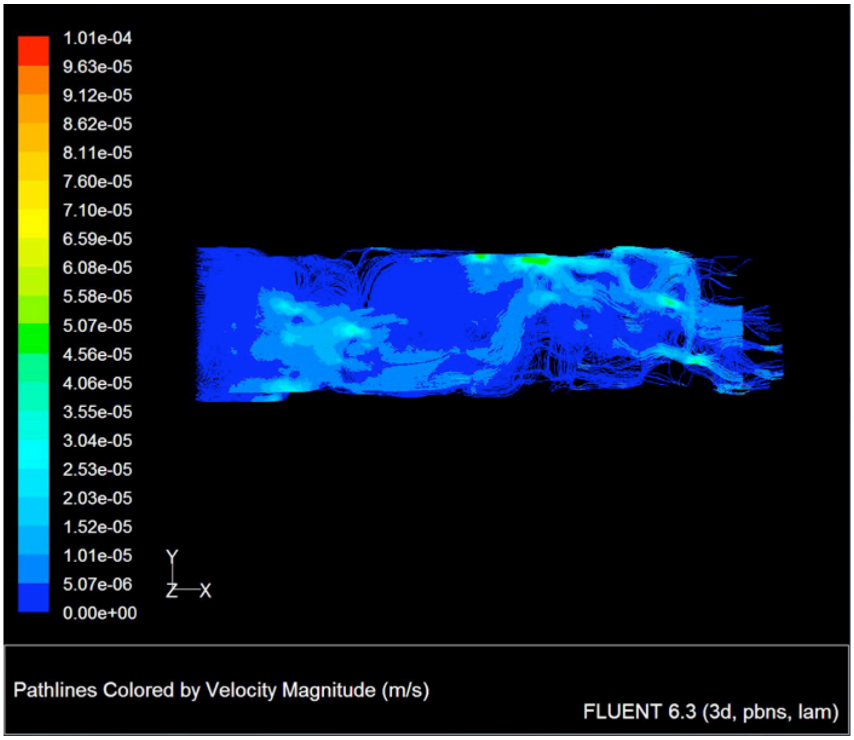

Figure 6.32 - Representative Ni-Al-W Cross Flow Case indicating constricted channels of connectivity between large liquid domains

Table 6.9 - Flow Path Ratios, ISA per unit volume & Permeability by Case for Ni-Al-W Simulations

	Case	Inlet Volume Fraction Liquid	$T_{avg.}$ {± Var}	Total S_v ($\times 10^4$ m^{-1})	Permeability ($\times 10^{-11}$ m^2)
Vertical Flow	NAW-Y1	0.10	1.30 ± 0.23	186	5.20
	NAW-Y2	0.20	1.18 ± 0.05	494	9.33
	NAW-Y3	0.30	1.16 ± 0.03	574	13.7
	NAW-Y4	0.40	1.25 ± 0.07	473	19.4
	NAW-Y5	0.50	1.19 ± 0.10	205	36.5
	NAW-Y6a	0.60	1.24 ± 0.17	73.7	52.9
	NAW-Y6b	0.60	1.27 ± 0.13	37.1	41.7
	Case	Volume Fraction Liquid	$T_{avg.}$ {± Var.}	Total S_v ($\times 10^4$ m^{-1})	Permeability ($\times 10^{-11}$ m^2)
Cross Flow	NAW-X1	20 – 30	1.51 ± 0.11	26	0.43
	NAW-X2	30 – 40	1.19 ± 0.01	88	0.12
	NAW-X3	40 – 50	1.32 ± 0.03	66	3.46
	NAW-X4	50 – 60	1.24 ± 0.01	37	2.99
	NAW-X5	60 – 70	1.10 ± 0.01	16	4.21
	NAW-X6	70 – 80	1.24 ± 0.02	5.4	27.0
	NAW-X7	80 – 90	1.07 ± 0.01	3.5	74.0

Across both flow types, increased interfacial surface area (S_V) was largely independent of increases in tortuosity ($T_{avg.}$) while interfacial surface area (S_V) scales inversely with permeability (K), Figures 6.33a and b. Tortuosity, (T_{avg}) is again defined as the ratio of distance traveled along streamlines through the structure divided by the length of the meshed domain in the principal direction of flow. For both vertical and cross flow cases, tortuosity is just greater than one across all simulation cases with very small variance. These findings are consistent with cross flow behavior in the René N4 and also confirm the linear character of the flow in vertical cases. When compared to local normalized interfacial surface area (S_V) in each simulation cell, permeability is seen to vary by power law with an exponent of -1.6 for cross flow cases and -0.5 for vertical flow cases. Both are less than the inverse dependence on ISA (S_V^{-2}) as found in the Kozeny-Carmen relationship for isotropic structures. However the exponential fit for vertical flow, Figure 6.33b, is likely reflective of the lessened ISA sensitivity created by the somewhat homogenous near-tubular flow existing at inlets throughout the heights investigated for vertical flow.

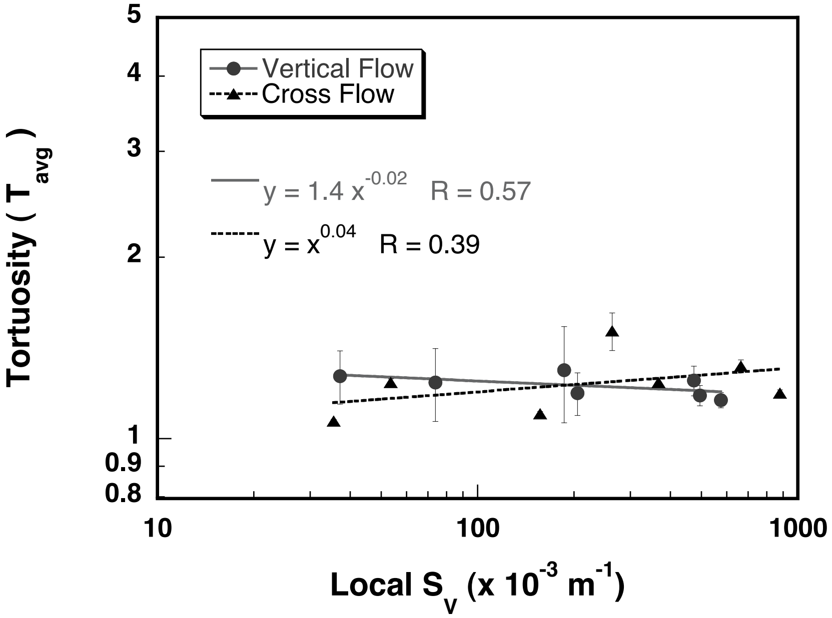

(a)

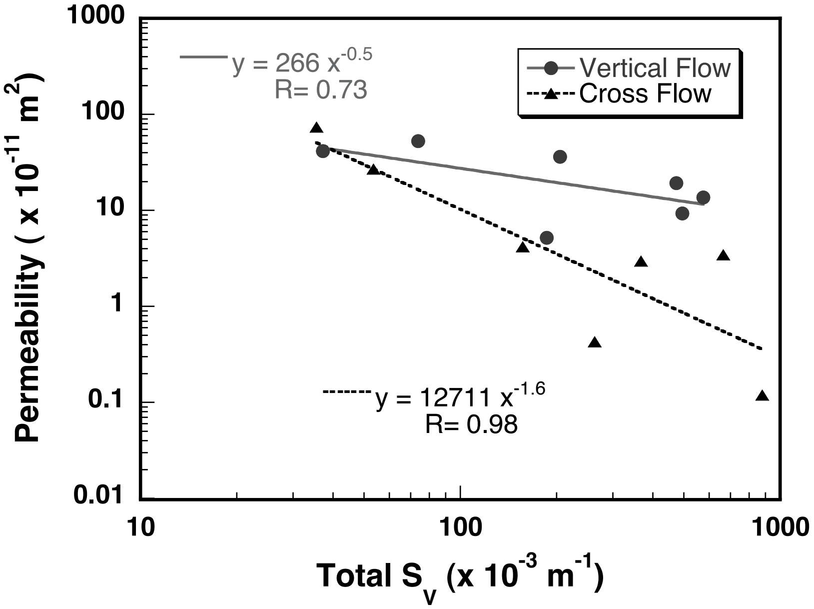

(b)

Figure 6.33 - (a) Tortuosity and (b) Permeability as functions of measured ISA per unit Volume (S_V)

6.5.6 Implications for Kozeny Relations

For comparison with well-developed empirical models such as the Blake-Kozeny and Kozeny Carmen relations, the permeability results are superimposed with Heinrich-Poirier modified Blake-Kozeny ($K_{BK(HP)}$) (Equations 2.12 and 2.13) [78, 82] as well as the traditional Kozeny-Carmen (Equation 2.8) [81, 83] (K_{KC}) relationships with measured and approximated S_V for K_{KC} profiles, Figure 6.34. Error bars in current study data correspond to total variations in solid fraction over the pressure gradient by which permeability was calculated in each simulation. Cross flow permeabilities (K_x) show reasonable correlation with $K_{BK(HP)}$ prediction with departures at $0.55f_S$ and $0.65f_S$ by a factor of ± 5X. The failure of the $K_{BK(HP)}$ criterion to predict permeability is likely due to the large constrictions existing in the cross flow domains inhibiting the overall flow and localizing the resultant pressure field. Conversely, vertical flow permeabilities (K_y) are higher than all $K_{BK(HP)}$ by a factor of 15 to 20. Interestingly, in comparison to Kozeny-Carman predictions with measured S_V, K_y are higher by a maximum factor of 5X across all fractions solid with convergence between simulation results and K_{KC} prediction at $0.4f_S$. Due to the nearly linear channels apparent in vertical flow cases, an empirical model describing permeability in an array of tubes was also considered [144, 145] Equation 6.1:

$$K_{Dvorkin} = \frac{N\pi}{A\tau 8}\left(\frac{2f_L}{S_V}\right)^4 \tag{6.1}$$

where N corresponds to the number of pipes within the array, A the combined cross-sectional area available for flow through pipes, and τ is equal to $\sin^{-1}\alpha$, the arcsin of the angle of inclination of the tubular array. Again, f_L and S_V are the volume fraction liquid and ISA per unit volume, respectively. To simplify the model, permeability was calculated assuming purely vertical flow by taking the angle of inclination to be 90^o, making the τ term equal to 1 and N was assumed to scale linearly with increases in volume fraction liquid. As shown in Figure 6.34, the Dvorkin tubular permeability ($K_{Dvorkin}$) compares reasonably well across all vertical flow simulation results with minor departures at 0.40, 0.70, and 0.80 f_S. These fraction solids coincide with deviations with the K_{KC}. This suggests that the divergence from the globally approximated ISA may also play a role in the lack of fit for the $K_{Dvorkin}$ at these discrete fraction solids but is a much better indication of the vertical flow behavior.

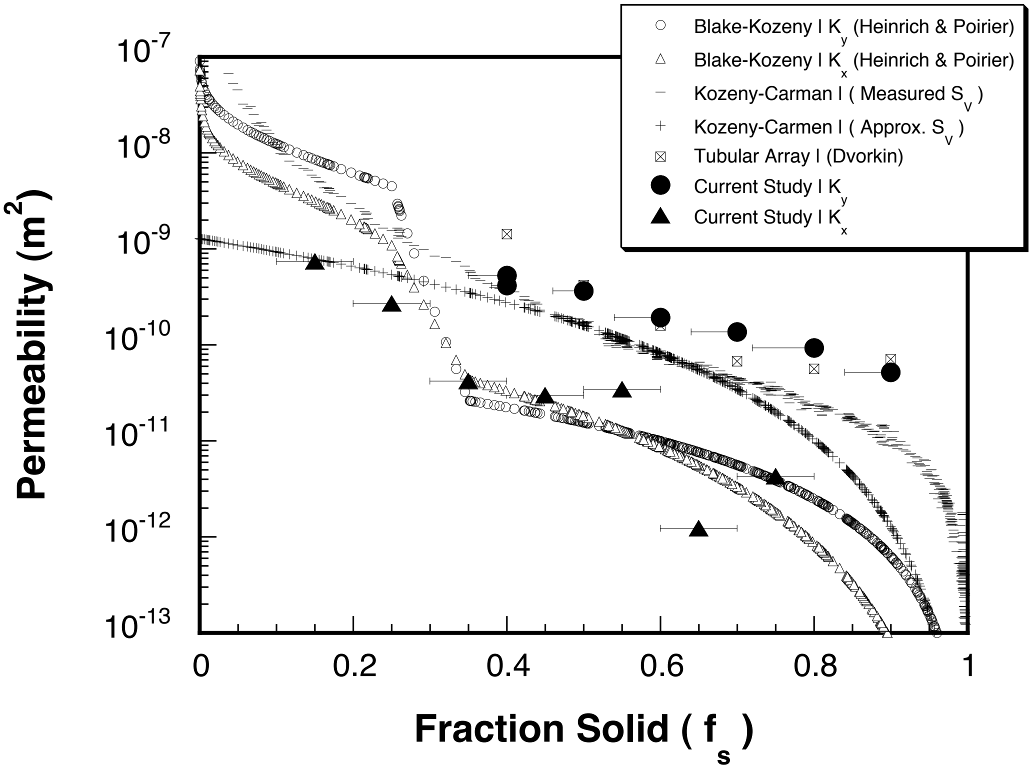

Figure 6.34 - Calculated Results Compared to Empirical Revisions of the Blake-Kozeny, Kozeny Carmen and Dvorkin models for Permeability all plotted as functions of Fraction Solid

CHAPTER 7

DISCUSSION AND CONCLUSIONS

7.1 EFFECTS OF DENDRITIC STRUCTURE ON FLUID FLOW

The impact of dendritic structure on flow behavior has been evaluated in two nickel-base alloys systems by means of vertical and cross flow simulations. Each simulation domain was extracted from portions of three-dimensionally reconstructed as-cast dendritic structures obtained by decant casting. The overall effects of dendritic structure on flow within the mushy zone are addressed and the implications for defect formation during solidification are discussed in the following sections.

7.1.1 Permeability of Dendritic Structures

The structural dependencies of permeability ($K_{y,x}$) for cases of simple flow (isothermal, incompressible and steady-state) in the mushy zone can be successfully evaluated by reconstruction and simulation. One intrinsic benefit of such a method relative to prior assessments of this property is the ability to ascertain permeability at high fraction liquid levels. Prior permeability assessments conducted experimentally with permeameters or by post-mortem investigation of quenched samples encounter difficulty in maintaining solid phase coherency at high fraction liquid levels. This is due to coarsening or remelting of isolated solid in regions surrounded by molten liquid. Thus permeability evaluation in the high fraction liquid regime has been limited. An additional benefit of this new 3-D approach is that direct relationships between permeability, fraction solid and interfacial surface area have been experimentally derived.

To predict defect formation, prior analyses of the Rayleigh number have used an average permeability of the liquid in the upper region of the mushy zone. In this study variation in permeability of up to two orders of magnitude as a function of fraction solid has been observed in both vertical and cross flow cases. Furthermore, K_x varies up to three orders of magnitude for cases in which abrupt evolution of volume fraction occurs with height. This indicates the use of an average permeability over a range of volume fractions may not provide an accurate estimate of the relevant permeability, with errors possibly as large as 2 - 3 orders of magnitude for a given volume fraction.

7.1.3 Interfacial Surface Area in the Dendritic Array

Interfacial Surface Area (ISA) per unit volume (S_V) exhibits a near parabolic relationship with volume fraction solid with a maximum in S_V occurring at or near 0.65 f_S. This behavior is independent of solid fraction profiles with respect to height. This inflection point indicates a physical location in the dendritic structure by which maximum ISA (S_{VMAX}) can be determined. Furthermore, estimations of S_V for other volume fractions can be developed from this value. A more accurate assessment of the relationship between S_V and the local structure presents an opportunity for inclusion of a more accurate characteristic length. Previous use of the inverse of the secondary dendrite arm spacing may provide a reasonable approximation in magnitude; however, this single value does not accurately describe the significant variation that has been measured in this study throughout the height of the mushy zone. Furthermore from direct assessment of

S_V, ISA per unit volume solid (S_{VS}) can also be readily calculated by dividing by the local volume fraction solid.

7.1.4 Tortuosity and Interfacial Surface Area

Tortuosity ($T_{avg.}$) in vertical flow among typical dendritic structures has been shown to vary directly with S_V. However, in cross flow, tortuosity is only weakly dependent on S_V given the relatively small quantifiable change in tortuosity and the comparably large variation in S_V. Tortuosity was shown to vary by power law such that $T_{avg} = S_V^{0.04}$ for cross flow and $T_{avg} = S_V^{0.2}$ for vertical flow. For vertical flow cases in the Ni-Al-W system in which flow was highly dominated by concentrations of near-linear vertical flow paths $T_{avg} = S_V^{-0.02}$.

7.1.5 Permeability and Interfacial Surface Area

Permeability ($K_{y,x}$) is inversely proportional to S_V across all vertical and cross flow simulations. The rate of dependence of $K_{y,x}$ on S_V is best described by a power law, where $K_x = K_o S_V^{-1.6}$, with K_o equal to 19000, 13000 (m^{-4}) for René N4 K_x and Ni-Al-W K_x, respectively and $K_y = K_o S_V^{-1.7}$, with K_o equal to 11000 (m^{-3}) for René N4 K_y. The only departure from an exponent of -1.5 occurs in instances of highly uni-directional flow, which dominates flow behavior under vertical flow conditions in the Ni-Al-W simulation cells.

When unidirectional flow prevails the dependence of K on S_V decreases. In such cases, the available cross-sectional area rather than channel shape is a more descriptive metric for variation in K as seen in the vertical flow cases of the Ni-Al-W system. In the case examined, the power law dependence of S_V with K appropriates a relationship in which $K_y = K_o S_V^{-0.5}$ where $K_o = 260$ ($m^{1.5}$).

7.1.7 Dissipation of Flow in High Velocity Channels

The spacings of channels with high velocity flow rates indicate dendritic structure inhibits high speed flow over the length of the mushy zone. In all cases, the flow in the high velocity channels is dissipated such that the spacing of high velocity channels decreases to one or less than one after travel of 1mm or less through the mushy zone. For cases in which no uni-directional flow paths are provided, high velocity channels are dispersed and rapidly decrease in number to one or fewer instances after travel through 0.25mm or less of the mushy zone height. The presence of the high flow velocity channels is important as dendrite fragmentation events are likely enhanced in regions of high velocity flow and by dendritic arrangements that allow for persistence of this flow up to the dendrite tips.

7.1.8 Considerations for Cross Flow

It is interesting to note that multiple cross flow simulation domains, particularly in the case of the René N4 system, are relatively thin compared to their cross-sectional area. However, as previously shown, cross flow permeabilities calculated in this study yield reasonable agreement with empirical permeability models, Figures 5.30 and 6.34 with limited departures. Furthermore, direct comparison with additional independent assessments of permeability show further agreement for cross flow results, Figure 7.2, and will be discussed in detail in the following section. The pressure drop occurring in cross flow is dominated by the constrictions of flow channels between closely neighboring in-plane secondary arms not flow above or below them, Figures 5.25, 6.27, 6.28 and 6.32. As shown, assessment of cross flow permeability in the thesis has been performed with relatively thin (Figure 5.23) and comparably thick (Figure 6.24) heights yielding comparable permeabilities. Therefore, thin heights that accurately capture flow constriction due to secondary dendrite arms may prove sufficient for permeability calculation. Additionally, cross flow in this thesis has only been investigated in one flow direction with respect to each dataset. As discussed in Section 2.3.2, Bhat and co-workers have shown lateral flow orientations have negligible impact on cross flow permeability [71]. The predominance of flow constrictions being the controlling factor in flow through the dendritic network supports this observation.

7.2 COMPARISON OF PERMEABILITY ASSESSMENTS

K_y (vertical) and K_x (cross) permeabilities presented by various investigators using both numerical and experimental approaches are in general agreement with the permeabilities determined in this study as a function of volume fraction, with the exception of vertical flow in Ni-Al-W, Figures 7.1 and 7.2. The advantages of this new 3-D technique for permeability assessment will now be considered and departures from prior findings and new insights to the flow process will also be addressed.

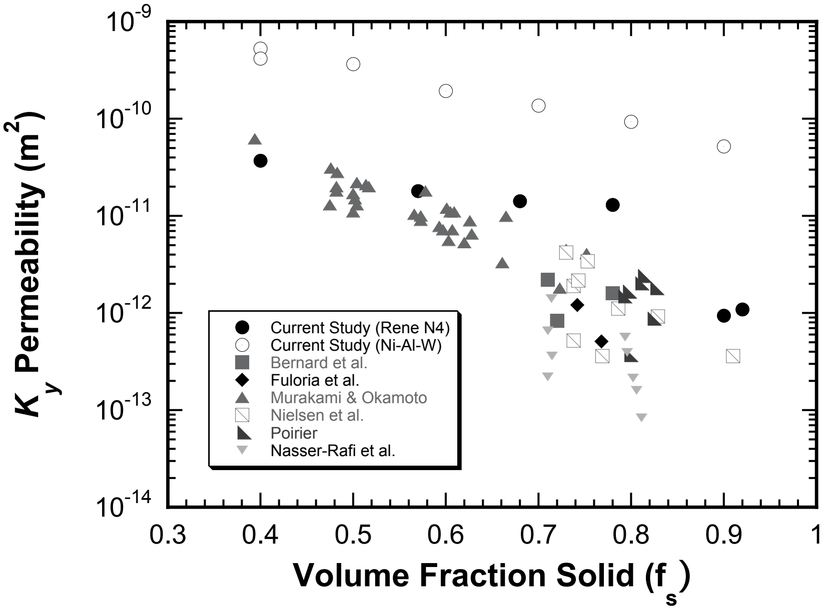

Figure 7.1 - Comparison of Calculated Vertical Flow Permeabilities (K_y)

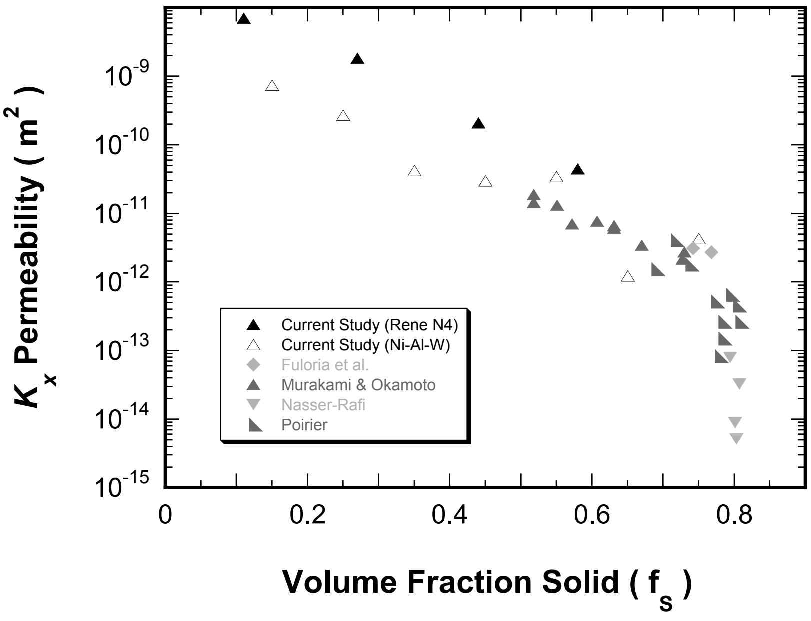

Figure 7.2 – Comparison of Calculated Cross Flow Permeabilities (K_x)

One of the inherent benefits of the approach detailed in this thesis is the ability to directly assess vertical or cross flow permeability independently within the same mushy zone. Furthermore, the method described in the current study allows for reliable, direct assessment of permeability over the broadest range of fraction solid by use of a single method to be reported to date. Thirdly, this method allows for practical interrogation of a morphologically complex domain providing correlation of physical features of the dendritic structure to local and global flow behavior. This in itself is a notable accomplishment given the susceptibility of the mushy zone to dynamic evolution in most physical experiments, regardless of material system.

In spite of overall agreement with the permeabilities determined in prior studies, in the present study, K_y for the Ni-Al-W alloy were substantially higher than other reported values. Vertical flow in the Ni-Al-W dataset is more accurately described by flow through an array of parallel cylinders as previously shown by comparison with the Dvorkin permeability model, Section 6.5.6. Comparison of the fraction solid profiles over the height of both reconstructed mushy zones in this study, Figure 7.3, indicate the presence of greater amounts of liquid at lower portions of the mushy zone in the Ni-Al-W dataset which do in fact contribute to the uni-directional vertical flow paths at very low heights. In Figure 7.3, heights are normalized to make the direct comparison clear. These highly uni-directional flow channels are likely due to the irregular casting geometry, orientation of mold to encourage decanting and the alloy chemistry. Furthermore, linear channels in the liquid domain were observed to span the entire height of the reconstructed mushy zone regardless of volume fraction inlet level.

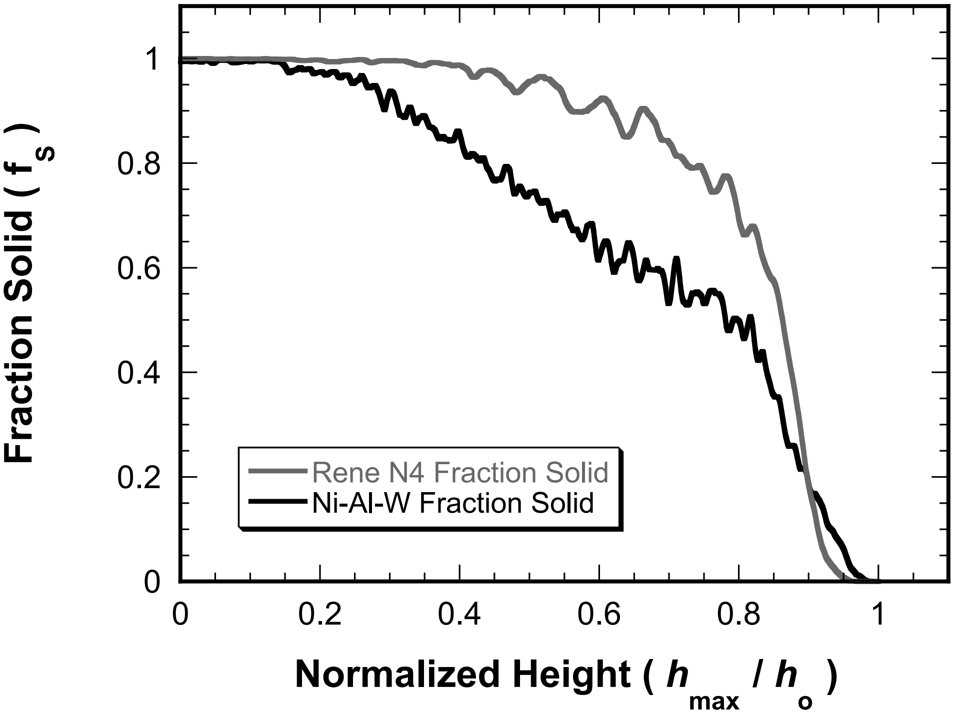

Figure 7.3 - Fraction Solid Profiles for both René N4 and Ni-Al-W datasets over Normalized Heights

While these factors have affected vertical flow behavior through the Ni-Al-W dendritic array, primary and secondary dendrite arm spacing and porosity follow expected trends given the casting conditions. Since permeability in directionally solidified systems is traditionally predicted by use of dendrite arm spacing and volume fraction, the present 3-D assessments provide additional opportunity for identification of factors influencing permeability through flow channels in dendritic arrangements. In the cases of cross flow, cited values shown in the literature converge well with those reported here. Furthermore, the current study has allowed investigation in the low fraction solid regime, which has been largely untreated due to difficulties associated with maintaining dendritic solid in the range of very high fraction liquid levels where f_L approaches or is greater than 60 – 70%. This has been a source of significant challenge in experimental approaches using permeameters for direct assessment of permeability or by direct application of D'Arcy's Law in numeric approaches which yield erroneous results at fraction liquid > 0.7 [71, 78, 143].

7.3 CALCULATION OF THE RAYLEIGH NUMBER

To address the effect of the current permeability observations on defect formation processes, it is useful to consider the Rayleigh (Ra) criterion. While the numeric and theoretical basis for the Rayleigh value was presented in Section 2.1 of Chapter 2, the impact of contributing quantities and their physical meaning will be quickly summarized here to frame the discussion. The local Rayleigh number (Ra_h) for the two alloys investigated in this thesis will then be provided as a function of fraction solid based on the permeabilities (K_y and K_x) calculated in this thesis. These trends will then be compared to the local Rayleigh numbers (Ra_h) generated by use of a conventional permeability approximation. In order to first provide a frame of reference for the expected range of Ra_h in directionally solidified nickel-base superalloys, Rayleigh values for the widely referenced, single-crystal nickel-base alloy of Pollock & Murphy, SX-1 [1, 2, 56, 62, 65, 66, 146] will be presented for a variety of casting parameters. This will provide a basis upon which to describe the competing effects of density gradient and permeability in the Rayleigh number. Lastly, a modified permeability relation taking into account the effects of interfacial surface area will be presented and discussed in terms of its benefits and limitations in practice.

As discussed in Section 2.1.5, the Rayleigh number (Ra) is a ratio of the buoyancy to drag forces occurring in the melt. As solidification proceeds, elements segregate from the solute resulting in lighter liquid densities deeper in the mushy zone. When this density inversion reaches a critical value, the buoyancy force can overcome the frictional force required to keep the lighter elements suppressed within the melt. The Rayleigh criterion is the metric used to quantify this critical ratio:

$$Ra_h = \frac{(\Delta\rho/\rho_o)g\overline{K}h}{\alpha v} \tag{7.1}$$

Acceleration due to gravity (g) is acting upon the product of the density inversion $(\Delta\rho/\rho_0)$, over some length h and combined with a measure of average, or as returned in this current work, 3-D dendritic array permeability ($\overline{K}$ or K, respectively). This value is then divided by the product of the thermal diffusivity, (α) and kinematic viscosity, (ν). For the ensuing calculations, the product of $\alpha\nu$ is approximated as 5×10^{-12} $\mathrm{m}^4/\mathrm{s}^2$ and h corresponds to the height in the mushy zone determined by assuming a linear thermal gradient between the $T_{solidus}$ and $T_{liquidus}$. Equation 7.1 reveals that variation in Rayleigh number under the above circumstances is strongly influenced by the density gradient and permeability. Additionally, these terms are, in themselves, largely influenced by the thermal gradient. Figure 7.3 shows the Rayleigh number calculated using Equation 7.1, as a function of solid fraction for the single crystal alloy SX-1 [1, 2], under a number of experimental configurations of thermal gradient (G) and solidification front velocity (V), as initially shown by Beckermann, Gu and Boettinger [56]. The nominal elemental composition for SX-1, presented by Tin in multiple freckling studies is shown in Table 7.1 [8, 65, 66, 146].

Table 7.1 – Elemental Composition of Nickel-Base Alloy SX-1 (wt%)

Alloy	Al	C	Cr	Co	Hf	Re	Ta	W	Ni
SX-1	6.0	0.05	4.5	12.5	0.16	6.3	7.0	5.8	bal

For calculation of compositional variation between the solidus ($T_{solidus}$) and liquidus ($T_{liquidus}$) temperatures, two methods were employed. First, a modified Scheil relation, Equation 7.2, accounting for back diffusion, was used to determine compositional variation. Distribution coefficients measured specifically for this alloy, and their validations are discussed in [8].

$$C_l = C_o(1-(1-2\alpha k)f_S)^{\frac{k-1}{1-2\alpha k}} \tag{7.2}$$

In an effort to develop a method for cases in which alloy specific distribution coefficients are not available, Scheil calculations using PANDAT by CompuTherm were also performed. The results of the variation in alloying elements from the CALPHAD simulation are shown in Figure 7.4. Distribution coefficients from the PANDAT C_s/C_l ratios yield nominal agreement with directly measured distribution coefficients for all elements with exception to Cr and Re. However, Equation 7.2, predicts a more rapid change in composition with temperature than CALPHAD results. The effect of this variation on the calculated Rayleigh number will be shown subsequently.

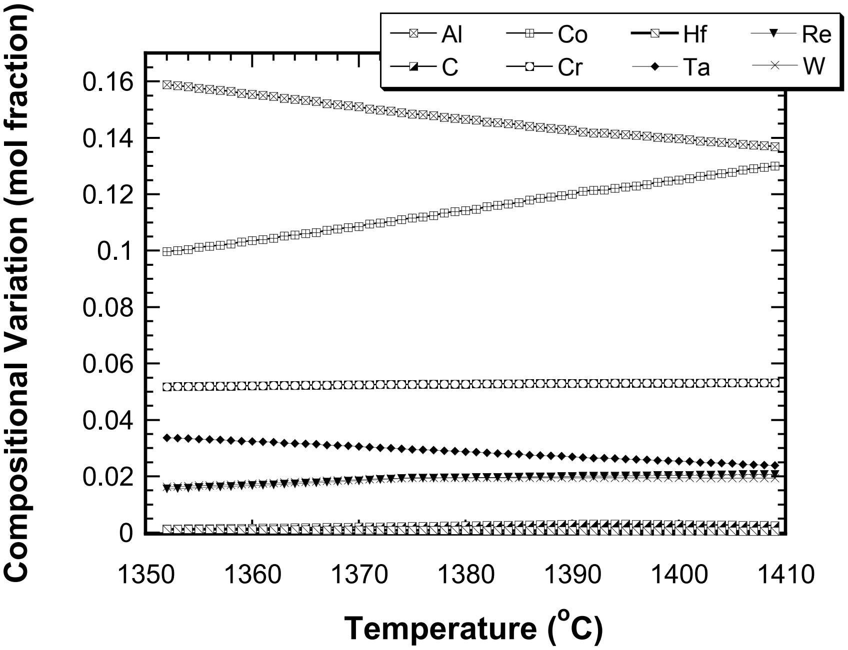

Figure 7.4 – Compositonal Variation in Alloying Elements within SX-1 between T$_{solidus}$ - T$_{liquidus}$

Both sets of temperature specific compositions were then used in the partial molar volume equations of Mukai et al. [130] as shown in Equations 7.3 – 7.12 in which *T* corresponds to temperature in degrees Celsius.

$$V_{Ni}(10^{-6}m^3 \cdot mol^{-1}) = 7.4287 + 1.4091\times 10^{-3}(T - 1455) \tag{7.3}$$

$$V_{Cr}(10^{-6}m^3 \cdot mol^{-1}) = 8.1686 + 7.7257\times 10^{-4}T \tag{7.4}$$

$$V_{Co}(10^{-6}m^3 \cdot mol^{-1}) = (4.5795 + 2.0501\times 10^{-3}T) + (15.0911 - 8.8179\times 10^{-3}T)X_{co} \tag{7.5}$$

$$V_{W}(10^{-6}m^3 \cdot mol^{-1}) = (45.1768 - 1.92\times 10^{-2}T) + (-605.8481 + 0.3210T)X_{W} \tag{7.6}$$

$$V_{Ta}(10^{-6}m^3 \cdot mol^{-1}) = (97.6917 - 4.6711\times 10^{-2}T) + (-2223.0992 + 1.1553T)X_{Ta} \tag{7.7}$$

$$V_{Al}(10^{-6}m^3 \cdot mol^{-1}) = 9.3859 - 2.3468\times 10^{-4}T \tag{7.8}$$

$$V_{Mo}(10^{-6}m^3 \cdot mol^{-1}) = 11.8445 - 1.3703\times 10^{-3}T \tag{7.9}$$

$$V_{Hf}(10^{-6}m^3 \cdot mol^{-1}) = 11.5393 + 1.3144\times 10^{-3}T \tag{7.10}$$

$$V_{Ti}(10^{-6}m^3 \cdot mol^{-1}) = 7.8304 + 1.9697\times 10^{-3}T \tag{7.11}$$

$$V_{Nb}(10^{-6}m^{3}\cdot mol^{-1}) = 9.2650 + 9.28\times10^{-4}T \tag{7.12}$$

The only adjustment to the aforementioned relationships was made in the approximation of the partial molar volumes of tantalum. The nominal Ta composition of the alloy was used in Equation 7.6 for approximation of the partial molar volume V_{Ta} across all temperatures as calculations utilizing the predicted compositional variation resulted in a substantial increase in total alloy density with decreasing temperature. Reasons for this adverse behavior may include inaccurate prediction of compositional variation with regards to Tantulum by PANDAT or shortcomings in the adoption of the partial molar volume model to thermal regimes corresponding to compositional variation in these alloys. All other relationships were utilized as presented in [130]. This data was then used in the approach of Sung et al. [132] to derive the combined thermal and solutal induced density variation within the solute as a function of temperature according to the following relation;

$$\rho = \frac{\sum X_i M_i}{\sum X_i V_i} \tag{7.12}$$

where X_i is the mole fraction of element i, M_i is the molecular weight of element i, and V_i is the partial molar volume of element i. For the purposes of this example, the conventional approximation for K is used and assumes the following G and V dependent value as appropriated by various investigators [56, 62, 65, 135].

$$\overline{K} = 6\times10^{-4}\lambda_1^2\frac{(1-f_S)^3}{f_S^2} \tag{7.13}$$

where λ_1 is the primary dendrite arm spacing in micrometers and is defined as;

$$\lambda_1 = 147(G \times R)^{-0.3384} \tag{7.14}$$

Others have used an average volume fraction ($\overline{\varepsilon_S}$) for f_s in Equation 7.13 according to the following relation;

$$\overline{\varepsilon_s} = \frac{1}{h}\int_0^h \varepsilon_s dy \tag{7.15}$$

In the following calculations, explicit volume fractions were used with exception to $h = 0$. Figures 7.5a and 7.5b illustrate the overall trends. Rayleigh values shown in Figure 7.5a were calculated with compositions determined by Equation 7.2, while Ra_h values shown in Figure 7.5b were calculated with compositions determined by PANDAT. As can be seen, results differ by a factor of 10. Since directly measured distribution coefficients have a greater degree of certainty, a scaling factor of 10 was employed to the Ra_h calculated with subsequent CALPHAD estimates to account for the likely underestimations of composition change and subsequent density gradient. However, even with a scaling factor of 10, it is unclear how Beckermann, Gu and Boettinger derived their reported magnitudes for the Ra_h in SX-1 at these processing conditions [56] as neither approach presented here returns equivalent values.

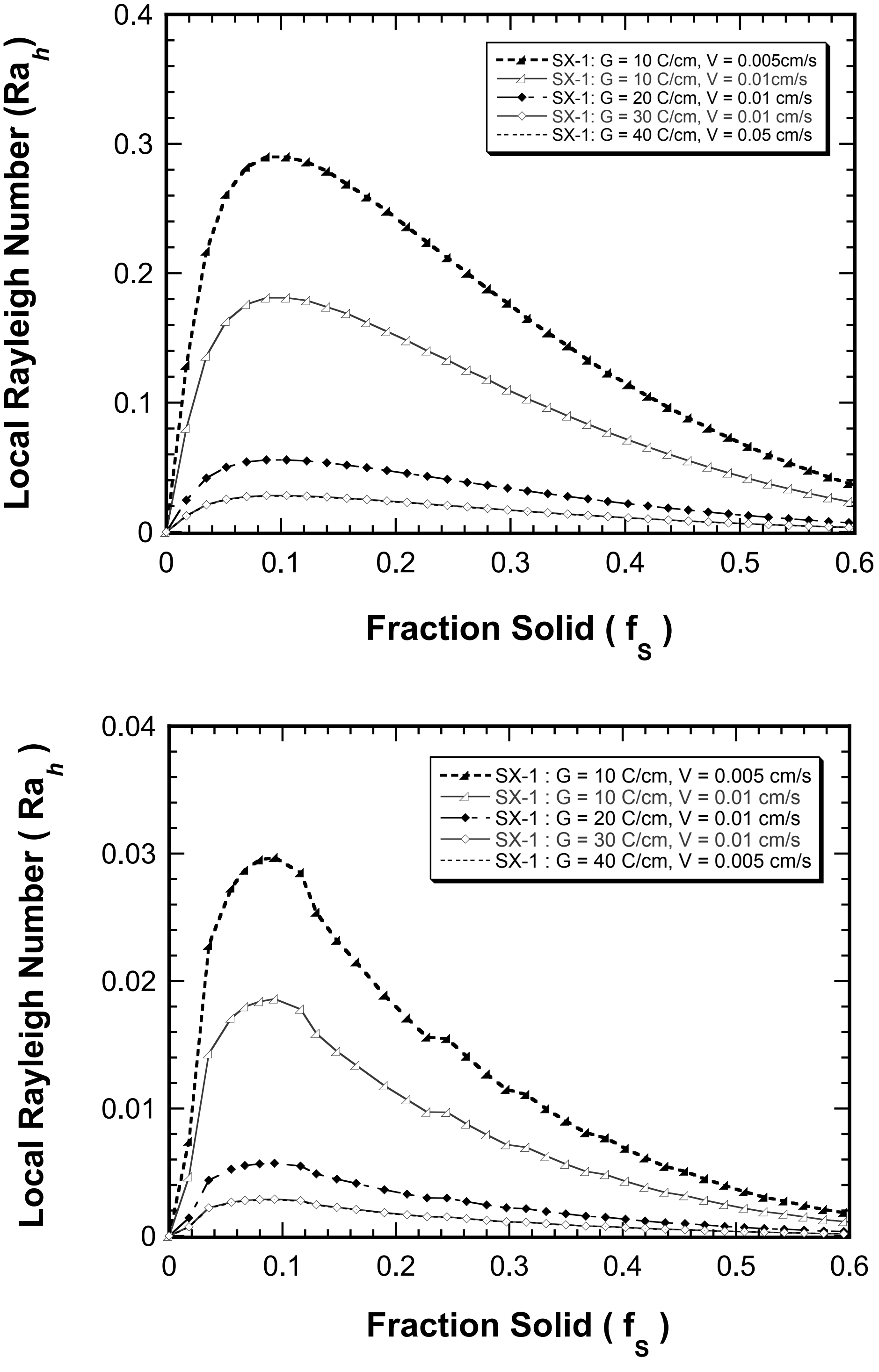

Figure 7.5 - Calculated Rayleigh Number for Alloy SX-1 at various experimental conditions of G and V with (a) liquid compositions determined by Equation 7.2 and (b) liquid compositions determined by CALPHAD simulation

In Figure 7.5a and b, it is shown that calculated Rayleigh values reach a maximum in the vicinity of 0.1 f_S regardless of thermal gradient and withdrawal rate, due to the increasing density gradient. This increase however, is soon overcome by a rapidly decreasing permeability. To illustrate the rapid reduction of permeability with volume fraction, Figure 7.6 shows corresponding permeabilities for the G and V pairings of calculated local Rayleigh values (Ra_h) of Figure 7.5 using Equation 7.13 and 7.14. As shown, permeability decreases quite rapidly up to 0.6 f_S and approaches very high numbers at zero fraction solid.

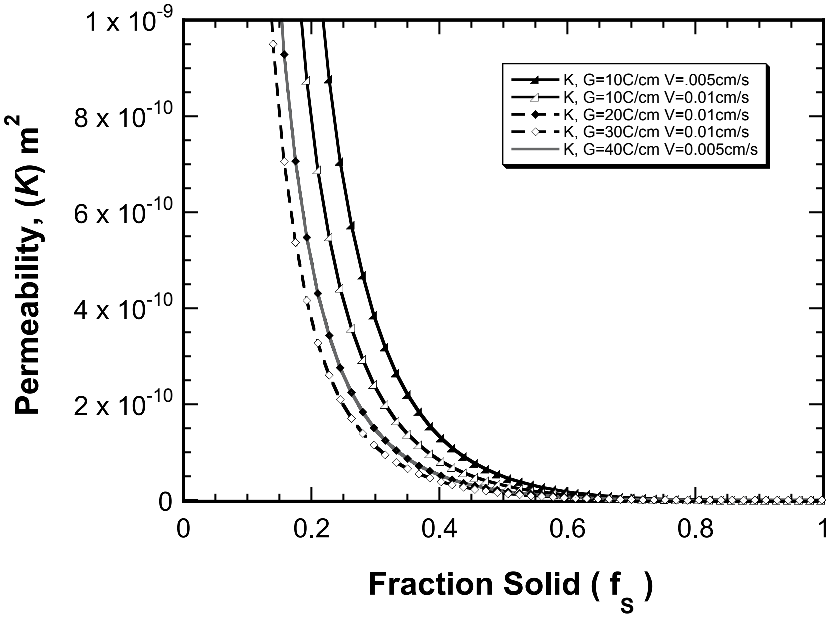

Figure 7.6 - General Trend for Permeability with increasing fraction solid in model alloy SX-1

With changes in G or V, the entire Ra_h curve scales upward or downward. Increases in thermal gradient scale Ra_h values down while increases in withdrawal rate also scale Ra_h provided G remains constant. Now that the basic effects of processing conditions, permeability and density gradient have been noted with regards to the calculation of a local Rayleigh value, Ra_h for the alloy systems considered in this thesis, René N4 and the

Ni-Al-W ternary are computed based on the permeabilities obtained in this investigation and then compared to resultant Rayleigh values using the above method.

Compositional variations in both René N4 and the model ternary were determined by PANDAT and ThermoCalc respectively and are shown in Figures 7.7 and 7.8.

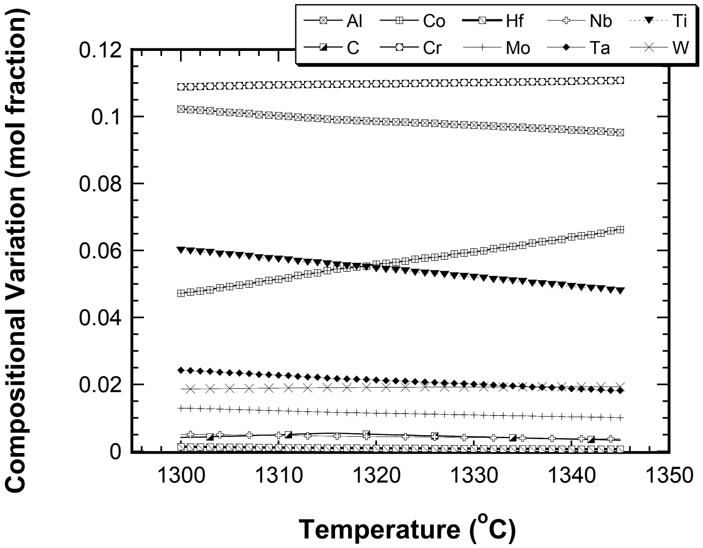

Figure 7.7 - Rene N4 Compositional Variation of Alloying Elements between Liquidus and Solidus Temperatures determined by PANDAT

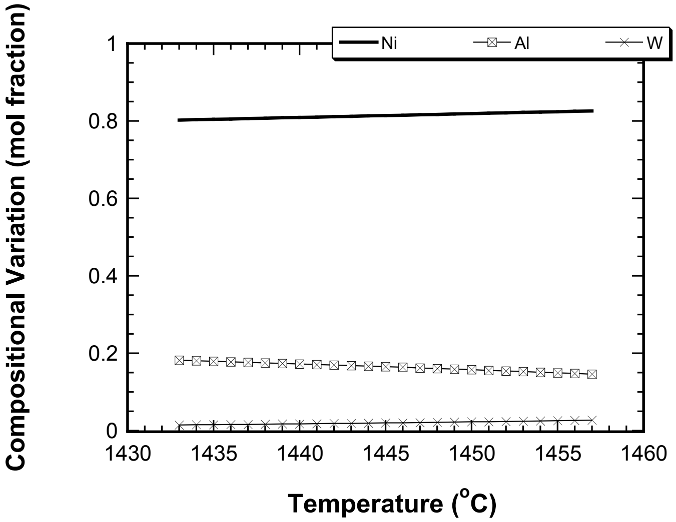

Figure 7.8 - Ni-Al-W Compositional Variation between Liquidus and Solidus Temperatures determined by ThermoCalc

Using these compositions, Rayleigh values based on the experimental permeabilities presented in Chapters 5 and 6 were computed in two manners. First, a temperature profile based upon the product of the $T_{liquidus}$ - $T_{solidus}$ temperature difference and the experimental thermal gradient was used for correlation of temperature specific densities at given heights. Secondly, a height based temperature profile was determined by fitting the $T_{liquidus}$ - $T_{solidus}$ thermal difference to the reconstruction height. Since such heights are shorter than predicted given their withdrawal rates and axial thermal gradients present during processing, significant non-axial heat extraction during casting is a likely explanation for the shortened mushy zone heights given that samples for this investigation were located within 1 – 7 mm of the external walls of the castings. For this reason, the second set of discrete local Ra_h calculations will be denoted as (non-axial ΔT). The former will be denoted as (axial ΔT). These curve fits, based on both sets of 3-D dendritic permeabilities are then compared to local Ra_h using conventional calculations of permeability as shown in Equations 7.13 and 7.14. The 3-D dendritic permeabilities (K_y and K_x) in both alloy systems are each compared to conventiaonally calculated Ra_h separately and will be discussed in pairs for the purposes of highlighting specific observations.

In René N4, the conventional Rayleigh number with K determined according to Equations 7.13 and 7.14 are compared to the Rayleigh number calculated by the 3-D dendritic vertical flow permeabilities, K_y, and the cross flow permeabilities, K_x, obtained in this study. This comparison is shown in Figures 7.9a and 7.9b respectively. In Figure 7.9a, it is shown that over the fraction solid investigated, vertical flow permeabilities do not influence the overall Rayleigh value, due to the fact that the cross flow permeabilities constrain the overall process, as apparent in Figure 7.7b. The axial ΔT Ra_h suggests a critical Rayleigh number approximately 25% lower than the conventional Ra_h with average permeability calculated with Equations 7.13 and 7.14. However the non-axial ΔT Ra_h predicts a critical Rayleigh number over 3 times higher than the conventional Ra_h.

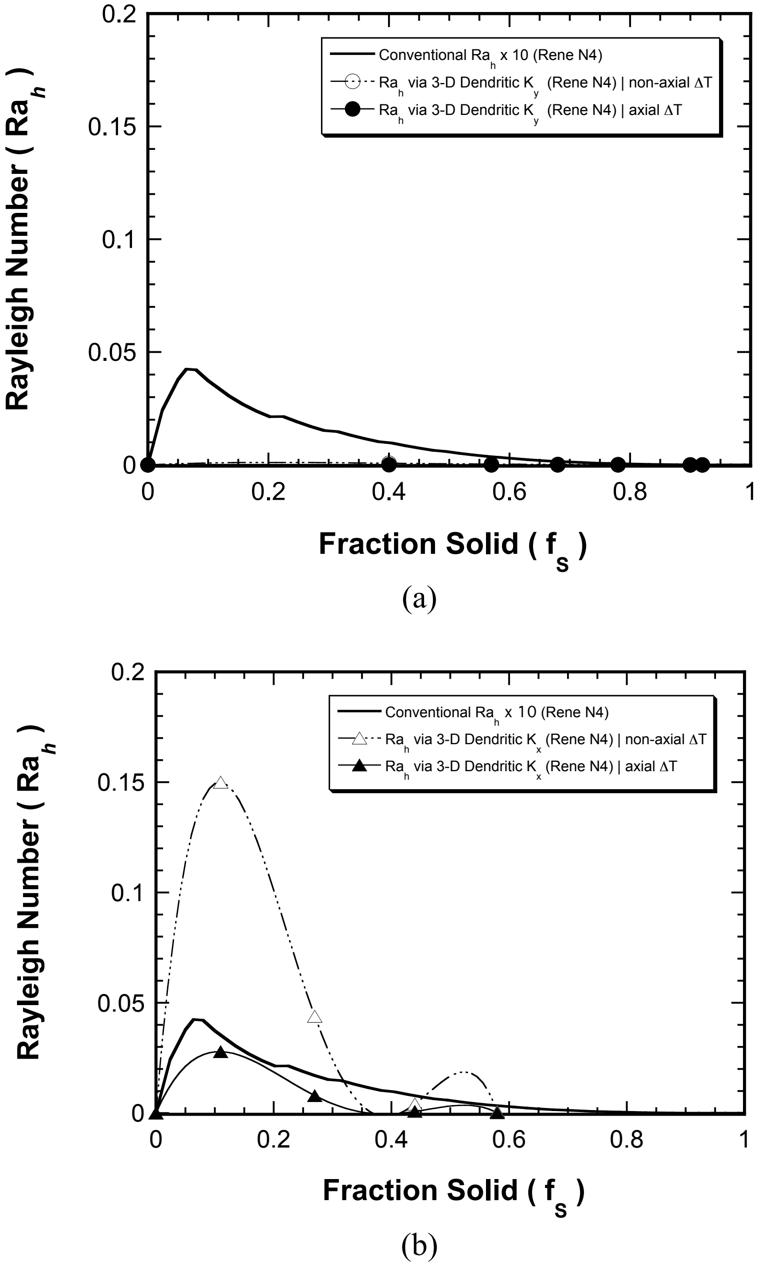

(a)

(b)

Figure 7.9 - Conventional Ra_h for René N4 as a function of solid fraction compared to Ra_h calculated by the (a) 3-D dendritic K_y obtained in the current study and (b) 3-D dendritic K_x obtained in the current study

In the Ni-Al-W system, the local Rayleigh number (Ra_h) with K determined by Equations 7.13 and 7.14 are again compared to Ra_h calculated by vertical flow permeabilities and cross flow permeabilities obtained in the current study. These comparisons are shown in Figures 7.10a and 7.10b respectively. Again, axial ΔT and non-axial ΔT curves correspond to density gradient calculations based upon thermal gradient and reconstruction height determined temperature profiles. In Figure 7.8a, it is shown that over the fraction solid investigated, vertical flow permeabilities approach the critical Rayleigh value anticipated by the conventional Ra_h but at higher volume fraction solid. The curve fit of the remaining data also suggests a slightly higher critical Ra_h than the traditional form at 0.25 f_S. In Figure 7.10b, two additional observations can be made. Direct permeability assessments of this study suggest a critical Ra_h 1.5 - 2X higher than the conventional Ra_h with K determined by Equations 7.13 and 7.14. A value 1.5X higher than the traditional Ra_h corresponds to the lowest direct K_x assessment by simulation while 2X higher than the traditional Ra_h corresponds to the highest point of the curve fit based on all higher fraction solid data. Secondly, direct permeability assessments indicate a much steeper decrease in Ra_h from the maximum value with increases in fraction solid than traditional Ra_h suggests.

Before describing global observations for Rayleigh calculations in both alloys, it should be stated the results of Ra_h determined by Ni-Al-W K_y values should be considered in more detail considering the unidirectional flow. It has previously been shown such flow cells were more accurately described by flow through an array of parallel cylindrical domains. These flow paths lacked the complexity in vertical flow most descriptive of typical dendritic networks.

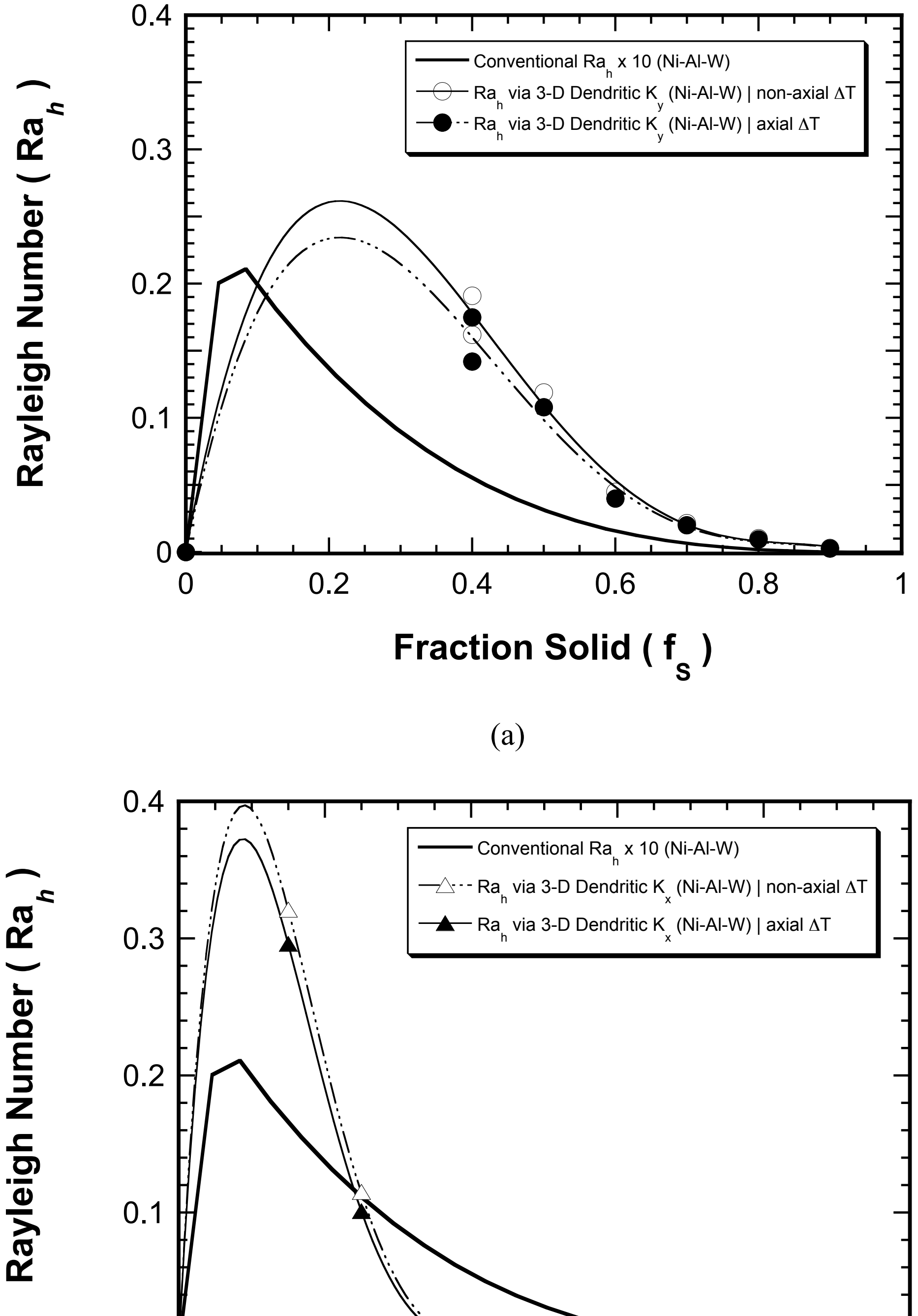

(a)

(b)

Figure 7.10 - Local Ra_h for Ni-Al-W as a function of solid fraction compared to Ra_h calculated by (a) K_y obtained in the current study and (b) K_x obtained in the current study

Overall, Rayleigh numbers determined with input from this new 3-D approach compared to conventional Ra_h calculations differ in one significant way. Permeabilities of the current study have been directly determined by simulation within 3D microstructural domains while conventional Ra_h approximations utilize average permeability values based on empirical relationships such as the Kozeny-Carmen, Blake-Kozeny or specifically, those shown in Equations 7.13 and 7.14. From this comparison, three key observations can be made: First, direct permeability assessment indicates vertical and cross flow permeabilities begin affecting the total Rayleigh values in a substantial way at volume fractions less than 0.3 f_S. This suggests, focusing future studies to volume fractions less than 0.3 f_S as the critical range for future investigations of permeability (K), and Rayleigh numbers (Ra_h). Secondly, non-axial thermal gradients, which indicate shortened mushy zone heights, predict higher local Rayleigh values than those calculated by use of an axial thermal gradient over the same microstructure. This in turn, results in higher Rayleigh values across volume fractions less than 0.3 f_S. This observation may provide explanation as to why freckles demonstrate a tremendous propensity to form on the surface. This observation holds particular importance to processes that involve significant amounts of heat extraction laterally such as Liquid Metal Cooling (LMC) processes. The findings of this thesis suggest these arrangements are likely subject to higher Rayleigh values and increased propensity to freckles based on their ability to extract large amounts of heat laterally. Experience however, has shown LMC processes to produce very few freckles at a variety of withdrawal rates. Additional parameters produced by LMC such as the finer arrangement of primary arms may supersede the local thermal fluctuations anticipated in the analysis here and would be worth further investigation. Thirdly, direct calculations of Ra_h using 3-D dendritic permeabilities, indicate maximum Rayleigh values on the order of 1.5 to 3 times higher than those of the conventional Ra_h calculation based upon averaged permeability. These observations indicate cross flow can likely be considered the determining permeability for assessment of the critical Ra_h value as suggested by Roper et al. [147, 148]. Multiple observations support the notion that limitation of permeability in the 0.10 f_S range is most likely dominated by cross flow. Mesh domains for vertical flow at or below 0.10 f_S encapsulating significant portions of dendritic structure were unattainable from reconstructed datasets. Furthermore, in a physical sense, at these heights flow is essentially occurring at and above dendrite tips. In these instances, cross flow is understandably influenced by dendritic solid while vertical flow does not interact with sufficient amounts of dendritic structure to affect flow resistance.

7.4 IMPLICATIONS FOR DEFECT FORMATION CRITERIA

7.4.1 Permeability

This research has demonstrated that direct assessments of permeability based on actual dendritic morphologies can be used for improved assessment of the Rayleigh number (Ra_h). In this study, 3-D datasets of René N4 a model Ni-6.5Al-9.5W (wt%) ternary alloy were used to directly calculate vertical and cross flow permeabilities (K_y and K_x, respectively). Permeabilities suggest higher Rayleigh numbers in the mushy zone compared to previous assessments produced by conventional permeability approximations, such as those given in Equations 7.13 and 7.14. Additionally, it has been shown that permeability scales inversely with interfacial surface area. In an effort to relate this behavior to practical defect prediction, the correspondence of K, and ISA are now related to fraction liquid (f_L) based on results from all simulations of this thesis. To consider the role of alloying, dimensionless permeability across all volume fractions, S_V^2 and S_{VS}^2 are considered in the following comparisons.

Figure 7.9 illustrates the dependence of dimensionless permeability (KS_V^2) and (KS_{VS}^2) on fraction liquid. S_V is the interfacial surface area per unit volume while S_{VS} is the interfacial surface area per unit volume solid. `

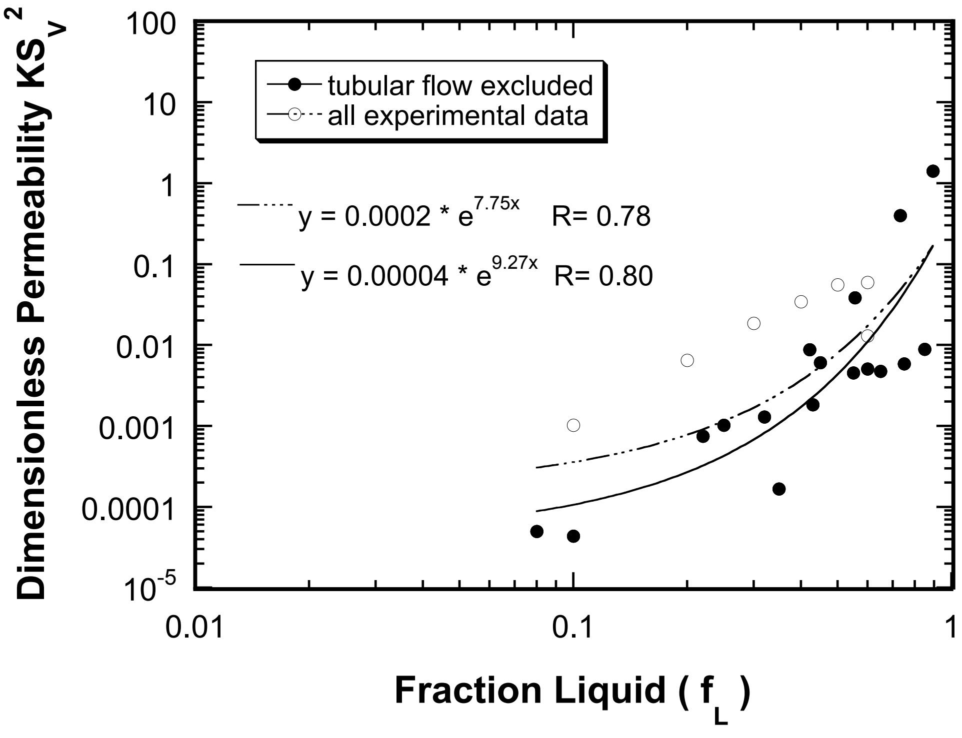

(a)

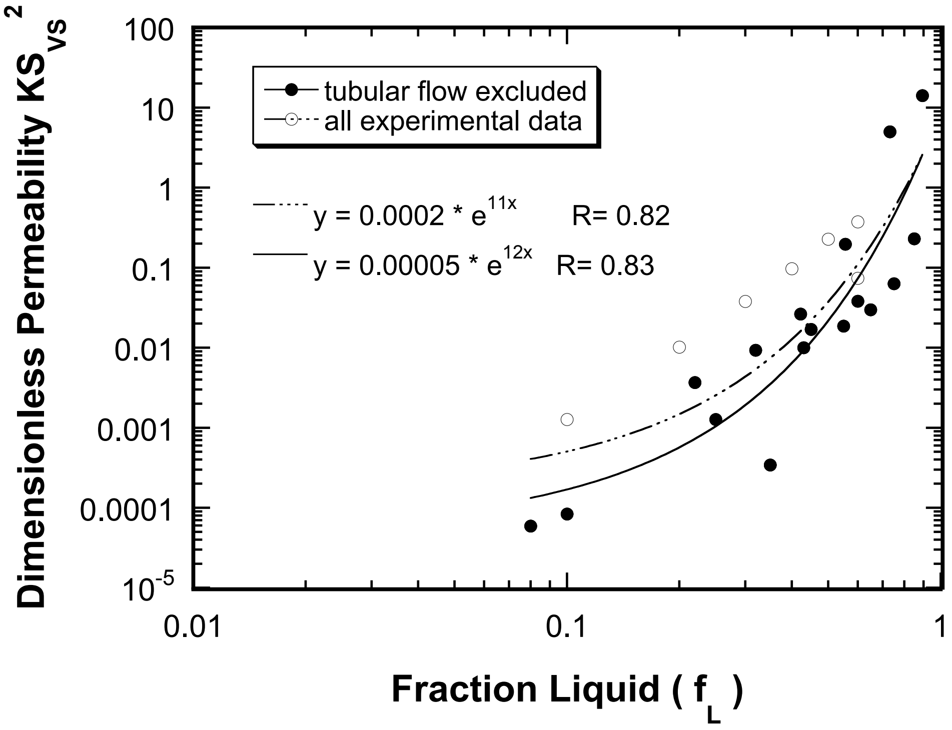

(b)

Figure 7.11 - Dimensionaless Permeabilities (a) KS_V^2 and (b) KS_{VS}^2 dependence on Fraction Liquid

In Figures 7.11a and 7.11b, two trendlines are shown in each plot, providing curve fits for all experimental permeabilities of this study with and without tubular flow cases in the Ni-Al-W system. Curve fits are slightly better for KS_{VS}^2 as a function of fraction liquid as compared to KS_V^2 as indicated by the associated "R" values of each. This slight improvement is due to decreased variance in KS_{VS}^2 at higher fraction liquid levels. This is particularly noteworthy as the critical Rayleigh value has been shown to occur in the range $0.05 < f_L < 0.2$. Since S_V is implicitly considered in many permeability models, it is worth considering how the presently measured values would influence these models and the approximations that are typically employed regarding permeability.

Figures 7.10a and 7.10b illustrate the variation of KS_V^2 and KS_{VS}^2 with the quantity $f_L^3/(1-f_L)^2$, present in the Kozeny relationship shown in Equation 2.9. Again, the quality of the curve fit for permeability scaled by ISA per unit volume solid, KS_{VS}^2 is slightly better than that of ISA per unit volume, KS_V^2. While the empirical ratio of $f_L^3/(1-f_L)^2$, derived from Kozeny's seminal work, reasonably approximates the increase in permeability, a variation up to 2 orders of magnitude at a given volume fraction must be accepted even with accurate assessments of S_V or S_{VS} across the full range of fraction liquid. Additionally, only when dimensionless permeability is combined with the value S_{VS}^2 does the dependence with the empirical liquid ratio approach a power law exponent of 1 for the directly assessed local permeabilities of this study.

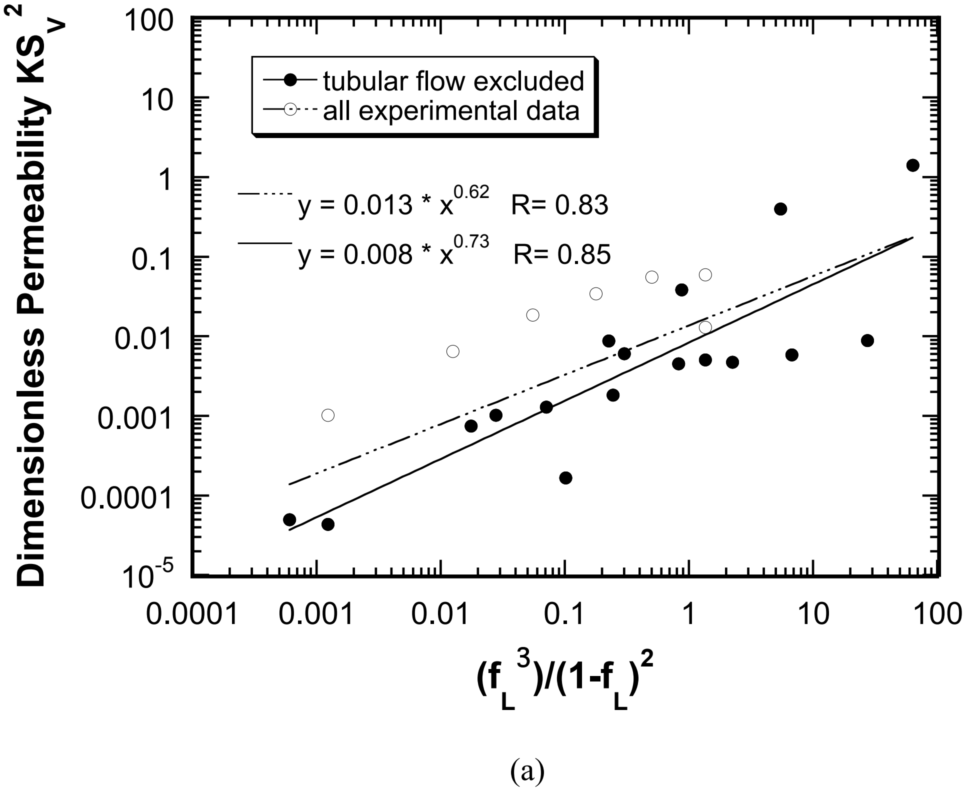

(a)

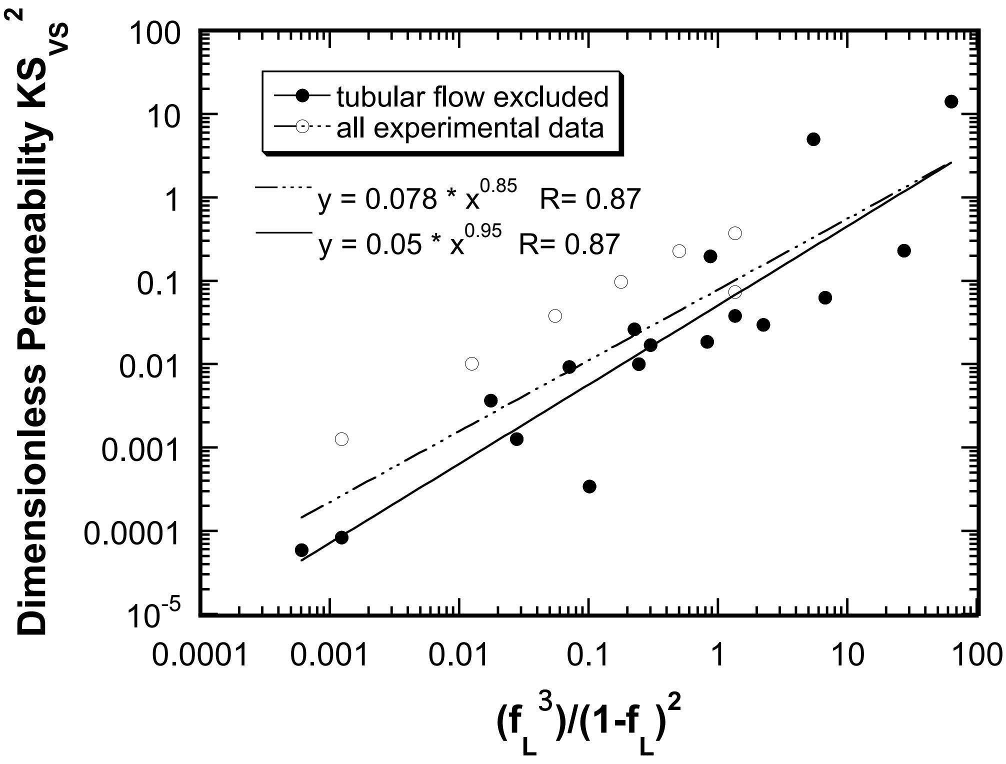

(b)

Figure 7.12 - Dimensionless Permeabilities (a) scaled by the ISA/unit volume squared KS_V^2, and (b) scaled by the ISA/unit volume solid squared, KS_{VS}^2, and their dependence on Fraction Liquid Ratio $(f_L^3)/(1-f_L)^2$

The results of this thesis suggest that permeability is best determined by accurate assessment of the local interfacial surface area and the local flow behavior through the three-dimensional domain. If this information is not available, the liquid ratio utilized in most empirical models, $f_L^3/(1-f_L)^2$, can yield a useful estimate of permeability provided a reasonable measure of the interfacial surface area per unit volume solid (S_{VS}) is known. Regardless of volume fraction profile, the maximum S_V occurs at or near 0.60 f_L. For practicality, S_{VS} can be observed in quenching studies in the range of 0.55 - 0.65 f_L for investigation of maximum S_V. Extrapolation of the decrease in S_V toward zero fraction liquid and alternatively, toward 1.0 fraction solid based on the trends illustrated in Figure 6.15 and 7.16. Additionally, maximum S_{VS} has been shown to have a magnitude roughly equivalent to 3 × S_{VMAX}. The decrease in S_{VS} can also be approximated at high fraction solid by its near convergence with S_V at fraction solid equal to 0.8 or greater.

7.4.2 Remaining Uncertainties in Ra_h

In the systems investigated, Rayleigh values do not exceed 1 with conventional or 3-D dendritic array permeabilities, suggesting instabilities should not occur in either alloy. However, as stated in Section 3.1, freckles have been observed. This suggests errors in other terms in the Rayleigh analysis. Among the uncertainties are the density gradient ($\Delta\rho/\rho_o$), the kinematic viscosity (α) and the thermal diffusivity (ν). The density gradient has multiple related uncertainties that are somewhat difficult to directly quantify. These include uncertainties in the compositional predictions of phase calculation software as well as the partial molar volume equations used to calculate the specific density at local temperatures. While use of partial molar volumes for density calculations have been shown to be accurate to within 5% [130, 132], a larger error may arise due to uncertainty in the liquid composition. The accuracy of phase calculation software is limited by the database used and can vary substantially for unexplored compositions as well as in select commercial nickel-base superalloys which have been investigated up to significant amounts of alloying elements. As such, it is plausible to estimate an order of magnitude error in density gradient values based on analysis of composition. Since ($\Delta\rho/\rho_o$) is directly proportional to Ra_h, such an increase in density gradient would affect a factor of 10 increase in the local Rayleigh number. The kinematic viscosity and thermal diffusivity are maintained as constants and are, as a product, considered equal to the value $5\times10^{-12}m^4/s^2$. Since this is a consistent approximation utilized by various investigators, no uncertainty between the results of this and other investigations are introduced by its use. However, it is very unlikely kinematic viscosity, thermal diffusivity, or their product, remain constant over the entire liquidus to solidus temperature range for a given alloy. Without validation of both properties as a function of temperature and composition, it is practically impossible to assert their true values. From available data on commercial nickel-base superalloys, the aforementioned approximation is a reasonable order of magnitude estimate. However, the absence of variation with temperature or composition is likely to have an uncertainty on the order of ± 5% for each value. Since $(\alpha\nu)$ is inversely proportional to Ra_h, a 25% decrease in the product of the thermal diffusivity and kinematic viscosity would produce a 25% increase in the local Rayleigh value. It is therefore also reasonable to assert the greatest amount of error in the current Rayleigh calculations likely resides in this quantity or the actual density gradient.

7.5 CONCLUSIONS

1. A combined experimental and computational protocol for 3D reconstruction and flow modeling through experimentally established dendritic networks has been developed and demonstrated in two alloys; the second generation commercial nickel-base superalloy, René N4, and a model ternary of Ni-6.5Al-9.5W (wt%).

2. In three-dimensional reconstructions in both alloy systems, interfacial surface area (ISA) per unit volume, (S_V) reaches a maximum at $f_s = 0.65$ independent of fraction solid profile with respect to height. Furthermore, maximum ISA per unit volume solid (S_{VS}) has a maximum magnitude roughly 3 × maximum S_V

3. Interfacial surface area per unit volume, (S_V) varies inversely with permeability for both vertical and cross-flow with slightly less sensitivity than previously reported. For cases in which a uni-directional dominance of flow channels is observed, S_V dependence on permeability is significantly lessened.

4. In vertical flow cells with a uniform velocity inlet, high velocity channels occur with spacing on the order of the primary dendrite arms (PDAS), but rapidly increase to 3 – 4×PDAS at higher liquid fraction levels due to flow paths dictated by the dendritic structure.

5. Average tortuosity (T_{avg}), has been measured in all vertical and lateral flow simulation cells and varies inversely with S_V for vertical flow through typical dendritic structures but is largely unaffected for wide ranges of S_V for cross flow.

6. Increases in S_V coincide with minor increases in T_{avg} while similar increases in S_V correspond with significant decreases in permeability (K) of equivalent magnitude order. Therefore microstructures that increase ISA can expect decreases in K and greater flow resistance in the mushy zone.

7. Calculation of local Rayleigh number (Ra_h) based on direct permeability assessments, suggest cross flow permeabilities (K_x) may maximize Ra_h value. Furthermore, 3D dendritic permeability obtained in this thesis yield critical Ra_h 1.5 to 3× higher than conventional Ra_h calculations using average permeabilities.

8. Rayleigh calculations performed with discrete permeabilities obtained in this thesis also show higher local Rayleigh values across nearly all fraction solid when significant heat extraction occurs laterally in addition to axially.

9. In lieu of direct assessment, permeability in vertical or cross flow within directionally solidified dendritic structures can effectively be approximated by the following relation; $K = f_L^3 / S_{VS}^2 (1 - f_L)^2$ where f_L is the fraction liquid, and S_{VS} is the interfacial surface area per unit volume solid. However, variability up to 2 orders of magnitude for a given volume fraction is likely with the use of this relationship.

CHAPTER 8

RECOMMENDATIONS FOR FUTURE WORK

8.1 APPLICABILITY OF THREE-DIMENSIONAL RECONSTRUCTION IN MATERIALS STUDIES

In this thesis, three-dimensional reconstructions at the solid-liquid interface within single crystals of two nickel-base superalloy were created by serial-sectioning. The automated sectioning system; RoboMET.3D, was used to polish and acquire images while the Interactive Data Language (IDL™) and Adobe Photoshop™ were used to post-process all micrographs. Three-dimensional reconstructions were then generated and rendered in IDL™. Volume meshes for fluid flow simulation in FLUENT™ were then generated directly from reconstruction data. Initial reconstruction in IDL™ allowed for characterization of dendritic structures while flow simulations provided for direct assessment of local permeability and microstructural effects on flow behavior. While the dependence of permeability on dendritic structures was evaluated and the implications for defect criteria have been considered. This thesis also indicates a growing opportunity for collaboration between experimental and computational materials science and engineering.

Experimental and computational materials investigations have long been influenced by one another in terms of the problems approached, the comparisons made and the information sought by each. However, it can be argued that both fields have developed largely independent of one another in terms of methods, underlying assumptions and length-scales of observation. Many of these variations are due to practical limitations of experimental methodology and computational domain. However, in recent years, an increasing numbers of materials investigations are directly linking experimental data with computational approaches [149-151]. Whether experimental results are used as direct inputs for simulation models as illustrated in this thesis, or computational results promote identification and investigation of alloy compositions, as evident in phase-modeling software such as; ThermoCalc, Pandat and ChemSage, the synergies between both fields are apparent.

Three-dimensional reconstructions present an opportunity to gain greater physical insight to solidification phenomena. It should be mentioned that regardless of method employed, the time and resources required in reconstruction efforts require techniques for data collection and image segmentation receive greater amounts of development before such methods can be used practically as diagnostic tools. However, for cases in which an accurate understanding of features and morphology are unattainable by two-dimensional methods, the benefits of a three-dimensional understanding should not be underestimated. Therefore, for current 3D reconstruction efforts in solidification studies to be effective, they must have impact broad enough to inform mechanical behavior estimates and predictive models. This has been shown in many recent studies [152-164]. Specific suggestions for further studies, capitalizing on the results of this thesis will be provided in the following section.

8.2 SUGGESTED SUBSEQUENT STUDIES

The following suggestions include investigations within and beyond the scope of the topics addressed in this thesis. The following suggested areas for further investigation can be categorized into two groups. The first three suggestions concern further experimental and modeling work based directly upon the protocols developed in this thesis. The remaining two suggestions address the broader issue of predicting defect formation during solidification.

8.2.1 Casting Experiments

It may prove useful to revisit the current experiments while refining the experimental approach in the following ways; 1) Utilize smaller cross-sectional castings, for the purposes of decreasing the variability in resultant microstructure due to thermal gradient differentials throughout larger cross-section samples. 2) Increase the number of experimental castings in a single run to introduce redundancy in experimentation by using multi-bar molds. This would serve dual purposes in achieving smaller-cross-sectional castings with equivalent raw material, while providing "companion" samples representing multiple equivalent castings from the same run. In this way, multiple bars could be decanted at various heights and/or time, while allowing one or more bars to solidify undisturbed for microstructural analysis and comparison with decanted samples. 3) Utilize thermocouples in casting experiments for direct measurement of temperature variation and direct correlation of thermal gradient at the height of decanting and throughout the mold. Should combining decanting and thermocouples prove impractical, thermocouple use within a non-decanting "companion" sample may prove equally useful. This suggestion does not necessitate a variation in methodology beyond the initial materials processing. However, the information it would provide could increase understanding regarding the full effects of the decanting process and any variation in microstructure unidentifiable through exclusive investigation of the post-mortem decanted dendritic structures.

8.2.2 Microstructural Evolution with Time or Thermal Gradient

A study of flow through dendritic networks as a function of time or thermal gradient may yield interesting results. Taking the dataset presented in this thesis as an initial condition, the dendritic structure can be evolved with time or thermal environment as has been performed in other metallic systems [103, 104, 123], and simulate flow through such structures at various time steps of evolution to address the effects of flow under conditions of coarsening or local dendrite arm spacing. While the dependence of K with S_V shows wide applicability for dendritic morphology, uni-directional flow has been observed to render better correlation with cross-sectional area. The transition point at which flow channel size and not S_V assumes dominance in permeability is unclear. Furthermore, changes caused by variation in curvature on local and global flow behavior may be equally interesting. Ideally, a study of this bearing would identify the effects of S_V, f_L, H_G or H_M on mean and local velocity and pressure fields. Such a study would also be able to identify or negate the existence of a critical value or morphology for which one metric becomes a more effective measure of global or local flow and or permeability.

8.2.3 Localized Domains

Thirdly, examination of smaller domains from within the documented microstructural volumes of the current thesis can provide ideal opportunity for introduction of variation in flow media properties such as; temperature, composition, density and viscosity. Such domains could be on the order of 400 × 400 × 400 μm or as large as possible to reasonably introduce compositional variation in the liquid. A domain size 400 μm^3 is suggested to provide a cube with a cross-sectional area encompassing the primary dendrite arm spacing in both dimensions. The findings of the current study can be used to indicate velocity and pressure fields to serve as boundary conditions for more localized simulation cases. Such cases could be used to further understand the distribution of pressure and stresses imposed upon solid material and the conditions necessary for fracture and transport of solid material. Variation in temperature can be treated individually or coupled with density and viscosity differences while variation in composition could be imposed in the liquid medium as well as the solid to more accurately reflect segregation and constitutional supercooling in the solidification event.

8.2.4 Composition Specific Density Gradient

A discussion of uncertainties associated with calculation of the local Rayleigh value was given in Section 7.4.2. In it, error associated with the density gradient specific to phase calculation software and composition predictions were given. Conversely, atomistic modeling has seen significant measures of success in determining the partial molar volumes for density approximation in the completely liquid regime [133]. It would be tremendously useful if atomistic models could begin to treat compositional variations for density prediction as the thermal change between the solidus and liquidus range is accompanied by significant compositional variation. Provided such densities are correlated to discrete temperatures, they would represent a significant advance in improving the accuracy of the Ra_h criterion and eliminate a noteworthy amount of uncertainty in conventional and advancing calculations of its value.

8.2.5 Investigation of Thermal Diffusivity and Kinematic Viscosity

To reduce further uncertainty in Ra_h calculations, it would be worthwhile to have thermal diffusivity and kinematic viscosities as functions of temperature and composition for nickel-base superalloys throughout the liquidus to solidus temperature range. Cherne [131] has investigated and reported viscosities for liquid nickel by molecular dynamics (MD) simulations. Additionally, Iiada and Guthrie [165] present viscosity and diffusivity data for individual liquid metals. However, to the knowledge of the author, very little work is publicly available detailing diffusivities or viscosities for nickel-base superalloys, particularly those undergoing solidification. While use of the conventional quantity $5\times10^{-12} m^4/s^2$ as the product of the two is useful in eliminating unnecessary variation between investigators, selection of its use completely independent of alloy lends a significant amount of uncertainty to the calculated value regardless of method. Actual values would eliminate the inherent uncertainty in the use of the estimated constant. Thermal diffusivity could be experimentally measured in various commercial nickel-base alloys by flash diffusivity [166-170] or with MD approaches as shown by Yang et al. [171]. Furthermore, MD protocols presented by Cherne and Deymier [131] or Alemany et al. [172] could be employed for viscosity calculation in commercial nickel-base superalloys for return as functions of composition and temperature.

REFERENCES

[1] Pollock, T. M. (1995). The growth and elevated temperature stability of high refractory nickel-base single crystals. *Mat. Sci. Eng. B*, *B32*, 255-266.

[2] Pollock, T. M., & Murphy, W. H. (1996). The Breakdown of Single-Crystal Solidification in High Refractory Nickel-Base Alloys. *Metallurgical and Materials Transactions A*, *27A*(4), 1081-1094.

[3] Decker, R. F., & Sims, C. T. (1972). The Metallurgy of Nickel-Base Alloys. In C. T. Sims, & W. C. Hagel (Eds.), *The Superalloys - Vital High Temperature Gas Turbine Materials for Aerospace and Industrial Power* (pp. 97-131). New York, NY: Wiley Interscience.

[4] Erickson, G. L. (1996). *The Development and Application of CMSX-10*. Paper presented at the Superalloys 1996, Warrendale, PA.

[5] Erickson, G. L., Sikkenga, S. L., Brentall, W. D., Aurrecoechea, J. M., & Kubarych, K. G. (1992). *Development of the Rhenium Containing Superalloys CMSX-4 & CM 186 LC for Single Crystal Blade and Directionally Solidified Vane Applications in Advanced Turbine Engines*. Paper presented at the Superalloys 1992, Warrendale, PA.

[6] Gell, M., Duhl, D. N., & Giamei, A. F. (1980). *The Development of Single Crystal Superalloy Turbine Blades*. Paper presented at the Superalloys 1980, Warrendale, PA.

[7] Ross, E. W., & O'Hara, K. S. (1996). *Rene N4: A First Generation Single Crystal Turbine Airfoil Alloy with Improved Oxidation Resistance, Low Angle Boundary Strength and Superior Long Time Rupture Strength*. Paper presented at the Superalloys 1996, Warrendale, PA.

[8] Tin, S. (2001). Carbon Additions and Grain Defect Formation In Directionally Solidified Nickel-Base Superalloys. *University of Michigan, Ph.D. Thesis,* 1-155.

[9] Walston, W. S., O'Hara, K. S., Ross, E. W., Pollock, T. M., & Murphy, W. H. (1996). *Rene N6: Third Generation Single Crystal Superalloy*. Paper presented at the Superalloys 1996, Warrendale, PA.

[10] Rowland, L. J. (2005). *Creep and Microstructural Stability of Ruthenium-Containing Nickel-Base Single Crystal Superalloys*. Ph.D. Thesis: Mat. Sci. & Engineering, University of Michigan, Ann Arbor.

[11] Pollock, T. M., & Tin, S. (2006). Nickel-Based Superalloys for Advanced Turbine Engines: Chemistry, Microstructure, and Properties. *Journal of Propulsion and Power*, *22*(2), 361-374.

[12] Davis, S. H. (2001). Binary Substances. In *Theory of Solidification* (pp. 42-45). Cambridge: Cambridge University Press.

[13] Kurz, W., & Fisher, D. J. (1998). Solute Redistribution. In *Fundamentals of Solidification* (pp. 117-130). Enfield, NH: Trans Tech Publications.

[14] Duhl, D. N. (1989). Single Crystal Superalloys. In J. K. Tien, & T. Caulfield (Eds.), *Superalloys, Supercomposites and Superceramics* (pp. 149-182). San Diego, CA: Academic Press, Inc.

[15] Versnyder, F. L., & Shank, M. E. (1970). The Development of Columnar Grain and Single Crystal High Temperature Materials Through Directional Solidification. *Mat. Sci. Eng. A*, *6*(4), 213-247.

[16] Versnyder, F. L., & Shank, M. E. (1979). Role of Directional Solidification. In E. F. Bradley (Ed.), *Source Book on Materials for Elevated-Temperature Applications* (pp. 334-368). Metals Park, OH: American Society for Metals.

[17] Elliott, A. J., Tin, S., King, W. T., Huang, S. C., Gigliotti, M. F. X., & Pollock, T. M. (2004). Directional Solidification of Large Superalloy Castings with Radiation and Liquid-Metal Cooling: A Comparative Assessment. *Metallurgical and Materials Transactions A*, *35A*, 3221-3231.

[18] Scheppe, F., Wagner, I., & Sahm, P. R. (2001). *Advancement of the Directional Solidification Process of a Ni-Al-W Alloy*. Paper presented at the Mat. Res. Soc. Symp, Boston, MA.

[19] Zhu, X., Shyam, A., Jones, J. W., Mayer, H., Lasecki, J. V., & Allison, J. E. (2006). Effects of Microstructure and Temperature on Fatigue Behavior of E319-T7 Cast Aluminum in Very Long Life Cycles. *Int. J. Fatigue*, *28*, 1566-1571.

[20] Osorio, W. R., Goulart, P. R., Santos, G. A., Moura Neto, C., & Garcia, A. (2006). Effect of Dendrite Arm Spacing on Mechanical Properties and Corrosion Resistance of Al 9 Wt Pct Si and Zn 27 Wt Pct Al Alloys. *Met. Trans. A*, *37A*(8), 2525-2538.

[21] Baldan, A. (1994). Effect of Secondary Dendrite Arm Spacing on the Section Size-Dependent Creep Strength of a Nickel-Base Superalloy. *J. Mat. Sci. Lettrs*, *13*, 734-737.

[22] Porter, D. A., & Easterling, K. E. (2001). Solidification. In *Phase Transformations in Metals and Alloys* (pp. 212-222). Cheltenham, UK: CRC Press.

[23] Flemings, M. C. (1974). Cellular Solidification. In *Solidification Processing* (pp. 58-90). McGraw-Hill, Inc.

[24] Kurz, W., & Fisher, D. J. (1998). Morphological Instability of a Solid/Liquid Interface. In *Fundamentals of Solidification* (pp. 48-52). Enfield, NH: Trans Tech Publications.

[25] Kurz, W., & Fisher, D. J. (1998). Solidification Microstructure: Cells and Dendrites. In *Fundamentals of Solidification* (pp. 80-87). Enfield, NH: Trans Tech Publications.

[26] Morris, L. R., & Winegard, W. C. (1969). The Cell To Dendrite Transition. *J. Crystal Growth*, *6*, 61-66.

[27] Huang, S. C., & Glicksman, M. E. (1981). Fundamentals of Dendritic Solidification-II. Development of Sidebranch Structure. *Acta Metallurgica*, *29*, 717-734.

[28] Bower, T. F., & Flemings, M. C. (1967). Structures of Dendrites at Chill Surfaces. *Trans. Met. Soc. AIME*, *239*, 1620-1625.

[29] Chopra, M. A., & Tewari, S. N. (1991). Growth-Speed Dependence of Primary Arm Spacings in Directionally Solidified Pb-10 Wt Pct Sn. *Metallurgical and Materials Transactions A*, *22A*(10), 2467-2474.

[30] Dougherty, A., Kaplan, P. D., & Gollub, J. P. (1987). Development of Side Branching in Dendritic Crystal Growth. *Phys. Rev. Let*, *58*(16), 1652-1655.

[31] Klaren, C. M., Verhoeven, J. D., & Trivedi, R. (1980). Primary Dendrite Spacing of Lead Dendrites in Pb-Sn and Pb-Au Alloys. *Metallurgical and Materials Transactions A*, *11A*(11), 1853-1861.

[32] McCartney, D. G., & Hunt, J. D. (1981). Measurements of Cell and Primary Dendrite Arm Spacings in Directionally Solidified Aluminum Allloys. *Acta Metallurgica*, *29*, 1851-1863.

[33] Bouchard, D., & Kirkaldy, J. S. (1996). Scaling of Intragranular Dendritic Microsture in Ingot Solidification. *Metallurgical and Materials Transactions B*, *27B*, 101-113.

[34] Kurz, W., & Fisher, D. J. (1981). Dendrite Growth at the Limit of Stability: Tip Radius and Spacing. *Acta Metallurgica*, *29*, 11-20.

[35] Langer, J. S., & Muller-Krumbhaar, H. (1978). Theory of Dendritic Growth-I. Elements of a Stability Analysis. *Acta Metallurgica*, *26*, 1681-1687.

[36] Langer, J. S., & Muller-Krumbhaar, H. (1987). Theory of Dendritic Growth-III. Effects of Surface Tension. *Acta Metallurgica*, *26*, 1697-1708.

[37] Makkon, L. (1991). Primary dendrite spacing in constrained solidification. *Mat. Sci. Eng. A*, *A148*, 141-143.

[38] Pieters, R., & Langer, J. S. (1986). Noise-Driven Sidebranching in the Boundary-Layer Model of Dendritic Solidification. *Phys. Rev Lett*, *56*(18), 1948-1951.

[39] Li, Q., & Beckermann, C. (1998). Scaling behavior of three-dimensional dendrites. *Physical Review E*, *57*(3), 3176-3188.

[40] Glenn, A. M., Russo, S. P., & Paterson, P. J. K. (2003). The Effect of Grain Refining on Macrosegregation and Dendrite Arm Spacing of Direct Chill Cast AA5182. *Metallurgical and Materials Transactions A*, *34A*, 1513-1523.

[41] Grugel, R. N., & Zhou, Y. (1989). Primary Dendrite Spacing and the Effect of Off-Axis Heat Flow. *Metallurgical and Materials Transactions A*, *20A*, 969-973.

[42] Huang, S. C., & Glicksman, M. E. (1981). Fundamentals of Dendritic Solidification-I. Steady-State Tip Growth. *Acta Metallurgica*, *29*, 701-715.

[43] Somboonsuk, K., Mason, J. T., & Trivedi, R. (1984). Interdendritic Spacing: Part I. Experimental Studies. *Metallurgical Transactions A*, *15A*, 967-975.

[44] Trivedi, R. (1984). Interdendritic Spacing: Part II. A Comparison of Theory and Experiment. *Metallurgical Transactions A*, *15A*, 977-982.

[45] Vijayakumar, M., & Tewari, S. N. (1991). Dendrite spacings in directionally solidified superalloy PWA-1480. *Mat. Sci. Eng. A*, *A132*, 195-201.

[46] Flemings, M. C. (1974). Solidification of Castings and Ingots. In *Solidification Processing* (pp. 146-154). New York, NY: McGraw-Hill, Inc.

[47] Elliott, A. J. (2005). *Directional Solidification of Large Cross-Section Ni-Base Superalloy Castings via Liquid-Metal Cooling*. Ph.D. Thesis: Mat. Sci.& Engineering, University of Michigan, Ann Arbor, MI.

[48] Cole, G. S., & Cremisio, R. S. (1972). Solidification and Structure Control in Superalloys. In C. T. Sims, & W. C. Hagel(pp. 479-506). New York, NY: John Wiley & Sons.

[49] Copley, S. M., Giamei, A. F., Johnson, S. M., & Hornbecker, M. F. (1970). The Origin of Freckles in Unidirectionally Solidified Castings. *Metall. Trans*, *1*(A), 2193-2204.

[50] Giamei, A. F., & Kear, B. H. (1970). On the Nature of Freckles in Nickel Base Superalloys. *Metall. Trans*, *1*(A), 2185-2192.

[51] Pollock, T. M. Convective instability trails. *unpublished work*.

[52] Flemings, M. C. (1974). Fluid Flow. In *Solidification Processing* (pp. 214-258). New York, NY: McGraw-Hill Inc.

[53] Incropera, F. P., & DeWitt, D. P. (2002). *Fundamentals of Heat and Mass Transfer* (5th Ed.). New York, NY: John Wiley & Sons, Inc.

[54] Kou, S. (1996). Fluid Flow, Heat Transfer, and Mass Transfer: Similarities and Coupling. In *Transport Phenomena and Materials Processing* (pp. 298-299). New York, NY: John Wiley & Sons, Inc.

[55] Baumgartl, J., Budweiser, W., Muller, G., & Neumann, G. (1989). Studies of Buoyancy Driven Convection in a Vertical Cylinder with Parabolic Temperature Profile. *J. Crystal Growth*, *97*, 9-17.

[56] Beckermann, C., Gu, J. P., & Boettinger, W. J. (2000). Development of a Freckle Predictor via Rayleigh Number Method for Single-Crystal Nickel-Base Superalloy Casting. *Metallurgical and Materials Transactions A*, *31A*(10), 2545-2557.

[57] Bennon, W. D., & Incropera, F. P. (1987). A Continuum Model for Momentum, Heat and Species Transport in Binary Solid-Liquid Phase Chage Systems-II. Application to Solidification in a Rectangular Cavity. *Int. J. Heat Mass Transfer*, *30*(10), 2171-2187.

[58] Heinrich, J. C., Felicelli, S., Nandapurkar, P., & Poirier, D. R. (1989). Thermosolutal Convection during Dendritic Solidification of Alloys: Part II. Nonlinear Convection. *Metallurgical Transactions B*, *20B*, 883-891.

[59] Motakef, S. (1990). Interference of Buoyancy-Induced Convection with Segregation During Directional Solidification: Scaling Laws. *J. Crystal Growth*, *102*, 197-213.

[60] Muller, G., Neumann, G., & Matz, H. (1987). A Two-Rayleigh Number Model of Buoyancy-Driven Convection in Vertical Melt Growth Configurations. *J. Crystal Growth*, *84*, 36-49.

[61] Nield, D. A. (1967). The Thermohaline Rayleigh-Jeffreys Problem. *J. Fluid Mech*, *29*(3), 545-558.

[62] Ramirez, J. C., & Beckermann, C. (2003). Evaluation of a Rayleigh-Number-Based Freckle Criterion for Pb-Sn Alloys and Ni-Base Superalloys. *Metallurgical and Materials Transactions A*, *34A*(7), 1525-1536.

[63] Sarazin, J. R., & Hellawell, A. (1988). Channel Formation in Pb-Sn, Pb-Sb, and Pb-Sn-Sb Alloy Ingots and Comparison with the System NH4Cl-H20. *Metallurgical Transactions A*, *19A*, 1861-1871.

[64] Stewart, M. J., & Weinberg, F. (1972). Fluid Flow in Liquid Metals. *J. Crystal Growth*, *12*, 217-227.

[65] Tin, S., & Pollock, T. M. (2003). Stabilization of Thermosolutal Convective Instabilities in Ni-Based Single-Crystal Superalloys: Carbide Precipitation and Rayleigh Numbers. *Metallurgical and Materials Transactions A*, *34A*, 1953-1967.

[66] Tin, S., & Pollock, T. M. (2004). Predicting Freckle Formation in Single Crystal Ni-Base Superalloy. *Journal of Materials Science*, *39*, 7199-7205.

[67] Worster, M. G. (1992). Instabilities of the Liquid and Mushy Regions During Solidification of Alloys. *J. Fluid Mech*, *237*, 649-669.

[68] Yang, W., Chen, W., Chang, K., Mannan, S., & deBarbadillo, J. (2001). Freckle Criteria for the Upward Directional Solidification of Alloys. *Metallurgical and Materials Transactions A*, *32A*, 397-406.

[69] Bear, J. (1972). The Fundamental Fluid Transport Equations in Porous Media. In *Dynamics of Fluid in Porous Media* (pp. 108-109). New York, NY: American Elsevier.

[70] Apelian, D., Flemings, M. C., & Mehrabian, R. (1974). Specific Permeability of Partially Solidified Dendritic Networks of Al-Si Alloys. *Met. Trans*, *5*, 2533-2537.

[71] Bhat, M. S., Poirier, D. R., & Heinrich, J. C. (1995). Permeability for Cross Flow Through Columnar-Dendritic Alloys. *Metallurgical and Materials Transactions B*, *26B*, 1049-1056.

[72] Ganesan, S., Chan, C. L., & Poirier, D. R. (1992). Permeability for flow parallel to primary dendrite arms. *Mat. Sci. Eng. A*, *A151*, 97-105.

[73] Mehrabian, R., Keane, M., & Flemings, M. C. (1970). Interdendritic Fluid Flow and Macrosegregation; Influence of Gravity. *Met. Trans*, *1*, 1209-1220.

[74] Murakami, K., & Okamoto, T. (1984). Fluid Flow in the Mushy Zone Composed of Granular Grains. *Acta Metallurgica*, *32*(10), 1741-1744.

[75] Murakami, K., Shiraishi, A., & Okamoto, T. (1984). Fluid Flow In Interdendritic Space In Cubic Alloys. *Acta Metallurgica*, *32*(9), 1423-1428.

[76] Nasser-Rafi, R., Deshmukh, R., & Poirier, D. R. (1985). Flow of Interdendritic Liquid and Permeability in Pb-20 wt Pct Sn Alloys. *Met. Trans. A*, *16A*, 2263-2271.

[77] Piwonka, T. S., & Flemings, M. C. (1966). Pore Formation in Solidification. *Trans. Met. Soc. AIME*, *236*, 1157-1165.

[78] Poirier, D. R. (1987). Permeability for Flow of Interdendritic Liquid in Columnar-Dendritic Alloys. *Met. Trans. B*, *18B*, 245-255.

[79] Streat, N., & Weinberg, F. (1974). Macrosegregation During Solidification Resulting From Density Differences in the Liquid. *Met. Trans*, *1974*, 2539-2548.

[80] Streat, N., & Weinberg, F. (1976). Interdendritic Fluid Flow in a Lead-Tin Alloy. *Met. Trans. B*, *7B*, 417-423.

[81] Carman, P. C. (1956). *Flow of Gases Through Porous Media.* New York: Academic Press, Inc. Publishers.

[82] Geiger, G. H., & Poirier, D. R. (1973). *Transport Phenomena In Metallurgy.* Reading, MA: Addison-Wesley Publishing Company.

[83] Nielsen, O., Arnberg, L., Mo, A., & Thevik, H. (1999). Experimental Determination of Mushy Zone Permeability in Aluminum-Copper Alloys with Equiaxed Microstructures. *Metallurgical and Materials Transactions A*, *30A*, 2455-2462.

[84] Heinrich, J. C., & Poirier, D. R. (2004). Convection Modeling in Directional Solidification. *C.R. Mecanique*, *332*, 429-445.

[85] Forsman, O. (1918). Undersokning av rymdstrukturen hos ett kolstal av hypereutektoid sammansatning. *Jernkontorets Ann*, *102*, 1-30.

[86] Hillert, M. (1962). The Formation of Pearlite. In V. F. Zackay, & H. Aaronson (Eds.), *Decomposition of Austenite by Diffusional Processes* (pp. 197-247). New York, NY: Wiley Interscience.

[87] Hull, D. A., McCammond, D., Hoeppner, D. W., & Hellier, W. G. (1991). Titanium Prior-Beta Grain Volume Distribution by Quantitative Serial Sectioning Techniques. *Materials Characterization*, *26*, 63-71.

[88] Mangan, M. A., & Shiflet, G. J. (1994). *Three-Dimensional Reconstructions of Pearlite Colonies*. Paper presented at the Solid-Solid Phase Transformations, Warrendale, PA.

[89] Mangan, M. A., Lauren, P. D., & Shiflet, G. J. (1997). Three-dimensional reconstruction of Widmanstätten plates in Fe-12.3Mn0.8C. *Journal of Microscopy*, *188*(1), 36-41.

[90] Mangan, M. A., & Shiflet, G. J. (1997). Three Dimensional Investigation of Cu-Ti Discontinuous Precipitation. *Scripta. Mat*, *37*(4), 517-522.

[91] Herman, G. T., Zheng, J., & Bucholtz, C. A. (1992). Shape-based Interpolation. *IEEE Comp. Graph. Appl*, *12*(3), 69-79.

[92] Raya, S. P., & Udupa, J. K. (1990). Shape-Based Interpolation of Multidimensional Objects. *IEEE Trans. Medical Imaging*, *9*(1), 32-42.

[93] Kral, M. V., & Spanos, G. (1997). Three Dimensional Morphology of Cementite Precipitates. *Scripta. Mat*, *36*(8), 875-882.

[94] Kral, M. V., & Spanos, G. (1999). Three-Dimensional Analysis of Proeutectoid Cementite Precipitates. *Acta Materialia*, *47*(2), 711 - 724.

[95] Hung, C. Y., Spanos, G., Rosenberg, R. O., & Kral, M. V. (2002). Three-dimensional observations of proeutectoid cementite precipitates at short isothermal transformation times. *Acta Materialia*, *50*, 3781-3788.

[96] Kral, M. V., Manga, M. A., Spanos, G., & Rosenberg, R. O. (2000). Three-dimensional analysis of microstructures. *Materials Characterization*, *45*, 17-23.

[97] Kral, M. V., & Spanos, G. (2003). Crystallography of grain boundary cementite dendrites. *Acta Materialia*, *51*(2), 301-311.

[98] Kral, M. V., & Spanos, G. (2005). Three-Dimensional Analysis and Classification of Grain Boundary-Nucleated Proeutectoid Ferrite Precipitates. *Metallurgical and Materials Transactions A*, *36A*(5), 1199-1207.

[99] Spanos, G., Wilson, A. W., & Kral, M. V. (2005). New Insights into the Widmanstatten Proeutectoid Ferrite Transformation: Integration of Crystallographic and Three-Dimensional Morphological Observations. *Metallurgical and Materials Transactions A*, *36A*(5), 1209-1218.

[100] Wolfsdorf, T. L., Bender, W. H., & Voorhees, P. W. (1997). The Morphology of High Volume Fraction Solid-Liquid Mixtures: An Application of Microstructural Tomography. *Acta Materialia*, *45*(6), 2279-2295.

[101] Alkemper, J., & Voorhees, P. (2001). Quantitative Serial Sectioning Analysis. *Journal of Microscopy*, *201*(3), 388-394.

[102] Kammer, D., Mendoza, R., & Voorhees, P. W. (2006). Cylindrical domain formation in topologically complex structures. *Scripta. Mat*, *55*, 17-22.

[103] Kammer, D., & Voorhees, P. W. (2006). The morphological evolution of dendritic microstructures during coarsening. *Acta Materialia*, *54*, 1549-1558.

[104] Mendoza, R., Alkemper, J., & Voorhees, P. (2003). The Morphological Evolution of Dendritic Microstructures during Coarsening. *Metallurgical and Materials Transactions A*, *34A*, 481-489.

[105] Spowart, J. E., Mullens, H. M., & Puchala, B. T. (2003). Collecting and Analyzing Microstructures in Three Dimensions: A Fully Automated Approach. *J. Mat*, *55*(10), 35-37.

[106] Maruyama, B., Spowart, J. E., Hooper, D. J., Mullens, H. M., Druma, A. M., Druma, C. et al. (2006). A new technique for obtaining three-dimensional structures in pitch-based carbon foams. *Scripta. Mat*, *54*, 1709-1713.

[107] Spowart, J. E. (2006). Automated serial sectioning for 3-D analysis of microstructures. *Scripta. Mat*, *55*, 5-10.

[108] Bhat, M. S., Poirier, D. R., Heinrich, J. C., & Nagelhout, D. (1994). Permeability Normal to Columar Dendrites at High Fraction Liquid. *Scripta. Met. et Mat*, *31*(3), 339-344.

[109] Felicelli, S. D., Poirier, D. R., & Heinrich, J. C. (1998). Modeling Freckle Formation in Three Dimensions during Solidification of Multicomponent Alloys. *Met. Trans. B*, *29B*, 847-855.

[110] Bernard, D., Nielsen, O., Salvo, L., & Cloetens, P. (2005). Permeability Assessment by 3D Interdendritic Flow Simulations on Microtomography Mappings of Al-Cu Alloys. *Mat. Sci. Eng. A*, *392*, 112-120.

[111] Fuloria, D., Lee, P. D., & Bernard, D. (2008). Microtomographic characterization of columnar Al-Cu dendrites for fluid flow and flow stress determination. *Mat. Sci. Eng. A*, *A494*, 3-9.

[112] Duncan, A. J., Han, Q., & Viswanathan, S. (1999). Measurement of Liquid Permeability in the Mushy Zones of Aluminum-Copper Alloys. *Metallurgical and Materials Transactions B*, *30B*, 745-750.

[113] Han, Q., Duncan, A. J., & Viswanathan, S. (2003). Permeability Measurements of the Flow of Interdendritic Liquid in Equiaxed Aluminum-Silicon Alloys. *Metallurgical and Materials Transactions B*, *34B*, 25-28.

[114] Poirier, D. R., & Ganesan, S. (1992). Permeabilities for flow of interdendritic liquid in equiaxial structures. *Mat. Sci. Eng. A*, *A157*, 113-123.

[115] Poirier, D. R., & Ocansey, P. (1993). Permeability for flow of liquid through equiaxial mushy zones. *Mat. Sci. Eng. A*, *A171*, 231-240.

[116] Elliott, A. J., Karney, G. B., Gigliotti, M. F. X., & Pollock, T. M. (2004). Issues in Processing By the Liquid-Sn Assisted Directional Solidification Technique. In K. A. Green, T. M. Pollock, H. Harada, T. E. Howson, R. C. Reed, J. J. Schirra, & S. Walston (Eds.), *Superalloys 2004* (pp. 421-430). Warrendale, PA: The Minerals, Metals & Materials Society.

[117] Elliott, A. J., & Pollock, T. M. (2007). Thermal Analysis of the Bridgman and Liquid-Metal-Cooled Directional Solidification Investment Casting Processes. *Met. Trans. A*, *38*(4), 871-882.

[118] Carlbom, I., Terzopoulos, D., & Harris, K. M. (1994). *Computer-Assisted Registration, Segmentation, and 3D Reconstruction from Images of Neuronal Tissue Sections*. Paper presented at the IEEE Trans. Medical Imaging.

[119] Chawla, N., & Ganesh, V. V. (2005). Three-Dimensional (3D) Microstructure Visualization and Finite Element Modeling of the Mechanical Behavior of Heterogeneous Materials. *Microsc. Microanal*, *11*(Suppl 2), 1642-1643.

[120] Leung, C., & Lovell, B. C. (2003). *3D Reconstruction Through Segmentation of Multi-View Image Sequences*. Paper presented at the Workshop on Digital Image Computing, Brisbane.

[121] Wolf, I., Eid, A., Vetter, M., Hassenpflug, P., & Meinzer, H. P. (2003). *Extension of 2D segmentation methods into 3D by means of Coons-patch interpolation*. Paper presented at the Proceedings of SPIE.

[122] Rowenhorst, D. J., Gupta, A., Feng, C. R., & Spanos, G. (2006). 3D Crystallographic and morphological analysis of coarse martensite: Combining EBSD and serial sectioning. *Scripta. Mat*, *55*, 11-16.

[123] Rowenhorst, D. J., Kuang, J. P., Thornton, K., & Voorhees, P. (2006). Three-Dimensional Analysis of Particle Coarsening in High Volume Fraction Solid-Liquid Mixtures. *Acta Mat*, *54*, 2027-2039.

[124] Spanos, G., Rowenhorst, D. J., Lewis, A. C., & Geltmacher, A. B. (2008). Combining Serial Sectioning, EBSD Analysis, and Image-Based Finite Element Modeling. *MRS Bulletin*, *33*, 597-602.

[125] Wojnar, L., Kurzydlowski, K. J., & Szala, J. (2004). Quantitative Image Analysis. In G. F. Vander Voort (Ed.), *ASM Handbook Volume 9* (pp. 403 - 427). Materials Park, OH: ASM International.

[126] Alkemper, J., & Voorhees, P. W. (2001). Three-Dimensional Characterization of Dendritic Microstructures. *Acta Mat*, *49*, 897-902.

[127] Genau, A. L., Voorhees, P., & Thornton, K. (2009). The morphology of topologically complex interfaces. *Scripta Materialia*, *60*, 301-304.

[128] Kammer, D., & Voorhees, P. W. (2008). Analysis of Complex Microstructures: Serial Sectioning and Phase-Field Simulations. *MRS Bulletin*, *33*, 603-610.

[129] Kou, S. (1996). Introduction to Fluid Flow. In *Transport Phenomena and Materials Processing* (pp. 53-57). New York, NY: John Wiley & Sons, Inc.

[130] Mukai, K., Li, Z., & Mills, K. C. (2005). Prediction of the Densities of Liquid Ni-Based Superalloys. *Metallurgical and Materials Transactions B*, *36B*, 255-262.

[131] Cherne III, F. J., & Deymier, P. A. (1998). Calculation of Viscosity of Liquid Nickel by Molecular Dynamics Methods. *Acta Mat*, *39*(11), 1613-1616.

[132] Sung, P. K., Poirier, D. R., & McBride, E. (1997). Estimating densities of liquid transition-metals and Ni-base superalloys. *Materials Science and Engineering A*, *231*, 189-197.

[133] Asta, M., Trinkle, D., & Woodward, C. (2006). *Ab-Initio Molecular Dynamics Simulations of Molten Ni-Based Superalloys*. Paper presented at the HPCMP Users Group Conference.

[134] Gu, J. P., Beckermann, C., & Giamei, A. F. (1997). Motion and Remelting of Dendrite Fragments during Directional Solidification of a Nickel-Base Superalloy. *Met. Trans. B*, *28A*, 1533-1542.

[135] Schneider, M. C., Beckermann, C., Boettinger, W. J., & Kattner, U. R. (1997). Modeling of Micro- and Macrosegregation and Freckle Formation in Single-Crystal Nickel-Base Superalloy Directional Solidification. *Metallurgical and Materials Transactions A*, *28A*, 1517-1531.

[136] Anton, D. L., & Giamei, A. F. (1985). Porosity Distribution and Growth During Homogenization in Single Crystals of a Nickel-base Superalloy. *Mat. Sci. Eng*, *76*, 173-180.

[137] Komenda, J., & Henderson, P. J. (1997). Growth of Pores During the Creep of A Single Crystal Nickel-Base Superalloy. *Scripta Materialia*, *37*(11), 1821-1826.

[138] Lecomte-Beckers, J. (1988). Study of Microporosity Formation in Nickel-Base Superalloys. *Met. Trans. A*, *19A*, 2341-2348.

[139] Link, T., Zabler, S., Epishin, A., Haibel, A., Bansal, M., & Thibault, X. (2006). Synchrotron Tompography of Porosity in Single-Crystal Nickel-Base Superalloys. *Mat. Sci. Eng. A*, *425*, 47-54.

[140] Kou, S. (1996). Selected Materials Processing Technologies. In *Transport Phenomena and Materials Processing* (pp. 375-377). New York, NY: John Wiley & Sons, Inc.

[141] Madison, J., Spowart, J. E., Rowenhorst, D. J., & Pollock, T. M. (2008). The Three-Dimensional Reconstruction of the Dendritic Structure at the Solid-Liquid Interface of a Ni-Based Single Crystal. *JOM*, *60*(7), 26-30.

[142] Jung, Y., & Torquato, S. (2005). Fluid Permeabilities of Triply Periodic Minimal Surfaces. *Physical Review E*, *72*, 53619-1 - 53619-8.

[143] Wang, C. Y., & Beckermann, C. (1993). A Multiphase Solute Diffusion Model for Dendritic Alloy Solidification. *Met. Trans. A*, *24A*, 2787-2802.

[144] Dvorkin, J. (2009). Personal Communication.

[145] Mavko, G., Mukerji, T., & Dvorkin, J. (2009). *The Rock Physics Handbook*. Cambridge University Press.

[146] Tin, S., Pollock, T. M., & Murphy, W. (2001). Stabilization of Thermosolutal Convective Instabillities in Ni-Based Single-Crystal Superalloys: Carbon Additions and Freckle Formation. *Metallurgical and Materials Transactions A*, *32A*, 1743-1753.

[147] Roper, S. M., Davis, S. H., & Voorhees, P. W. (2008). An Analysis of Convection in a Mushy Layer With a Deformable Permeable Interface. *J. Fluid Mech*, *596*, 333 - 352.

[148] Roper, S. M., Davis, S. H., & Voorhees, P. W. (2007). Convection in a Mushy Zone Forced by Sidewall Heat Lossess. *Metallurgical and Materials Transactions A*, *38A*(5), 1069 - 1079.

[149] (2006). Scripta Materialia Viewpoint Set on 3D characterization and analysis of materials. *Scripta Materialia*, *55 (1)*(1).

[150] (2006). Materials Characterization, Part II. *JOM*, *58 (12)*(12).

[151] (2008). Three-Dimensional Materials Science. *MRS Bulletin*, *33 (6)*(6).

[152] Buffiere, J.-Y., Cloetens, P., Ludwig, W., Maire, E., & Salvo, L. (2008). In Situ X-Ray Tomography Studies of Microstructural Evolution Combined with 3D Modeling. *MRS Bulletin*, *33*, 611-619.

[153] Chawla, N., Ganesh, V. V., & Wunsch, B. (2004). Three-Dimensional (3D) Microstructure Visualization and Finite Element Modeling of the Mechanical Behavior of SiC Particle Reinforced Aluminum Composites. *Scripta. Mat*, *51*(1), 161-165.

[154] Chawla, N., Sidhu, R. S., & Ganesh, V. V. (2006). Three-Dimensional Visualization and Microstructure-Based Modeling of Deformation in Particle-Reinforced Composites. *Acta Mat*, *54*, 1541-1548.

[155] Groeber, M. A., Ghosh, S., Uchic, M. D., & Dimiduk, D. M. (2008). A Framework for Automated Analysis and Simulation of 3D Polycrystalline Microstructures. Part 1: Statistical Characterization. *Acta Mat*, *56*, 1257-1273.

[156] Groeber, M. A., Ghosh, S., Uchic, M. D., & Dimiduk, D. M. (2008). A Framework for Automated Analysis and Simulation of 3D Polycrystalline Microstructures. Part 2: Synthetic Structure Generation. *Acta Mat*, *56*, 1274-1287.

[157] Hao, S., Liu, W. K., Moran, B., Vernerey, F. J., & Olson, G. B. (2004). Multi-scale constitutive model and computational framework for the design of ultra-high strength, high toughness steels. *Computational Methods in Applied Mechanics and Engineering*, *193*, 1865-1908.

[158] Jensen, D. J., Offerman, S. E., & Sietsma, J. (2008). 3DXRD Characterization and Modeling of Solid-State Transformation Processes. *MRS Bulletin*, *33*, 621-629.

[159] Khor, K. H., Buffiere, J.-Y., Ludwig, W., & Sinclair, I. (2006). High resolution X-ray tomography of micromechanisms of fatigue crack closure. *Scripta Materialia*, *55*, 47-50.

[160] Lapin, J., & Marecek, J. (2006). Effect of growth rate on microstructure and mechanical properties of directionally solidified multiphase intermetallic Ni-Al-Cr-Ta-Mo-Zr alloy. *Intermetallics*, *14*, 1339-1344.

[161] Lewis, A. C., & Geltmacher, A. B. (2006). Image-based modeling of the response of experimental 3D microstructures to mechanical loading. *Scripta Materialia*, *55*, 81-85.

[162] Thornton, K., & Poulsen, H. F. (2008). Three-Dimensional Materials Science: An Intersection of Three-Dimensional Reconstructions and Simulations. *MRS Bulletin*, *33*, 587-595.

[163] Vernerey, F. J., McVeigh, C., Liu, W. K., Moran, B., Tewari, D., Parks, D. M. et al. (2006). The 3-D Computational Modeling of Shear-Dominated Ductile Failure in Steel. *JOM*, *12*, 45-51.

[164] Wahab, A. A., Hutchinson, C. R., & Kral, M. V. (2006). A three-dimensional characterization of creep void formation in hydrogen reformer tubes. *Scripta Materialia*, *55*, 69-73.

[165] Iiada, T., & Guthrie, R. I. L. (1988). *The Physical Properties of Liquid Metals*. New York: Oxford University Press.

[166] Cape, J. A., & Lehman, G. W. (1963). Temperature and Finite Pulse-Time Effects in the Flash Method for Measuring Thermal Diffusivity. *J. Appl. Phys*, *34*, 1909-1913.

[167] Graham, S., McDowell, D. L., & Dinwiddie, R. B. (1999). Multidimensional Flash Diffusivity Measurements of Orthotropic Materials. *Int. J. Thermophysics*, *20*(2), 691-707.

[168] Kehoe, L., Kelly, P. V., & Crean, G. M. (1998). Application of the Laser Flash Diffusivity Method to Thin High Thermal Conductivity Materials. *Microsystem Technologies*, *5*, 18-21.

[169] Taylor, R. E. (1979). Heat-Pulse Thermal Diffusivity Measurements. *High Temperature - High Pressures*, *11*, 43-58.

[170] Taylor, R. E., & Cape, J. A. (1964). Finite Pulse-Time Effects in the Flash Diffusivity Technique. *Appl. Phys. Letters*, *5*, 212-213.

[171] Yang, S., Su, X., Wang, J., Yin, F., & Tang, N.-Y. (2009). Molecular Dynamics Analysis of Temperature Dependence of Liquid Metal Diffusivity. *Metallurgical and Materials Transactions A*, *40A*, 3108-3116.

[172] Alemany, M. M. G., Rey, C., & Gallego, L. J. (1998). Computer simulation study of the dynamic properties of liquid Ni using the embedded-atom model. *Phys. Rev. B*, *58*(2), 685-693.